A SPECTROSCOPIC STUDY OF POLYMER ELECTROLYTE MEMBRANES

A SPECTROSCOPIC STUDY OF STRUCTURE AND DYNAMICS IN PROTON-CONDUCTING POLYMERS FOR HYDROGEN FUEL CELLS

BY

Z. BLOSSOM YAN, B.Sc.

A Thesis Submitted to the School of Graduate Studies in Partial Fulfillment of the Requirements for the Degree DOCTOR OF PHILOSOPHY

McMaster University

McMaster University, Hamilton, Ontario
DOCTOR OF PHILOSOPHY (2018) Chemistry and Chemical Biology

TITLE: A Spectroscopic Study of Structure and Dynamics in Proton-Conducting Polymers for Hydrogen Fuel Cells

AUTHOR: Z. Blossom Yan, B.Sc. (McMaster University)

SUPERVISOR: Professor Gillian R. Goward

NUMBER OF PAGES: xxx, 235, A34

Lay Abstract

Proton exchange membrane fuel cells, which help to reduce the reliance on fossil fuels by locally producing only water and heat, have received a significant amount of research attention as an alternative power generator for vehicular and stand-alone energy applications. Perfluorosulfonic acid (PFSA) membranes, the most common commercial polymer electrolyte materials, have been investigated using modern analytical spectroscopies. Solid-state nuclear magnetic resonance (ssNMR) spectroscopy and synchrotron-based scanning transmission X-ray microscopy were used in elucidating material compositions with complementary information. Moreover, an advanced ssNMR method was developed and applied to a variety of PFSAs. Polymer backbones and side chains were separated spectroscopically, and were distinguished based on different local dynamics profiles extracted from the ssNMR experiments. Additionally, bulk material performance evaluations from electrochemical analyses were correlated to PFSA side chain local dynamics profiles. The integrated spectroscopic study illustrated in this thesis provided insight into understanding the structure-performance relationship of PFSA electrolytes.

Abstract

This thesis focuses on the state-of-the-art spectroscopic approaches in studying polymer electrolytes for proton exchange membrane fuel cells. With the aim to optimize architectural and chemical design of hydrogen fuel cells, a variety of perfluorosulfonic acid (PFSA) membranes were explored to establish characteristics that ultimately improve PFSA electrolyte performance. The results of the detailed spectroscopic analyses helped to unveil a structure-performance relationship. Solid-state nuclear magnetic resonance (ssNMR) spectroscopy was used to distinguish F and C environments, while scanning transmission X-ray microscopy coupled with X-ray absorption spectroscopy provided complementary chemical structural information with direct access to S and O environments. The combination of these two techniques provided advantages in identifying subtle chemical alterations in PFSAs. Furthermore, a novel ssNMR technique was developed with the purpose of probing local dynamics from the polymer perspective. This ^{19}F dipolar recoupling ssNMR approach was validated and applied to PFSA membranes by monitoring the normalized double quantum build-up curves as a function of relative humidity (%RH) and temperature, and the polymer side chain showed higher local motion as response to temperature and %RH elevation compared to the backbone. The effective dipolar coupling constant was extracted to represent local dynamics and compared amongst tested PFSAs. A standardized metric, the dynamic order parameter, was also introduced and applied to the materials to quantitatively compare them within the same class. This new method provided an alternative way to extract site-specific local dynamics profile for materials with multiple resonances. Additionally, the combination of *in situ* fuel cell performance evaluation and *ex situ* ssNMR characterization created a connection between fundamental chemistry and bulk electrochemical measurements. As the first study to correlate these physicochemical properties to material performances, this work parameterized the structural impact at a molecular level and provided insight into improving polymer electrolyte materials.

Acknowledgements

First and foremost, I would like to give my sincerest gratitude to my thesis advisor, Prof. Gillian Goward, for her incredible support and guidance. I consider myself very lucky that Gillian actually trained me on the spectrometer herself when I was an undergraduate summer research student. She offered me her patience, encouragement and friendship throughout my graduate studies. Gillian has given me a lot of freedom and trust such that I can manage my own projects and make decisions based on my research interests. With her support, I have had many opportunities to travel across North America to attend scientific conference meetings and participate in research collaborations, especially my industrial internship at Ballard Power Systems in Burnaby, BC. She is like a research mother to me, and I do not know a better way to express my thanks.

I am also very grateful to my two supervisory committee members: Prof. Adam Hitchcock and Prof. Darren Brouwer. They do not only serve as helpful committee members providing insightful comments regarding my research, but also more importantly as collaborators and mentors during my studies. I have been on many trips with Adam to the synchrotron facilities. We worked, hiked and road tripped as a team. His enthusiasm towards science and life has impacted me so much. Working alongside him has taught me how to be a serious scientist with open mind, critical thinking and optimism and also how to enjoy life and nature. Darren is also irreplaceable. Without his help, my research project might have been stalled for a significant amount of time. Seeing Darren at conferences always made me feel more at home. His wisdom and patience have shown me how to be a good teacher and a great listener. I am very fortunate that I have worked closely with my committee, and I have co-authored journal articles with each of them. Special thanks to my internship supervisor, Alan Young, at Ballard Power Systems, and the water management team, for training me, sharing their ideas and giving me all the support I needed in writing manuscripts. The success of our collaborated work would not be possible without him and his team.

I also wish to thank Dr. Bob Berno, Dr. Hilary Jenkins, Megan Fair, and Dr. Steve Kornic. Without their tireless efforts in training me at the beginning, troubleshooting along the way, and caring for the spectrometer, there would have been no research results for me. For their guidance and support, thank you to my TA supervisors Dr. Peter Kruse, Dr. Linda Davis, Dr. Randall Dumont, Dr. Guiseppe Melacini.

Moreover, my thanks go to all of my colleagues in the current and past Goward lab. Thank you to Lis, Xiaohui, Vincent and Slava from the Hitchcock lab for all the help and support with the STXM measurements. Special thank you to two past Goward group members: Leigh and Linda, for showing me how to be a good PhD student.

I also want to extend my thanks to the Department of Chemistry and Chemical Biology and all of the professors and TAs that taught me in my undergraduate and graduate studies. Without your help, there will not be a scientist Blossom. I want to extend my thanks to the provincial government of Ontario and Natural Sciences and Engineering Research Council of Canada for financial support.

For their unconditional love and eternal support, thank you so much to my amazing parents. Thank you for all the homemade food and road trips to cheer me up when I get stressed out. Thank you to my buddies, Sam and Steph, for years of friendship. Thank you to the 'Brains of Castamere' team, Annica, Chris, and Dave, for all the beers and cheers. Big thank you to my best buddy, Danielle Smiley, for all the memories, good and bad. Our paths in life are meant to be crossed, and I am sure of it.

Finally, my thanks go to my partner and former colleague, my Adam, or Dr. MacIntosh. I am so glad we met and we are together. Thank you for being so patient with me. Thank you for being the calm counter part of me for almost everything. I cannot wait for our journey together in the future.

TABLE OF CONTENTS

LAY ABSTRACT III

ABSTRACT IV

ACKNOWLEDGEMENTS V

TABLE OF CONTENTS VIIII

LIST OF FIGURES XIIIII

LIST OF TABLES XX

SYMBOLS AND ABBREVIATIONS XXIIII

DECLARATION OF ACADEMIC ACHIEVEMENT XXX

1. INTRODUCTION TO THE HYDROGEN FUEL CELL 1

1.1 THESIS LAYOUT 1

1.2 INTRODUCTION TO POLYMER ELECTROLYTE MEMBRANE FUEL CELL 4

1.2.1 Motivation for Fuel Cell Development 4
1.2.1.1 The Concept of a Fuel Cell 4
1.2.1.2 Development of the Fuel Cell: The Choice of Solid Electrolytes 4
1.2.1.3 Development of the Fuel Cell: The Use of Carbon 7
1.2.1.4 The Industry: Moving Forward 7

1.2.2 Principles of A Fuel Cell 9

1.2.3 Proton Exchange Membrane Fuel Cell 13
1.2.3.1 Important Reactions 14
1.2.3.2 Design of a Proton Exchange Membrane Fuel Cell 15
1.2.3.3 Issues and Challenges 17

1.3 SOLID POLYMER ELECTROLYTES 18

1.3.1 Historical Development of PEM 18

1.3.2 Perfluorosulfonic Acid Polymer 19
1.3.2.1 Nafion 20
1.3.2.2 Nafion Alternatives 23

1.3.3 Ionomer Material 25

1.4 EVALUATION OF SOLID POLYMER ELECTROLYTES 26

1.5 REFERENCES 27

2. METHODOLOGY 32

2.1 SOLID-STATE NMR SPECTROSCOPY 32

2.1.1 Interaction with External Magnetic Fields 33
2.1.1.1 Spin Behavior in an Applied Magnetic Field 33
2.1.1.2 Zeeman Splitting 35
2.1.1.3 Radiofrequency Pulses 37

2.1.2 Internal Interactions 39
2.1.2.1 Chemical Shielding 41
2.1.2.2 The Dipolar Interaction 44
2.1.2.3 Magic Angle Spinning 48

2.1.3 Nuclei Investigated in This Thesis 51

2.1.4 Dipolar Recoupling Method 51
2.1.4.1 Method Development for PFSA System 53
2.1.4.2 Recoupling Sequence Comparison 55
2.1.4.3 Normalization of DQ Build-Up Curve 58
2.1.4.4 Study of Fluorinated Polymers 60
2.1.4.5 Quantification of Dipolar Interaction 66
2.1.4.6 Robustness and Sensitivity Evaluation 67

2.2 STXM SPECTROSCOPY 72

2.2.1 Synchrotron Radiation 72

2.2.2 Beamline Instrumentation 73

2.2.3 Scanning Transmission X-ray Microscopy (STXM) 74

2.3 ELECTROCHEMICAL ANALYSIS 76

2.3.1 Cyclic Voltammetry 76
2.3.1.1 The Fundamentals 77
2.3.1.2 Application in Fuel Cell Research 78

2.3.2 Impedance Spectroscopy 79
2.3.2.1 The Fundamentals 79
2.3.2.2 Application in Fuel Cell Research 79

2.4 SUMMARY 80

2.5 REFERENCES 82

3. X-RAY ABSORPTION AND NMR SPECTROSCOPY OF FLUORINATED PROTON CONDUCTING POLYMERS 88

3.1 INTRODUCTION 88

3.2 EXPERIMENTAL 91

3.2.1 Materials and Sample Preparation 91
3.2.1.1 Membrane Sample Activation 91
3.2.1.2 Cast Film Preparation 91
3.2.1.3 Ionomer Dispersions for NMR Study 92

3.2.2 X-ray Absorption Spectroscopy 92

3.2.3 NMR Spectroscopy 94

3.3 RESULTS 95

3.3.1 X-ray absorption spectra 95
3.3.1.1 C 1s spectra 95
3.3.1.2 F 1s spectra 98
3.3.1.3 O 1s spectra 100
3.3.1.4 S 2p spectra 105

3.3.2 NMR Spectroscopy 108
3.3.2.1 ^{19}F NMR Spectroscopy 108
3.3.2.2 ^{13}C NMR Spectroscopy 111
3.3.2.3 Diffusion Profile Analysis 113
3.3.2.4 Concentration Dependent Diffusion Profile Analysis (Collaboration with AFCC) 116

3.4 DISCUSSION 125

3.5 SUMMARY 127

3.6 REFERENCES 130

4. ^{19}F DQ NMR – A NEW TOOL FOR PROBING DYNAMICS IN NAFION 138

4.1 INTRODUCTION 138

4.2 EXPERIMENTAL 140

4.2.1 Preparation of Fluorinated Polymer Materials 140

4.2.2 Relative Humidity Control for NMR Samples 141

4.2.3 ^{19}F NMR 141

4.3 RESULTS AND DISCUSSION 142

4.3.1 Spectral Resolution of Nafion 142

4.3.2 Dynamics Analysis: Nafion 143

4.3.3 Dynamic Order Parameter for Comparison of Perfluorinated Ionomers 148

4.4 SUMMARY 155

4.5 REFERENCES 157

5.LOCAL DYNAMICS OF PFSA MATERIALS: A ^{19}F SOLID-STATE NMR METHOD 162

PART 1

5.1 INTRODUCTION 162

5.2 EXPERIMENTAL 165

5.2.1 Activation of PFSA Membranes 165

5.2.2 Relative Humidity Regulation for Membranes 166

5.2.3 ^{19}F NMR Spectroscopy 166

5.3 RESULTS AND DISCUSSION 167

5.3.1 NMR Spectral Resolution 167

5.3.2 Local Dynamics Analysis 170

5.4 SUMMARY 180

PART 2

5.5 INTRODUCTION 181

5.6 METHODS 184

5.6.1 Electrochemical Analysis 184
5.6.1.1 Membrane Electrode Assembly (MEA) Preparation: A Single Cell Assembly 184
5.6.1.2 Electrochemical Characterizations 185

5.6.2 NMR Analysis 187
5.6.2.1 PFSA Materials and Preparation 187
5.6.2.2 Relative Humidity and Thermal Control 188
5.6.2.3 ^{19}F NMR Spectroscopy Dynamics Study 188

5.7 RESULTS AND DISCUSSION 190

5.7.1 Conductivity 191

5.7.2 Gas Permeability: H_2 Crossover 193

5.7.3 Local Dynamics Profile Parameter 197

5.7.4 Correlation between Local Motion and Performance 200

5.8 SUMMARY 210

5.9 REFERENCES 212

6. SUMMARY AND OUTLOOK 221

6.1 SUMMARY 221

6.1.1 Spectroscopic Analysis of PFSA 222

6.1.2 Dynamics Analysis Using ^{19}F Homonuclear Dipolar Recoupling Sequence 224

6.1.3 Linking the Material Performance to the Molecular Physicochemical Properties 225

6.2 FUTURE WORK AND OUTLOOK 228

6.3 REFERENCES 233

APPENDIX 1. MATERIAL PERFORMANCE STUDY A1

A.1.1 INTRODUCTION A1

A.1.2 EXPERIMENTAL A3

A.1.3 RESULTS AND DISCUSSION A4

A.1.3.1 Polarization Curves of MEAs A4

A.1.3.2 PFSA Membrane Resistance A5

A.1.4 SUMMARY AND REMARK A7

A.1.5 REFERENCES A8

APPENDIX 2.GAS PERMEABILITY STUDY A9

A.2.1 INTRODUCTION A9

A.2.2 METHODOLOGY A10

A.2.2.1 Time-Lag Method A10

A.2.2.2 ORR Limiting Current Analysis using RDE A11

A.2.3 RESULTS AND DISCUSSION A12

A.2.3.1 Gas Permeability Using Time-Lag Method A12

A.2.3.2 Limiting Current Analysis of the ORR using RDE A17

A.2.4 SUMMARY AND REMARK A22

A.2.5 REFERENCES A23

APPENDIX 3.PULSE SEQUENCE FOR ^{19}F DIPOLAR RECOUPLING NMR A24

APPENDIX 4.PULSE SEQUENCE FOR DIFFUSION NMR A29

APPENDIX 5.CALCIUM L-EDGE XAS ANALYSIS A34

LIST OF FIGURES

Figure 1. 1 Schematic drawing of a proton exchange membrane fuel cell, which is an example of a hydrogen/oxygen fuel cell system. **10**
Figure 1. 2 Fuel cell stack with flow field plates (or bipolar plates) and MEAs. (Figure reproduced from Ref.3) **17**
Figure 1. 3 Chemical structure of a copolymer Nafion, LSC-PFSA, where m is indicative of EW. It has a PTFE backbone and a perfluorinated polyvinyl ether side chain. **20**
Figure 1. 4 Chemical structures for two types of Nafion alternative PFSA materials: a) SSC-PFSA, commercially known as Aquivion; b) a new PFSA material delivered by 3M Company. They both only have one ether group in the side chain structure. **24**
Figure 2. 1 The quantized angular momentum values for I=1/2, 1 and 3/2. ..... **34**
Figure 2. 2 Energy level diagram of a spin 1/2 nucleus, showing the Zeeman splitting. **36**
Figure 2. 3 External magnetic field in the laboratory frame, B_0, is the applied field along z-axis. B_1 is the pulsed RF field applied in the xy-plane that is perpendicular to B_0. The coil represents the RF coil used in the spectrometer. **38**
Figure 2. 4 Demonstration of Euler angles used during frame transformations. The original axes are x, y, and z; while the new axes after rotation are X, Y, and Z. The dash line represents the N axis. During the transformation from the laboratory frame to principal axis system, angles α (or ϕ) and β (or θ) are important. **42**
Figure 2. 5 Pictorial representation of dipole-dipole interaction between two spins with respect to the external magnetic field. **47**
Figure 2. 6 The schematic double quantum filter (dipolar recoupling) NMR pulse sequence, which consist of the excitation, reconversion blocks and a read-out pulse before acquisition. **52**
Figure 2. 7 a) ^{19}F 15 kHz MAS NMR spectrum of Nafion 117 at ambient condition. b) Normalized DQ build-up curves using BABA pulse sequence. c) Normalized DQ build-up curves using $R26_4^{11}$ pulse sequence. Both b) and c) were analyzed in the same way, i.e. mathematically normalization as described previously. **58**
Figure 2. 8 Pseudo 2D ^{19}F NMR spectrum of PTFE under 15 kHz MAS, with alternating DQ and reference experiments. **59**
Figure 2. 9 Point-by-point normalization of the DQ term with experimental curves plotted. a) One set of the DQ NMR experimental curves: Absolute signal intensities for DQ and reference experiments as functions of DQ evolution time; ΣMQ is the sum of DQ and reference intensities. b) Normalized DQ curve based on the dataset in a). **60**
Figure 2. 10 ^{19}F 15 kHz MAS NMR spectra for a) PVDF membrane, where * indicates the spinning side bands for peak 1 and # indicates the spinning side bands for peak 2,3; b) PTFE membrane, where * indicates the spinning side bands. **61**
Figure 2. 11 The nDQ build-up curve comparison between PTFE and PVDF membranes at 310 K – 370 K. The curves are colour-coded with respect to temperatures. **62**

Figure 2. 12 The nDQ build-up curve comparison between PTFE membrane and powder at 310 K – 370 K. The curves are colour-coded with respect to temperatures. **65**

Figure 2. 13 a) Comparison of the *nDQ* build-up curves under $R26_4^{11}$ recoupling for isolated spin pair with D = 10 kHz and calculated curve. b) Simulated *nDQ* build-up curves with different apparent dipolar coupling constants, ranging from D_{app} = 10 kHz to 2 kHz. **67**

Figure 2. 14 Simulated *nDQ* build-up curve comparison between 0 ppm CSA span (red) and 100 ppm span (grey). **68**

Figure 2. 15 The graphical demonstration of the fitting deviation. **69**

Figure 2. 16 Dipolar coupling constant deviation as a function of the CSA magnitude. **69**

Figure 2. 17 Dipolar coupling constant deviation as a function of the offset frequency. **70**

Figure 2. 18 Offset effect is demonstrated by comparing the D_{app} values of three different fluorine sites (OCF_2 and CF_3 at -80 ppm, backbone CF_2 at -122 ppm, and SCF_2 at -117 ppm) at a range of temperatures with two different transmitter frequencies. **71**

Figure 2. 19 Schematic representation of ALS BL 5.3.2 and STXM.[40] **74**

Figure 2. 20 The schematic diagram of STXM microscope, which often consist of zone plate, OSA and a photon-counting detector.[41] **75**

Figure 2. 21 Schematic representation of a typical CV experiment: a) voltage sweep linearly back and forth between two voltage limits; b) typical CV voltammogram (duck-shape).[46, 50] **78**

Figure 2. 22 Transmission line equivalent circuit model used in fuel cell impedance evaluation.[52] **80**

Figure 3. 1 (a) Optical density (*OD*) image of an ultramicrotomed section of Nafion 117 PFSA, recorded with scanning transmission X-ray microscopy (STXM) at 200 eV. The yellow rectangle indicates the region for spectral study (blue rectangle in **Figure 3. 1b**) which was chosen to include an open area (rip in the microtomed section) to use as an internal Io. (b) *OD* image measured at 292.6 eV after measuring stacks at all 4 edges (F 1s, C 1s, O 1s and S 2p) using a 200 nm defocused beam. The stacks were measured in the area outlined by the blue dashed rectangle. This area was subjected to a total exposure time per pixel of 600 ms. **93**

Figure 3. 2 C 1s X-ray absorption spectra of Nafion 117, Aquivion 98, 3M 725 and polytetrafluoroethylene (PTFE) recorded using STXM. The spectra have been converted to an absolute intensity scale (optical density/nm thickness at standard density, *OD1*) using the procedures described in the text. Peak positions and tentative assignments are given in **Table 3.1.** **96**

Figure 3. 3 F 1s X-ray absorption spectra of Nafion 117, Aquivion 98 and 3M 725 recorded using STXM. The spectra have been converted to an absolute intensity scale (optical density/nm thickness at standard density, *OD1*) using the procedures described in the text. Peak positions and tentative assignments are given in **Table 3.2.** **99**

Figure 3. 4 (a) O 1s X-ray absorption spectra of Nafion 117, Aquivion 98 and 3M 725 recorded using STXM. The spectra have been converted to an absolute intensity scale (optical density/nm thickness at standard density, *OD1*) using the procedures described in the text. Peak positions and tentative assignments are given in **Table 3.3.** (b) O 1s spectra of H_2SO_4 and CH_3SO_3H. The absence of a feature at 532.0 eV indicates that the pre-peak observed in PFSA materials is not due to O 1s $\rightarrow \sigma^*_{O-H}$ or O 1s $\rightarrow \sigma^*_{S=O}$ transitions at the sulfonate group. **100**

Figure 3. 5 O 1s spectra of PFSA 825 and 770. The two PFSA materials were obtained from the Holdcroft Group at Simon Fraser University. The sample treatment history was untraceable. The difference in a feature at 532.0 eV suggests that the pre-peak observed in PFSA materials is due to O 1s $\rightarrow \sigma^*_{O-H}$ transition at the sulfonate group determined by different levels of protonation of the two PFSA. PFSA 825 has less intense transition at 532.0 eV, which shows the lower degree of protonation compared to PFSA 770. The Ca 2p spectra of the same materials were collected to detect possible cation contamination (shown in **Appendix 5**). The results suggest that there is a high Ca content in PFSA 825. ..... **102**

Figure 3. 6 (a) O 1s spectra of 5 sulfonate species. The spectra of the two ionic species are NEXAFS, measured using STXM. The spectra of the three molecular species are ISEELS recorded in the gas phase. (b) Plot of a σ^*_{S-O-H} orbital in methyl sulfonic acid from GSCF3 (Gaussian Self-Consistent Field version 3)[45] *ab initio* calculations. (c) Molecular orbital (MO) plots of 3 lowest unoccupied MOs from GSCF3 *ab initio* calculations of O 1s (S=O) excited methyl sulfonic acid, showing a dominant σ^*_{S-O} character. **103**

Figure 3. 7 (a) Comparison of O 1s spectra of Dupont ionomer (Nafion dispersion supplied by Ion Power Inc., mentioned in *3.2.1.3*) and Nafion 117 membrane. (b) Comparison of C 1s spectra of Dupont ionomer and Nafion 117 membrane. All spectra were measured in STXM using no-damage defocused beam conditions. **104**

Figure 3. 8 Comparison of NEXAFS spectra of PFSA membranes (microtomed) and spun cast films of ionomer dispersions. (a) C 1s. (b) O 1s. (c) F 1s. (d) S 2p. **105**

Figure 3. 9 S 2p X-ray absorption spectra of Nafion 117, Aquivion 98 and 3M 725 recorded using STXM. The as-recorded *OD* spectra were subjected to a spline fit to generate the non-sulfur background by extrapolating the pre-S 2p signal, which was then subtracted. The intensity scale was then set by matching to similarly background subtracted elemental response functions (*OD1*-S 2p). Further details are described in the text. Peak positions and tentative assignments are given in **Table 3.4.** **106**

Figure 3. 10 (a) S 2p spectra of 5 sulfonate species (quantitative intensity scales). The two ionic species are NEXAFS, measured using STXM. The three molecular species are ISEELS spectra recoded in the gas phase. (b) Expanded view of the lowest energy peak in the 3 molecular species. **107**

Figure 3. 11 ^{19}F MAS ssNMR of Nafion 117, Aquivion 98 and 3M 725. The * indicates spinning side bands. Different fluorine sites are labeled accordingly, separating the side chain and backbone signals based on the chemical shifts. Spectral intensities and assignments are given in **Table 3.5.** **109**

Figure 3. 12 ^{13}C ssNMR of (a) Nafion 117, (b) Nafion (EW1100) spun cast film, (c) Liquion (EW1100) spun cast film. **113**
Figure 3. 13 Plot of temperature dependent proton diffusion coefficients in Nafion and Liquion liquid dispersions. **115**
Figure 3. 14 Solution state ^{19}F NMR spectra for all the ionomer solutions. Solution concentrations are labeled as 'Ink conc.' and 'Overlap conc.' to help to distinguish a and b solutions in each pair. 1a,b and 2a,b share spectral similarity, which reflects the same ionomer in both pairs. 3a,b is Nafion-like LSC-PFSA, therefore both spectra have different spectral features: two distinguishable CF signals. **118**
Figure 3. 15 The diffusion profile comparison of sample 1a and 1b, using Dynamic Center software. Aquivion structure is used here to demonstrate results from a non-LSC PFSA material. The dashed lines serve as a guide for diffusion coefficient comparison. The 2D plot illustrates the diffusion coefficient as a function of chemical shift, and the contour indicates the signal intensities. **120**
Figure 3. 16 The diffusion profile for sample 2b, analyzed using Bruker's Dynamic Center software. **121**
Figure 3. 17 The diffusion profile comparison of sample 3a and 3b, using Dynamic Center software. Two sets of dashed lines are drawn here to demonstrate the difference in diffusion coefficients of polymer backbone and side chain signals. **123**
Figure 4. 1 The chemical structure of polymer material, long-side-chain PFSA (Nafion), and corresponding ^{19}F 15 kHz MAS NMR spectrum. Asterisks represent the spinning side bands. **143**
Figure 4. 2 A typical set of experimental *nDQ* curves of OCF_2/CF_3 (at -80 ppm) over a temperature range, which is used to extract dynamics information in the current study. Solid data points are used in the curve fitting to extract the apparent dipolar coupling constant D_{app}^{T} values from each data set. **144**
Figure 4. 3 The D_{app}^{T} value comparison of backbone branching point and side-chain terminal fluorines of Nafion 117 treated at 50 %RH (hydration level parameter, $\lambda \approx 4$) at 310 K – 370 K (a). The parallel analyses of backbone and side-chain fluorines of Nafion 117 treated at 100 %RH (hydration level parameter, $\lambda \approx 14$) are demonstated as (b). The solid line represents the trend line for the backbone signal while the dashed line highlights the behavior of the side-chain terminal SCF_2 signal. **146**
Figure 4. 4 The structures of C_6F_{14} (a) and $C_7F_{14}O_4S$ (b) are used in the D_{app}^{0} calculations. **150**
Figure 4. 5 Dynamic order parameter analyses for four fluorine sites: a) side-chain peak that corresponds to OCF_2 and CF_3 at -80 ppm; b) terminal side-chain SCF_2 signal at -117 ppm; c) backbone CF_2 at -122 ppm; d) branching point CF located on backbone at -138 ppm. The grey squares represent the values extracted for $\lambda \approx 4$ condition, while the clear dots demonstrate the values at $\lambda \approx 14$. **153**

Figure 4. 6 Pseudo-Arrhenius analysis of dynamic order parameters. a) side-chain terminal side-chain SCF_2 signal at -117 ppm; b) backbone branching point CF located on backbone at -138 ppm. The grey squares represent the $\lambda \approx 4$ condition, while the clear dots represent $\lambda \approx 14$. **154**

Figure 5. 1 ^{19}F MAS ssNMR spectrum of Nafion with deconvolution. Different fluorine sites are resolved and colour-coded based on the chemical structure. Asterisks represent the spinning side bands. **167**

Figure 5. 2 ^{19}F MAS ssNMR spectra with deconvolution: a) Aquivion (Aquivion 98 as an example); b) 3M (3M 825 as an example). Different fluorine sites are resolved and colour-coded based on the chemical structure. Asterisks represent the spinning side bands. **168**

Figure 5. 3 a) Stack plot of ^{19}F VT NMR spectra of 3M 825 PFSA. b) Detailed chemical structure of 3M 825 PFSA, with more specific fluorine site assignments: peak at -116 ppm is the side chain CF_2 in blue, while the one at -123 ppm is the backbone CF_2 group located the furthest from the branching point in green. **170**

Figure 5. 4 The *nDQ* build-up curves of Nafion (normalized DQ intensities against dipolar coupling time): a) backbone and b) side chain fluorines treated at 100 %RH at the temperature range 310 – 370 K. The parallel analyses of backbone and side chain fluorines of Nafion 117 treated at 50 %RH are demonstrated in c) and d). The data sets were coloured with corresponding temperatures. **171**

Figure 5. 5 D^T_{app} value comparisons of different fluorine sites of Aquivion and 3M PFSAs treated at 50 %RH (a, c, e, g) and 100 %RH (b, d, f, h). SCF_2- blue diamond points; CF_2- grey triangle points; CF- green square points; OCF_2- coral round points. Each pair of graphs represent one PFSA: Aquivion 98: a, b; Aquivion 87: c, d; 3M 825: e, f; 3M 725: g, h. **175**

Figure 5. 6 Structures of $C_4F_8O_3S$ (a) and $C_6F_{12}O_3S$ (b) are used in the D^0_{app} calculations for Aquivion and 3M PFSAs. **177**

Figure 5. 7 Dynamic order parameter analyses for CF and SCF_2 for Aquivion and 3M PFSAs. Each pair of graphs represent one PFSA: Aquivion 98: a, b; Aquivion 87: c, d; 3M 825: e, f; 3M 725: g, h. The grey squares represent the values extracted for 50 %RH, while the white circles demonstrate the values at 100 %RH. **179**

Figure 5. 8 Polymer conductivities at various %RH measured using EIS at Ballard research test station of different PFSA membranes: a) at 40 °C; b) at 80 °C. (Solid red square-3M725; Hollow red square-3M825; Light blue diamond-AQ870; Blue diamond-AQ980; Green triangle-NR211) **192**

Figure 5. 9 Example of CV curve (voltammogram) of NR211 MEA stack, where the crossover current density (arrow between the two dash lines) is identified as the offset from the mid-point of the double-layer current density (green dash line) to the zero value (grey dashed line). **194**

Figure 5. 10 H_2 crossover current measurements of PFSA at various %RH at a) 40 °C and b) 80 °C, the value variation among PFSAs was as a function of material thickness. H_2 permeability of PFSAs was calculated by normalizing the thickness of the materials, and then compared with respect to different temperature and %RH conditions in c) for 40 °C and d) for 80 °C. As the %RH increases, the permeability of H_2 increases. High temperature gives higher permeability as well when comparing d) to c). **196**

Figure 5. 11 ^{19}F MAS NMR spectra for three types of PFSAs with deconvolutions: a) Nafion (Nafion 117); b) Aquivion (Aquivion 98) c) 3M (3M 725). The experimental spectra are black, the deconvoluted resonances are red, and the spectral residue is navy located at the bottom of each set. Different fluorine sites are well labeled, and the purple shades indicate the side chain SCF_2 fluorine is the focus to reveal the local dynamics. Asterisks represent NMR spinning side bands. **200**

Figure 5. 12 Correlation between bulk membrane conductivity *via* EIS and local dynamics parameter, D_{app}, of the polymer side chain, SCF_2. Top left: at 80 °C, 100 %RH (red hollow squares). Bottom left: at 40 °C, 100 %RH (blue hollow circles). Top right: at 80 °C, 50 %RH (red solid squares). Bottom left: at 40 °C, 50 %RH (blue solid circles). Center plot: The overall correlation is summarized with color-coded regions indicating different conditions. The dashed curve is the exponential fitting of the overall correlation, which is illustrated in all parts. **204**

Figure 5. 13 A schematic demonstration of proton transport mechanisms.[67] a) Surface proton hopping between sulfonic acid groups and water molecules; b) Grotthuss mechanism between water molecules, and hydronium bulk diffusion (dashed line). **205**

Figure 5. 14 Correlation between H_2 permeability and local dynamics parameter, D_{app}, of the polymer side chain, SCF_2. Similar data point labeling scheme is applied here, as seen in Figure 5: 80 °C, 100 %RH - red hollow squares; 80 °C, 50 %RH - red solid squares; 40 °C, 100 %RH - blue hollow circles; 40 °C, 50 %RH - blue solid circles. The dashed exponential fitting is illustrated to represent the correlation for 80 °C data set, while the solid exponential fitting is for that at 40 °C. **207**

Figure 5. 15 Correlation between H_2 permeability and local dynamics parameter, D_{app}, of the polymer backbone, CF_2. Similar data point labeling scheme is applied here, as seen in Figure 5 and 6: 80 °C, 100 %RH - red hollow squares; 80 °C, 50 %RH - red solid squares; 40 °C, 100 %RH - blue hollow circles; 40 °C, 50 %RH - blue solid circles. The dashed exponential fitting is illustrated to represent the correlation for 80 °C data set, while the solid exponential fitting is for that at 40 °C. **209**

Figure A1. 1 Ideal polarization curve for an operating polymer electrolyte membrane fuel cell (PEMFC), with corresponding labels for different losses.[1, 2] [Reprinted with permission from Ref.2] **2**

Figure A1. 2 An example set of polarization curves with SL and DL MEA designs using NR211 membrane. The experiments were performed with 100% O_2 or 21% O_2 at 100 %RH 80 °C. **5**

Figure A1. 3 PFSA conductivity comparison between two different electrochemical methods: EIS and polarization performance analysis. **7**

Figure A2. 1 A set of permeability curves of NR211 MEA (SL PFSA) using time-lag method under four different gas conditions. a) N_2/N_2. b) $N_2/H2$. c) O_2/N_2. d) O_2/H_2. The line of best fit was resulted from linear regression analysis. **13**

Figure A2. 2 P_{H_2} comparison between the CV method and the time-lag method. Only three MEAs passed the leakage-imaging test (infrared camera), which were reported here. **14**

Figure A2. 3 Correlation between H_2 and O_2 permeability of the three MEAs tested using the time-lag method. The linear correlation is function: y=1.5x. **15**
Figure A2. 4 H_2 permeability comparison from CV analyses conducted in 2016 and 2017, along with information calculated from the time-lag method obtained in 2017. ..... **16**
Figure A2. 5 Work flow chart of ORR study using RDE. Objective – anion adsorption has been greyed out. The explanation is stated below... **17**
Figure A2. 6 The CV performance of bare Pt electrode comparison, and each analysis was done in three cycles: blue – ideal CV curves; black – non-ideal CV curves. **19**
Figure A2. 7 Limiting current comparison between bare Pt electrode and electrode coated with thin PFSA layer, at different rotating speeds. **20**

LIST OF TABLES

Table 1. 1 The different types of fuel cell systems that have been developed. The electrical efficiency values are gathered from the Fuel Cell Fact Sheet reports by the United States Department of Energy Hydrogen Program in 2006 and 2015.[26-27] **13**
Table 1. 2 Properties of membranes from literatures including ionic conductivity and glass transition temperatures (T_g). [46-47] **24**
Table 2. 1 Table of nuclei investigated in this thesis. **51**
Table 3. 1 Summary of peak positions and tentative assignments for spectral features in the C 1s spectra of PTFE, Nafion 117, Aquivion 98 and 3M 725. ..... **96**
Table 3. 2 Summary of peak positions and tentative assignments for spectral features in the F 1s spectra of PTFE, Nafion 117, Aquivion 98 and 3M 725. ..... **99**
Table 3. 3 Summary of peak positions and tentative assignments for spectral features in the O 1s spectra of Nafion 117, Aquivion 98 and 3M 725. ..... **100**
Table 3. 4 Summary of peak positions and tentative assignments for spectral features in the S 2p spectra of Nafion 117, Aquivion 98 and 3M 725. ..... **106**
Table 3. 5 Summary of peak positions (ppm), normalized relative intensities and assignments for spectral features in the ^{19}F MAS ssNMR spectra of Nafion 117, Aquivion 98 and 3M 725. ..... **110**
Table 3. 6 Information of ionomer dispersion solutions obtained from AFCC. **116**
Table 3. 7 Summary of diffusion coefficients for water molecules in different solvent systems. **117**
Table 3. 8 Summary of diffusion coefficients of 1a,b. Each resolved fluorine signal was analyzed and the overall average of all the sites representing the entire molecule is also stated here. **120**
Table 3. 9 Summary of diffusion coefficients of 2b. 2a has such low ionomer concentration, thus more experiments are needed to extract diffusion information. Each resolved fluorine signal was analyzed and the overall average of all the sites representing the entire molecule was also stated here. **121**
Table 3. 10 Summary of diffusion coefficients of 3a,b. Each resolved fluorine signal was analyzed and the overall average of all the sites representing the entire molecule was also stated here. **124**
Table 4. 1 D_{app} values extracted from the nDQ build-up curves in different %RH conditions at various temperatures. **145**
Table 4. 2 Summary of calculated dipolar coupling constants (between two fluorine nuclei) in model compound C_6F_{14}. Only interactions with internuclear distance within 5 Å were considered in the current study. **151**
Table 4. 3 D_{app}^{0} values for different fluorine sites in Nafion calculated based on the simplified model shown in **Figure 4.4** using **Equation 2.32.** **151**
Table 4. 4 Summary of slope values for the pseudo-Arrhenius analysis, for side chain SCF_2 and backbone CF. **154**

Table 5. 1 Summary of PFSA membranes materials used in this study, including their chemical compositions, and EWs. EW = 100× mass of PFSA per side chain. It is the unit molecular weight per sulfonic acid group. **165**
Table 5. 2 The summary of D^{T}_{app} values of spectroscopically resolved fluorine sites for the Aquivion and 3M PFSA samples. **173**
Table 5. 3 D^{0}_{app} values for all the fluorine sites in Aquivion and 3M PFSAs calculated based on the simplified models shown in **Figure 5.6.** **177**
Table 5. 4 Swelling test: PFSA thickness measurements before and after 80 °C water bath. **191**
Table A1. 1 Summary of PFSA resistance and conductivity in this study. **A6**

SYMBOLS AND ABBREVIATIONS

%RH	relative humidity
$\langle \phi^2 \rangle$	phase factor
2D	two-dimensional
α, β, γ	Euler angles used during rotation
$\alpha, \beta, \gamma, \delta$	different fluorine sites (Chapter 3.3)
a	pre-exponential factor in exponential fitting
A	active area
A	electrode area (Appendix 2)
AC	alternate current
AFC	alkaline fuel cell
AFCC	Automotive fuel cell cooperation
ALS	Advanced light source
b	exponential decay constant in exponential fitting
$\vec{B}_0$	external magnetic field
$\vec{B}_1$	applied RF field
BABA	Back-to-Back
BPS	Ballard Power System
C	analyte concentration (Appendix 2)
C^*	ionomer overlap concentration
C_{H^2}	H_2 gas concentration on the active electrode
CaRPE-FC	catalysis research for polymer electrolyte fuel cells
C_{dl}	double layer capacitance
C_{H^+}	concentration of proton produced
CL	catalyst layer

CLS	canadian light source
CSA	chemical shielding anisotropy
CV	cyclic voltammetry
δ	chemical shift
δ	length of the gradient pulse (Chapter 3.2)
Δ	diffusion time (Chapter 3.3)
Δ	shielding anisotropy
ΔE_0	the potential difference between the anode and the cathode of the cell at thermodynamic equilibrium
ΔG	the change in Gibbs free energy
ΔH	the enthalpy of a reaction
ΔM	difference in coherence order
D	diffusion coefficient of the analyte (Appendix 2)
D	diffusion coefficient (Chapter 3.3)
D_{app}	apparent (or effective) dipolar coupling constant (D_{eff})
DHE	dynamic hydrogen electrode
DIW	deionized water
D_{jk}	generic dipolar coupling constant between two spins
DL	double-layered (refer to the membrane layer in MEA)
DMFC	direct methanol fuel cell
DOSY	diffusion ordered spectroscopy
d_{PFSA}	thickness of the PFSA membrane
DQ	double quantum
DQC	double quantum coherence
DQF	double quantum filter
η	asymmetry parameter

η	the viscosity of the liquid (Chapter 3.3)
η_{ICE}	the maximum efficiency of a traditional internal combustion engine
η_{PEMFC}	the maximum efficiency of a proton exchange membrane fuel cell
E	cell potential (Chapter 2.3)
E	magnetic spin state (Chapter 2.1)
E_0	standard cell potential (Chapter 2.3)
EIS	electrochemical impedance spectroscopy
EW	equivalent weight
F	Faraday constant
FC	fuel cell
FID	free-induction decay
γ	gyromagnetic ratio
g	gradient strength
GDL	gas diffusion layer
GE	General Electric
GSCF3	Gaussian self-consistent field version 3
h	Planck constant
$\hbar$	reduced planck contant
$\hat{H}_x, \hat{H}_y, \hat{H}_z$	Hamiltonian for the RF pulse along x, y, z-axis
$\hat{H}_\lambda$	Hamiltonian for different internal interactions, λ=Chemical shielding, dipolar coupling, scalar coupling, quadrupolar coupling, Knight shift, paramagnetic effect
$\hat{H}_{ext}$	Hamiltonian for the total external applied field
HFR	high-frequency resistance
HOR	hydrogen oxidation reaction

I	transmitted signal intensity in stack frame (Chapter 3.2)
I	NMR signal intensity (attenuated) (Chapter 2.1)
I	limiting current (Chapter 5.6)
I	primary spin quantum number (Chapter 2.1)
$\bar{I}$	spin angular momentum
$\hat{I}_{\pm}$	raising and lowering spin operators
I_0	transmitted signal intensity outside the stack frame (Chapter 3.2)
ICE	internal combustion engine
IEC	ion exchange capacity
I_L	Levich current (limitting current in RDE study) (Appendix 2)
I_{max}	maximum signal intensity in DQ NMR experiment
ISEELS	inner shell electron energy loss spectroscopy/spectrum/spectra
I_x, I_y, I_z	elements of spin operator in the Cartesian coordinate system
$\bar{I}_z$	angular momentum along the z-axis
J	flux of reactant (Chapter 5.6)
K	scaling factor
k	Boltzmann constant
λ	hydration level (number of water molecules per sulfonic group)
l	ion conductive path length (Appendix 1)
L	magnitude of spin angular momentum
LAB	laboratory frame
LBNL	Lawrence berkeley national laboratory
LHV	lower heating value

LSC	long-side-chain
$\vec{\mu}$	magnetic moment
μ_0	vacuum permeability
$\vec{M}$	bulk magnetization
MAS	magic angle spinning
MCFC	molten carbonate fuel cell
MEA	membrane electrode assembly
m_I	spin quntum number
MO	molecular orbital
n	the number of electrons (Chapter 1.2)
n	number of moles of electrongs transferred in the half reaction (Appendix 2)
n	number of electrongs transferred (Chapter 2.3)
N	total number of spins
N_-, N_+	the number of spins in the higher/lower energy states
nDQ	normalized double quantum
NEXAFS	near edge X-ray absorption fine structure
NMR	nuclear magnetic spectroscopy
NPA	n-pronanol
ω	angular rotation rate of the electrode
ω_0	Larmor frequency
ω_1	frequency that corresponds to the oscillating B1 field
ω_H	transition frequency associated with the Hamiltonians (H stands for CSA or dipolar)
ω_r	spinning frequency
ω_{RF}	oscillating frequency under the applied field

Ω	offset frequency
O1	NMR transmitter frequency
OD	optical density
OD1	optical density per nm
ORR	oxygen reduction reaction
OSA	order-sorting aperture
φ	phase of the pulse
ϕ	the azimuth angle
PAF	principal axis frame
PAFC	phosphoric acid fuel cell
PEEK	poly (ether ether ketone)
PEM	polymer electrolyte membrane or proton exchange membrane
PEMFC	polymer electrolyte membrane fuel cell
PFSA	perfluorosolfonic acid
P_{H_2}	H_2 permeability
p_{H_2}	H_2 pressure
P_{O_2}	O_2 permeability
PTFE	polytetrafluoroethylene
PVDF	polyvinylidene fluoride
ρ	resistivity (Appendix 1)
R	gas constant
R	resistance (Appendix 1)
$\vec{r}$	the vector between two magnetic dipoles
R_{ct}	resistance from charge transfer
RDE	rotating disk electrode

R_{double}	resistance for double membrane MEA
REDOR	rotational-echo double-resonance
REF	reference spectrum
$R_{electron}$	resistance from electron transport
RF	radiofrequency
r_{jk}	internuclear distance
ROT	rotor frame
R_{proton}	resistance from proton transport
r_s	hydrodynamic radius
R_{single}	resistance for single membrane MEA
σ	ionic conductivity (Appendix 1)
σ	chemical shielding (shift) tensor
σ_{ij}	elements in the chemical shielding tensor (I,j=x,y,z)
σ_{iso}	isotropic chemical shift
ΣMQ	total quantum term
S^T	dynamic order parameter
SL	single-layered (refer to the membrane layer in MEA)
SOFC	solid oxide fuel cell
SPEEK	sulfonated poly (ether ether ketone)
SSC	short-side-chain
ssNMR	solid-state nuclear magnetic resonance
STXM	scanning transmission x-ray microscopy
τ_{DQ}	recoupling time/evolution time
τ_r	rotor period
θ	angle between the internuclear vector and the external magnetic field

θ_R	spinning angle with respect to B0
t	pulse length
T	temperature in kelvin
T_{high}	high temperature during the ICE operation cycle
T_{low}	low temperature during the ICE operation cycle
T_1	spin-lattice relaxation
T_2	spin-spin relaxation
TEM-EELS	transmission electron microscopy - electron energy loss spectroscopy
T_g	glass transition temperature
υ	solution viscosity
U	classical dipolar interaction
VBA	visual basic for applications
VT	variable temperature
XAS	X-ray absorption spectroscopy/spectrum/spectra
ZP	zone plate

DECLARATION OF ACADEMIC ACHIEVEMENT

Professor Darren H. Brouwer (Redeemer University College) was responsible for some of the initial double-quantum NMR experimental setup and data interpretation regarding the use of Mathematica software. Robin Hayes was responsible for inner shell electron energy loss spectra collection, STXM measurements, and orbital calculations for fluorinated small molecules. Lis G. A. Melo was a great help for PFSA spin cast sample preparations and was responsible for some of the STXM measurements for the cast films. All other sample preparation, data acquisition, and interpretation were performed by Z. Blossom Yan.

1.

Introduction to the Hydrogen Fuel Cell

1.1 Thesis Layout

This thesis highlights the use of modern analytical techniques, mainly solid-state nuclear magnetic resonance (solid-state NMR or ssNMR) spectroscopy, to elucidate the structures and local dynamics of polymer electrolyte materials. A novel approach using advanced ssNMR techniques in the evaluation of the local motion of perfluoro polymers has been developed and applied to different types of polymeric materials. Nafion and similar alternatives are the major focus of this collection of work. Other fluorinated polymers have been studied as well in the process of developing the NMR method. Meanwhile, other spectroscopic techniques have also been applied to compliment the ssNMR method.

Chapter 1 describes the background and motivation behind the work presented in this thesis. A brief history and review of the latest developments in hydrogen fuel cells with the current design and relevant materials are presented. The challenges and open questions regarding future fuel cell developments are also stated. **Chapter 2** introduces the analytical techniques used in this thesis, emphasizing the ssNMR method used to probe the homonuclear dipolar coupling interaction. This

chapter also describes scanning transmission X-ray microscopy (STXM) as a chemical speciation tool and the fundamentals of cyclic voltammetry (CV) and impedance spectroscopy used in electrochemical performance analysis.

At the start of the experimental section, **Chapter 3** focuses on the spectroscopic analyses for a class of perfluorosulfonic acid (PFSA) materials. STXM and NMR were used as a combined analytical spectroscopic tool to identify different functional groups and elucidate the polymer structures. ^{13}C and ^{19}F ssNMR were used to support the element-specific X-ray absorption spectra (XAS) obtained from STXM. Furthermore, ^{19}F diffusion NMR was used to evaluate the difference between two ionomer dispersion solutions. Some challenges using these two techniques on the PFSA materials are also described in this chapter along with suggestions that might help to overcome these challenges. **Chapter 4** outlines the local dynamics approach using a ^{19}F-^{19}F double quantum (DQ) ssNMR technique which was applied to a commercial Nafion membrane material. This chapter describes the experimental setup and the analysis of the results, as well as the introduction of a dynamic order parameter in perfluoro systems. For the first time, the ^{19}F-^{19}F homonuclear dipolar interaction was used as an indicator of local dynamics in a PFSA material. The higher local motion of the polymer side chain compared to the backbone in Nafion was revealed as evidenced by a lower apparent dipolar coupling constant. Some common factors that might cause skewed NMR results are also described here, and the validation of the DQ method for fluorine-containing systems is supported.

Chapter 5 reports an extended exploration using the DQ ssNMR method to probe local dynamics in PFSA systems. In the first part,

three types of PFSA differentiated by different types of side chain structures with different equivalent weight (EW) values were investigated by applying the newly developed NMR method. The samples were treated and conditioned in the same way as the Nafion membrane tested in the previous chapter. The overall result suggested that the EW controls the difference in morphology development under the conditions applied here. In the second part, these PFSA membranes were subject to electrochemical performance analyses under fuel cell operating conditions in membrane electrode assembly (MEA) form at Ballard Power Systems. Simultaneously, the materials were treated at the same conditions as the electrochemical analysis prior to the ssNMR dynamics study. The correlations between the polymer chain local dynamics and proton conductivity and hydrogen gas permeability were successfully established over the class of PFSA materials. It was suggested that the side chain local motion promotes the proton conductivity when the water network is not sufficiently formed at low hydration levels. In the gas permeation process, the correlation shows that the side chain motion has a more dominant influence towards gas transport compared to the backbone structure. The discovery of these correlations signifies the collaboration between academic and industrial sectors in fuel cell research. Despite promising results, the role of side chain structure could not be concluded based on the samples tested. Future directions were proposed and suggested at the end of both parts to conclude the experimental section. **Chapter 6** serves as a summary chapter, where the highlights and important results of this thesis are recapitulated; furthermore, a future outlook is outlined.

1.2 Introduction to Polymer Electrolyte Membrane Fuel Cell

1.2.1 Motivation for Fuel Cell Development

1.2.1.1 The Concept of a Fuel Cell

A fuel cell (FC) is an energy conversion system that converts chemical energy from fuel into electrical energy. The introduction of the fuel cell concept dates back to the 1830s.[1-3] Converting gaseous fuels into electricity within a fuel cell system is attributed to Sir William Grove in 1839.[4] Initially, the fuel cell was referred to as the 'gaseous voltaic battery' in which platinum electrodes and sulfuric acid electrolyte for the hydrogen/oxygen reaction were used to illustrate the fuel cell concept experimentally. It is believed that the discovery of the fuel cell principle belongs to a Swiss Professor, Christian F. Schönbein.[3, 5] He concluded that it was the chemical reaction between hydrogen and oxygen that generated the current.[3, 5] Between then and the late 19th century, scientists improved the fuel cell design through the usage of platinum mesh as electrodes[6] with higher surface area and the development of an electrode matrix (also called a diaphragm) to retain the liquid electrolyte for practical purposes.[3, 7]

1.2.1.2 Development of the Fuel Cell: The Choice of Solid Electrolytes

With the experimental results reported first by Lord Rayleigh, the use of impure hydrogen derived from a process where air and steam are passed through glowing coal, initiated the development of a 'direct coal' fuel cell.[3] Due to the low energy conversion rate from the chemical energy into mechanical energy in a steam engine, the idea of

designing a device that converts energy 'directly' through electrochemical processes without losing the heat required in the coal burning is desirable. A fuel cell converting chemical energy directly from coal into electricity was proposed and demonstrated[8-9] (where the electricity was believed to be converted directly from the chemical affinity of the coal for the oxygen); yet the direct oxidation of coal was proved to be 'indirect' instead, where the electrochemical reaction first occurs between the coal and the electrolyte and then with the electodes.[10]

By the early 20th century, several types of electrolytes had been explored during the development of the coal fuel cell.[11] To aim for the direct use of coal gas as fuel, molten alkaline carbonates were discovered to interact with the coal initially. During the 1940s to 1960s, molten carbonate fuel cells became the major focus of the fuel cell community.[3, 12-14] The reason behind this development was the desire to achieve high operating temperature in order to use the coal gas, while maintaining a low cost. However, an important issue associated with the molten carbonate electrolytes was that the electrolyte was not completely solid in which the liquid carbonate phase was often immobilized and supported by a solid matrix framework, therefore the circulation and seal of the electrolyte in the system became challenging.

To search for a more manageable electrolyte candidate, a solid electrolyte was discovered and suggested as a more suitable and practical alternative for fuel cell systems, and in 1937 the solid oxide fuel cell was developed based on a solid mixed metal oxide material.[15-16] Porous metal electrodes were applied in molten carbonate fuel cells in 1960 instead of the matrix type, which was typically a porous and

non-conducting solid. Additionally, a gas diffusion electrode was implemented as it was predicted to achieve high current density.[14]

The developments of molten carbonate and solid oxide fuel cells enabled high temperature fuel cell operation; unfortunately, the application is rather limited since it requires a large amount of heat input. For low temperature fuel cell devices, alkaline and phosphoric acid fuel cells were developed in which liquid alkaline solution and phosphoric acid were used as electrolytes, with the goal of reaching a wider range of applications. The alkaline fuel cells reduced electrode corrosion when compared to acid electrolytes[2-3, 17]; allowing them to be included in several applications such as the Apollo space missions, Orbiter space shuttles and an experimental fuel cell electro-van by General Motors.[2-3] However, the challenge in electrolyte management (including sealing and circulating within the system) associated with liquid electrolytes remained the same as in molten carbonate fuel cell devices. For low temperature fuel cell designs, an electrolyte material in solid form became necessary.

With the rapid expansion of the polymer industry, the first practical fuel cell application was a polymer membrane electrolyte (PEM) fuel cell by General Electric (GE) used in the Gemini space missions in the early 1960s.[18] With the discovery of the perfluorosulfonic acid polymer 'Nafion' by Du Pont company in 1972[19-20] the inclusion of Nafion in the catalyst layer was proposed at the Los Alamos National Laboratory in 1986.[21] Ballard Power Systems demonstrated polymer electrolyte fuel cell powered buses in the early 1990s as the pioneering commercial application with hydrogen as the primary fuel in the system.[1-3]

1.2.1.3 Development of the Fuel Cell: The Use of Carbon

In addition to hydrogen fuel cells, direct methanol fuel cells using methanol as the fuel source received a certain amount of attention throughout several decades, with the hope of using direct coal gas. This type of fuel cell was originally investigated using alkaline and acid electrolytes, but more recently the main focus has been on implementing a polymer electrolyte in this system.[1-3] Meanwhile, since the late 1960s phosphoric acid fuel cells where concentrated phosphoric acid acted as the electrolyte were being developed.[22] The original application for this technology was the Moonlight project in Japan during the 1980s.[22] More recently, it has been used commercially in stationary power generators.[1, 3] In the development of the phosphoric acid fuel cell, the use of carbon was widely investigated.[22-24] In its various fabricated forms, it was initially used as separator plates, following which it was included in current collectors, electrodes, and catalyst supports. This discovery was tremendously important for fuel cell research, since carbon is relatively chemically stable, cheap and light.[3] After years of development and investigation, the solid polymer fuel cell finally achieved success in large scale applications, specifically for electricity generation for the U.S. space programs at the beginning of space travel. Extensive research on fuel cell applications resulted in various commercial applications, thus establishing a new industry.[1, 3]

1.2.1.4 The Industry: Moving Forward

Over the last several decades, the urge to increase the versatility of power generations as well as the growing demand for electricity have attracted a significant amount of attention to the

development of powerful and efficient power generators. Ongoing dependence on fossil fuels as a primary energy source has the consequence of continuously increasing the anthropogenic production of the greenhouse gas CO_2, resulting in an unsustainable situation with a global shortage of the main energy supply. Most importantly, the increasing global awareness of the impacts of human activities on the environment has promoted research on reliable power sources to achieve environmental sustainability with increasing world population.[1-3] Fuel cells may assist the reduction of our reliance on fossil fuels and minimize the greenhouse gas and other toxic emissions from fossil fuel usage. By using hydrogen as a fuel supply, the only theoretical by-products of a fuel cell are water and heat, making it a zero or ultra-low emission system.[1-3] Hydrogen fuel cells using a polymer membrane as the electrolyte have demonstrated promising potential after the practical application used in space missions. Based on its light weight, high energy conversion efficiency, low or zero emissions, and simple and modular cell design, PEM fuel cells (PEMFCs) have a wide range of applications, such as transportation, stationary power generation and implementation in portable devices as an auxiliary power source.[1-3] Although the abbreviation 'PEM' initially represented 'polymer electrolyte membrane', it now primarily refers to 'proton exchange membrane' because of the nature of the polymer functionality in hydrogen fuel cell. Most major automobile manufacturers have demonstrated and experimented with FC-powered vehicles, and many have plans to introduce (or already have introduced) products on the commercial market. Most recently, United Parcel Service started a trial and development program using a fuel cell module for hybrid delivery vans in the Greater Los Angeles area, and Siemens will develop fuel cell

drive for its train platform to achieve high power density and high efficiency fuel cell systems.

1.2.2 Principles of A Fuel Cell

In a fuel cell, the free energy of a chemical reaction is converted into electrical current. It operates like a conventional galvanic cell with externally supplied reactants. The change in Gibbs free energy, ΔG, of a chemical reaction is related to cell potential[1-3, 25]:

$$\Delta G = -nF\Delta E_0 \quad \textbf{(Equation 1.1)}$$

where n is the number of electrons involved in the reaction, F is the Faraday constant, ΔE_0 is the potential difference between the anode and the cathode of the cell at thermodynamic equilibrium.

The anodic reaction of a fuel cell is essentially the oxidation of methanol or hydrogen (HOR), while the oxygen reduction reaction (ORR) occurs on the cathode. For a hydrogen fuel cell illustrated by a schematic diagram of a PEMFC (in **Figure 1.1**), the overall reaction is:

$$H_2 + \frac{1}{2} O_2 \rightarrow H_2O \text{ with } \Delta G = -237 \text{ kJ mol}^{-1} \quad \textbf{(Equation 1.2)}$$

with a cell potential at equilibrium for standard conditions of:

$$\Delta E_0 = -\frac{\Delta G}{nF} = 1.23V \quad \textbf{(Equation 1.3)}$$

which is often referred to as the theoretical hydrogen/oxygen fuel cell potential.[1-3]

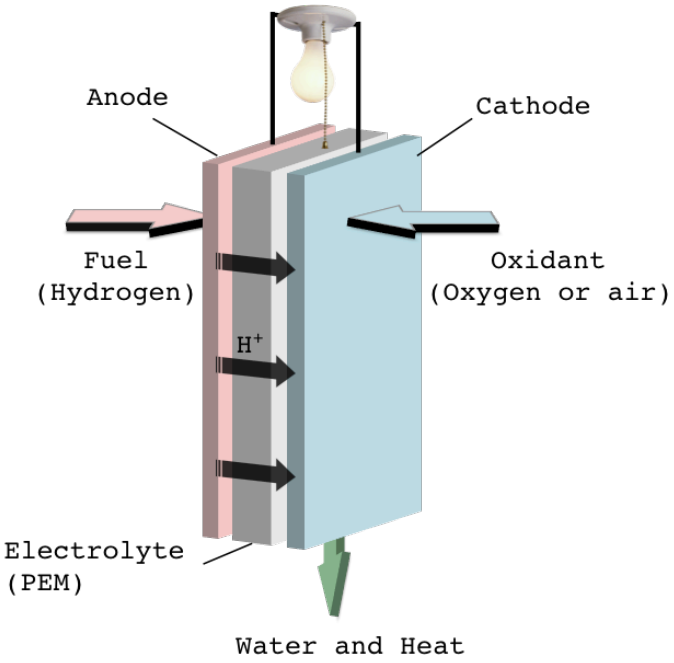

Figure 1. 1 Schematic drawing of a proton exchange membrane fuel cell, which is an example of a hydrogen/oxygen fuel cell system.

The fuel cell consists of two electrodes, which are separated by an electrolyte, in the case of **Figure 1.1** the electrolyte is solid polymer membrane, and are connected through an external circuit. The electrodes are usually porous materials that allow gas or liquid phase fuel and oxidant to permeate through in order to supply the fuel for the chemical reactions that occur on the electrodes. As an example demonstrated in **Figure 1.1**, in PEMFC the electrochemical reactions that occur at the two electrodes are as follows:

Cathode: $\frac{1}{2} O_2 + 2H^+ + 2e^- \rightarrow H_2O$ (**Equation 1.4**)

Anode: $H_2 \rightarrow 2H^+ + 2e^-$ (**Equation 1.5**)

The electrons flow through the external circuit that interconnects the two half-cell reactions, leading to the combination of oxygen ions and protons to produce water. The reactions may have several

intermediate steps due to the catalysis process in real fuel cell applications resulting in undesired by-products, which will be described in more detail later (section 1.2.3.1).

In a traditional internal combustion engine (ICE), chemical energy is transformed into mechanical energy, and it can then be further converted into electrical energy using an electromagnetic generator through rotations in power generator applications.[1-3, 25] The combustion of fossil fuels that are mainly hydrocarbons is an exothermic process. The maximum efficiency can be expressed by the Carnot cycle efficiency[1-3, 25], η_{ICE}, which is essentially the ratio between the energy output and input:

$$\eta_{ICE} = 1 - \frac{T_{low}}{T_{high}} \quad \textbf{(Equation 1.6)}$$

where T_{low} and T_{high} are the two temperatures during the operation cycle of the ICE. From a thermodynamic perspective, the efficiencies of ICEs can reach maximally 50% for the most efficient engines.

The reaction that occurs in a PEM fuel cell is the same as hydrogen combustion. The enthalpy for this exothermic reaction is the overall heat of formation of products and reactants. Therefore, the enthalpy ΔH for the overall reaction in **Equation 1.2** is -286 kJ mol^{-1}. Theoretically the free energy of the reaction can be fully converted into electrical energy; thus ΔG is used to represent the energy output. For the energy conversion efficiency in PEMFC, the maximum possible efficiency is the ratio between ΔG and ΔH:

$$\eta_{PEMFC} = \frac{\Delta G}{\Delta H} = \frac{237}{286} = 83\% \quad \textbf{(Equation 1.7)}$$

There are many factors that influence the practical cell efficiency, including the losses caused by electrode overpotentials (the potential difference between the theoretical potential and the experimental potential, which is needed to maintain the current flow) due to a slow ORR at the cathode and the electrolyte resistance. Despite the factors that reduce fuel cell electrochemical efficiency, the overall efficiency is still superior to conventional ICEs.[1-3]

Based on different types of electrolytes, fuel cell systems can be organized into several categories. **Table 1.1** summarizes the comparison of energy conversion efficiency, operating conditions, and fuel types among the different categories. As they are classified by the electrolyte type, direct methanol fuel cells (DMFC) are not considered to be a single class, and are instead usually included as a subset of PEMFCs due to the usage of a polymer membrane as the electrolyte.[1-2] Another way to categorize different types of fuel cells is to look at their operation temperatures. As demonstrated in **Table 1.1**, the different colour blocks represent the low-, medium-, and high-temperature fuel cells.[1-3]

Table 1. 1 The different types of fuel cell systems that have been developed. The electrical efficiency values are gathered from the Fuel Cell Fact Sheet reports by the United States Department of Energy Hydrogen Program in 2006 and 2015.[26-27]

Fuel Cell Types	Electrolyte	Fuel	Oxidant	Operating Temperature (°C)	Electrical Efficiency (%)
AFC (Alkaline Fuel Cell)	KOH	H_2	O_2	90-100	60-70 60(LHV)
PEMFC (Polymer Electrolyte Membrane Fuel Cell)	Solid Polymer	H_2	O_2, Air	50-100	50-60 40-60 (LHV)
DMFC (Direct Methanol Fuel Cell)	Solid Polymer	CH_3OH	O_2, Air	60-90	
PAFC (Phosphoric Acid Fuel Cell)	Phosphoric Acid	H_2	O_2, Air	150-200	36-42 40(LHV)
MCFC (Molten Carbonate Fuel Cell)	Alkaline Carbonate (Li, K)	H_2 CO CH_4	O_2, Air	600-700	60 50(LHV)
SOFC (Solid Oxide Fuel Cell)	Solid oxide (Y, Zr)	H_2 CO CH_4	O_2, Air	500-1000	60 60(LHV)

*LHV – Lower Heating value. It is essentially treating H_2O formed as vapor.

1.2.3 Proton Exchange Membrane Fuel Cell

Solid polymer electrolyte fuel cells have adopted the name 'proton exchange membrane electrolyte fuel cells' since the membrane electrolyte conducts the protons between electrodes in a hydrogen fuel cell.[1-3, 28]

The promise of zero or ultra-low emission associated with using hydrogen as fuel has made the development/improvement of hydrogen fuel cells gain exceptional attention. PEMFCs stand out and have been demonstrated with many successful commercially available examples, as compared to other types of fuel cells they do not require high thermal energy to operate, are low maintenance, and the solid electrolyte reduces system corrosion.[28] Besides the application in transportation such as fleet buses and cars, PEMFCs have also been utilized in stationary and portable power generation.[3, 28]

1.2.3.1 Important Reactions

The HOR in a fuel cell occurs readily at the anode. It typically involves the adsorption of H_2 onto the catalyst surface, followed by the dissociation of the molecule and the electrochemical reaction of proton formation. The general steps are as follow:

$$2Pt(s) + H_2 \rightarrow 2Pt - H_{ads} \quad \textbf{(Equation 1.8a)}$$

$$Pt - H_{ads} \rightarrow H^+ + e^- + Pt(s) \quad \textbf{(Equation 1.8b)}$$

where $Pt(s)$ represents the catalyst surface and $Pt - H_{ads}$ stands for the adsorbed hydrogen atom on the Pt surface after dissociation.[2] Even though the HOR has fast kinetics on the catalyst surface due to high catalytic activity, the Pt catalyst is very sensitive towards impurities. To reduce the cost of the H_2 fuel, reformed H_2 sources are often used, which contain gas impurities that can cause parasitic interactions with Pt leading to a reduction in catalytic activity. Carbon monoxide is one stubborn contaminant that has high adsorption affinity on the Pt surface, which blocks the active sites on the

catalyst surface. In order to combat this, low-Pt or nonprecious metal catalysts have been explored.[1-3]

In comparison to the rapid HOR, the ORR is considered a 'sluggish' reaction due to its slow kinetics.[1, 3, 29] It involves the adsorption of O_2 gas, the dissociation of molecular oxygen at the catalyst surface and the combination with protons to form water. These steps are critical for a PEMFC to function properly. It has been demonstrated that the ORR is sensitive towards properties of the catalyst such as particle size, catalyst structure, and geometry.[1-3] Unfortunately, many of the experimental results are controversial, and the catalyst structure-activity relationship is still not well described.

1.2.3.2 Design of a Proton Exchange Membrane Fuel Cell

As illustrated in the previous section, the system relies on the proton exchanging ability of the membrane electrolyte. The revolutionary design of the MEA combines the the key parts of a PEMFC by integrating the anode, cathode, and the electrolyte into a compact thin unit, about several hundred microns in thickness.[1-3]

The main component in the MEA is the solid polymer material. It is required to be an electronic insulator and a gas barrier between the two electrodes, while also being a thin material that enables high current densities and fast proton transport.[28] A properly designed MEA leads to high power densities in fuel cell stacks for transportation applications. To achieve sufficient proton conductivity, based on the proton transport mechanisms (described in greater detail in **Chapter 5**) the membrane needs the presence of water to form an interconnected hydrophilic network, which limits the operating temperature in order to retain water in the system. Therefore, effective catalysis under the

temperature limitation is required for successful PEMFC operation. A catalyst blended with a carbon support forms thin layers on either side of the polymer membrane, which are often referred as catalyst layers (CLs). A liquid dispersion form of the membrane, called the ionomer solution, is commonly used in CLs to enhance the ionic conductivity, while at the same time serving as a binding material.[2-3] The combination of the CLs and the membrane electrolyte is often referred to as the catalyst coated membrane, which is the centerpiece of the MEA and the entire fuel cell system.

As a result of the use of gaseous reagents, the delivery from the reagent supply to the catalyst active sites is crucial to the overall efficiency of the system. Gas diffusion layers (GDLs) are usually implemented onto electrode substrates to achieve gas permeability and electrical conductivity.[1-3] This component provides a pathway for reagent gases to reach the catalyst layer, and due to the mechanical properties of the GDL (usually made of carbon fibers) it also offers a nice physical support for the MEA.

To put PEMFCs into practical applications, a series of MEAs are put together to form a fuel cell stack where gas supplies for both electrodes requires a compromise in order to satisfy the low Ohmic losses with a flat gas supply design while maintaining sufficient access of reactant gases to the electrodes. Flow field plates (see **Figure 1.2**), also called 'bipolar plates' with gas channels on both sides, are employed in an attempt to solve this problem.[1-3] The flow field plates are essentially graphite plates with gas flow path patterns etched on either side, and are placed in between MEAs. With this layout, the fuel can be fed into one side of the plate to reach the

cathode of one MEA, and the oxidant is lead into the anode side of the adjacent MEA; hence, the term 'bipolar'.

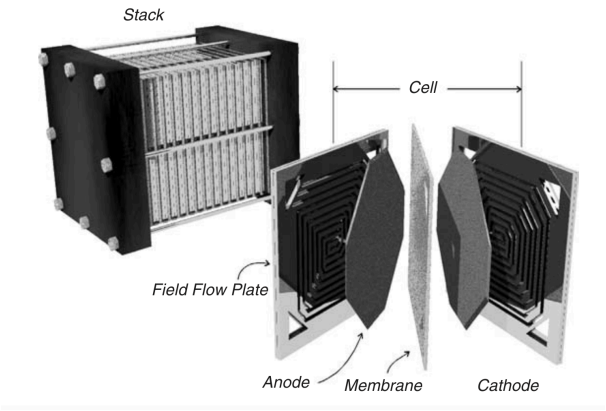

Figure 1. 2 Fuel cell stack with flow field plates (or bipolar plates) and MEAs. (Figure reproduced from Ref.3)

1.2.3.3 Issues and Challenges

With decades of dedicated work done by scientists and engineers from both academic and industrial sectors, the performance of fuel cells in various applications is impressive. Yet, there are still some challenges that need to be overcome. The cost, mainly attributed to the use of precious metal Pt as catalyst, limits the mass production of PEMFC-powered automotive applications.[1-3] Fuel storage and distribution issues can also limit the portability of the applications. Furthermore, how 'green' is a PEMFC actually? The answer to this question really depends on the H_2 source. If the H_2 economy relies on fossil fuels (for H_2 reformation), the goal of reducing the greenhouse gas emissions is not achieved. Moreover, the active catalyst in PEMFCs is very sensitive towards impurities in the hydrogen fuel source, and thus fuel purity is very important. The impurities can cause CO poisoning, where the CO molecules block the active catalysis sites, which causes membrane/ionomer degradation and essentially reduces the overall cell efficiency.[1-3]

Additionally, based on the mechanisms of proton transport, water is necessary for PEMFCs to work effectively, thus water management in the cell structure during operation becomes critical. As the gaseous reagents require a clear pathway to reach to the CLs if the MEA is flooded, such corridors are not available.[1-3] In general, the resistivity of proton transport through the electrolyte depends on the pathway length, i.e. membrane thickness. To overcome the resistivity issue for thick electrolytes, thinning the membrane becomes one approach; however, because of the porous nature of a polymer membrane, the fuel gas often permeates through the electrolyte, especially when the membrane is thin, which leads to fuel loss and efficiency loss.[1-3, 30-31] There is therefore a desire for the development of an ideal material and cell design to combat these issues.

1.3 Solid Polymer Electrolytes

1.3.1 Historical Development of PEM

GE started testing solid polymer materials as electrolytes for fuel cells in 1959.[1-3, 28] The membranes studied initially were phenol-sulfonic acid based. To improve the power density, GE developed partially sulfonated polystyrene sulfonic acid membranes (used in the Gemini space programs). Due to the poor mechanical properties in a dry state, a cross-linked polystyrene-divinylbenzene sulfonic acid membrane was introduced, although the power density was still not high enough to make an adequate fuel cell system. The big breakthrough was the introduction of Nafion, a perfluorosulfonic acid (PFSA), by DuPont in the 1970s.[19-20] Fuel cells that incorporated Nafion exhibited a much longer lifetime and higher proton conductivity. Due to its outstanding

performance, it soon became, and still is, the standard PEM electrolyte. Chemical companies like the Dow Chemical Company, the 3M Company and Asahi Kasei Corporation have developed PFSA materials with shorter side chains and various ratios of SO_3H to CF_2 groups. PFSA was the first of a class of synthetic polymers that exhibited ionic conductivity (called ionomers). Meanwhile, other classes of PEMs have been developed, such as partially fluorinated, non-fluorinated like sulfonated poly (ether ether ketone) (SPEEK), acid-base blends, etc.[2, 28] These hydrocarbon-based membrane alternatives are less expensive and are much easier to modify compared to traditional PFSA membranes, however they come with their own set of challenges, and are not studied within this thesis.

The membrane electrolyte is the key component of the PEMFC, and the desired properties of PEM are listed as follows[1-3, 28]:

- High proton conductivity
- Good mechanical strength and stability
- Chemical and electrochemical stability over fuel cell operating conditions
- Ability to retain moisture
- Low gas permeability to prevent fuel loss
- Low cost
- Electronic insulator

1.3.2 Perfluorosulfonic Acid Polymer

PFSA ionomer materials consist of a polytetrafluoroethylene (PTFE) backbone and perfluorinated polyvinyl ether side chains terminated with sulfonic acid groups. The characteristic measure for a PEM is the equivalent weight (EW), which is the molecular weight of the polymer per sulfonic acid pendent group and is also inversely proportional to the

ion exchange capacity (IEC).[2, 28] Therefore, if a PFSA has lower EW, it means that the sulfonic acid groups show up more frequently along the polymer chain, which implies higher ionic conducting site population, hence higher IEC. The nomenclature of this class of material is usually constructed with the type or brand of PFSA (eg. 3M, Gore, etc.) followed by its EW. In this thesis, the work involves three types of PFSA materials based on different side chain structures, with various EWs.

1.3.2.1 Nafion

Nafion is a so-called long-side-chain (LSC) PFSA and is the benchmark PFSA membrane in PEMFCs. It is probably the most studied electrolyte for PEMFCs both in the broader fuel cell research community, and in this thesis. Its structure is demonstrated in **Figure 1.3.**

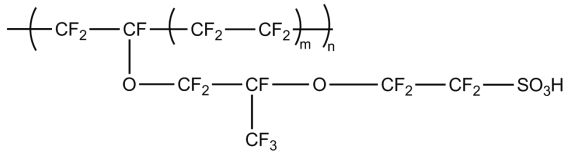

Figure 1. 3 Chemical structure of a copolymer Nafion, LSC-PFSA, where m is indicative of EW. It has a PTFE backbone and a perfluorinated polyvinyl ether side chain.

Analogous to the other PFSAs, Nafion consists of PTFE hydrophobic backbones and perfluorinated sulfonic acid side chains with two ether groups. The backbone structure has superb chemical resistivity, which is attributed to the high bond energy of C-F, 480 kJ mol^{-1}.[25] It has been differentiated as a long-side-chain PFSA based on its side chain structure compared to alternative structures. It is typically categorized by its EW and membrane thickness. For example, Nafion 117, the star material discussed in this thesis, refers to a membrane that has an EW of 1100 g mol^{-1} per sulfonic acid group and a thickness of 0.007 inches (178 μm). The number of CF_2-CF_2 repeating units is an

average value, which describes the distribution of the co-monomer sequence along the polymer chain. For Nafion 117 with EW of 1100, there are 6.5 repeating units of CF_2-CF_2. In other words, the adjacent side chains are separated by 14 CF_2 groups on the backbone.

Nafion's excellent chemical resistivity and ionic conductivity have led to its mass popularity since the date it was first introduced.[2-3, 28] The structure-performance relationship has been under investigation over the past several decades using numerous techniques, including diffraction and light scattering, in an attempt to understand Nafion morphology. Largely due to the lack of crystallinity and complicated phase separation that occurs due to a difference in hydrophilicity of the copolymer chain, there have been many models proposed to aid the fundamental understanding of diffusion and conduction processes in Nafion.[28] The most referenced model, the 'cluster network', proposed by Gierke and Hsu[32-34], was the basis for all the related models that describe the microscopic structures. According to this model, the polymer forms an inverted micellar structure where the ion-exchange sites are separated from the hydrophobic backbones, which leads to the formation of spherical clusters. Recent studies have modified the model into a 'random network' model, in which an intermediate region is involved wherein the side chains tend to cluster and form hydrated regions. This microscopic model that describes the distribution of the hydrated regions is much more random than the previous version, and it has been experimentally supported by small angle X-ray scattering measurements.[35]

The idea of a phase separated Nafion polymer has been widely accepted based on evidence from various modeling and X-ray scattering studies.[36-37] The sulfonic acid terminated side chain forms hydrophilic

domains that become ionic clusters, while the PTFE backbones form hydrophobic domains, especially when a higher degree of hydration is reached in the system. Several studies agreed with the ionic cluster-network model as Gierke and Hsu proposed[32-34], where the clusters are interconnected forming a proton conducting network. The hydration level of the system strongly affects the proton conductivity, which was demonstrated in the pioneering work by Zawodzinski et al. in 1993.[38] The free water molecules together with the interconnected ionic clusters form a network to promote the overall proton diffusion and transportation. The vehicular mechanism of proton transport has been proposed and accepted for conditions where there is a large amount of water present, in which the protons migrate in the form of hydronium ions, H_3O^+.[39] On the other hand, at low water content protons are transported with a 'hopping' style motion, a process that is often referred to as the 'Grotthuss mechanism', where the protons are passed from one conducting site to the other.[40-41] Therefore, retaining water in the membrane is essential to maintain a functioning fuel cell system, which implies that this class of proton conducting membranes will not be useful for high–temperature applications where the water molecules cannot be contained.

An additional problem related with low operating temperatures is that the use of a reformed H_2 source containing CO impurities causes poisoning of the Pt catalyst as discussed previously.[3, 28] Unfortunately, the binding affinity of CO on the Pt surface is much higher than that of H_2, specifically at the typical Nafion PEMFC operating temperature. Although increasing the operating temperature to above 100 °C can overcome the catalyst poisoning issue, this is beyond the optimal operating temperature for Nafion.

Another issue associated with the use of Nafion is that Nafion operates optimally at a temperature close to the boiling point of water, which leads to water condensation on the electrodes where the pores used for the reagent gas diffusion become occupied by condensed water. The gas feed therefore needs to be pressurized to keep the fuel cell operating with a hydrated membrane at a temperature below the boiling point of water, which unfortunately reduces the overall system efficiency.[1, 3]

Although Nafion has good chemical resistivity overall, it still suffers from mechanical, chemical, and thermal degradation as demonstrated by issues such as pinhole formation and membrane thinning that have been observed during end-of-life fuel cell operation studies.[31, 42] Thermal stability tests of Nafion have also demonstrated that a change in chemical structure occurs when the material is simply heated.[43] Moreover, chemical degradation of Nafion has been investigated by many techniques in both qualitative and quantitative ways aiming to identify the degradation products and mechanisms.[44-45] The main source of chemical degradation comes from hydroxyl radical attack, which has been demonstrated based on NMR analysis.[44-45] The radical typically targets the vulnerable $-O-CF_2-$ ether bond to cleave off the sulfonic acid pendent group, which leads to the loss of the proton conducting site. Put together, these various degradation mechanisms can significantly limit the PEMFC system efficiency.

1.3.2.2 Nafion Alternatives

Operating at higher temperatures, good proton conductivity at low hydration level, low risk of degradation, etc., have become the main obstacles for the improvement of ionomer materials like Nafion used in

PEMFCs.[2-3, 28] By taking advantage of the high chemical resistivity in perfluorinated polymer materials, short-side-chain (SSC) PFSA materials have been developed.[2-3, 28] One recent development that has been reported by Solvay Solexis, is a material referred to commercially as Aquivion (formerly known as Hyflon) that has only one ether group and a much shorter side chain (**Figure 1.4a**). Another new type of PFSA was developed by 3M, and has one ether group on the side chain as well but has two extra $-CF_2-$ compared to Aquivion (**Figure 1.4b**). Neither of these two alternative PFSAs have a $-O-CF_2-CF(CF_3)-$ segment connected to the PTFE backbone, which reduces the possibility of side chain cleavage from radical attack at that ether bond.

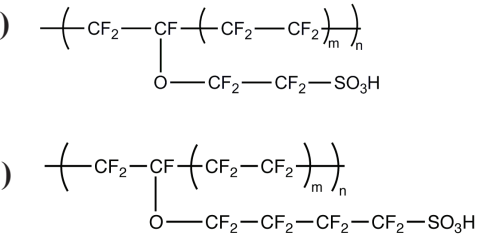

Figure 1. 4 Chemical structures for two types of Nafion alternative PFSA materials: a) SSC-PFSA, commercially known as Aquivion; b) a new PFSA material delivered by 3M Company. They both only have one ether group in the side chain structure.

Studies have demonstrated a higher degree of crystallinity and glass transition temperatures of SSC-PFSAs, which could potentially lead to comparable proton conductivity and better stability.[2-3, 28] The literature values for the three types of PFSA are summarized in **Table 1.2.**[46-47]

Table 1. 2 Properties of membranes from literatures including ionic conductivity and glass transition temperatures (T_g). [46-47]

PFSA Type	Nafion (Figure 1.3)	Aquivion (Figure 1.4a)	3M (Figure 1.4b)
Conductivity (S/cm)	0.10	0.13	0.14
T_g (°C)	123	148	144

Another approach to improve Nafion is to combine the ionomer with a matrix to form a composite. Gore and Associates have introduced a Gore-Select® membrane where the perfluorinated ionomer material is interpenetrated with PTFE, which is proven to increase the mechanical durability of the membrane.[48-49] Composite membranes can also be made by mixing the ionomer with solid oxides. Nafion with TiO_2 or SiO_2 composite membranes were introduced, which has led to excellent thermal stability.[50] The composite membranes also have been shown to have better proton conductivity at higher temperature and require a lower hydration level compared to the regular PEMFC operating conditions. Moreover, additive materials that do not rely on water content to conduct protons can help to maintain the proton conductivity under less ideal operating conditions for Nafion. For example, Nafion doped with H_3PO_4 was reported to have excellent mechanical stability at 200 °C. This approach has presented some potential to overcome the disadvantages of Nafion, but no applications have been developed yet.

1.3.3 Ionomer Material

Although the term ionomer comes from the ionic conductive polymer when Nafion was first introduced, it is now often used to refer to the liquid dispersion solution that is used in CL and MEA fabrications.[1, 3] Ionomers have the same chemical structures/formulae as the membrane materials, except that during the process of making the dispersion, stabilizing chemical additives are often present.

1.4 Evaluation of Solid Polymer Electrolytes

To develop a PEMFC system with excellent performance and a long lifetime, understanding the structure-performance relationship is vital. This includes unraveling the structures of the materials and connecting the physicochemical properties to their performance as electrolytes.

Evaluation of polymer electrolyte materials requires knowledge of chemical composition and structure, gas diffusion resistivity, and ionic conductivity. With the growing interest in fuel cells, there are many techniques that have been developed for such evaluations. Due to the soft nature of these membranes that lack crystallinity, studying the materials in their original polymer form requires a non-destructive technique. These materials are also used in CL fabrications, and therefore for future studies on the role of the ionomer in CLs, the evaluation techniques need to have good chemical sensitivity. The next chapter provides a brief background and general descriptions of the methods used throughout this thesis to probe polymer electrolyte properties.

1.5 References

1. Barbir, F., *PEM fuel cells: theory and practice*. Academic Press: New York, 2012.

2. Carrette, L.; Friedrich, K. A.; Stimming, U., Fuel cells–fundamentals and applications. *Fuel cells* **2001,** *1* (1), 5-39.

3. Hoogers, G., *Fuel cell technology handbook*. CRC press: 2002.

4. Grove, W. R., XXIV. On voltaic series and the combination of gases by platinum. *Philosophical Magazine Series 3* **1839,** *14* (86-87), 127-130.

5. Bossel, U., *The Birth of the Fuel Cell: 1835-1945*. European Fuel Cell Forum: Oberrohrdorf, 2000.

6. Rayleigh, L., *Cambridge Phil. Soc.Proc.* **1882,** *4*, 198.

7. Mond, L.; Langer, C., A new form of gas battery. *Proceedings of the Royal Society of London* **1889,** *46*, 296-304.

8. Jacques, W. W., Electricity direct from coal. *Harper's New Monthly Magazine* **1896,** *94*, 144-150.

9. Ostwald, W., Die wissenschaftliche Elektrochemie der Gegenwart und die technische der Zukunft. *Z. Phys. Chem.* **1894,** *15* (1), 409-421.

10. Haber, F.; Bruner, L., Das Kohlenelement, eine Knallgaskette. *Zeitschrift für Elektrochemie und angewandte physikalische Chemie* **1904,** *10* (37), 697-713.

11. Baur, E.; Ehrenberg, H., Über neue Brennstoffketten. *Zeitschrift für Elektrochemie und angewandte physikalische Chemie* **1912,** *18* (22), 1002-1011.

12. Baur, E.; Preis, H., Über Brennstoff-Ketten mit Festleitern. *Zeitschrift für Elektrochemie und angewandte physikalische Chemie* **1937,** *43* (9), 727-732.

13. Broers, G.; Ketelaar, J., High temperature fuel cells. *Industrial & Engineering Chemistry* **1960,** *52* (4), 303-306.

14. Douglas, D., Molten Carbonate Cells with Gas-Diffusion Electrodes. *Industrial & Engineering Chemistry* **1960,** *52* (4), 308-309.

15. Baur, E.; Brunner, R., Über das Verhalten von Sauerstoff-Elektroden in Carbonatschmelzen. *Zeitschrift für Elektrochemie und angewandte physikalische Chemie* **1935,** *41* (11), 794-796.

16. Baur, E.; Brunner, R., Über die Eisenoxyd-Kathode in der Kohle-Luft-Kette. *Zeitschrift für Elektrochemie und angewandte physikalische Chemie* **1937,** *43* (9), 725-727.

17. Bacon, F., Fuel cells, past, present and future. *Electrochim. Acta* **1969,** *14* (7), 569-585.

18. Grubb, W.; Niedrach, L., Batteries with Solid Ion-Exchange Membrane Electrolytes II. Low-Temperature Hydrogen-Oxygen Fuel Cells. *J. Electrochem. Soc.* **1960,** *107* (2), 131-135.

19. Grot, W., Perfluorierte Ionenaustauscher-Membrane von hoher chemischer und thermischer Stabilität. *Chem. Ing. Tech.* **1972,** *44* (4), 167-169.

20. Grot, W., Perfluorierte Kationenaustauscher-Polymere. *Chem. Ing. Tech.* **1975,** *47* (14), 617-617.

21. Raistrick, I. In *Modified gas diffusion electrode for proton exchange membrane fuel cells*, Proceedingsof the Symposium on Diaphragms, Separators, and Ion-Exchange Membranes, Pennington, NJ, Van Zee, J. W.; White, R. E.; Kinoshita, K.; Barney, H. S., Eds. Electrochemical Society: Pennington, NJ, 1986; p 72.

22. Appleby, A. J., Fuel cell handbook. **1988.**

23. Trocciola, J. C. Novel fuel cell structure. 1975.

24. Petrow, H. G.; Allen, R. J. Catalytic platinum metal particles on a substrate and method of preparing the catalyst. 1976.

25. Atkins, P. W., *Physical Chemistry*. 4 ed.; Oxford University Press: Oxford, 1990.

26. Energy, T. D. o. *Hydrogen Fuel Cell*; 2006.

27. Energy, T. D. o. *Fuel Cell Fact Sheet*; 2015.

28. Smitha, B.; Sridhar, S.; Khan, A., Solid polymer electrolyte membranes for fuel cell applications—a review. *Journal of membrane science* **2005**, *259* (1-2), 10-26.

29. Wu, J.; Yuan, X. Z.; Wang, H.; Blanco, M.; Martin, J. J.; Zhang, J., Diagnostic tools in PEM fuel cell research: Part I Electrochemical techniques. *Int. J. Hydrogen Energy* **2008**, *33* (6), 1735-1746.

30. Zhang, H.; Li, J.; Tang, H.; Lin, Y.; Pan, M., Hydrogen crossover through perfluorosulfonic acid membranes with variable side chains and its influence in fuel cell lifetime. *Int. J. Hydrogen Energy* **2014**, *39* (28), 15989-15995.

31. Weber, A. Z., Gas-crossover and membrane-pinhole effects in polymer-electrolyte fuel cells. *J. Electrochem. Soc.* **2008**, *155* (6), B521-B531.

32. Yeager, H.; Eisenberg, A. In *Perfluorinated ionomer membranes-introduction*, ACS Symp. Ser., AMER CHEMICAL SOC 1155 16TH ST, NW, WASHINGTON, DC 20036: 1982; pp 1-6.

33. Mauritz, K. A.; Moore, R. B., State of understanding of Nafion. *Chem. Rev.* **2004**, *104* (10), 4535-4586.

34. Gierke, T.; Munn, G.; Wilson, F., The morphology in nafion perfluorinated membrane products, as determined by wide-and small-angle x-ray studies. *Journal of Polymer Science: Polymer Physics Edition* **1981**, *19* (11), 1687-1704.

35. Haubold, H.-G.; Vad, T.; Jungbluth, H.; Hiller, P., Nano structure of NAFION: a SAXS study. *Electrochim. Acta* **2001**, *46* (10-11), 1559-1563.

36. Kreuer, K.-D.; Paddison, S. J.; Spohr, E.; Schuster, M., Transport in proton conductors for fuel-cell applications: simulations, elementary reactions, and phenomenology. *Chem. Rev.* **2004**, *104* (10), 4637-4678.

37. Meresi, G.; Wang, Y.; Bandis, A.; Inglefield, P.; Jones, A.; Wen, W.-Y., Morphology of dry and swollen perfluorosulfonate ionomer by fluorine-19 MAS, NMR and xenon-129 NMR. *Polymer* **2001**, *42* (14), 6153-6160.

38. Zawodzinski, T. A.; Derouin, C.; Radzinski, S.; Sherman, R. J.; Smith, V. T.; Springer, T. E.; Gottesfeld, S., Water uptake by and transport through Nafion® 117 membranes. *J. Electrochem. Soc.* **1993**, *140* (4), 1041-1047.

39. Kreuer, K. D.; Rabenau, A.; Weppner, W., Vehicle mechanism, a new model for the interpretation of the conductivity of fast proton conductors. *Angewandte Chemie International Edition in English* **1982**, *21* (3), 208-209.

40. Grotthuss, C. J. D. v., *Ann. Chim.* **1806**, *LVIII* 54.

41. Agmon, N., The grotthuss mechanism. *Chem. Phys. Lett.* **1995**, *244* (5-6), 456-462.

42. Mittal, V. O.; Kunz, H. R.; Fenton, J. M., Membrane degradation mechanisms in PEMFCs. *J. Electrochem. Soc.* **2007**, *154* (7), B652-B656.

43. Kim, H. N.; Hwang, R. Y.; Han, O. H., Behavior of Channel Water and CF_2H Side-Chain Terminal Groups in Swollen Nafion Polymer Electrolyte Membranes after Thermal Treatment. *ACS Macro Letters* **2016**, *5* (7), 801-804.

44. Ghassemzadeh, L.; Holdcroft, S., Quantifying the Structural Changes of Perfluorosulfonated Acid Ionomer upon Reaction with Hydroxyl Radicals. *J. Am. Chem. Soc.* **2013,** *135* (22), 8181-8184.

45. Ghassemzadeh, L.; Kreuer, K. D.; Maier, J.; Müller, K., Evaluating chemical degradation of proton conducting perfluorosulfonic acid ionomers in a Fenton test by solid-state< sup> 19</sup> F NMR spectroscopy. *J. Power Sources* **2011,** *196* (5), 2490-2497.

46. Hamrock, S. J.; Yandrasits, M. A., Proton exchange membranes for fuel cell applications. *Journal of Macromolecular Science, Part C: Polymer Reviews* **2006,** *46* (3), 219-244.

47. Ikeda, M.; Uematsu, N.; Saitou, H.; Hoshi, N.; Hattori, M.; Iijima, H., Novel fluorinated polymer electrolyte for fuel cell. *Polymer Preprints, Japan* **2005,** *54* (2), 4521-4522.

48. Kerres, J. A., Development of ionomer membranes for fuel cells. *Journal of Membrane Science* **2001,** *185* (1), 3-27.

49. Bahar, B.; Hobson, A. R.; Kolde, J. A.; Zuckerbrod, D., Ultra-thin integral composite membrane. Google Patents: 1996.

50. Shao, Z.-G.; Xu, H.; Li, M.; Hsing, I.-M., Hybrid Nafion—inorganic oxides membrane doped with heteropolyacids for high temperature operation of proton exchange membrane fuel cell. *Solid State Ionics* **2006,** *177* (7-8), 779-785.

2.

Methodology

In this chapter, a brief introduction of the physical techniques used in the current thesis study is delivered. The chapter starts with an introduction of the solid-state nuclear magnetic resonance (solid-state NMR or ssNMR) technique, with emphasis on the double quantum recoupling method used throughout this thesis, which was adapted with permission from *Macromolecules*. Copyright 2016 American Chemical Society (Z. B. Yan, D. H. Brouwer, G. R. Goward. **2016**, *49*, 7331-7339). Scanning transmission X-ray microscopy (STXM) coupled with near edge X-ray absorption fine structure (NEXAFS) is then discussed, followed by an explanation of the basic theory behind the electrochemical performance analysis.

2.1 Solid-State NMR Spectroscopy

Numerous NMR methods have been used in structure characterization and dynamics analysis for a wide range of polymeric materials.[1-5] The nature of the molecules, the morphology, and the phase structure can all be probed by NMR techniques in the solid state. Characterization of the molecular dynamics of solid polymer electrolyte materials is required to be performed in the solid state. Throughout this thesis, ssNMR

spectroscopy has been used to evaluate a class of perfluorosulfonic acid (PFSA) materials to probe the local dynamics with the goal of understanding the structure-property relationship. This section introduces the basics of ssNMR including nuclear spin interactions with the applied magnetic field and under radio frequency pulses. The homonuclear dipolar coupling interaction is the key to the advanced ssNMR method to study local dynamics that is use significantly throughout this thesis. This method is also explained and validated in this chapter.

2.1.1 Interaction with External Magnetic Fields

NMR is a physical phenomenon where an atomic nucleus in a magnetic field emits or absorbs electromagnetic radiation during transitions between magnetic energy levels.[6] The energy of the radiation is at a specific frequency depending on the magnetic field strength and the nucleus, which is also known as the resonance frequency. To observe this phenomenon, NMR spectroscopy can be applied by manipulating the nuclear spins to study the specific quantum mechanical magnetic properties of the nucleus.[7-8]

2.1.1.1 Spin Behavior in an Applied Magnetic Field

In quantum mechanics, angular momentum is quantized and spin is a form of angular momentum.[7-8] Nuclei with an odd number of protons, neutrons or both have intrinsic non-zero spin angular momentum, $\vec{I}$, which is used in NMR spectroscopy. The angular momentum state of the nuclear spin is described by the spin quantum number, m_I, where $m_I = -I, -I+1, -I+2, \ldots, I-1, I$, and I denotes the primary spin quantum

number. Therefore, the total number of states is *2I+1*, which is also referred to as the state degeneracy.[6] The vector model describing the spin angular momentum is provided by a magnitude *L* along with the spin quantum number m_I to indicate the direction. Hence,

$$L = \hbar\sqrt{I(I+1)} \quad \textbf{(Equation 2.1)}$$

and angular momentum along the z-axis is

$$I_z = m_I\hbar \quad \textbf{(Equation 2.2)}$$

where $\hbar$ is the reduced Planck constant. The pictorial representation is shown in **Figure 2.1** for *I=1/2*, *1*, and *3/2*.

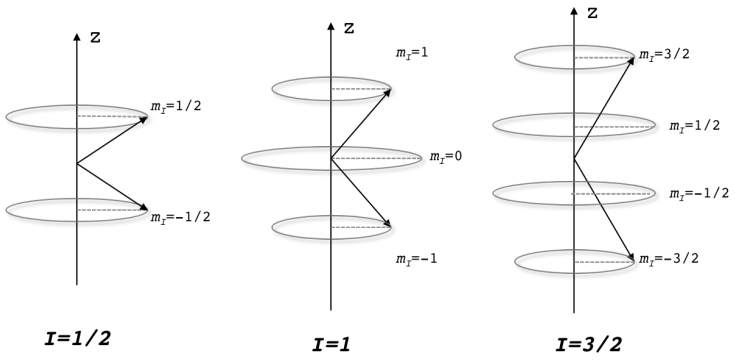

Figure 2. 1 The quantized angular momentum values for I=1/2, 1 and 3/2.

Each spin possesses a magnetic moment $\vec{\mu}$, which is related to the spin angular momentum,

$$\vec{\mu} = \gamma\hbar\vec{I} \quad \textbf{(Equation 2.3)}$$

where γ is the gyromagnetic ratio of the nucleus.[7-9] Thus, the bulk magnetization is essentially the sum of all the individual magnetic moments, denoted as:

$$\vec{M} = \sum\vec{\mu} \quad \textbf{(Equation 2.4)}.$$

Without the help of an external magnetic field to align all of the magnetic moment vectors, the bulk magnetization of the nucleus is often

zero. Under an applied magnetic field, the spins are aligned resulting in a non-zero bulk magnetization.

Under the magnetic field, B_0, the magnetic spin state has energy of:

$$E = -\vec{\mu} \cdot \vec{B}_0 = -\gamma \hbar \vec{I} \cdot \vec{B}_0 \quad \textbf{(Equation 2.5)}$$

where the energy also depends on the orientations of $\vec{\mu}$ and $\vec{B}_0$. In the Cartesian coordinate system, $\vec{B}_0$ is usually defined along the z-direction.[7-9] The spin operators in this coordinate system are denoted by I_x, I_y, and I_z. The perturbation of the magnetic field to a nuclear spin along the z-direction has the Hamiltonian (Zeeman Hamiltonian):

$$\hat{H}_z = -\gamma \hbar \vec{I} \cdot \vec{B}_0 = -\gamma \hbar \begin{pmatrix} I_x \\ I_y \\ I_z \end{pmatrix} \cdot \begin{pmatrix} 0 \\ 0 \\ B_0 \end{pmatrix} = -\gamma \hbar I_z \cdot B_0 = \hbar \omega_0 I_z \quad \textbf{(Equation 2.6)}$$

The spin precession that arises from the angular momentum around the external magnetic field is given a frequency, which is called the Larmor frequency, ω_0, and can be expressed as:

$$\omega_0 = -\gamma B_0 \quad \textbf{(Equation 2.7)}.$$

The perturbation of the external magnetic field causes the ground spin state to split into sub-levels, a phenomenon which is also known as the Zeeman interaction (or effect).[7-9]

2.1.1.2 Zeeman Splitting

Spin 1/2 nuclei, like the proton (one isotope of the hydrogen atom) which is the most commonly studied nucleus *via* NMR spectroscopy, have spin *I=1/2* and m_I*=-1/2* or *1/2*. This gives the spin two energy

levels (high and low) due to the splitting under the magnetic field.[7-9] The spin population distribution is then described with the Boltzmann distribution in terms of the occupancy of these two states:

$$\frac{N_-}{N_+} = e^{-\frac{\Delta E}{kT}} \quad \textbf{(Equation 2.7)}$$

where k is the Boltzmann constant, T is the temperature in Kelvin, N_- is the number of spins in the higher energy level and N_+ is the number of spins in the lower energy state. The total number of spins, N, is the sum of N_+ and N_-. The spin population difference between the two states becomes:

$$\Delta N = N\frac{1-e^{-\frac{\Delta E}{kT}}}{1+e^{-\frac{\Delta E}{kT}}} \quad \textbf{(Equation 2.8)}$$

The energy level splitting for spin 1/2 nuclei is illustrated in **Figure 2.2.** The transition energy between $m_I=1/2$ and $-1/2$ leads to the population difference between the two states:

$$\Delta E = E_{-1/2} - E_{1/2} = \hbar\omega_0 \quad \textbf{(Equation 2.9)}$$

where the ω_0 is the Larmor frequency of the nuclei.

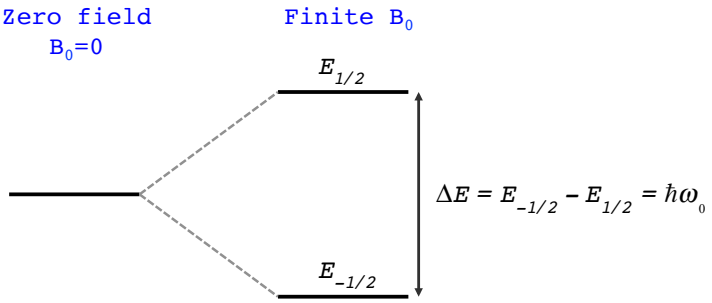

Figure 2. 2 Energy level diagram of a spin 1/2 nucleus, showing the Zeeman splitting.

2.1.1.3 Radiofrequency Pulses

Unfortunately, the longitudinal spin magnetization (along the external field) is challenging to measure, and NMR spectroscopy therefore measures the magnetization perpendicular to the field, which is called the transverse magnetization.[8] NMR signals result from the population difference between different spin states, as described in **Equation 2.8** and shown in **Figure 2.2.** In order to manipulate the spin population by placing some of them in an excited state, a radiofrequency (RF) field is applied in the xy-plane that is perpendicular to the external magnetic field, $\vec{B}_0$, in the laboratory frame. This is done by applying RF pulses to the nuclear spins in the sample, generating an oscillating magnetic field, $\vec{B}_1$. The longitudinal magnetization is then transferred to the transverse plane after the RF pulse. The precession of the transverse magnetization generates a rotating magnetic field that produces a small electric field. The oscillating electric current generated from this is called the free-induction decay (FID), which is detected by the quadrature detector. The RF field is time dependent, and for a pulse applied along the x-axis with an oscillating frequency ω_{rf} the applied field strength can be expressed as:

$$B(t) = B_1 cos(\omega_{rf} t + \varphi) \quad \textbf{(Equation 2.10)}$$

where B_1 is the field strength and φ is the phase of the pulse.[8-9] The Hamiltonian of this applied pulse is:

$$\hat{H}_{rf} = -\gamma\hbar \begin{pmatrix} I_x \\ I_y \\ I_z \end{pmatrix} \cdot \begin{pmatrix} B(t) \\ 0 \\ 0 \end{pmatrix} = -\gamma\hbar B_1 I_x cos(\omega_{rf} t + \varphi) \quad \textbf{(Equation 2.11)}$$

$$\hat{H}_{rf} = \hbar\omega_1 I_x cos\left(\omega_{rf} t + \varphi\right) \quad \textbf{(Equation 2.12)}$$

where ω_1 is the frequency that corresponds to the oscillating B_1 field. The Hamiltonian for the total external applied field becomes:

$$\hat{H}_{ext} = \hat{H}_z + \hat{H}_{rf} = \hbar\omega_0 I_z + \hbar\omega_1 I_x cos\left(\omega_{rf} t + \varphi\right) \quad \textbf{(Equation 2.13)}$$

where the first term represents the interaction of the nuclear spin with the external magnetic field, and the second term represents the interaction with the applied B_1 field.[8-9] The figurative representation is shown in **Figure 2.3.**

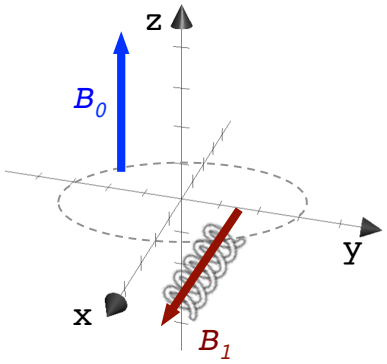

Figure 2. 3 External magnetic field in the laboratory frame, B_0, is the applied field along z-axis. B_1 is the pulsed RF field applied in the xy-plane that is perpendicular to B_0. The coil represents the RF coil used in the spectrometer.

The rotating frame is used instead of the laboratory frame when pulses are applied, where the oscillating spin precesses around the z-axis (B_0 direction). The rotation occurs at a frequency, ω_{rf}, which causes the precession to be at $\omega_0 - \omega_{rf}$, also known as the offset frequency, Ω.[7-9] Therefore the translation from the laboratory frame to the rotating frame removes the time dependence of the applied field, and **Equation 2.13** becomes time-independent:

$$\hat{H}_{ext} = \hbar\left(\omega_0 - \omega_{rf}\right) I_z + \hbar\omega_1 I_x = \hbar\Omega I_z + \hbar\omega_1 I_x \quad \textbf{(Equation 2.14)}$$

When the rotation frequency is close to the Larmor frequency, the offset frequency can be ignored. Therefore, the Hamiltonians for the RF pulse along x-axis and y-axis can be written as:

$$\begin{cases} \hat{H}_x = \hbar\omega_1 I_x \\ \hat{H}_y = \hbar\omega_1 I_y \end{cases} \quad \textbf{(Equation 2.15)}$$

In summary, the goal is to steer the spin magnetization into the xy-plane that is perpendicular to the external field, allowing the magnetization to become the observable by the NMR spectrometer RF receiver. During an NMR spectroscopy experiment, the signal detected is essentially the precession of the magnetization in the rotating frame.

2.1.2 Internal Interactions

The internal Hamiltonian of a nuclear spin is contributed to by all the nuclear interactions, which can be expressed as the sum of all the individual contributions including the nuclei and the surrounding electrons, as follow:

$$\hat{H}_{int} = \hat{H}_{CS} + \hat{H}_D + \hat{H}_J + \hat{H}_Q + \hat{H}_K + \hat{H}_P \quad \textbf{(Equation 2.16)}.^{8-9}$$

For a diamagnetic system with spin 1/2 nuclei, the nuclear spins experience interactions such as:

- $\hat{H}_{CS}$: Chemical shielding, perturbation of the magnetic field at the nucleus by the surrounding electrons;
- $\hat{H}_D$: Dipolar interaction, a through-space type of interaction with other nearby spins (homonuclear and heteronuclear);
- $\hat{H}_J$: Scalar coupling or *J*-coupling, indirect spin-spin coupling through chemical bonding.

For nuclear spins with spin > 1/2, the internal energy is also influenced by the quadrupolar interaction governed by $\hat{H}_Q$, which is the interaction between the nuclear electric field gradient at the nucleus and the nuclear quadrupole moment. In samples that contain conducting electrons, the Knight shift impacts the internal energy of the spin by $\hat{H}_K$, which arises from the interaction between the nuclear spin and the conduction electrons through contact that can cause a large shift and faster spin relaxation. Furthermore, in a paramagnetic system, the unpaired electrons interact strongly with the nuclear spin as governed by $\hat{H}_P$, which often leads to a large shift and wide range of NMR signals. For the PFSA system studied in this thesis, only the first three terms in **Equation 2.16** are applicable, although the *J*-coupling interaction is less dominant compared to the dipolar and chemical shielding interactions.

To simplify the analysis of the internal Hamiltonian of the nuclear spin, each individual internal interaction can be expressed in the form of spherical tensor representation. At the first-order perturbation level, only the d_z^2-component of the spherical tensor representation remains (where z is along the external field, B_0, direction). This has the angular-dependent term $(3\cos^2\theta-1)$, where θ is the angle between the internuclear vector and the external magnetic field.

The interactions that are important for the PFSA system are described in the rest of this section.

2.1.2.1 Chemical Shielding

The electrons surrounding a nuclear spin induce a local magnetic field experienced by the spin. This induced field contributes to the overall field strength that the nucleus senses, thus the precessing resonance frequency of the nucleus can be altered by the additional magnetic field.[7-9] This phenomenon is known as the chemical shielding interaction, and the Hamiltonian $\hat{H}_{cs}$ is used to describe the perturbation from the electrons. The precession frequency difference is observed in the NMR spectrum, which is referred as the chemical shift.

The Hamiltonian can be expressed in a similar fashion as **Equation 2.6,**

$$\hat{H}_{cs} = -\gamma\hbar\vec{I}\cdot\sigma\cdot\vec{B}_0 \quad (\textbf{Equation 2.17})$$

where σ is the chemical shielding (shift) tensor. The contribution of the electron around the nuclear spin usually depends on the orientation of the material in the external magnetic field B_0. The shielding tensor describes the chemical shielding with respect to the orientation of the nuclear spin, and is often represented by a 3×3 matrix in the Cartesian coordinate system (the laboratory frame):

$$\sigma = \begin{pmatrix} \sigma_{xx} & \sigma_{xy} & \sigma_{xz} \\ \sigma_{yx} & \sigma_{yy} & \sigma_{yz} \\ \sigma_{zx} & \sigma_{zy} & \sigma_{zz} \end{pmatrix} \quad (\textbf{Equation 2.18})$$

The Hamiltonian can be transformed into time-dependent and non-time-dependent terms based on density matrix theory.[9] Only the time-dependent part contributes to the spectrum to the first order. The Hamiltonian in **Equation 2.17** becomes:

$$\hat{H}_{CS} = -\gamma\hbar \begin{pmatrix} I_x \\ I_y \\ I_z \end{pmatrix} \cdot \begin{pmatrix} \sigma_{xx} & \sigma_{xy} & \sigma_{xz} \\ \sigma_{yx} & \sigma_{yy} & \sigma_{yz} \\ \sigma_{zx} & \sigma_{zy} & \sigma_{zz} \end{pmatrix} \cdot \begin{pmatrix} 0 \\ 0 \\ B_0 \end{pmatrix} = -\gamma B_0 \left(\sigma_{zx} I_x + \sigma_{zy} I_y + \sigma_{zz} I_z \right)$$

(**Equation 2.19**)

$$\hat{H}_{CS} \Rightarrow \hbar\omega_0 \sigma_{zz} I_z \quad \text{(**Equation 2.20**)}$$

The tensor element σ_{zz} is a function of spin orientations with respect to B_0, which can be challenging to analyze. The tensor matrix can be made diagonal by simply switching the axis system by rotating the axes based on the Euler angles (shown in **Figure 2.4**).[7-9]

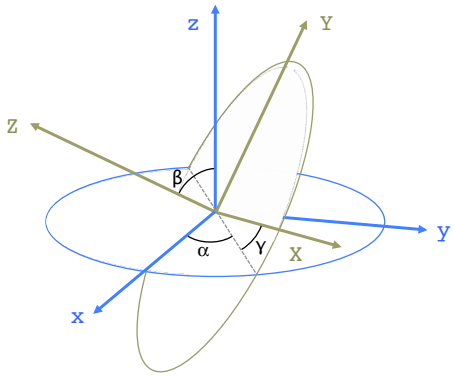

Figure 2. 4 Demonstration of Euler angles used during frame transformations. The original axes are x, y, and z; while the new axes after rotation are X, Y, and Z. The dash line represents the N axis. During the transformation from the laboratory frame to principal axis system, angles α (or ϕ) and β (or θ) are important.

The resulting axis frame is called the principal axis frame, denoted by PAF. The chemical shielding (shift) tensor representation becomes:

$$\sigma^{PAF} = \begin{pmatrix} \sigma_{xx}^{PAF} & 0 & 0 \\ 0 & \sigma_{yy}^{PAF} & 0 \\ 0 & 0 & \sigma_{zz}^{PAF} \end{pmatrix} \quad \text{(**Equation 2.21**)}$$

and the values on the diagonal are the principal values of the tensor along the different principal axes. The off-diagonal elements in the chemical shielding tensor in the PAF are all zero. The orientation of the PAF depends on the electronic structure of the sample system; in other words it is molecule dependent. Based on these values, the isotropic value is defined as the trace of σ^{PAF}:

$$\sigma_{iso} = \frac{1}{3}\left(\sigma_{xx}^{PAF} + \sigma_{yy}^{PAF} + \sigma_{zz}^{PAF}\right) \quad \textbf{(Equation 2.22)}$$

If two or more principal values are different, σ^{PAF} becomes anisotropic. The shielding anisotropy is defined as:

$$\Delta = \sigma_{zz}^{PAF} - \sigma_{iso} \quad \textbf{(Equation 2.23)}$$

based on the conventional assignment of the principal axes where the Z principal axis is the principal value that is the furthest from the isotropic value. The asymmetry parameter for the shielding (shift) tensor is defined as:

$$\eta = \left(\sigma_{xx}^{PAF} - \sigma_{yy}^{PAF}\right) \Big/ \sigma_{zz}^{PAF} \quad \textbf{(Equation 2.24)}$$

The chemical shift value observed in a typical NMR experiment (laboratory frame system, denoted as LAB) is described after the rotation transformation from the PAF to the LAB (**Figure 2.4**):

$$\sigma_{zz}^{LAB} = \sigma_{iso} + \frac{1}{2}\Delta\left(3\cos^2\theta - 1 + \eta\sin^2\theta\cos 2\phi\right) \quad \textbf{(Equation 2.24)}$$

and it is the sample-dependent resonance frequency which consists of the isotropic component with the anisotropic chemical shielding contribution. This value is usually normalized in parts per million (ppm) by frequency. The ppm value is calculated from the difference in resonance frequency between the detected frequency and referenced

frequency (different standard materials are used for different nuclei) relative to the referenced frequency.[7-9] The isotropic chemical shift in ppm is independent of the external field strength, yet the anisotropy fluctuates with time in the applied field and its magnitude depends on the field strength.[7-10]

In a solid sample (not single crystal), the nuclear spins are in random orientations with respect to the field direction. The distribution of the orientation gives rise to the superposition of all the narrow signals with a range of frequencies, where each signal represents a particular orientation relative to the external magnetic field. The resulting broad lineshape is called a powder pattern in solid-state NMR. In general, the molecular (isotropic) tumbling occurs if the molecule (the spin) is rotating in all possible directions, resulting in averaging the orientation-dependent anisotropic term. Therefore, the CSA is sensitive towards the motion of the system of interest, and it is also considered to be one of the possible spin relaxation mechanisms.[10]

2.1.2.2 The Dipolar Interaction

Nuclear spins are magnetic, and the magnetic moments that the spins exhibit can interact with each other through space. This phenomenon is known as the dipole-dipole or dipolar coupling interaction.[8-9] The dipolar interaction follows the classical expression of the interactions between two magnetic dipoles:

$$U = -\frac{\mu_0}{4\pi}\left\{\frac{3\left(\vec{\mu}_1\cdot\vec{r}\right)\left(\vec{\mu}_2\cdot\vec{r}\right)}{r^5} - \frac{\vec{\mu}_1\cdot\vec{\mu}_2}{r^3}\right\} \quad \textbf{(Equation 2.25)}$$

where $\vec{\mu}_1$ and $\vec{\mu}_2$ are magnetic dipoles, $\vec{r}$ is the vector between the two dipoles with magnitude/distance r, and μ_0 is the magnetic vacuum permeability. When considering the quantum mechanical representation of the spin magnetic moment of the nuclear spin in **Equation 2.3**, the Hamiltonian of the dipolar interaction between two spins, $\vec{I}_1$ and $\vec{I}_2$, can be expressed as:

$$\hat{H}_D = -\frac{\mu_0}{4\pi}\frac{\gamma_1\gamma_2}{r^3}\left\{\frac{3\left(\vec{I}_1\cdot\vec{r}\right)\left(\vec{I}_2\cdot\vec{r}\right)}{r^2} - \vec{I}_1\cdot\vec{I}_2\right\} \quad \textbf{(Equation 2.26a)}$$

The scalar products in the equation can be expanded with expressions under polar coordinates.[9, 11] θ is used to describe the angle between the internuclear vector (between spin 1 and 2) and the external magnetic field or z-axis in the Cartesian coordinate system. ϕ is the azimuth angle that describes the angle between the projection of the internuclear vector onto the Cartesian x-y plane and x-axis. Therefore, **Equation 2.26a** is expressed as:

$$\hat{H}_D = -\frac{\mu_0}{4\pi}\frac{\gamma_1\gamma_2}{r^3}\left[A + B + C + D + E + F\right] \quad \textbf{(Equation 2.26b)}.$$

with

$$A = \hat{I}_1\hat{I}_2\left(3\cos^2\theta - 1\right)$$

$$B = -\frac{1}{4}\left[\hat{I}_{1+}\hat{I}_{2-} + \hat{I}_{1-}\hat{I}_{2+}\right]\left(3\cos^2\theta - 1\right)$$

$$C = -\frac{3}{2}\left[\hat{I}_{1z}\hat{I}_{2+} + \hat{I}_{1+}\hat{I}_{2z}\right]\sin\theta\cos\theta\ e^{-i\phi}$$

$$D = -\frac{3}{2}\left[\hat{I}_{1z}\hat{I}_{2-} + \hat{I}_{1-}\hat{I}_{2z}\right]\sin\theta\cos\theta\ e^{i\phi}$$

$$E = -\frac{3}{4}\hat{I}_{1+}\hat{I}_{2+}\sin^2\theta\ e^{-2i\phi}$$

$$F = -\frac{3}{4}\hat{I}_{1-}\hat{I}_{2-}\sin^2\theta\ e^{2i\phi}$$

$\hat{I}_{i+}$ and $\hat{I}_{i-}$ are the raising and lowering spin operators for the spin systems respectively, where $\hat{I}_{i\pm} = \hat{I}_{ix} \pm i\hat{I}_{iy}$.

This general expression is complicated, and to simplify this the secular approximation is used.[8-9] The Hamiltonian can be considered as the combination of two groups of contributions. One group represents the effect that the internal spin interactions experience predominately caused by the external magnetic field, which is known as the 'secular' term, which means the term in the Hamiltonian commutes with the Zeeman Hamiltonian (sharing the same eigenfunctions).[8-9] This makes the term simultaneously observable in the presence of Zeeman splitting. The other group is referred to as the 'non-secular' term, in which the term does not commute with the Zeeman Hamiltonian for the spin system, and their contribution is not observable with the Zeeman effect.

For a homonuclear spin pair (j and k), i.e. both spins are the same isotopic species, only term A and B in **Equation 2.26b** are secular. The B_0 field has a significant contribution towards both terms by directly affecting the Cartesian spin operators. Therefore, the non-secular terms of **Equation 2.26** can be ignored since they do not have a notable contribution to the energy of the spin system. Therefore the secular term of the Hamiltonian of homonuclear dipole-dipole interaction can be expressed as:

$$\hat{H}_D^{Homo} = -D_{jk}\left(3\cos^2\theta - 1\right)\frac{\left(3\hat{I}_{jz}\hat{I}_{kz} - \hat{I}_j\hat{I}_k\right)}{2} \quad \textbf{(Equation 2.27)}$$

in which

$$D_{jk} = \frac{\mu_0}{4\pi}\frac{\gamma_j\gamma_k\hbar}{r_{jk}^3} \quad \textbf{(Equation 2.28)}$$

where D_{jk} is the dipolar coupling constant in units of angular frequency. In these two equations, θ is the angle between the internuclear vector and the external magnetic field, $\hat{I}_{jz}$ and $\hat{I}_{kz}$ are spin operators for interactions between the spins and the magnetic field, $\hat{I}_j$ and $\hat{I}_k$ are the spin operators, γ_j and γ_k are the gyromagnetic ratio of the nuclei or spins, and r_{jk} is the internuclear distance between the two spins (as demonstrated in **Figure 2.5**). Similar to the homonuclear dipolar interaction, in the heteronuclear case term A in **Equation 2.26** is the only one that commutes with the Zeeman Hamiltonian, i.e. has secular contribution, which leads to the geometry dependent term $\left(3\cos^2\theta - 1\right)$ in the heteronuclear dipolar interaction.

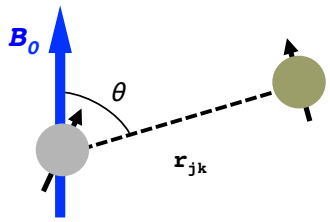

Figure 2. 5 Pictorial representation of dipole-dipole interaction between two spins with respect to the external magnetic field.

The strength of the dipolar interaction depends on the internuclear distance and its orientation with respect to the external magnetic field. Molecular motions lead to a reduction in the observed dipolar coupling constant due to changing orientations of the internuclear vectors and time-dependent changes in the internuclear distances. The dipole-dipole interaction is used to describe the isolated spin pair, yet in a multi-spin system, the introduction of an effective dipolar coupling constant is necessary to analyze the system

analytically.[4-5, 12] This value is often referred to as the apparent dipolar coupling constant, and is defined as:

$$D_{eff} = D_{app} = \sqrt{\sum_{i<j} D_{ij}^2} \quad \textbf{(Equation 2.29)}$$

where *i* and *j* indicate different spins. This concept will be expanded upon in the section where the development of the dipolar recoupling method is introduced.

2.1.2.3 Magic Angle Spinning

The internal interactions between spins, like CSA and dipolar coupling, have angular dependent terms as shown in **Equation 2.24** and **2.27.** In the solution state, the rapid molecular tumbling motion averages the orientation or geometry dependent term; however in the solid state the random orientations of the spins with respect to the external magnetic field make those internal interactions play a significant role, which leads to signal line broadening in NMR spectral features. In order to achieve good spectral resolution, one approach is to remove the anisotropic components *via* spatial averaging, i.e. manipulating the geometry dependent parts of the Hamiltonians.[13,14-15] As one of the most significant developments to achieve spectral resolution, magic angle spinning (MAS) has been routinely applied in ssNMR field. This technique was first introduced by Andrew[13] and Lowe[14] in the 1950s, and significant progress has been made towards ultra-fast MAS speeds up to 130 kHz with modern equipment.[16]

The solid sample is packed into a cylindrical container (usually is made of ZrO_2), often referred as a rotor. It then spins rapidly at a fixed angle to the external magnetic field, B_0, about its symmetry axis. The anisotropic components of the majority NMR interactions are

proportional to the second Legendre polynomial, $P_2(\cos\theta)$, which becomes 0 when the angle is 54.74°. This angle is referred as the magic angle, and it is the angle between the body diagonal of a cube and its edge. If the MAS speed is fast enough, the orientation dependent components are reduced to zero in both chemical shielding and dipolar interactions.[9] Under MAS conditions, the NMR Hamiltonians become time-dependent. This spatial averaging of the Hamiltonians by MAS relies on the time-dependent average of the Hamiltonians when the spinning frequency ω_r is much faster than the transition frequency associated with the Hamiltonians ω_H (H can stands for CSA or dipolar interactions), such that the anisotropies are averaged out. Only the spatial parts of the Hamiltonians remain time-dependent under MAS.

For a spin like fluorine that experiences strong anisotropic chemical shielding, under MAS the spectral frequency is time-dependent and can be expressed based on the shielding tensor in a rotor frame (ROT):

$$\begin{aligned}\omega_{CS} = -\omega_0 \Bigg\{ & \sigma_{iso} + \frac{1}{2}\left(3\cos^2\theta_R - 1\right)\left(\sigma_{zz}^{ROT} - \sigma_{iso}\right) \\ & + \sin^2\theta_R \left[\frac{1}{2}\left(\sigma_{xx}^{ROT} - s_{yy}^{ROT}\right)\cos\left(2\omega_R t\right) + \sigma_{xy}^{ROT} sin\left(2\omega_R t\right)\right] \\ & + 2\sin\theta_R \cos\theta_R \left[\sigma_{zz}^{ROT}\cos\left(\omega_R t\right) + \sigma_{yz}^{ROT}\sin\left(\omega_R t\right)\right]\Bigg\}\end{aligned}$$ **(Equation 2.30)**[9]

where ω_R is the spinning frequency and θ_R is the spinning angle with respect to B_0. This equation can also be expressed in the PAF using the Euler angles generated from rotating the PAF into ROT, as:

$$\begin{aligned}\omega_{CS} = -\omega_0 \Big\{ & \sigma_{iso} + \left[A_1\cos\left(\omega_R t + \gamma\right) + B_1\sin\left(\omega_R t + \gamma\right)\right] \\ & + \left[A_2\cos\left(2\omega_R t + 2\gamma\right) + B_2\sin\left(2\omega_R t + 2\gamma\right)\right]\Big\}\end{aligned}$$ **(Equation 2.31)**.[9]

where the coefficients A_1, A_2, B_1, and B_2 depend on the Euler angles α and β (PAF to ROT) and the anisotropy parameters Δ and η.[9, 11] The

anisotropic terms in **2.31** oscillate at frequencies ω_R and $2\omega_R$. If $\omega_R >> \Delta$, the effect contributed by these terms can be neglected; however, if $\omega_R << \Delta$, these terms create the spectral features that show up periodically at integer multiples of the spinning frequency. These features are typically referred to as the spinning sidebands (SSBs).[9, 11] The frequency range of the SSB pattern is close to the span of the static powder pattern signal, which can often be used to extract CSA information more efficiently compared to collecting the static powder pattern.

The MAS also imposes the time-dependence onto the homonuclear dipole-dipole interactions. The orientation dependent part in **Equation 2.27**, $\frac{1}{2}\left(3\cos^2\theta - 1\right)$ (1/2 has been absorbed here for conversion convenience), has become $\frac{1}{2}\sin^2\beta\cos\left(2\omega_R t + 2\gamma\right) - \frac{1}{\sqrt{2}}\sin 2\beta\cos\left(\omega_R t + \gamma\right)$ with the dependence on spinning frequency ω_R and the Euler angles. This conversion implies that the dipolar Hamiltonian vanishes after each rotor period resulting in a narrow signal under fast MAS. If ω_R is much faster than the homonuclear dipolar coupling linewidth, spatial averaging by MAS eliminates the orientation dependent term (=0). If ω_R is much less than the dipolar linewidth, MAS does not affect the spectral resolution significantly, therefore dipolar line-broadening will present in the spectrum.

At an intermediate spinning speed, the time-dependent homonuclear dipolar coupling interactions can also cause SSBs. The component B in **Equation 2.26b** represents the interchange of the Zeeman spin states in the spin system for spins that are dipolar coupled, which generates non-stationary time evolution.[9, 11] This evolution happens on the

timescale of spinning, which means the geometric dependence oscillates within one rotor period. This stops the spatial averaging of the homonuclear dipolar interactions under MAS. This phenomenon is very different than the SSBs caused by the incomplete spatial averaging of the CSA and the heteronuclear dipolar interaction. The SSBs caused by CSA and heteronuclear dipolar coupling are usually sharper than the ones caused by the homonuclear dipolar coupling interactions.

Overall, faster spinning speeds result in highly efficient averaging; however, the choice of spinning speed is determined by the overall evaluation of the nature of the sample, instrumentation limits and the type of the NMR experiment.

2.1.3 Nuclei Investigated in This Thesis

The current thesis mainly focuses on the PFSA electrolyte materials mentioned in the previous chapter. The nuclei studied in this thesis are summarized in **Table 2.1**[17], along with respective Larmor frequencies at corresponding field strengths. ^{1}H, the most commonly studied NMR nucleus is included in the table as reference.

Table 2. 1 Table of nuclei investigated in this thesis.

Nucleus	Spin	Natural Abundance (%)	Gyromagnetic Ratio (10^6 rad $T^{-1}s^{-1}$)	Molar Receptivity Relative to ^{1}H	ω_0 at 7.0 T (MHz)	ω_0 at 20.0 T (MHz)
^{1}H	1/2	99.9885	267.51	1.00E+00	300.130	850.130
^{19}F	1/2	100	251.67	8.32E-01	282.404	799.921
^{13}C	1/2	1.07	67.26	1.59E-02	75.468	213.765

*The underlined values are the Larmor frequencies that used in the NMR experiments throughout this thesis.

2.1.4 Dipolar Recoupling Method

On one hand, the MAS technique helps to achieve chemical speciation with well-resolved spectra by a motion averaging of the dipolar interactions. On the other hand, based on the Hamiltonian of the dipolar interaction, this anisotropic interaction is informative regarding local spin environment.[9] After the removal of the dipolar couplings by MAS, using some clever NMR pulse sequences when the double-quantum coherence (DQC) is excited and evolved, the dipolar interaction can be re-introduced into the spin system, after which the DQC is monitored as a function of evolution time. The schematic of a general DQ recoupling NMR pulse sequence is illustrated in **Figure 2.6**, which consists of DQ excitation and reconversion periods followed by a 90° pulse before the signal acquisition. The spins change their spin states between $\alpha\alpha$ and $\beta\beta$ during the excitation, which corresponds to the transition between coherence order +1 and -1 generating the DQC (ΔM=2).[7, 9, 18-19] During the reconversion periods, the DQCs that have been averaged out by MAS during the excitation period are reintroduced. The DQCs are then converted into an NMR observable state, i.e. the single quantum coherences, based on selection rules before the acquisition period.

The signal intensity after the recoupling of the DQC can be monitored as a function of the DQ evolution time, which is represented as the excitation/reconversion time in the pulse sequence and is labeled as τ_{DQ} in **Figure 2.6.**

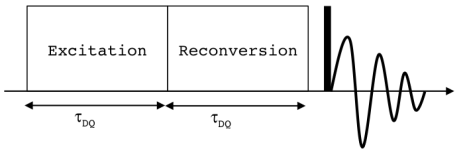

Figure 2. 6 The schematic double quantum filter (dipolar recoupling) NMR pulse sequence, which consist of the excitation, reconversion blocks and a read-out pulse before acquisition.

Homonuclear dipole-dipole recoupling ssNMR pulse sequences have been applied to understand the structure[3, 5, 20] and local dynamics of small molecules in the solid state.[21-24] For example, proton local mobility has been analyzed by monitoring the ^{1}H–^{1}H dipolar coupling interactions using a ^{1}H MAS DQ recoupling technique, which has helped to establish proton conducting mechanism in solid acid materials by observing changes in H-bonding networks.[22-23] This DQ NMR technique has also been applied to compare proton conductivity in Nafion and sulfonated poly (ether ether ketone) (SPEEK) by probing the difference in H-bonding interactions.[24] In SPEEK materials, the investigation has been focused on the proton dynamics and resulting proton conduction mechanism in membrane materials. For the PFSA ionomer performance study presented here, polymer dynamics are evaluated at the molecular level through ^{19}F NMR to directly characterize the behaviour of the backbone versus the side chain. In this study, we take advantage of the ^{19}F spectral resolution under MAS and full assignment to provide spectroscopic handles on backbone versus side-chain dynamics in PFSAs utilizing the specific homonuclear ^{19}F-^{19}F couplings in these domains. Ultimately, this data can be used as a metric to compare local motion properties of PFSA materials that have similar structures.

2.1.4.1 Method Development for PFSA System

In highly fluorinated materials such as PFSA, in which the ^{19}F nuclei form a strongly coupled multi-spin network rather than occurring as isolated spin pairs, the dipolar coupling constant is better described as an "apparent dipolar coupling" (D_{app}). In the absence of molecular motions, this can be calculated by taking the root-sum-square

of the dipolar coupling constants calculated to each of its neighboring within a specified cutoff distance (similar to **Equation 2.29**):

$$D_{app}^{0} = \left(\sum_{i<j} D_{ij}^{2} \right)^{1/2} \quad \textbf{(Equation 2.32)}^{12, 25}$$

In the presence of molecular motions at a particular temperature T, the observed apparent dipolar coupling constant for a nucleus will be reduced from this no-motion limit, and this reduction can be quantified in terms of a "dynamic order parameter" S^{T} which is defined as the ratio:

$$S^{T} = D_{app}^{T} \Big/ D_{app}^{0} \quad \textbf{(Equation 2.33)}.$$

This concept has been introduced to soft matter[26] and applied to macromolecular systems to quantify the amplitude of motion.[3, 27] The dynamic order parameter encodes a combination of the rate and amplitude of the local motion, which cause a local averaging of D_{ij} for a particular spin system. In some cases, such motion can be modeled using the relative orientations of the interaction tensors for all of the spins involved. These interactions could be modeled to change as a result of a particular geometric reorientation such as a helical jump. However, for the case of the complicated multi-spin system within the amorphous PFSA ionomer, it is beyond the scope of this work to develop a specific model with respect to the geometry of the local motions. Instead, we note that the relative orientations of the CSA and D_{ij} tensors are ill-defined for the PFSA. We utilize the observed value of S^{T} under particular conditions as a measure of the impact of the combination of changes in the rate and amplitude of local motions. Moreover, we compare the relative values of S^{T} under various conditions and with respect to a calculated rigid structure in order to describe

the changes in local motion within different chemically distinct regions of the ionomer. Finally, we note that it is not expected that the motion of the side-chain or backbone would ever be fully isotropic, and thus the value of S^T would not go to zero in this system.

There are different types of DQ recoupling NMR pulse sequences available to probe homonuclear dipolar interactions. In the current study, the $R26_4^{11}$ symmetry-based recoupling pulse sequence was used (the nomenclature will be elucidated in the next section).[18, 28-29] A useful property of the $R26_4^{11}$ symmetry is that it is possible to sample the double quantum coherences (DQCs) after any even number of *R* elements, without having to complete a full block of 26 *R* elements. Compared to the commonly used C-symmetry sequences, like POST-C7[30] where there are more interfering second order terms involving the CSA contribution, and the Back-to-Back (BABA) sequence[3, 5, 12, 20] in which the DQCs must be sampled after full rotor periods, this feature of the $R26_4^{11}$ sequence allows for closer time incrementation, which is advantageous in that the initial build-up region of the DQ build-up curves can be much better defined.[5, 12, 31-32]

2.1.4.2 Recoupling Sequence Comparison

To demonstrate the difference, the BABA and $R26_4^{11}$ symmetry pulse sequences are compared. These two symmetry pulse sequences follow the same DQ evolution scheme, however they are different in terms of the composition of the excitation and reconversion pulses. These elements often consist of composite pulses, which have the same composition but differ in terms of pulse phases. The phases of the pulses determine the coherence pathways that are selected for observation at the end of the

experiment. In BABA and $R26_4^{11}$, the selected coherence pathways are slightly different but DQ coherences can be observed effectively via both pulse sequences. The numbers, 26, 4 and 11, are symmetry numbers: 26 is the number of the R elements; 4 indicates the number of complete sample revolutions; and 11 determines the RF pulse phase change. Both of these two pulse sequences are rotor-synchronized, which means that the application of the RF pulses depends on the rotor period (τ_r) i.e. the time elapsed during one rotation of the sample rotor. BABA, which consists of $C4_2^1$ elements, is designed in a way such that four 90° RF pulses are applied sequentially during each rotor revolution, thus the pulse length is determined by the spinning speed. However, in the $R26_4^{11}$ pulse sequence design, each R-type symmetry block lasts $4\tau_r$.[19] Therefore, the power level used in each sequence is dictated by the spinning speed. The time τ_{DQ} is a multiple of τ_r in BABA, but a multiple of $2 \times \left(\frac{4\tau_r}{26}\right)$ in $R26_4^{11}$. Due to the difference in pulse sequence design, the increments of DQ evolution/reconversion time for these two sequences are quite different.

In order to choose a suitable pulse sequence, Nafion is studied using these two different pulse sequences. The protonated Nafion 117 material is studied under ambient conditions. The ^{19}F MAS NMR spectrum of Nafion is shown in **Figure 2.7a** with the corresponding peak assignments. The backbone CF_2 signal is at -122 ppm and the backbone branching point CF(b) is observed at -138 ppm; while the side chain fluorine signals are assigned as SCF_2 at -117 ppm, CF_3 and OCF_2 groups at -80 ppm, and CF(s) at -144 ppm, where signals from CF_3 and OCF_2 have similar chemical shifts. With this resolution, the signal at -122 ppm

contributed to by the backbone CF_2 and the signal at -80 ppm generated from side chain fluorines are chosen for investigation. These two signals are well resolved, and are representative of the two different regimes, i.e. hydrophobic backbone and hydrophilic side chain. The DQ build-up curves are analyzed using these two different DQ recoupling experiments, shown in **Figure 2.7b** and **2.7c.** These DQ build-up curves are normalized mathematically with respect to the most intense signal in each data set (I/I_{MAX}). By normalizing the signals, the build-up trends from two different NMR experiments can be compared without bias.

With our experimental setup, the τ_r in BABA experiment is 40.0 μs under 25 kHz MAS, thus the smallest DQ evolution/reconversion increment time is 40.0 μs, while the smallest DQ evolution increment time in $R26_4^{11}$ experiment is 20.5 μs, even though the τ_r is 66.7 μs with a much slower spinning speed of 15 kHz. Additionally, a smaller dipolar scaling factor for $R26_4^{11}$ compared to BABA affects the determination of the number of points on the DQ build-up curve. From **Figure 2.7**, the DQ build-up curves generated from $R26_4^{11}$ experiments (**2.7c**) have more data points in the initial build-up region before the curves reach their maximum, compared to the ones from BABA experiments (**2.7b**). The data points in terms of DQ evolution time during the initial build up period are critical to the local dynamics analysis, since these data points define how strong the dipole-dipole interactions are. More data points give rise to more defined build-up profiles. The tailing of the DQ build-up curves after their local maxima becomes zero in both cases, an effect which results from motion-related relaxation or other dephasing mechanisms.[5, 12] Based on the comparison between these two sets of DQ

build-up curves, $R26_4^{11}$, the pulse sequence with more data points defining the DQ initial rise, is selected in this local dynamics study of ionomer materials, as it provides reliable sources for the extraction of the dipolar coupling which is the key to the local dynamics analysis.

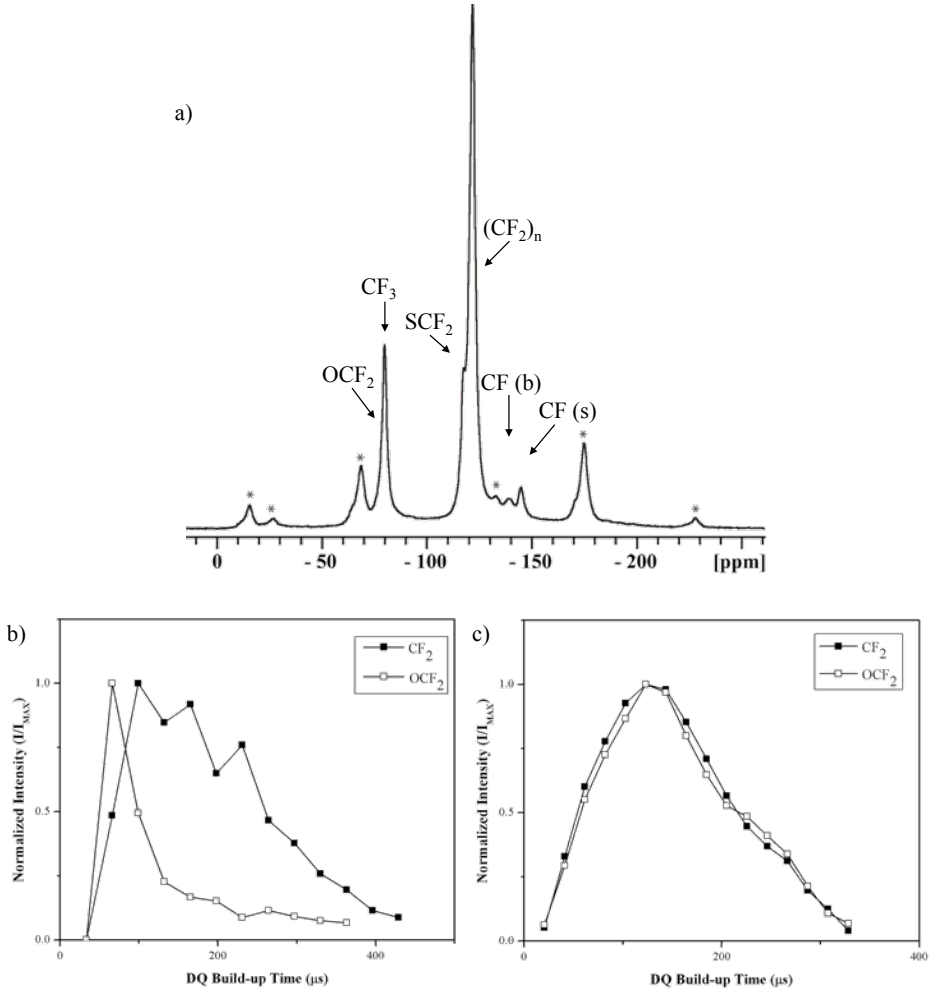

Figure 2. 7 a) ^{19}F 15 kHz MAS NMR spectrum of Nafion 117 at ambient condition. b) Normalized DQ build-up curves using BABA pulse sequence. c) Normalized DQ build-up curves using $R26_4^{11}$ pulse sequence. Both b) and c) were analyzed in the same way, i.e. mathematically normalization as described previously.

2.1.4.3 Normalization of DQ Build-Up Curve

To accurately probe the dipole-dipole interactions, it is important to normalize the DQ build-up curves in order to compensate for

relaxation effects and pulse sequence imperfections. The normalization procedure that was introduced in the ^{1}H DQ study of polymer melts by Graf et al.[4] and later elaborated on by Saalwächter,[5, 12] was employed here in which two spectra were collected at each value of the dipolar recoupling time τ_{DQ}: a "reference" (REF) spectrum and a "double quantum" (DQ) spectrum, the difference being found in the selected coherence pathways due to different phase cycling.[5, 12] The interleaved pseudo two-dimensional (2D) NMR spectrum is demonstrated in **Figure 2.8**, in which polytetrafluoroethylene (PTFE) was measured to demonstrate. The 2D NMR data is one set of ^{19}F DQ recoupling NMR data of PTFE at room temperature. In the direct dimension (F2), each row is a ^{19}F MAS NMR spectrum but with alternating experiment sequence, where the odd-numbered slices are the DQ experiments and the even-numbered ones are the reference. The indirect dimension (F1) is the projection of the spectrum of each row, which is observed as a 'zig-zag' pattern due to the difference in intensity between the DQ and reference experiments.

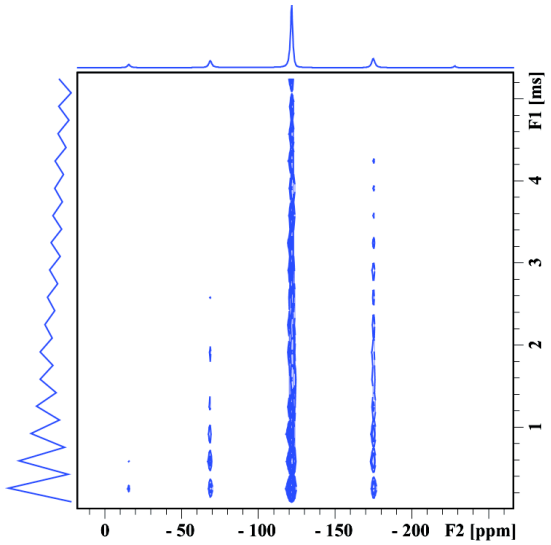

Figure 2. 8 Pseudo 2D ^{19}F NMR spectrum of PTFE under 15 kHz MAS, with alternating DQ and reference experiments.

The normalized double quantum (*nDQ*) build-up curve was generated by calculating $nDQ = DQ/\sum MQ$, where $\sum MQ = DQ + REF$ at each recoupling time, as illustrated in **Figure 2.9.** The initial rise of the *nDQ* curve is indicative of the effective dipolar interaction the system experiences. Qualitatively, the slope of the initial build-up curve is a direct way to visualize the strength of the dipolar interaction that is probed.

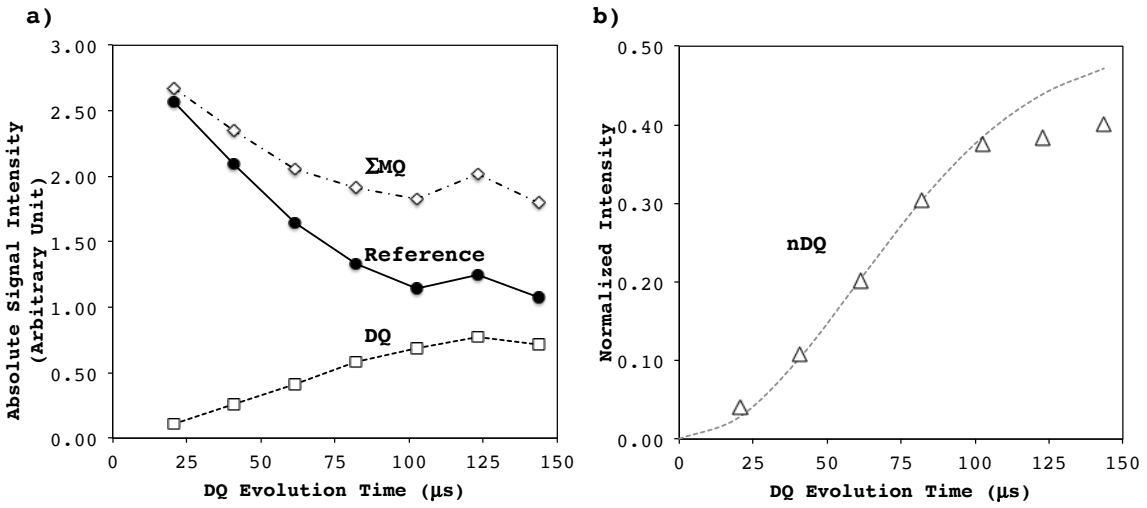

Figure 2. 9 Point-by-point normalization of the DQ term with experimental curves plotted. a) One set of the DQ NMR experimental curves: Absolute signal intensities for DQ and reference experiments as functions of DQ evolution time; ΣMQ is the sum of DQ and reference intensities. b) Normalized DQ curve based on the dataset in a).

2.1.4.4 Study of Fluorinated Polymers

The *nDQ* build-up curves are used to investigate the apparent dipolar coupling interactions between spins, in this study, ^{19}F and ^{19}F, at different ^{19}F environments. The homonuclear dipolar coupling interaction is described in terms of a dipolar coupling constant, which is inversely proportional to the internuclear distance. PTFE and polyvinylidene fluoride (PVDF) share the same basic structure as polyethylene albeit with different degrees of fluorination, thus the

PTFE and PVDF membranes are used in model ^{19}F DQ recoupling experiments using the $R26_4^{11}$ sequence. The ^{19}F–^{19}F dipolar interactions in PVDF are diluted by a factor of two with $-CH_2-$ groups compared to those in PTFE. The conventional ^{19}F MAS NMR with no ^{1}H decoupling indicates that there is only one fluorine site in PTFE and multiple fluorine signals in PVDF, as shown in **Figure 2.10.**

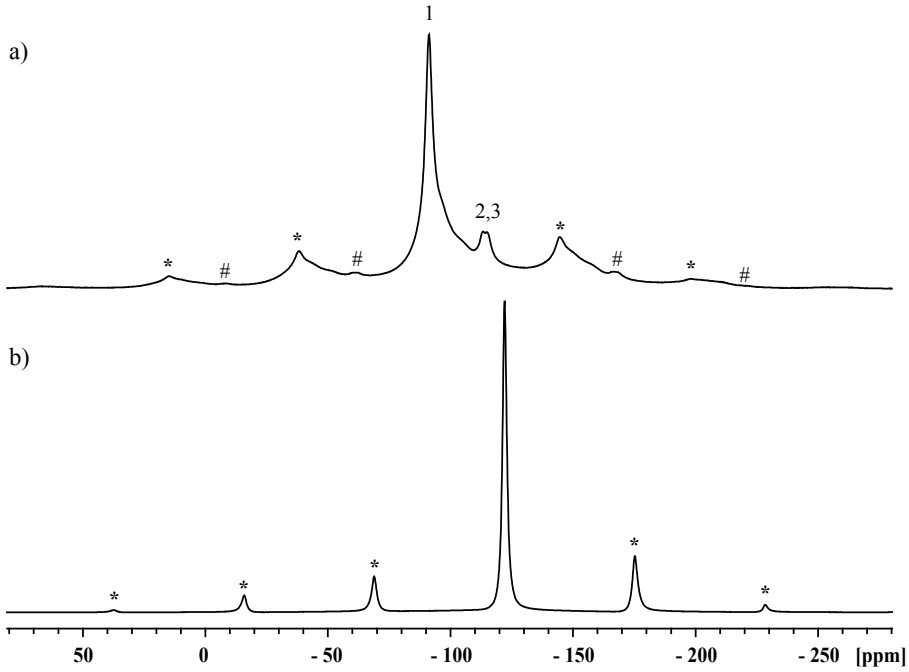

Figure 2. 10 ^{19}F 15 kHz MAS NMR spectra for a) PVDF membrane, where * indicates the spinning side bands for peak 1 and # indicates the spinning side bands for peak 2,3; b) PTFE membrane, where * indicates the spinning side bands.

The ^{19}F signals in PVDF are consistent with previous studies using SSNMR to monitor the amorphous and crystalline ^{19}F sites. The signals at -112 ppm and -115 ppm, labeled as 2 and 3 in **Figure 2.10a**, correspond to the CF_2 sites with head-to-head configurations in the structure.[33-34] A series of ^{19}F DQ recoupling NMR experiments at variable temperatures using the $R26_4^{11}$ sequence are then applied to these two materials.

Peak 1, the most populated ^{19}F site in PVDF as indicated in **Figure 2.10a**, and the isotropic peak of PTFE in **Figure 2.10b** are normalized and analyzed. The *nDQ* build-up curves of PTFE and PVDF are extrapolated by normalizing the intensity from the DQ experiment with respect to the corresponding reference experiment shown in **Figure 2.11.** DQ build-up behaviors are studied at a range of temperatures between 310 K – 370 K.

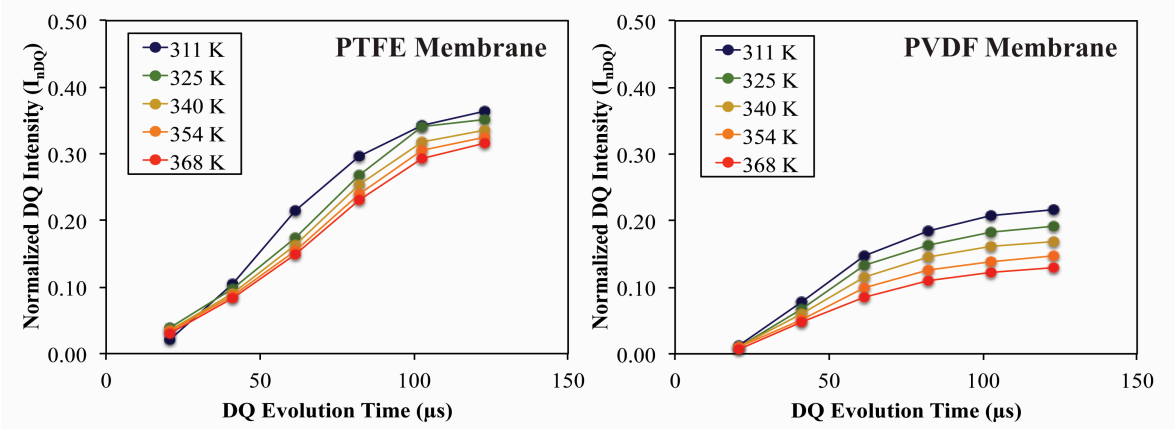

Figure 2. 11 The nDQ build-up curve comparison between PTFE and PVDF membranes at 310 K – 370 K. The curves are colour-coded with respect to temperatures.

At the same temperature, the slope of initial *nDQ* build-up curve for PVDF is shallower than that for PTFE. This observation is the result of the distance dependence of the dipole-dipole interaction, which plays a dominant role in this case. Theoretically, the dipolar coupling constant describes one isolated spin pair with a constant internuclear distance. In the system studied here there are many spin pairs that contribute to the apparent dipolar coupling interaction, a situation referred to as the multi-spin effect. The D_{app} observed from the *nDQ* build-up curves is the result of the combination of all of the homonuclear dipole-dipole interactions in the system. In PTFE, the apparent dipole-dipole interaction observed is primarily contributed to by the interaction between the two fluorines that are bonded with the

same carbon atom since they are close to each other; the surrounding fluorines are additionally dipolar coupled with the CF_2 through space, and thus also contribute to the apparent dipole-dipole interaction. In contrast, the interaction between the geminal fluorines in the CF_2 unit in PVDF is the dominant contribution to the apparent dipole-dipole interaction; however, the through-space interactions from the surrounding fluorines are diluted with the $-CH_2-$ groups. Therefore, the net dipole-dipole interaction is weaker in PVDF than that in PTFE, i.e. $D_{app}(PVDF) < D_{app}(PTFE)$. Furthermore, the protons in the adjacent $-CH_2-$ units accelerate the relaxation of the fluorines in the $-CF_2-$ groups through a heteronuclear dipole-dipole interaction induced relaxation mechanism, which affects the normalized intensity in *nDQ* build-up curves.

The slope of the initial build-up curve becomes much shallower as temperature increases in both PTFE and PVDF, which means it takes more time for the DQ term to reaches its local maximum at elevated temperature. The increase in temperature introduces thermal energy that triggers a higher degree of molecular tumbling, altering the orientation of the internuclear vector between the two fluorines with respect to the magnetic field; thus changing the orientation-dependent space term of the DQ Hamiltonian. This leads to the decrease in D_{app}, which is represented by a shallower slope of the initial *nDQ* build-up curve with the temperature elevation. Furthermore, within the same experimental temperature range, the change in the slopes of the initial *nDQ* build-up curves of PVDF is much greater than those in PTFE, which indicates that the ^{19}F-^{19}F DQ interactions in PVDF are more temperature-dependent compared to the ones in PTFE. The weaker the dipole-dipole interaction is, the more sensitive it will be towards the temperature change. In

the cases of PTFE and PVDF, there is neither spin exchange nor dynamics occurring in either system. The change in build-up curve slope is purely from the increase of molecular motion due to temperature elevation. DQ build-up behaviour analysis is able to distinguish between systems with different strengths of dipolar coupling interactions. Coupled with variable temperature experimental conditions, the temperature dependence of the spin system can also be studied using the *nDQ* build-up behavior analysis.

In order to further investigate the relationship between local dynamics and *nDQ* build-up curve behaviors, a PTFE membrane and powder are studied using the same method. The *nDQ* build-up curves are provided in **Figure 2.12.** The PTFE membrane and powder are expected to have the same chemical composition but in different physical forms. The general trends of the curves are almost identical. At 311 K, the curves from both the membrane and the powder reach their local maxima at ~0.4 normalized DQ intensity; and also both of the *nDQ* curves take ~120 μs to reach their local maxima. Under these conditions, the PTFE membrane and powder behave similarly in *nDQ* build-up analysis, since the fluorines in both forms are sitting in identical spin systems with the same ^{19}F–^{19}F internuclear distances in the multi-spin system. As discussed in the previous section of this chapter, the dependence on internuclear distance of the apparent dipole-dipole interactions in both forms is exactly the same. As shown in **Figure 2.12**, as the temperature increases the slope of initial *nDQ* build-up curve becomes shallower for the PTFE membrane, while for the PTFE powder the *nDQ* build-up curves analyzed from variable temperature experiments have little variation.

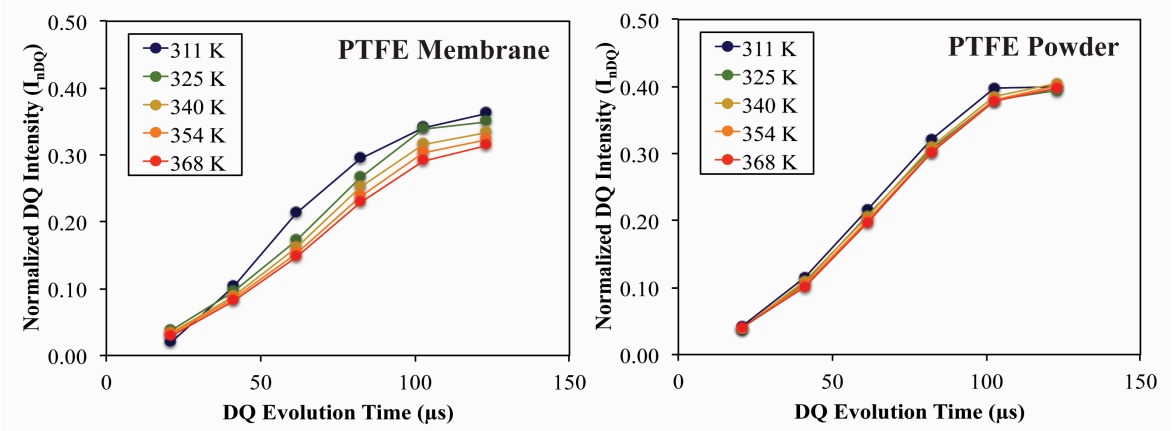

Figure 2. 12 The nDQ build-up curve comparison between PTFE membrane and powder at 310 K – 370 K. The curves are colour-coded with respect to temperatures.

This difference in the initial slope changing as the temperature elevates between PTFE membrane and powder materials is a significant observation. The internuclear-distance dependency does not dominate the change in slope with the temperature range, since the spins experience identical environments. The major contributor to the changing slope in PTFE membrane is the changing orientation of the internuclear vector between two fluorines with respect to the external magnetic field. The PTFE powder is more crystalline than the PTFE membrane. In the PTFE powder, the internuclear vectors are fixed even at increased temperatures; on the other hand, in the PTFE membrane the material itself is soft and loose, which causes in the internuclear vectors to change orientations after absorbing external thermal energy. It is suggested that the membrane's mechanical properties bring more degrees of freedom in molecular motion compared to the powder form. The comparison between the PTFE membrane and powder further establishes the viability of the ^{19}F DQ recoupling NMR method applied here in the investigation of local dynamics.

2.1.4.5 Quantification of Dipolar Interaction

To fit the initial rise of normalized DQ curves for multi-spin systems, the relatively simple fitting function based on a second-moment approximation has been employed:

$$I_{nDQ} = \frac{1}{2}\left(1 - e^{-2\langle\phi^2\rangle}\right) \quad \textbf{(Equation 2.34)}$$

Saalwächter et al. suggested that the apparent dipolar coupling constant, D_{app}, can be extracted and used to quantify the dipolar interactions in multi-spin systems in the presence of dynamics by fitting the normalized DQ build-up curve.[5] The exact form of $\langle\phi^2\rangle$ depends on the recoupling sequence used, particularly the scaling factor κ and whether the sequence is γ-encoded or non–γ–encoded. The $R26_4^{11}$ symmetry sequence used here in this work is γ-encoded and the scaling factor was determined to be $\kappa = 0.1708$.[35] The resulting expression for $\langle\phi^2\rangle$ for the $R26_4^{11}$ sequence is:

$$\langle\phi^2\rangle = \frac{8}{15}\left(\frac{3}{2}\kappa\,(2\pi)\,D_{app}\right)^2 \tau_{DQ}^2 \quad \textbf{(Equation 2.35)}$$

where τ_{DQ} is the recoupling time and D_{app} is the apparent dipolar coupling constant in Hz.

Figure 2.13a compares the normalized DQ build-up curves under $R26_4^{11}$ recoupling for an isolated pair of ^{19}F nuclei with a dipolar coupling constant of D = 10 kHz (simulated with the SIMPSON program) to the curve calculated using **Equation 2.34** with an apparent dipolar coupling of D_{app} = 10 kHz. An isolated $-CF_2-$ group has a dipolar coupling constant of about 10 kHz based on an internuclear distance of 2.18 Å. This comparison demonstrates that the relatively simple form of

Equation 2.34 well-reproduces the initial rise of the *nDQ* curve up to an intensity of approximately $I_{nDQ} \approx 0.25$. **Figure 2.13b** displays a series of normalized DQ build-up curves calculated with **Equation 2.34** with apparent dipolar couplings ranging from D_{app}= 2 to 10 kHz, clearly showing how the initial rise of the *nDQ* curves is governed by the strength of the apparent dipolar coupling.

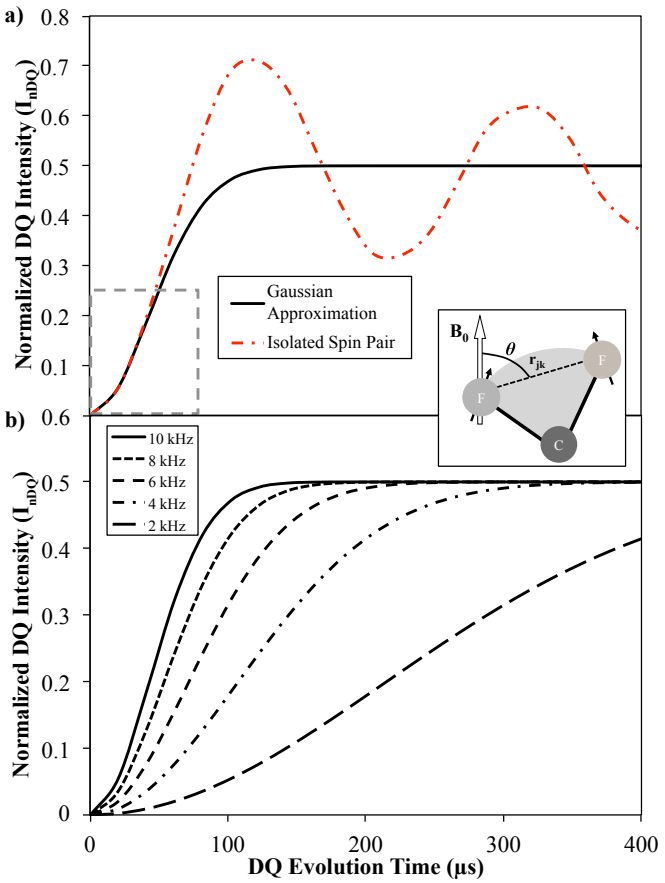

Figure 2. 13 a) Comparison of the *nDQ* build-up curves under $R26_4^{11}$ recoupling for isolated spin pair with D = 10 kHz and calculated curve. b) Simulated *nDQ* build-up curves with different apparent dipolar coupling constants, ranging from D_{app} = 10 kHz to 2 kHz.

2.1.4.6 Robustness and Sensitivity Evaluation

The $R26_4^{11}$ symmetry sequence is relatively robust with respect to the quite large ^{19}F chemical shift anisotropy and chemical shift range,

leading to an underestimation of the measured apparent dipolar couplings by no more than 10%.

Effect of Chemical Shift Anisotropy

Simulations of *nDQ* curves obtained with the $R26_4^{11}$ symmetry-based dipolar recoupling sequence were carried out using the SIMPSON program in order to investigate the effects of the ^{19}F CSA on the DQ signal trajectories and the resulting dipolar coupling constants extracted from these curves. **Figure 2.14** shows the *nDQ* curves for a spin system with a CSA of 0 ppm (red curve) along with the set of nDQ curves for 25 spin systems with CSAs of 100 ppm with randomly generated Euler angles for the chemical shift tensors of each ^{19}F nucleus (grey curves).

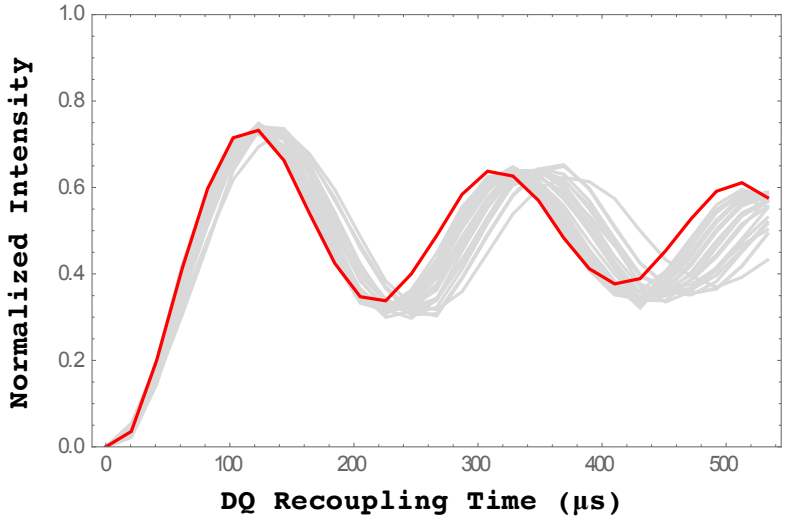

Figure 2. 14 Simulated *nDQ* build-up curve comparison between 0 ppm CSA span (red) and 100 ppm span (grey).

In **Figure 2.15**, the left figure below shows the distribution of dipolar coupling constants extracted from fitting the set of grey curves shown above. The right figure below shows the *nDQ* curve with the mean dipolar coupling (red) overlaid on the full set of curves.

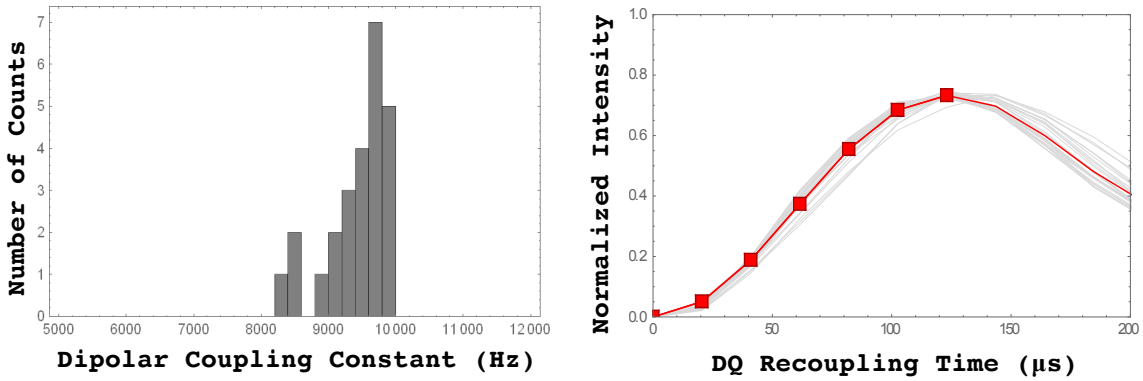

Figure 2. 15 The graphical demonstration of the fitting deviation.

Finally, the figure below shows the mean and standard deviation of the dipolar coupling constants extracted from the simulations as a function of the chemical shift anisotropy (**Figure 2.16**):

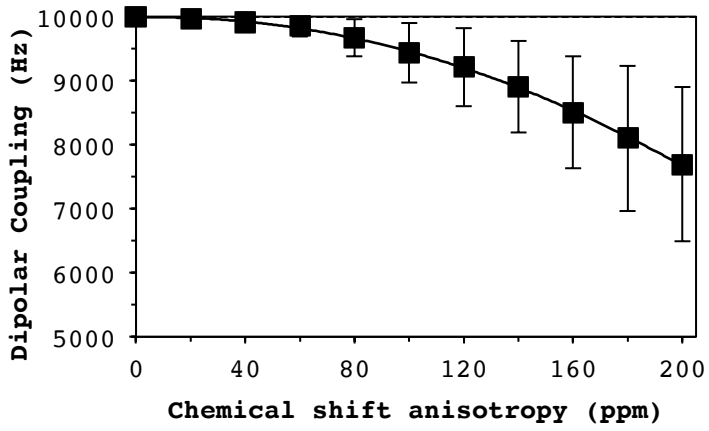

Figure 2. 16 Dipolar coupling constant deviation as a function of the CSA magnitude.

Klaus Schmidt-Rohr[36] reports chemical shift anisotropies for PTFE and Nafion on the order of 60 ppm, with η = 0. The mean and standard deviation of the dipolar coupling constants extracted from the simulations with ^{19}F CSA of 60 ppm are 9860 ± 170 Hz.

Effect of Offset

The offset effect is analyzed through simulation in a similar fashion as the CSA effect analysis. **Figure 2.17** shows the influence of

offset on the fitted dipolar coupling constant. The red dashed line is for the chemical shift anisotropy set to 0 ppm, while the black data points with error bars are the mean and standard deviation for a set of 25 spin system with a chemical shift anisotropy of 60 ppm and randomly generated Euler angles.

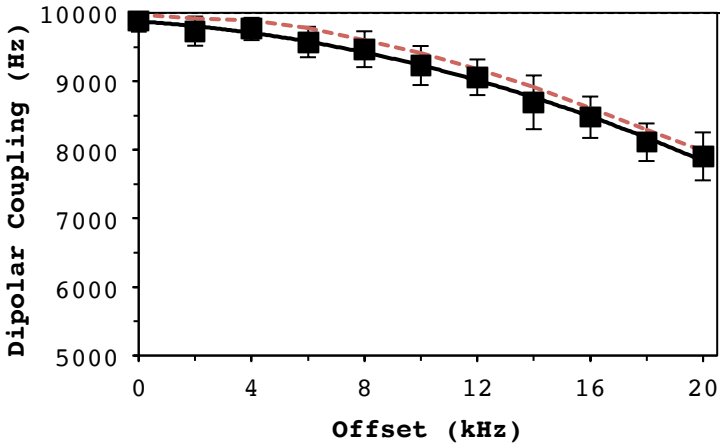

Figure 2. 17 Dipolar coupling constant deviation as a function of the offset frequency.

Assuming the offset was placed at about 120 ppm near the backbone CF_2 resonance, the side-chain resonances at 80 ppm are about 11300 Hz (40 ppm) from the carrier frequency. The mean and standard deviation of the simulations with a ^{19}F CSA of 60 ppm and an offset of 11300 Hz are on the order of 9100 ± 250 Hz. This means these dipolar coupling constants extracted from the peaks at 80 ppm could be underestimated by about 10%. The peaks closer to resonance could be underestimated by no more than 5%. This has also been tested experimentally. The DQ recoupling experiments are carried out with different transmitter (O1) locations on the same Nafion PFSA membrane sample, shown in **Figure 2.18.**

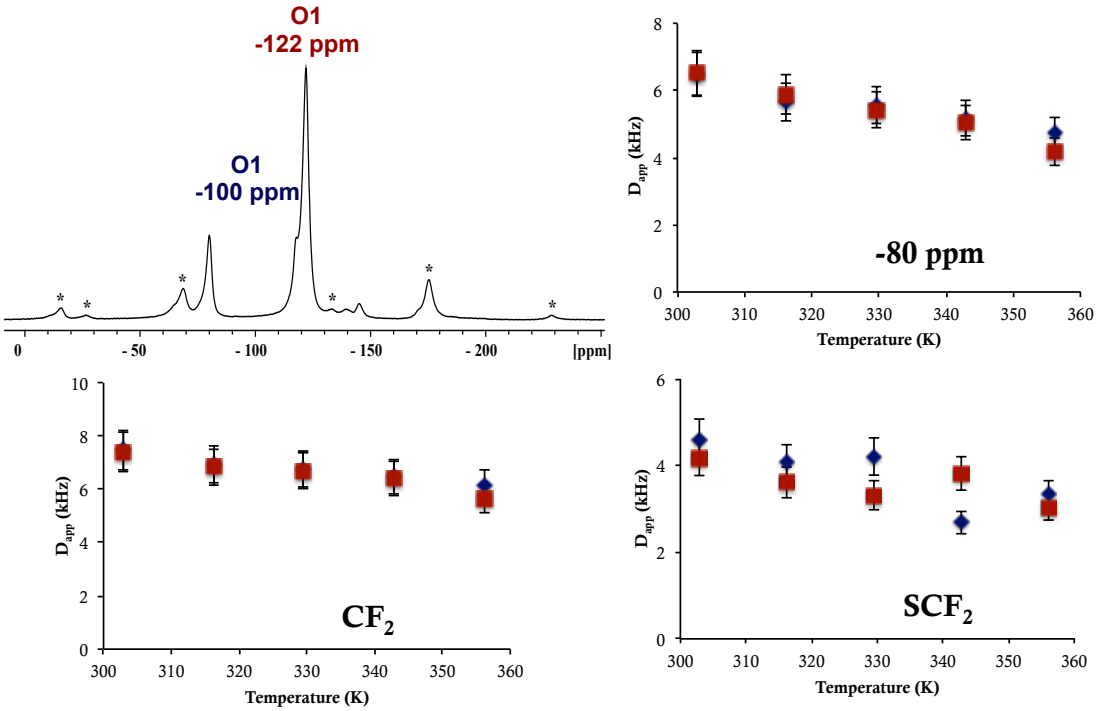

Figure 2. 18 Offset effect is demonstrated by comparing the D_{app} values of three different fluorine sites (OCF_2 and CF_3 at -80 ppm, backbone CF_2 at -122 ppm, and SCF_2 at -117 ppm) at a range of temperatures with two different transmitter frequencies.

Three fluorine sites with different chemical shift regions are under investigation and the D_{app} values are extracted. The diamond data points (blue) in **Figure 2.18** are the data extracted for experiments collected with O1 at -100 ppm, which is superimposed on the data from experiments with O1= -122 ppm presented in squares (red). Therefore, the experimental analysis demonstrates that the offset effect does not play a significant role in the PFSA system under the current experimental conditions. Noticeably, the data comparison for the SCF_2 site has a variation. This is possibly due to a systematic deconvolution error, since the SCF_2 and CF_2 signals have a significant amount of overlap in the NMR spectra.

2.2 STXM Spectroscopy

Synchrotron-based soft X-ray spectroscopy techniques have been developed over several decades into powerful tools in materials characterization qualitatively and quantitatively.[37] Scanning transmission X-ray microscopy (STXM) coupled with near-edge X-ray absorption fine structure (NEXAFS) spectroscopy is capable of determining and differentiating soft matter with a spatial resolution of better than 30 nm.[37-38] Constructed with ultrahigh vacuum in the STXM chamber, contaminations introduced by air in most of the X-ray microscopy techniques can be eliminated, providing STXM's efficient 'photon-in, photon-out' character.[37]

2.2.1 Synchrotron Radiation

When an electron beam is forced to travel in a curved trajectory by magnetic fields with constantly accelerated speeds, it emits electromagnetic radiation in the direction of its motion.[6, 39] The radiation is referred as synchrotron radiation, and spans a wide range of frequencies from the infrared up to the soft and hard X-ray regions. This radiation is much more intense than most conventional sources.[39]

Synchrotron radiation is often generated from synchrotron storage rings. They are built with circular vacuum pipes where the beams of electron bunches are forced to travel in curved paths by bending magnets installed along the pathways. The electrons pass a linear accelerator and then a booster ring, so that the electron energies are boosted to billions or giga electron volts. Eventually the electron beams are injected into a storage ring where the bending magnets modify/direct the trajectory of electrons. At each turn the electron beams make, they

emit synchrotron radiation. The loss of energy is compensated by passing the beams through radiofrequency (RF) cavities, where the energies are boosted from the synchronization between the electromagnetic field and the electrons. The synchrotron radiation that is emitted at each turn then travels through vacuum lines downstream, called beamlines. At each beamline, the radiation is then optimized for a specific energy range and type of experiment. At the end of each beamline, experimental setups, like microscopes and diffractometers, are assembled and connected using the radiation as the light sources.

Synchrotron radiation based imaging and spectroscopic techniques have brought significant improvements to materials characterization at the atomic and molecular level, because of the unique properties of synchrotron radiation listed as follows[39]:

- High intensity/flux
- Broad and continuous frequency range
- High degree of collimation, narrow angular distribution
- Pulsed time structure, i.e. emission with pulse widths
- High degree of polarization
- High beam stability

These features give synchrotron radiation many advantages compared to other conventional light sources.

2.2.2 Beamline Instrumentation

A schematic diagram of beamline 5.3.2 at Advanced Light Source (ALS) is shown in **Figure 2.19**, which is the beamline setup At BL 5.3.2, synchrotron radiations are supplied from a bending magnet. The toroidal mirror directs the light source onto the spherical grating

momochromator, which disperses the soft X-rays with different energies depending on the exit slit. At this beamline, the radiation is optimized for the energy range from 250 eV to 600 eV, which covers the C 1s, N 1s, and O 1s absorption edges. This is extremely important for soft matter characterization. The X-rays are then lead to a scanning transmission X-ray microscope (STXM) end station.

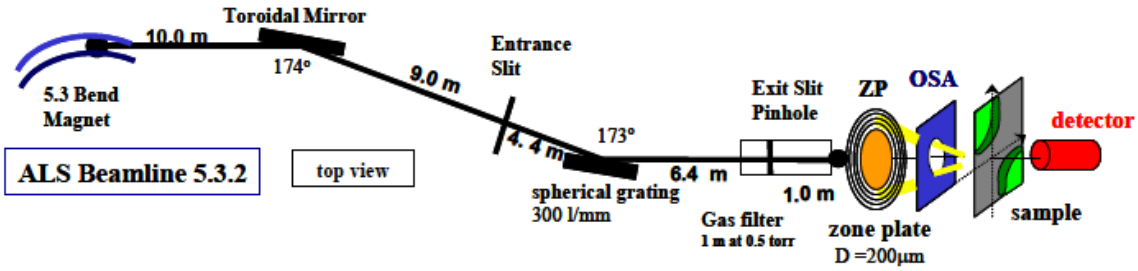

Figure 2. 19 Schematic representation of ALS BL 5.3.2 and STXM.[40]

2.2.3 Scanning Transmission X-ray Microscopy (STXM)

The schematic diagram of a STXM microscope is demonstrated in **Figure 2.20.**[41] The monochromated X-rays get focused by a Fresnel zone plate (ZP) lens that is a circular diffraction grating. An order-sorting aperture (OSA) is then used to block the zeroth order light. The sample is positioned at the X-ray focal spot and X-Y raster scanned under interferometer control while detecting the transmitted X-rays. The transmitted X-rays are detected in a single photon counting mode using a photomultiplier tube (PMT) where the phosphors convert soft X-rays to a pulse of visible light.[42]

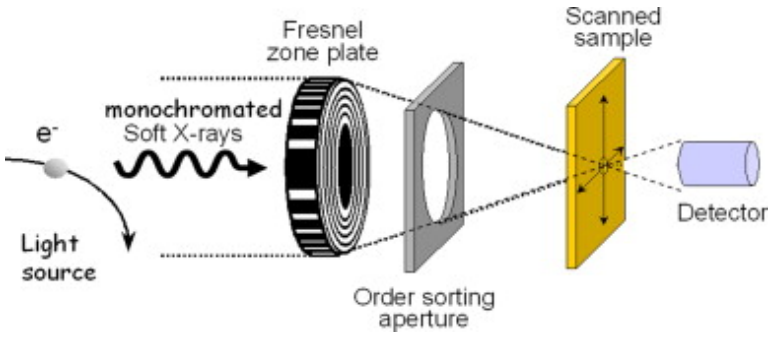

Figure 2. 20 The schematic diagram of STXM microscope, which often consist of zone plate, OSA and a photon-counting detector.[41]

The sample is exposed to X-rays with a tunable range of energies. Images at a single energy are measured by recording the intensity at each pixel. The intensity at each pixel as a function of energy can then be converted into X-ray absorption spectra by applying the Beer-Lambert Law. Spectral information is obtained by collecting a sequence of images over an energy range. The image sequences are referred to as a 'stack'. From the 'stack', at each pixel the X-ray absorption intensity can be plotted as a function of energy. The X-ray absorption spectra (XAS) are also known as the near edge X-ray absorption spectra (NEXAFS). The transitions in the NEXAFS are related to chemical bonding around the core-excited atom, and resulting NEXAFS spectra are used to identify and quantify the chemical structure of different chemical species.

The physics behind XAS or NEXAFS is that as an inner shell spectroscopy, the X-rays with tunable energies are able to excite a core electron from an atom to eject or promote it into the core-excited state.[43-44] Each core shell has a distinct binding energy; hence the plot of X-ray absorption as a function of energy through the binding energy of a core shell gives rise to an absorption edge. Each edge represents a unique core-electron binding energy depending on the atoms and the

core electron being promoted.[44] The NEXAFS signal is sensitive towards electron density of the target atom; therefore, it is informative regarding chemical bonding and coordination.

The aXis2000 software is used to extract NEXAFS from the measured image sequences.[42, 45] The analysis consists of the following steps: (1) alignment of the images in the stack; (2) converting transmitted intensities into optical densities (OD); (3) obtaining reference spectra for chemical components in the selected region and converting OD to OD1 (optical density per nm thickness); (4) chemical mapping by fitting the stack to reference spectra; (5) confirming the validation of the fit. As the spectra with absolute intensity scales (OD1) are used as the reference during the analysis, the intensities of the maps correspond to the absolute thickness (in nm).

2.3 Electrochemical Analysis

Electron transfer processes are at the center of fuel cell operation. Molecular electrochemistry has become the key tool for material performance evaluations in the development of renewable energy technologies.[6, 46-49] Electrochemical analysis is a direct approach to characterize reactions involving electron transfers. For the core reaction in the hydrogen fuel cell system, the resulting chemical changes are the oxidation of hydrogen and the reduction of oxygen. In electrochemical analysis, the driving force of the reaction is controlled by a potentiostat, so that the thermodynamic and kinetic parameters can be extracted and measured.[47]

2.3.1 Cyclic Voltammetry

2.3.1.1 The Fundamentals

Cyclic voltammetry (CV) is a common analytical electrochemical measurement, especially in fuel cell research.[46] This technique usually provides a measure of the effective catalyst surface area of the gas diffusion electrodes; moreover, it can provide the H_2 crossover capacity.[46]

The CV profile is often called the cyclic voltammogram, in which the x-axis represents the applied potential (E) and the y-axis is the response, i.e. the resulting current (i) passing through the system. The potential of the system is linearly cycled between two voltage limits, while the current is monitored. The responsive current is governed by the Nernst equation[6, 48-49].

$$E = E^0 + \frac{RT}{nF} ln\left(\frac{Ox}{Red}\right) \quad \textbf{(Equation 2.36)}$$

The Nernst equation describes the potential of an electrochemical cell (E) as it relates to the standard potential of the redox species (E^0) and the relative activities of the oxidized and reduced components at equilibrium, in which F is the Faraday's constant, R is the gas constant, n is the number of electrons, and T is the temperature of the system. The equation provides an effective way to predict how the system will respond in the form of the electrode potential to changes in analyte concentrations near the electrode over time.[6, 47] If the reductant and oxidant activities are kinetically equal, the CV voltammogram theoretically will exhibit true exponential behavior with minimum hysteresis. In real CV analysis, the concentrations of oxidant and reductant relate to the potential applied on the electrode, how far away from the surface of the electrode, and the diffusivities of the species. All of these factors contribute to the more realistic CV

profile, known as the 'duck-shaped' voltammogram. Generally, during the forward CV scan (cathodic) a peak current is often observed, which is caused by the reduction of the oxidant near the electrode. When the oxidant is quickly consumed near the electrode surface, the additional oxidant diffuses from the bulk solution. Within that diffusion layer at the electrode surface, the reductant concentration constantly grows throughout the scan, which blocks the transport of oxidant to the electrode.[6, 46-47, 49] Therefore, a drop in current (after the peak current) is observed as the scan continues, and the diffusion of oxidant from the solution to the electrode surface slows down until the high potential limit where the CV scan changes into the reverse direction (anodic). During the reverse scan a similar phenomenon occurs, where the anodic peak current is observed, as shown in **Figure 2.21.**

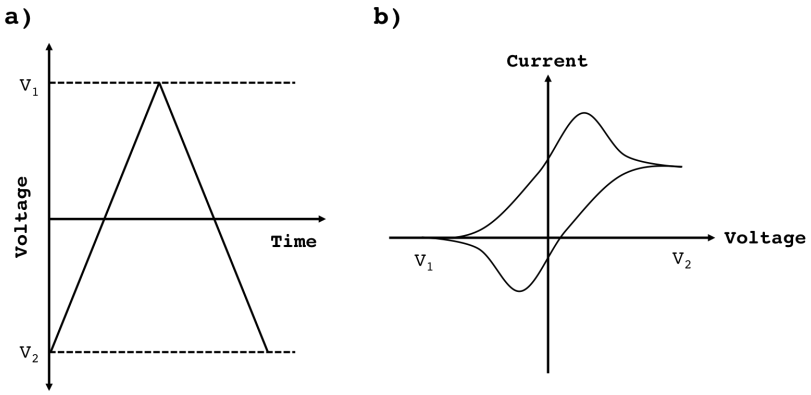

Figure 2. 21 Schematic representation of a typical CV experiment: a) voltage sweep linearly back and forth between two voltage limits; b) typical CV voltammogram (duck-shape).[46, 50]

2.3.1.2 Application in Fuel Cell Research

In a hydrogen fuel cell, CV analysis can be simplified as a three-electrode system, where H_2 is fed to anode side acting as the counter electrode and reference electrode. This is also known as the dynamic hydrogen electrode (DHE). The other side, the cathode side, is

fed with N_2 and connected to the working electrode. The example and explanation of measuring H_2 crossover capacity from CV analysis is detailed in **Chapter 5**.

2.3.2 Impedance Spectroscopy

2.3.2.1 The Fundamentals

Electrochemical impedance spectroscopy (EIS) applies an alternate current (AC) voltage to the cell with a range of frequencies. The amplitude and phase of the resulting response are monitored as a function of frequency.[48-49] The complex impedance of the electrochemical system can be determined, which is an evaluation of a system's ability to delay the electric current flow. EIS has been widely used in fuel cell research to efficiently unravel the origins of polarization losses. Commonly, EIS is used to evaluate Ohmic resistance and electrode properties in MEA optimization.[46]

EIS analysis is usually extrapolated in both Bode and Nyquist plots. A typical Bode plot, in which the magnitude and phase of the impedance is a function of frequency, differs greatly compared to the Nyquist plot where the imaginary impedance is against the real impedance component at each frequency point collected.[46, 48-49]

2.3.2.2 Application in Fuel Cell Research

Because of the different kinetics of hydrogen oxidation reaction (HOR) and oxygen reduction reaction (ORR), as well as various components in a PEMFC system such as CLs and gas diffusion electrodes, the impedance study of hydrogen fuel cells is informative yet challenging. Analyzing the resulting signal with a corresponding model circuit is critical.[46, 51]

The transmission line circuit model was used to extract the MEA resistances, which was introduced by Eikerling and Kornyshev when employed the macrohomogeneous model to described the impedance responses of PEMFCs.[52] By doing so, parameters such as Ohmic resistance and electrolyte resistance in the CL can be extracted and separated.[51] The transmission line model consists of two parallel resistive elements, one for electron transport ($R_{electron}$) and the other for proton transport (R_{proton}). The elements are connected through a double layer capacitance (C_{dl}) in parallel to the charge transfer resistance (R_{ct}), which is shown in **Figure 2.22.**[52]

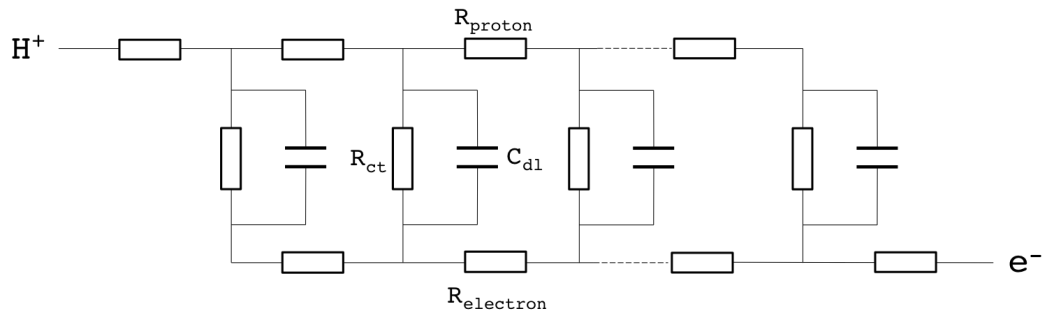

Figure 2. 22 Transmission line equivalent circuit model used in fuel cell impedance evaluation.[52]

Due to the complexity of the fuel cell system, it is challenging to fully decipher the EIS measurement; although, with a proper model and sophisticated experimental design, electrochemical information of fuel cell performance evaluation can be extracted and compared. Detailed examples showcasing this are described in **Chapter 5.**

2.4 Summary

Each technique introduced in this chapter provides some unique aspect in fuel cell research. Spectroscopies are important analytical

tools for materials analysis. A detailed interpretation of spectral features from any spectroscopic study can provide vivid and rich information regarding the material under investigation. ^{19}F MAS NMR provides exquisite chemical site differentiation averaged over the entire material.[21, 36] With the observation of distinguishable chemical environments after a meticulous ^{19}F spectral deconvolution, an advanced NMR technique recently developed allows one to analyze the D_{app} as an indicator of local dynamics, which provides a handle to link the molecular structure information to performance evaluations.[53] Soft X-ray STXM, with its sensitivity towards O and S that are NMR challenging, provides XAS of PFSA without spectroscopically noticeable damage. The extent to which these two spectroscopies can provide complementary information about PFSA materials has been investigated and will be described later in this thesis. In general, the main advantage of electrochemical techniques is that they provide *in situ/in operando* performance information regarding the PFSA in an MEA form. The electrochemical evaluation of PFSA can be correlated to the local dynamics studied using NMR, which is addressed in more detail in later chapters. With all of those unique features, the techniques mentioned above provide useful insight into the structure-performance relationship of the PFSA materials.

2.5 References

1. Cheng, H.; English, A. D., *NMR Spectroscopy of Polymers in Solution and in the Solid State*. ACS Publications: 2002.

2. Harris, R., NMR studies of solid polymer. In *Polymer spectroscopy*, Fawcell, A., Ed. John Wiley & Sons: England, 1996.

3. Hansen, M. R.; Graf, R.; Spiess, H. W., Interplay of Structure and Dynamics in Functional Macromolecular and Supramolecular Systems As Revealed by Magnetic Resonance Spectroscopy. *Chem. Rev.* **2016,** *116* (3), 1272-308.

4. Graf, R.; Heuer, A.; Spiess, H. W., Chain-Order Effects in Polymer Melts Probed by H 1 Double-Quantum NMR Spectroscopy. *Phys. Rev. Lett.* **1998,** *80* (26), 5738.

5. Saalwächter, K.; Lange, F.; Matyjaszewski, K.; Huang, C.-F.; Graf, R., BaBa-xy16: Robust and broadband homonuclear DQ recoupling for applications in rigid and soft solids up to the highest MAS frequencies. *J. Magn. Reson.* **2011,** *212* (1), 204-215.

6. Atkins, P. W., *Physical Chemistry*. 4 ed.; Oxford University Press: Oxford, 1990.

7. Keeler, J., *Understanding NMR spectroscopy*. John Wiley & Sons: 2011.

8. Levitt, M. H., *Spin dynamics: basics of nuclear magnetic resonance*. John Wiley & Sons: Chichester, 2001.

9. Duer, M. J., *Introduction to Solid-state NMR Spectroscopy*. Blackwell Science: Oxford, UK, 2004.

10. Dong, R. Y., *Encyclopedia of Spectroscopy and Spectrometry: I-N*. Academic Press: 2000; Vol. 2.

11. Harris, R., *Nuclear Magnetic Resonance Spectroscopy: A Physiochemical View*. 1986.

12. Saalwächter, K., Robust NMR Approaches for the Determination of Homonuclear Dipole–Dipole Coupling Constants in Studies of Solid Materials and Biomolecules. *ChemPhysChem* **2013,** *14* (13), 3000-3014.

13. Andrew, E. R.; Bradbury, A.; Eades, R., Nuclear magnetic resonance spectra from a crystal rotated at high speed. *Nature* **1958,** *182* (4650), 1659.

14. Lowe, I., Free induction decays of rotating solids. *Phys. Rev. Lett.* **1959,** *2* (7), 285.

15. Maricq, M. M.; Waugh, J., NMR in rotating solids. *The Journal of Chemical Physics* **1979,** *70* (7), 3300-3316.

16. Zhang, R.; Mroue, K. H.; Ramamoorthy, A., Proton-based ultrafast magic angle spinning solid-state NMR spectroscopy. *Acc. Chem. Res.* **2017,** *50* (4), 1105-1113.

17. Harris, R. K.; Becker, E. D.; De Menezes, S. M. C.; Goodfellow, R.; Granger, P., NMR nomenclature. Nuclear spin properties and conventions for chemical shifts (IUPAC Recommendations 2001). *Pure Appl. Chem.* **2001,** *73* (11), 1795-1818.

18. Levitt, M. H., Symmetry-based pulse sequences in magic-angle spinning solid-state NMR. In *Encyclopedia of Nuclear Magnetic Resonance*, Grant, D. M., Harris, R. K., Ed. John Wiley & Sons: Chichester U.K., 2002; Vol. 9, pp 165-196.

19. Levitt, M. H., Symmetry-Based Pulse Sequences in Magic-Angle Spinning Solid-State NMR. *eMagRes* **2007.**

20. Brown, S. P.; Spiess, H. W., Advanced solid-state NMR methods for the elucidation of structure and dynamics of molecular, macromolecular, and supramolecular systems. *Chem. Rev.* **2001,** *101* (12), 4125-4156.

21. Chen, Q.; Schmidt-Rohr, K., 19F and 13C NMR signal assignment and analysis in a perfluorinated ionomer (Nafion) by two-dimensional solid-state NMR. *Macromolecules* **2004,** *37* (16), 5995-6003.

22. Traer, J. W.; Britten, J. F.; Goward, G. R., A solid-state NMR study of hydrogen-bonding networks and ion dynamics in benzimidazole salts. *J. Phys. Chem. B* **2007,** *111* (20), 5602-5609.

23. Yan, Z. B.; De Almeida, N. E.; Traer, J. W.; Goward, G. R., Dynamics of benzimidazole ethylphosphonate: a solid-state NMR study of anhydrous composite proton-conducting electrolytes. *Phys. Chem. Chem. Phys.* **2013,** *15* (41), 17983-17992.

24. Ye, G.; Janzen, N.; Goward, G. R., Solid-state NMR study of two classic proton conducting polymers: Nafion and sulfonated poly (ether ether ketone) s. *Macromolecules* **2006,** *39* (9), 3283-3290.

25. Zorin, V. E.; Brown, S. P.; Hodgkinson, P., Quantification of homonuclear dipolar coupling networks from magic-angle spinning1H NMR. *Mol. Phys.* **2006,** *104* (2), 293-304.

26. Torchia, D.; Szabo, A., Spin-lattice relaxation in solids. *J. Magn. Reson.* **1982,** *49* (1), 107-121.

27. Hansen, M. R.; Graf, R.; Spiess, H. W., Solid-State NMR in Macromolecular Systems:
Insights on How Molecular Entities Move. *Acc. Chem. Res.* **2013,** *46* (9), 1996-2007.

28. Carravetta, M.; Eden, M.; Zhao, X.; Brinkmann, A.; Levitt, M. H., Symmetry principles for the design of radiofrequency pulse sequences in the nuclear magnetic resonance of rotating solids. *Chem. Phys. Lett.* **2000,** *321* (3), 205-215.

29. Kristiansen, P. E.; Mitchell, D. J.; Evans, J. N., Double-quantum dipolar recoupling at high magic-angle spinning rates. *J. Magn. Reson.* **2002,** *157* (2), 253-266.

30. Bradley, J. P.; Tripon, C.; Filip, C.; Brown, S. P., Determining relative proton–proton proximities from the build-up of two-dimensional correlation peaks in 1H double-quantum MAS NMR: insight from multi-spin density-matrix simulations. *Phys. Chem. Chem. Phys.* **2009,** *11* (32), 6941-6952.

31. Ren, J.; Eckert, H., A Homonuclear Rotational Echo Double-Resonance Method for Measuring Site-Resolved Distance Distributions in I= 1/2 Spin Pairs, Clusters, and Multispin Systems. *Angew. Chem. Int. Ed.* **2012,** *51* (51), 12888-12891.

32. Ren, J.; Eckert, H., DQ-DRENAR: A new NMR technique to measure site-resolved magnetic dipole-dipole interactions in multispin-1/2 systems: Theory and validation on crystalline phosphates. *The Journal of chemical physics* **2013,** *138* (16), 164201.

33. Ando, S.; Harris, R. K.; Scheler, U., Fluorine-19 NMR of Solids Containing Both Fluorine and Hydrogen. *eMagRes* **2002.**

34. Holstein, P.; Scheler, U.; Harris, R. K., Semicrystallinity and polymorphism in PVDF: A solid-state< sup> 19</sup> F nmr investigation. *Polymer* **1998,** *39* (20), 4937-4941.

35. Brinkmann, A.; Levitt, M. H., Symmetry principles in the nuclear magnetic resonance of spinning solids: heteronuclear recoupling by generalized Hartmann–Hahn sequences. *The Journal of chemical physics* **2001,** *115* (1), 357-384.

36. Chen, Q.; Schmidt-Rohr, K., Backbone Dynamics of the Nafion Ionomer Studied by 19F-13C Solid-State NMR. *Macromol. Chem. Phys.* **2007,** *208* (19-20), 2189-2203.

37. Hitchcock, A. P., Soft X-Ray Imaging and Spectromicroscopy. In *Handbook of Nanoscopy, Volume 1&2*, 2012; pp 745-791.

38. Hitchcock, A.; Dynes, J.; Lawrence, J.; Obst, M.; Swerhone, G.; Korber, D.; Leppard, G., Soft X-ray spectromicroscopy of nickel sorption in a natural river biofilm. *Geobiology* **2009**, *7* (4), 432-453.

39. Balerna, A.; Mobilio, S., Introduction to synchrotron radiation. In *Synchrotron radiation*, Springer: 2015; pp 3-28.

40. Hitchcock, A. P., *STXM 5.3.2 User Manual*. ALS: Berkeley, USA, 2003.

41. Hitchcock, A. P.; Berejnov, V.; Lee, V.; West, M.; Colbow, V.; Dutta, M.; Wessel, S., Carbon corrosion of proton exchange membrane fuel cell catalyst layers studied by scanning transmission X-ray microscopy. *J. Power Sources* **2014**, *266*, 66-78.

42. Berejnov, V.; Martin, Z.; West, M.; Kundu, S.; Bessarabov, D.; Stumper, J.; Susac, D.; Hitchcock, A. P., Probing platinum degradation in polymer electrolyte membrane fuel cells by synchrotron X-ray microscopy. *Phys. Chem. Chem. Phys.* **2012**, *14* (14), 4835-4843.

43. Penner-Hahn, J. E., *X-ray Absorption Spectroscopy*. 2005.

44. Stohr, J., *NEXAFS Spectroscopy. Vol. 25*. Springer-Verlag, NY: 1992.

45. Hitchcock, A., aXis2000 is written in Interactive Data Language (IDL). *It is available free for noncommercial use from* http://unicorn.mcmaster.ca/aXis2000.html **2008**.

46. Wu, J.; Yuan, X. Z.; Wang, H.; Blanco, M.; Martin, J. J.; Zhang, J., Diagnostic tools in PEM fuel cell research: Part I Electrochemical techniques. *Int. J. Hydrogen Energy* **2008**, *33* (6), 1735-1746.

47. Elgrishi, N. m.; Rountree, K. J.; McCarthy, B. D.; Rountree, E. S.; Eisenhart, T. T.; Dempsey, J. L., A Practical Beginner's Guide to Cyclic Voltammetry. *J. Chem. Educ.* **2017**.

48. Hoogers, G., *Fuel cell technology handbook*. CRC press: 2002.

49. Barbir, F., *PEM fuel cells: theory and practice*. Academic Press: New York, 2012.

50. O'hayre, R.; Cha, S.-W.; Prinz, F. B.; Colella, W., *Fuel cell fundamentals*. John Wiley & Sons: 2016.

51. Makharia, R.; Mathias, M. F.; Baker, D. R., Measurement of catalyst layer electrolyte resistance in PEFCs using electrochemical impedance spectroscopy. *J. Electrochem. Soc.* **2005**, *152* (5), A970-A977.

52. Eikerling, M.; Kornyshev, A., Electrochemical impedance of the cathode catalyst layer in polymer electrolyte fuel cells. *J. Electroanal. Chem.* **1999**, *475* (2), 107-123.

53. Yan, Z. B.; Brouwer, D. H.; Goward, G. R., 19F Double Quantum NMR Spectroscopy: A Tool for Probing Dynamics in Proton-Conducting Fluorinated Polymer Materials. *Macromolecules* **2016**, *49* (19), 7331-7339.

3.

X-ray Absorption and NMR Spectroscopy of Fluorinated Proton Conducting Polymers

3.1 Introduction

This chapter discusses the use of two state-of-the-art analytical methods, X-ray absorption spectroscopy (XAS) *via* STXM and ssNMR spectroscopy, in unveiling the spectral features of various PFSA polymers and to investigate the extent to which these two spectroscopies can provide complementary information about these materials. Three types of PFSA were under inspection, including Nafion, Aquivion and a new PFSA derivative developed by 3M. These materials serve as proton conductors both in the electrolyte membrane and ionomer in the catalyst-coated electrodes, which ideally allow the protons to be transported from the anode to the cathode while remaining electronically resistive. The current commercial proton conducting material, PFSA, undergoes micro-phase separation of hydrophilic and hydrophobic domains caused by differential hydration of the sulfonated side chains and backbone. This separation provides a dense nanoscale distribution of

sulfonate-rich pockets[1] which create pathways for proton transport during fuel cell operation.[1-4]

Understanding in detail how the material performance depends on its molecular structure as well as its distribution in the electrodes is critical to the improvement of hydrogen fuel cell performance and lifetime.

This work was adapted with permission from, *The Journal of Physical Chemistry C.* Copyright 2018 American Chemical Society (Z. B. Yan, R. Hayes, L. G. A. Melo, G. R, Goward and A. P. Hitchcock. **2018**, *122*(6), 3233-3244). In addition to the solution-state diffusion NMR study of the ionomer dispersions at the end in the published article, reported here is a preliminary investigation regarding the diffusion profiles of different ionomer dispersion solutions with various concentrations done in collaboration with Automotive Fuel Cell Cooperation (AFCC).

The preparation and treatment of all materials discussed here were done at McMaster University. PFSA membrane samples for STXM measurements were prepared at the Department of Pathology and Molecular Medicine at McMaster University. Preparation of PFSA spin cast samples from the ionomer solutions as well as the STXM measurements of the cast films were carried out with the help of Lis G. A. Melo (co-author). Inner shell electron energy loss spectra (ISEELS), STXM measurements, and orbital calculations for small molecules were done by Robin Hayes (co-author), the results of which were included in her Undergraduate Honours Thesis both in print and electronically. The solution-state ^{19}F diffusion NMR experiments were performed with the help of Dr. Sergey Krachkovskiy. All ssNMR experiments were performed at the NMR facility at McMaster University, and analyzed under the supervision of Prof.

Gillian Goward. The initial drafts of the manuscript were written by the current author, Z. B. Yan.

In general, spectroscopies are important tools for materials analysis as they can provide useful information, such as structures, chemical compositions and morphology. In particular, STXM has been used to quantitatively map the molecular composition of the ionomer, carbon support and catalysts in membrane electrode assemblies (MEAs).[5-13] Other techniques, such as analytical transmission electron microscopy (TEM) based on core level electron energy loss spectroscopy (TEM-EELS), have also been applied to the study of PFSA materials.[14-15] STXM has a significant advantage as it causes significantly less radiation damage despite providing a similar level of analytical information.[11, 16-18] NMR spectroscopy is a powerful approach that can be used to probe the structure of materials with chemical bonding information. ^{19}F ssNMR provides exquisite chemical site differentiation averaged over the whole sample. Unfortunately, ^{13}C and ^{33}S ssNMR are typically very challenging due to the low sensitivities associated with the low natural isotopic abundances of both nuclei, as well as the low gyromagnetic ratio and large quadruple moment of ^{33}S. Thus, an integrated method that combines XAS and ssNMR has the potential to provide detailed structural information at the molecular level for all of the elements in various classes of PFSA materials. While the combination of NMR and XAS has been applied to biopolymers[19] and solid heterogeneous polymeric catalyst materials,[20-21] this is, to our knowledge, the first report of combined NMR and near edge X-ray absorption fine structure (NEXAFS) spectroscopy applied to the same PFSA materials.

3.2 Experimental

3.2.1 Materials and Sample Preparation

3.2.1.1 Membrane Sample Activation

Pristine Nafion 117 was purchased from Sigma-Aldrich. Aquivion PFSA ionomer membranes were obtained from Solvay, Italy. 3M 'new' PFSA ionomer membranes[22] were obtained from 3M, MN, USA. The PFSA materials were first washed in 3 wt% H_2O_2 for 1 hour at 90 °C and then washed with deionized water for another hour, changing the water every 15 minutes. Subsequently, they were washed in 0.5 M H_2SO_4 solution for 1 hour. They were then washed in deionized water until a constant pH was obtained. Finally, the materials were dried in vacuum oven at 80 °C for 24 hours.

3.2.1.2 Cast Film Preparation

An aqueous dispersion with 60 wt % PTFE was purchased from Sigma-Aldrich. It was diluted to 2 wt% using H_2O (HPLC grade) and spun coated on to freshly cleaved mica (1000 rpm/30 s), annealed at 190 °C for 2 hours. Nafion and Liquion alcoholic dispersions (EW=1100) with 5 wt% were obtained from Ion Power Inc. and diluted with isopropanol into 3 wt% concentrated solutions. These solutions were spun coat (30 s at 3000 rpm) on to freshly cleaved, 1 cm x 1 cm mica squares. The film-covered mica was scored into an array of 1 mm x 1 mm squares. The polymer film was then transferred via a clean surface of deionized water to a silicon nitride window. The film chip on the SiN_x window was vacuum annealed at 70 °C for 2 hours, then used for STXM measurements. Some spectra were also measured from ultra-microtomed blocks (see **Figure 1a** and **1b**) or were recorded from the membrane area of PEMFC MEAs.

3.2.1.3 Ionomer Dispersions for NMR Study

For the solution-state diffusion study, Nafion and Liquion dispersions (EW=1100) were obtained from Ion Power Inc. and diluted with n-propanol (NPA) aqueous solution with volume ratio NPA: H_2O=3:1 into 1% concentrated solutions. For ssNMR spectral analyses, the dispersions were cast onto clean petri dishes at 80 °C under active vacuum for 4 hours, then dried overnight.

3.2.2 X-ray Absorption Spectroscopy

The X-ray absorption spectra were recorded using the STXM microscope[23] on beamline 5.3.2.2[24] at the Advanced Light Source (ALS, Lawrence Berkeley National Laboratory (LBNL), Berkeley, USA), and the ambient STXM on beamline 10ID1[25] at the Canadian Light Source (CLS, Saskatoon, Canada). In STXM a monochromated X-ray beam is focused to a small spot (~30 nm) using a Fresnel zone plate and an order sorting aperture to select only the first order light. The sample is positioned at the X-ray focal spot and x-y raster scanned under interferometer control while detecting the transmitted X-rays. Further details are given in recent review articles.[26-28]

The PFSA samples studied by STXM were prepared using ultramicrotomy at the Department of Pathology and Molecular Medicine at McMaster University. Sections with a nominal 100 nm thickness were prepared for each PFSA sample, and placed on formvar coated TEM grids. In addition to allowing measurements of areas of near uniform thickness, the transmission detection used in STXM does not suffer from artifacts which can occur with yield based detection like total electron yield or X-ray fluorescence yield. **Figure 3.1** presents STXM optical density (*OD*) images of the Nafion 117 sample, measured at 200 eV before, and 292.6 eV

after the spectral measurements. The absence of rectilinear contrast at the area of spectral measurement in **Figure 3.1b** verifies the measurements were performed without significant radiation damage.

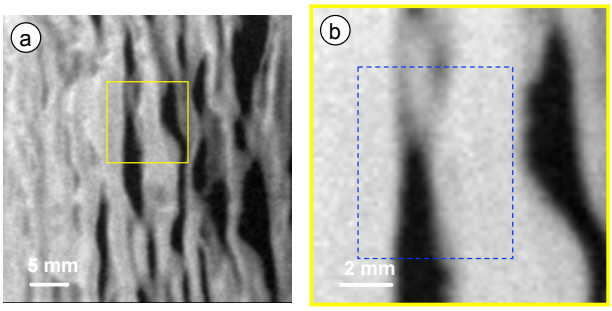

Figure 3. 1 (a) Optical density (*OD*) image of an ultramicrotomed section of Nafion 117 PFSA, recorded with scanning transmission X-ray microscopy (STXM) at 200 eV. The yellow rectangle indicates the region for spectral study (blue rectangle in **Figure 3. 1b**) which was chosen to include an open area (rip in the microtomed section) to use as an internal Io. (b) *OD* image measured at 292.6 eV after measuring stacks at all 4 edges (F 1s, C 1s, O 1s and S 2p) using a 200 nm defocused beam. The stacks were measured in the area outlined by the blue dashed rectangle. This area was subjected to a total exposure time per pixel of 600 ms.

Soft X-rays from 150 – 780 eV, covering the S 2p, C 1s, O 1s and F 1s edges, were used. After loading the sample, the STXM chamber was evacuated to a pressure of 0.1 mbar, and then the tank was backfilled with 0.3 bar of He gas. A N_2 gas filter (at ALS 5.3.2.2) or a Ti filter (at CLS 10ID1) was used to block second order light when measuring the C 1s spectra. The spectra were acquired using image sequences ('stacks'[29]) over a large area, using a defocused beam and a step size the same or larger than the defocused spot size in order to minimize radiation damage, which is a severe problem with PFSA materials.[16] For the C 1s, F 1s and O 1s edges, a dwell time of 1 ms per pixel was used. For the S 2p edge, where the incident flux is much smaller and the amount of S small, a dwell time of 4 ms per pixel was used. The I_0 was measured simultaneously with the I signal by including an area in the stack with just the formvar or silicon nitride support (**Figure 3.1**).

After each stack an area larger than the stack area was imaged at 292.6 eV where the radiation damage has its strongest effect. If the change in intensity between outside and inside the stack frame was more than 5% the stack was re-measured using a less focused beam. After image alignment, the transmitted I and I_0 signals were combined to generate the optical density (*OD*, or absorbance) signal from the Beer-Lambert law, $OD = -\ln\left(I/I_0\right)$. The spectra reported are the average over all areas with an *OD* less than 1.2. The C 1s, O 1s and F 1s spectra were then converted to an absolute intensity scale - optical density per nm (*OD1*) - by scaling to match the pre- and post-edge spectral intensities to that predicted for the elemental composition of the material, using X-ray absorption coefficients from the literature.[30] For the S 2p spectra, which have a low signal to background ratio, the underlying non-S 2p signal was subtracted using a spline curve fit to the pre-edge signal in order to properly visualize the S 2p spectral features. All data processing was performed using aXis2000.[31]

3.2.3 NMR Spectroscopy

The ^{19}F ssNMR spectra of the activated PFSA materials and cast dispersion samples (prepared as described in 3.2.1) were measured on a Bruker Widebore – 300 MHz Avance III system using a double-resonance probe that supports rotors with an outer diameter of 4.0 mm with 15 kHz magic-angle-spinning (MAS) speed (chemical shift referenced using trichlorofluoromethane, $CFCl_3$, δ = 0 ppm). All ^{19}F NMR experiments were performed using a pulse at 97.5 kHz radiofrequency (RF) field, with a 5 s recycle delay. The solution state diffusion NMR spectroscopy was done using a Diff50 diffusion probehead at variable temperatures ranging

from 295 K to 350 K. A pulse field gradient stimulated echo pulse sequence was used. This sequence and the associated gradient parameters are described in **Appendix 4.** The ^{13}C ssNMR measurements were conducted using a 1.9 mm outer diameter rotor with 40 kHz MAS on a Bruker Ascend 850 MHz system (chemical shift referenced using adamantane, $C_{10}H_{16}$ δ = 38.5 ppm for high-frequency peak). All measurements were performed using an 83.3 kHz RF field, with a 15 s recycle delay.

3.3 Results

3.3.1 X-ray absorption spectra

3.3.1.1 C 1s spectra

Each peak in an XAS spectrum arises from transitions from the ground state to an inner shell (core) excited state where the core hole is localized on one specific atom.[32] The intensities are determined by the electric dipole transition matrix element. Thus the spectral features provide information about chemical bonding around that core-excited atom. We focus on peak shapes and energies of the observed features. Detailed assignment of the C 1s, F 1s, O 1s and S 2p spectra provides links between the spectral features and the chemical structures of the three types of PFSA. The S 2p edge spectrum is sensitive to the side chain in PFSA materials, since that signal arises exclusively from the sulfonic acid groups. This is particularly relevant, as the sulfonic acid site controls the proton conductivity of the membrane.

Figure 3.2 compares the C 1s spectra of Nafion 117, Aquivion 98, and 3M 725 PFSA to that of PTFE. Proposed peak assignments are presented in **Table 3.1.**

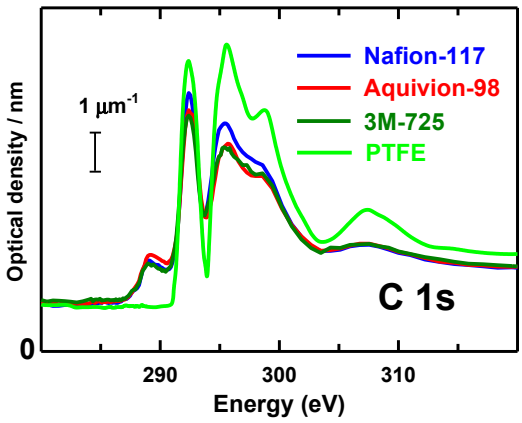

Figure 3. 2 C 1s X-ray absorption spectra of Nafion 117, Aquivion 98, 3M 725 and polytetrafluoroethylene (PTFE) recorded using STXM. The spectra have been converted to an absolute intensity scale (optical density/nm thickness at standard density, *OD1*) using the procedures described in the text. Peak positions and tentative assignments are given in **Table 3.1.**

Table 3. 1 Summary of peak positions and tentative assignments for spectral features in the C 1s spectra of PTFE, Nafion 117, Aquivion 98 and 3M 725.

Energy (eV)				Assignment	
PTFE	**Nafion 117**	**Aquivion 98**	**3M 725**	**C-O**	**CF_2**
–	287.8 (sh)	287.8 (sh)	287.8 (sh)		
–	289.1	289.2	289.1	σ*(C-O)	
292.4 [(a)]	292.4 [(a)]	292.5 [(a)]	292.4 [(a)]		σ*(C-F) //
294.8 (sh)	–	–	–		σ*(C-C)
295.6	295.4	295.7	295.4		σ*(C-F) ⊥
298.7	298.8	298.6	298.5		σ*(C-F) //
307.6	307.2	307.4	307.2		σ*(C-C)
326 (br)	326 (br)	326 (br)	326 (br)		σ*(C-C)

[(a)] Calibration: PTFE: -2.56(4) eV; Nafion 117: -2.54(4) eV); Aquivion 98: -2.48(4) eV); 3M 725 -2.46(4) eV relative to C 1s → 3p transition of CO_2 (294.96(2)[33])

The C 1s spectra are dominated by four strong peaks at 292.5, 295.5, 299.0 and 307.5 eV, which are also seen in other heavily fluorinated saturated[34] and unsaturated fluoro-organic compounds,[35] as well as polymers such as PTFE (Teflon®).[36-38] The peaks at 292.5, 295.5 and 299.0 eV, correspond to C 1s(CF_2) → σ^*_{C-F} transitions, while

those at 295.0, 307.5 and 326.0 eV correspond to C 1s(CF_2) → σ^*_{C-C} transitions. From C 1s XAS studies of aligned PTFE[36, 38] the peak at 292.4 eV is associated with C 1s(CF_2) → σ^*_{C-F} (//) excitations, where the σ^*_{C-F} (//) orbital is aligned perpendicular to the C-C chain. The peaks at 295.6 eV and 299.0 eV are associated with C 1s(CF_2) → σ^*_{C-F} (⊥) and C 1s(CF_2) → σ^*_{C-C} (⊥) excitations, where σ^*_{C-F} (⊥) and σ^*_{C-C} (⊥) orbitals are aligned along the C-C chain. All three PFSA species have a branch carbon site with two ($-CF_2$), one F and one O attached, while Nafion has a second similar C 1s(CF) site in its side chain. The C 1s level for this site will be ~1 eV lower in binding energy than the majority C 1s(CF_2) sites which would shift the σ^*_{C-F} and σ^*_{C-C} transitions to lower energy. However, these sites are 1 in ~14 of the carbons in Aquivion 98 and 1 in ~7 of the carbons in Nafion 117 and 3M 725, so these transitions are masked by the much stronger C 1s(CF_2) features. Note this is in sharp contrast to the ^{19}F ssNMR, where signals from each chemically distinct site are detected (section 3.3.2.1).

In addition to the peaks seen in PTFE, the C 1s spectra of all three PFSA show a structured peak at 289.1 eV. We attribute this striking difference to the presence of oxygen in the PFSA materials. Initially we attributed the 289.1 eV signal to C 1s(CF_2) → σ^*_{C-O} transitions at the ether groups in the side chains. However, C 1s → σ^*_{C-O} features are typically observed at higher energies.[39] At present we attribute the 289.1 eV peak to C 1s(COOR) → $\pi^*_{C=O}$ transitions at the termination of the $-(CF_2)-$ main chain. For comparison, the C 1s(COOR) → $\pi^*_{C=O}$ transition in CF_3COOH occurs at 288.2 eV.[35] In partial support for this tentative assignment, the ^{13}C ssNMR provides evidence of carbonyl signal (see section 3.3.2.2).

From a comparative point of view, Aquivion 98 and Nafion 117 have similar EW despite having different side-chain lengths. Nafion 117 has more C–C bonds per formula unit compared to Aquivion 98, while 3M 725 has the smallest number of C–C bonds per repeating unit. This is consistent with the relative intensities of the transition at 295.0 eV (**Figure 3.2**) which arises primarily from C 1s(CF_2) → σ^*_{C-F} (⊥) and C 1s(CF_2) → σ^*_{C-C} (⊥) excitations, in the main chain.

3.3.1.2 F 1s spectra

Figure 3.3 compares the F 1s spectra of Nafion 117, Aquivion 98, 3M 725 PFSA with that of PTFE. Detailed transition assignments are presented in **Table 3.2.** As with the C 1s spectra, the F 1s spectra of the three PFSA are very similar, with each PFSA having the same F 1s spectral features with very similar intensities. In contrast to the C 1s edge, the F 1s spectra of all three PFSA species are much closer to that of PTFE. The F 1s spectra are dominated by strong F 1s → σ^*_{C-F} peaks at 689.8 and 694.0 eV. By comparison to the F 1s spectra of aligned PTFE[36] the first peak at 689.8 eV is associated with excitations to σ^*_{C-F} (⊥) orbitals oriented across the C-C chain direction while the peaks at 693.4, 704.0 and 723.0 eV are associated with σ^*_{C-F} (//) orbitals oriented along the C-C chain direction. There are small but reproducible differences in the intensities of the two main F 1s peaks among the three PFSA. Given that the relative intensities of the two main F 1s NEXAFS peaks can change dramatically with molecular orientation,[36] one might suspect that the variations in the spectra of the 3 species could be related to partial alignment of the polymer chains. However the spectra shown were recorded with 100% circularly polarized light which is insensitive to molecular orientation.[32] Several

spun cast films (to achieve uniform thickness) were examined using 100% linearly polarized light in several orientations, but there was no evidence of linear dichroic response. We conclude the variations seen among the F 1s spectra plotted in **Figure 3.3** are due to the chemical bonding changes, not to partial alignment.

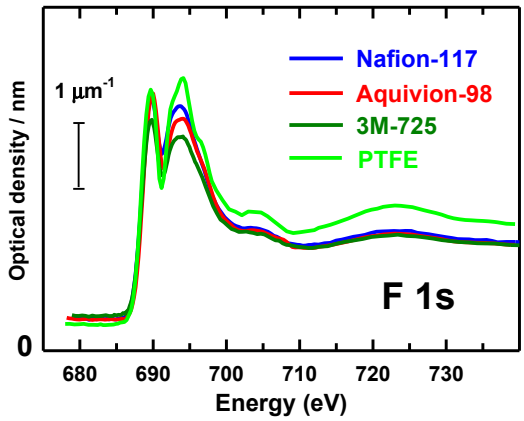

Figure 3. 3 F 1s X-ray absorption spectra of Nafion 117, Aquivion 98 and 3M 725 recorded using STXM. The spectra have been converted to an absolute intensity scale (optical density/nm thickness at standard density, *OD1*) using the procedures described in the text. Peak positions and tentative assignments are given in **Table 3.2.**

Table 3. 2 Summary of peak positions and tentative assignments for spectral features in the F 1s spectra of PTFE, Nafion 117, Aquivion 98 and 3M 725.

Energy (eV)				Assignment
PTFE	**Nafion 117**	**Aquivion 98**	**3M 725**	**CF_2**
689.7	689.8	689.9	689.8	σ*(C-F) ⊥
692.7 (sh)		692.8 (sh)		
694.1 [(a)]	693.8 [(a)]	694.2 [(a)]	693.7 [(a)]	σ*(C-F) //
696.7 (sh)	-	697.1 (sh)	-	
704.1	704.2	704.6	704.3	σ*(C-F) //
723 (br)	723 (br)	723 (br)	723 (br)	σ*(C-F) //

[(a)] Calibration: PTFE: +5.8(1) eV; Nafion 117: +5.5(1) eV; Aquivion 98: +5.9(1) eV; 3M 725: +5.4(1) eV, relative to F 1s → a_{1g} transition of SF_6 (688.27(15)[40]).

3.3.1.3 O 1s spectra

The O 1s spectra of the Nafion 117, Aquivion 98, and 3M 725 PFSAs are presented in **Figure 3.4a.** Detailed transition assignments are summarized in **Table 3.3.**

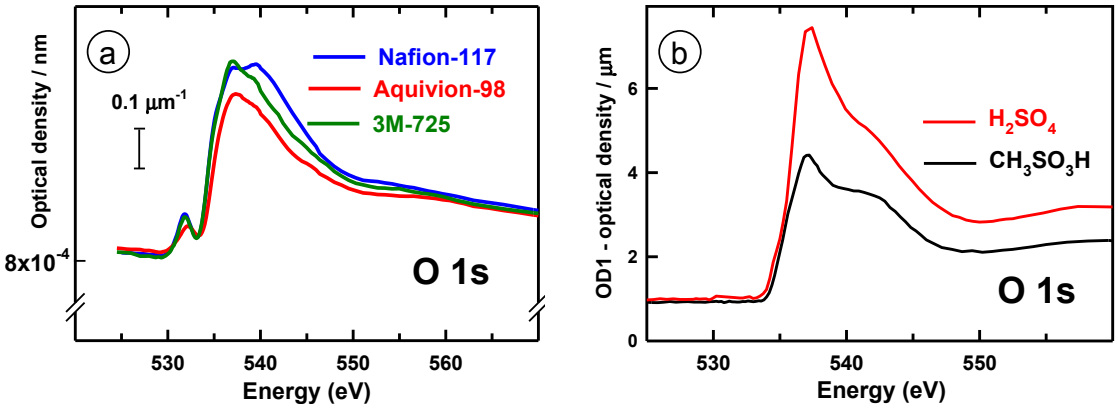

Figure 3. 4 (a) O 1s X-ray absorption spectra of Nafion 117, Aquivion 98 and 3M 725 recorded using STXM. The spectra have been converted to an absolute intensity scale (optical density/nm thickness at standard density, *OD1*) using the procedures described in the text. Peak positions and tentative assignments are given in **Table 3.3.** (b) O 1s spectra of H_2SO_4 and CH_3SO_3H. The absence of a feature at 532.0 eV indicates that the pre-peak observed in PFSA materials is not due to O 1s → σ^*_{O-H} or O 1s → $\sigma^*_{S=O}$ transitions at the sulfonate group.

Table 3. 3 Summary of peak positions and tentative assignments for spectral features in the O 1s spectra of Nafion 117, Aquivion 98 and 3M 725.

Energy (eV)			Assignment			
Nafion 117	**Aquivion 98**	**3M 725**	**C=O(OR)**	**COOR**	**C-O-C**	**SO_3**
531.8 [(a)]	532.2 [(a)]	531.9 [(a)]	$\pi^*_{C=O}$		-	-
535.4 (sh)	535.1 (sh)	535.0 (sh)		$\pi^*_{C=O}$		
537.0	537.5	537.1				σ*(S-O)
539.6	540.8 (sh)	539.5 (sh)			σ*(C-O)	
558 (br)	558 (br)	558 (br)				σ*(S-O)

[(a)] Calibration: Nafion 117: -7.1 (1) eV; Aquivion 98: -6.7 (1) eV; 3M 725: -7.0 (1) eV, relative to O 1s → 3s transition of CO_2 (538.9(1) eV[41])

An O 1s spectral signal was also measured from PTFE. Although it should only contain C and F, the very weak O 1s spectrum of PTFE (not shown) was very different from the spectra of PFSA (**Figure 3.4a**) and

likely arose from residual polymerization catalysts or impurities. The main intensity of the O 1s spectra of PFSA is contained in a broad structure between 535.0 and 545.0 eV, which is the region where both O 1s(C-O) $\rightarrow \sigma^*_{C-O}$[42] and O 1s(S-O) $\rightarrow \sigma^*_{S-O}$ transitions are expected. This region has a significantly different shape in each of the three species, with that of Aquivion being asymmetric on the high energy side, that of 3M 725 showing signs of a separate peak, and that of Nafion 117 having two distinct components, with maxima at 537.0 and 539.6 eV. Nafion 117, has two ether (C—O) bonds, whereas the short-side-chain (SSC) alternatives only have one ether bond. This gives rise to the difference in O 1s NEXAFS observed at both 537.0 eV and 540.0 eV. The difference in intensity at ~540.0 eV is introduced by the extra ether bond in the Nafion 117 structure. Therefore, the 540.0 eV transition corresponds to the O 1s $\rightarrow \sigma^*_{C-O}$ transition at the ether bond that is closer to the terminal sulfonic acid group. In addition to the broad σ^*_{C-O} signal there is a weak but sharp feature at 532.0 eV. This is the region where O 1s $\rightarrow \pi^*_{C=O}$ transitions occur. Since PFSA is usually synthesized with the main PTFE chains terminated by carboxylic acid or carboxylate groups,[43-44] it is likely the 532.0 eV feature arises from these end carboxyl groups.

In early studies we noted a significant difference in the strength of the O 1s pre-edge peak at 532.0 eV between two different ionomer species (**Figure 3.5**). Initially we attributed the 532.0 eV peak to O 1s $\rightarrow \sigma^*_{O-H}$ transitions at the sulfonic acid group based on a hypothesis suggested from a small molecule core excitation study (shown in **Figure 3.6**).

If the sulfonic acid was the reason behind the 532.0 eV transition, differences in the intensity of this peak would track the differences in degree of protonation of the PFSA, which would be a very useful probe for PEMFC studies. A peak at 532.0 eV has been reported in the O 1s NEXAFS spectra of $ZnSO_4$ and ionic liquid anti-wear engine additives which have sulfonate groups.[46] In order to test that initial hypothesis we used STXM to measure the O 1s spectra of $H_2SO_4(l)$ and $CH_3SO_3H(l)$ in sealed wet cells (see **Figure 3.4b**). Contrary to our expectations based on the initial (and clearly incorrect) spectral interpretation, the O 1s spectra of sulfuric acid and methyl sulfonate do not exhibit a peak at 532.0 eV, indicating the 532.0 eV peak observed in PFSA species cannot be due to O 1s $\rightarrow \sigma^*_{O-H}$ transitions at the sulfonate group.

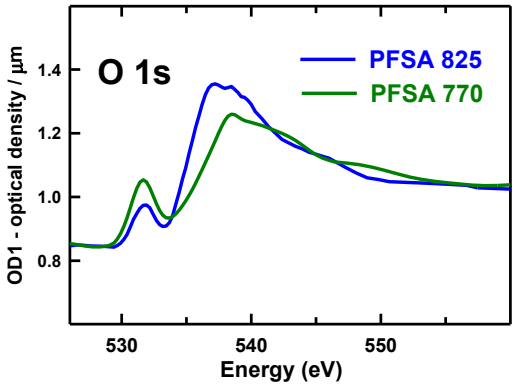

Figure 3. 5 O 1s spectra of PFSA 825 and 770. The two PFSA materials were obtained from the Holdcroft Group at Simon Fraser University. The sample treatment history was untraceable. The difference in a feature at 532.0 eV suggests that the pre-peak observed in PFSA materials is due to O 1s $\rightarrow \sigma^*_{O-H}$ transition at the sulfonate group determined by different levels of protonation of the two PFSA. PFSA 825 has less intense transition at 532.0 eV, which shows the lower degree of protonation compared to PFSA 770. The Ca 2p spectra of the same materials were collected to detect possible cation contamination (shown in **Appendix 5**). The results suggest that there is a high Ca content in PFSA 825.

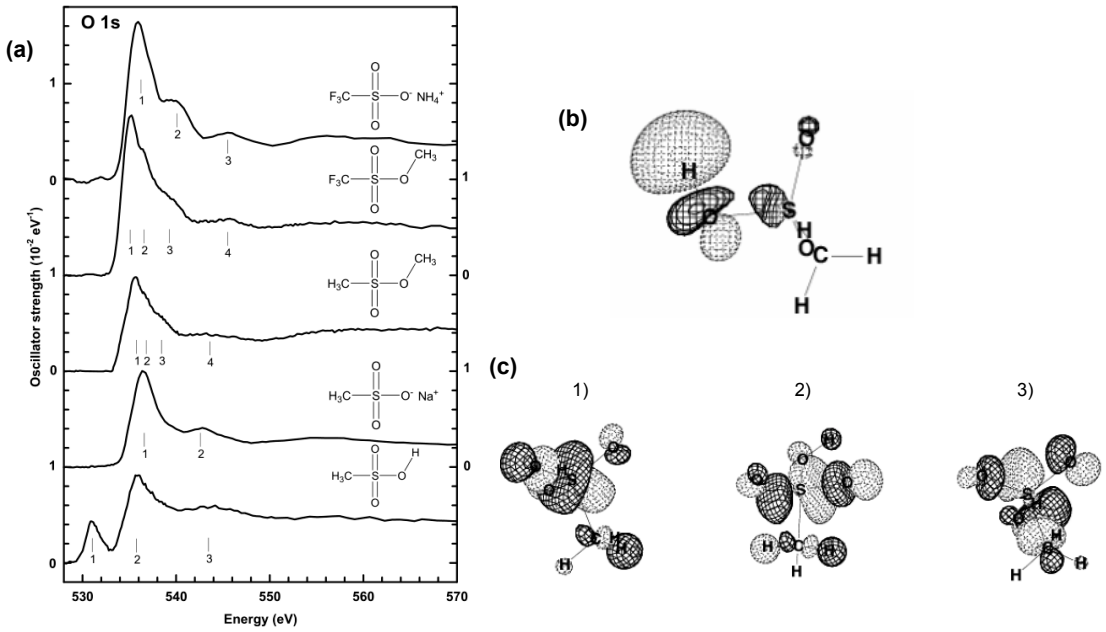

Figure 3. 6 (a) O 1s spectra of 5 sulfonate species. The spectra of the two ionic species are NEXAFS, measured using STXM. The spectra of the three molecular species are ISEELS recorded in the gas phase. (b) Plot of a σ^*_{S-O-H} orbital in methyl sulfonic acid from GSCF3 (Gaussian Self-Consistent Field version 3)[45] *ab initio* calculations. (c) Molecular orbital (MO) plots of 3 lowest unoccupied MOs from GSCF3 *ab initio* calculations of O 1s (S=O) excited methyl sulfonic acid, showing a dominant σ^*_{S-O} character.

Rather we assign the 532.0 eV peak to O 1s → $\pi^*_{C=O}$ transitions at carbonyl groups in the terminal carboxylates. This is consistent with the known energies and relatively sharp peaks for O 1s(COOR) → $\pi^*_{C=O}$ transitions, and supported by ^{13}C ssNMR (see section 3.3.2.2) as well as our interpretation of the 289.0 eV peak in the C 1s spectra of the PFSA materials. Unfortunately the 532.0 eV transition cannot be used as an indication of the degree of protonation of the material.

Another interesting observation related to the 532.0 eV peak is that this feature is significantly more intense in spun cast films of ionomer dispersions than in microtomed bulk membrane PFSA – see **Figure 3.7a.**

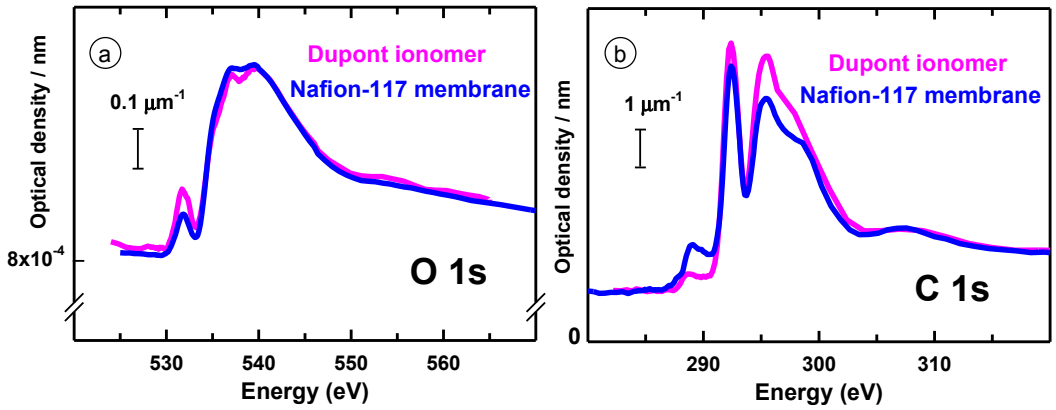

Figure 3. 7 (a) Comparison of O 1s spectra of Dupont ionomer (Nafion dispersion supplied by Ion Power Inc., mentioned in *3.2.1.3*) and Nafion 117 membrane. (b) Comparison of C 1s spectra of Dupont ionomer and Nafion 117 membrane. All spectra were measured in STXM using no-damage defocused beam conditions.

This could indicate a smaller mean molecular weight, i.e. shorter mean polymer chain, for ionomer (which is expected from the need to solubilize the ionomer in the catalyst ink dispersions) and thus a greater number of carboxylate termination sites relative to ether oxygen side chain sites. However, if that was the case, and our assignment of the 289.0 eV peak as the corresponding C 1s(COOX) $\rightarrow \pi^*_{C=O}$ transition is correct, then the 289.0 eV peak should be relatively stronger in the ionomer than in the membrane. In fact the opposite is the case, - see **Figure 3.7b.** In studies of several different types of ionomers, we consistently found these observations, as shown in **Figure 3.8.** At present these observations remain a puzzle.

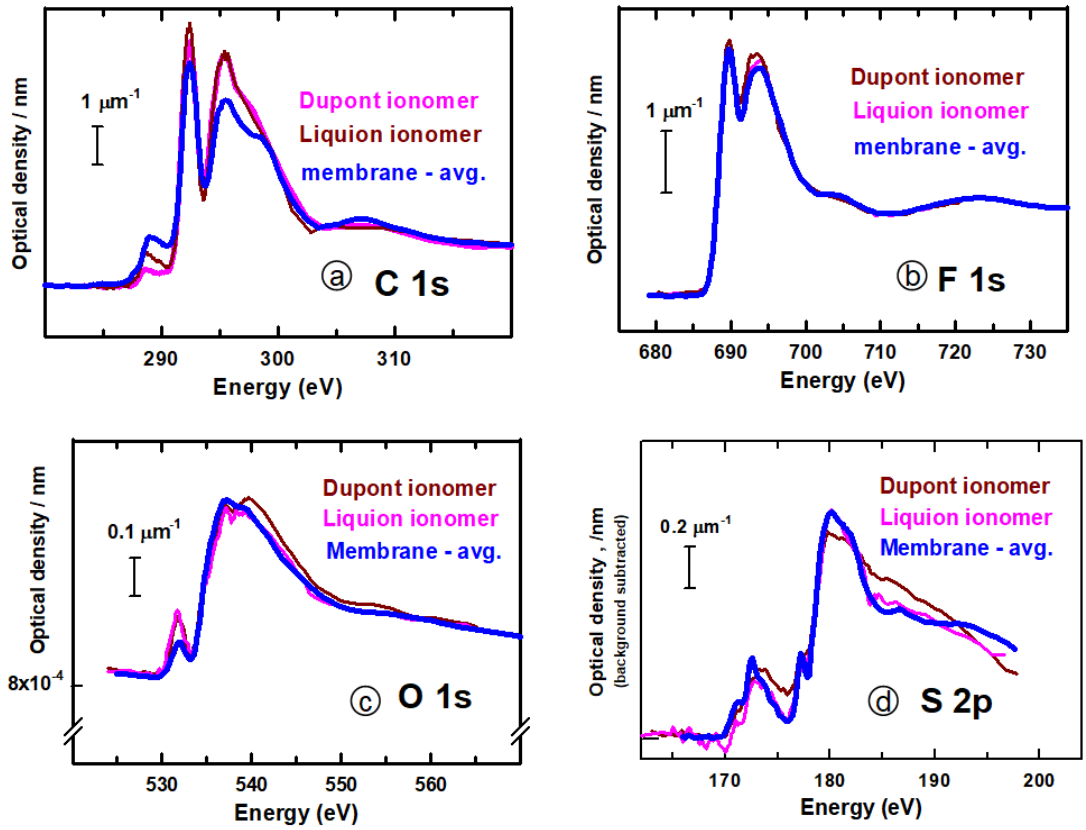

Figure 3. 8 Comparison of NEXAFS spectra of PFSA membranes (microtomed) and spun cast films of ionomer dispersions. (a) C 1s. (b) O 1s. (c) F 1s. (d) S 2p.

3.3.1.4 S 2p spectra

S 2p spectra are sensitive to the local bonding environment of the S[47] and informative in material speciation. The S 2p spectra of the Nafion 117, Aquivion 98, and 3M 725 PFSAs are presented in **Figure 3.9.** Detailed transition assignments are summarized in **Table 3.4.** The low lying transition at 172.0 eV is assigned to overlapping S $2p_{3/2,1/2}$ (S-C) → 4s and S $2p_{3/2,1/2}$ (S-O) → 4s transitions which form a characteristic 'triplet' structure due to spin-orbital coupling.[49] Transitions in the 178.0 – 186.0 eV region are attributed to spin orbit pairs of S 2p(S-C) → 3d (t_{2g}) and S 2p(S-O) → 3d (t_{2g}) transitions. For all three PFSA materials, the spectral features are very similar,

with only slight intensity differences. This is consistent with expectations since the sulfur environments in all three PFSA materials are very similar because the S centers are all in sulfonic acid or sulfonate groups, depending on the pH.

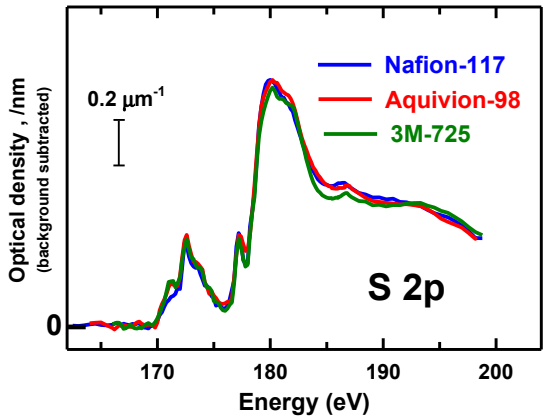

Figure 3. 9 S 2p X-ray absorption spectra of Nafion 117, Aquivion 98 and 3M 725 recorded using STXM. The as-recorded *OD* spectra were subjected to a spline fit to generate the non-sulfur background by extrapolating the pre-S 2p signal, which was then subtracted. The intensity scale was then set by matching to similarly background subtracted elemental response functions (*OD1*-S 2p). Further details are described in the text. Peak positions and tentative assignments are given in **Table 3.4.**

Table 3. 4 Summary of peak positions and tentative assignments for spectral features in the S 2p spectra of Nafion 117, Aquivion 98 and 3M 725.

Energy (eV)			Assignment			
			S-C		SO_3	
Nafion 117	**Aquivion 98**	**3M 725**	**$2p_{3/2}$**	**$2p_{1/2}$**	**$2p_{3/2}$**	**$2p_{1/2}$**
171.1	171.2	171.1	4s			
172.5 [(a)]	172.6 [(a)]	172.6 [(a)]		4s	4s	
174.1	173.8	174.0				4s
177.3	177.3	177.2	3d (t_{2g})			
178.2 (sh)	179.0 (sh)	178.5		3d (t_{2g})		
180.0	180.2	180.3			3d (t_{2g})	
182.0 (sh)	181.9	182.0				3d (t_{2g})
186.6	186.9	186.8	3d (e_g)	3d (e_g)		
194 (br)	193 (br)	194 (br)			3d (e_g)	3d (e_g)

[(a)] Calibration : Nafion 117: -12.1 eV; Aquivion 98: -12.0 eV; 3M 725: -12.0 eV relative to S 2p → t_{2g} transition of SF_6 (184.57(6)[48])

The change could be due to changes in the degree of protonation of the sulfonate sites, but, as seen from the O 1s edge, a localized σ^*_{S-O-H}

orbital either does not exist or the O 1s → σ^*_{S-O-H} and S 2p → σ^*_{S-O-H} transitions are too weak to be detected. The S 2p spectra of these three PFSA materials are similar to the S 2p spectra of gas phase trifluoromethanesulfonate and two other sulfonates, recorded in a complementary ISEELS study in **Figure 3.10.**

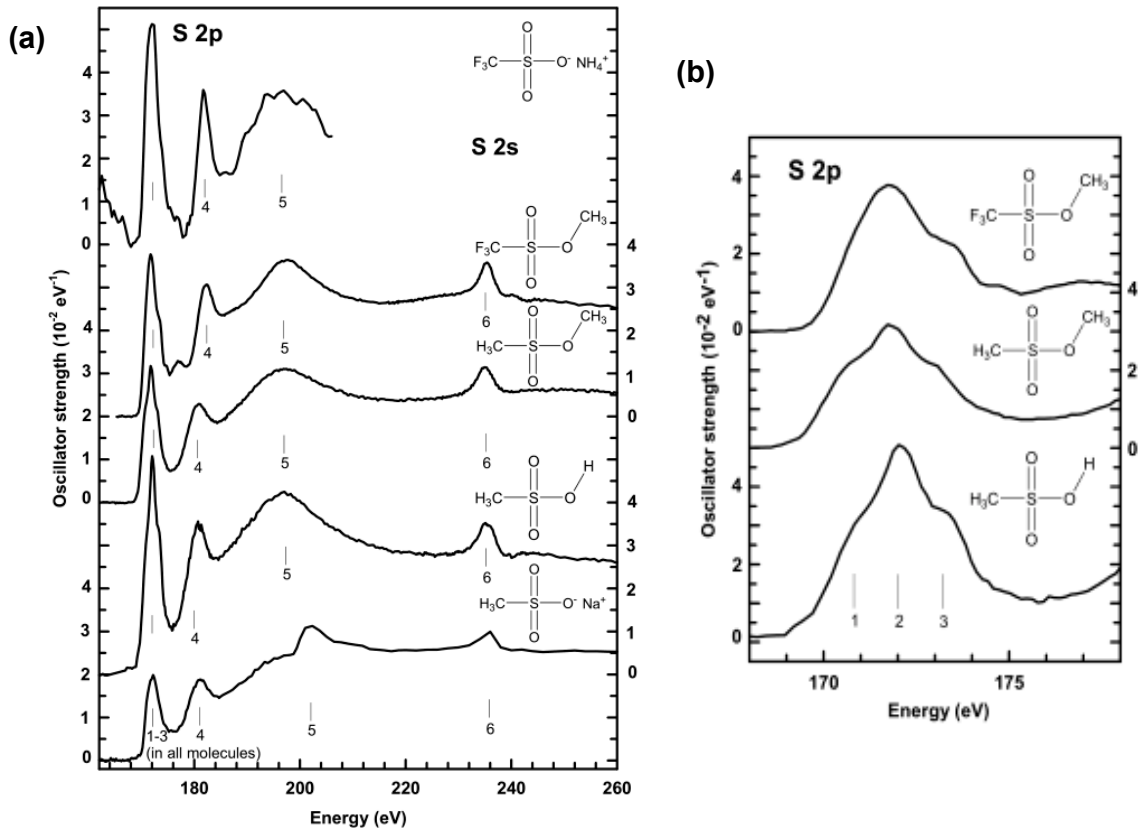

Figure 3. 10 (a) S 2p spectra of 5 sulfonate species (quantitative intensity scales). The two ionic species are NEXAFS, measured using STXM. The three molecular species are ISEELS spectra recoded in the gas phase. (b) Expanded view of the lowest energy peak in the 3 molecular species.

Since the S 2p spectra of all PFSA samples are identical, we conclude that the sulfonic acid groups in all 3 species have similar local bonding and environments, at least in the dehydrated state. It is important to note that the intensities in **Figure 3.9** do not correlate with the number of sulfonic acid groups present since the spectra have

been converted to *OD1* scale which normalizes the S 2p spectra on a per-S basis.

3.3.2 NMR Spectroscopy

3.3.2.1 ^{19}F NMR Spectroscopy

^{19}F NMR spectroscopy was performed at ambient temperature and humidity on three PFSA membrane materials after the activation treatment described in the experimental section. With careful deconvolution of the ^{19}F ssNMR signals, each of the different fluorine sites in each PFSA sample are distinguished and assigned, as shown in **Figure 3.11.** Peak locations and assignments are summarized in **Table 3.5.**

The Nafion 117 spectrum (**Figure 3.11a**) agrees with previous reports.[12] The signal from the side-chain fluorine atoms is well-resolved from those of the backbone. The alternative PFSA materials, Aquivion 98 (**Figure 3.11b**) and 3M 725 (**Figure 3.11c**), have not been studied in detail previously using ^{19}F ssNMR. Importantly, our meticulous deconvolution routine[50-52] is an effective tool for distinguishing the molecular structure of the PFSAs. In the spectra of all three PFSAs, the signal at -122 ppm is dominant, and is assigned to the backbone CF_2 moieties, which are the major building blocks of PFSAs. The most noticeable difference of the ^{19}F spectrum of Nafion compared to those of Aquivion 98 and 3M 725, is that two -OCF signals observed: one is from the backbone branch point; the other is from that in the side-chain.

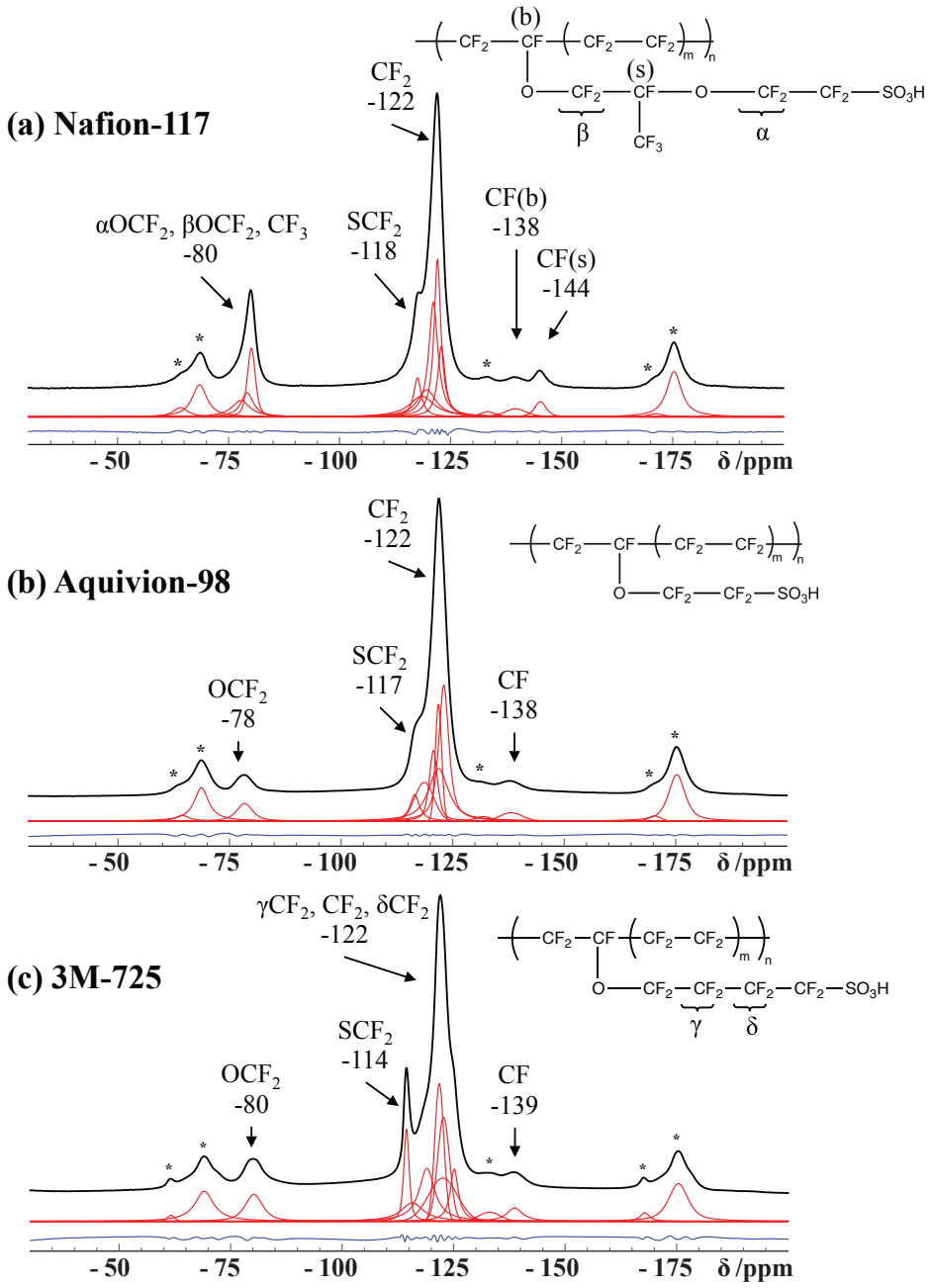

Figure 3. 11 ^{19}F MAS ssNMR of Nafion 117, Aquivion 98 and 3M 725. The * indicates spinning side bands. Different fluorine sites are labeled accordingly, separating the side chain and backbone signals based on the chemical shifts. Spectral intensities and assignments are given in **Table 3.5.**

Table 3. 5 Summary of peak positions (ppm), normalized relative intensities and assignments for spectral features in the ^{19}F MAS ssNMR spectra of Nafion 117, Aquivion 98 and 3M 725.

PFSA	^{19}F ssNMR Spectra Analysis – Chemical Shift (ppm) and Normalized Relative Intensity[a]						
Nafion 117	Type	αOCF_2	βOCF_2	CF_3	SCF_2		
	δ	−80	−80	−80	−118		
	Relative Intensity	2	2	3	2		
Aquivion 98	Type	OCF_2			SCF_2		
	δ	−78			−117		
	Relative Intensity	2			2		
3M 725	Type	OCF_2			SCF_2		
	δ	−80			−114		
	Relative Intensity	2			2		
Nafion 117	Type	CF_2			CF(b)	CF(s)	
	δ	−122			−138	−144	
	Relative Intensity	28			1	1	
Aquivion 98	Type	CF_2			CF		
	δ	−122			−138		
	Relative Intensity	30			1		
3M 725	Type	γCF_2	CF_2	δCF_2	CF		
	δ	−122	−122	−122	−139		
	Relative Intensity	2	16	2	1		

[a] Spinning side bands are included in relative intensity normalization.

The OCF_2 signals are found at approximately -80 ppm in all three PFSAs, however the relative signal intensity in Nafion 117 is much higher than in the other two PFSAs. This is due to the fact that the signal at -80 ppm in Nafion 117 includes contributions from three different fluorine sites, i.e. signal overlap. The SCF_2 site, the terminal fluorine site that is adjacent to the sulfonic acid group, is partially resolved in the spectra. Its signal is very close to that of the backbone CF_2 but the SCF_2 signal intensity can be easily analyzed with deconvolution. Another interesting observation is that the SCF_2 signal in 3M 725 is better resolved than in Nafion 117 or Aquivion 98.

This is possibly caused by the fluorine environment in the material, where the surrounding electronegative fluorines are pulling the electrons more since there are more fluorines nearby in 3M 725. Therefore, the chemical shift of the SCF_2 site is at a relatively higher frequency than the SCF_2 sites in Nafion and Aquivion. Thus, by looking at the general spectral features, these three PFSA materials can be differentiated with sufficient clarity that an unknown material exhibiting one of these three ^{19}F ssNMR spectra could be unambiguously identified.

Quantitative analysis of PFSA composition can also be performed using ^{19}F NMR study. Normalized integrated signal intensities for each fluorine site are summarized in **Table 3.5.** The relative intensity ratios agree with the chemical formulae provided by the manufacturers. This indicates that ^{19}F ssNMR can provide quantitative analysis of PFSA materials. ^{19}F ssNMR specifically probes the fluorine environments in PFSA, which can provide unambiguous evidence to identify/distinguish PFSA materials.

3.3.2.2 ^{13}C NMR Spectroscopy

^{13}C ssNMR is a challenging experiment due to the low natural abundance of NMR active ^{13}C nuclei. In order to assist transition identification in STXM C 1s NEXAFS analysis, ^{13}C ssNMR spectroscopy was used to identify different carbon environments in three different PFSA materials. The ^{13}C NMR data was collected on materials without ^{13}C enrichment. A 20 T field strength magnet was used to enhance signal sensitivity. The materials selected were activated Nafion 117, and cast film samples from Nafion and Liquion dispersions. It is known that the terminal end group of the polymer chains can be –COOH, $-CF_2H$ or $-CF_2=CF_2$

from polymer manufacture.[43-44] A proton decoupling sequence was applied during detection to achieve good signal resolution. All of the carbon sites located on the polymer chains were observed in the chemical shift range, 100 ppm – 120 ppm, shown in **Figure 3.12.** The chemical shifts observed agree with the literature for all of the carbon signals expected from the PFSA materials.[50]

In each of the three PFSA samples studied, a carbonyl signal was observed in the ^{13}C ssNMR spectra. These signals have not been reported previously using ssNMR, or any other NMR method, to our knowledge. In Nafion 117, this signal occurs at 175.5 ppm (**Figure 3.12a**), but in both Nafion and Liquion cast film samples, the carbonyl signals are present at 179 ppm (**Figure 3.12b, 3.12c**). This chemical shift range has been observed for carbonyl carbons in various materials.[53-54] The variation in chemical shift in these three PFSA materials is possibly due to different cations being associated with the carbonyl groups. The cast films were not prepared in fully protonated form; identification of the cations was not in the scope of this study. Another interesting spectral feature observed was the different broad signals around -120 to -130 ppm, which suggests different signal intensities of sp^2 carbon (introduced by $-CF_2=CF_2$ as terminal groups).

Nonetheless, observation of ^{13}C ssNMR signal associated with carbonyl groups in all of the PFSA materials tested is consistent with the literature with regard to the possibility of carboxyl groups as the main chain termination.[43-44] It also supports assignment of the 289.0 eV NEXAFS peak as the C 1s(COOR)$\rightarrow\sigma^*_{C=O}$ transition and the 532.0 eV NEXAFS peak as the O 1s(COOR)$\rightarrow\sigma^*_{C=O}$ transition at a chain termination carbonyl group.

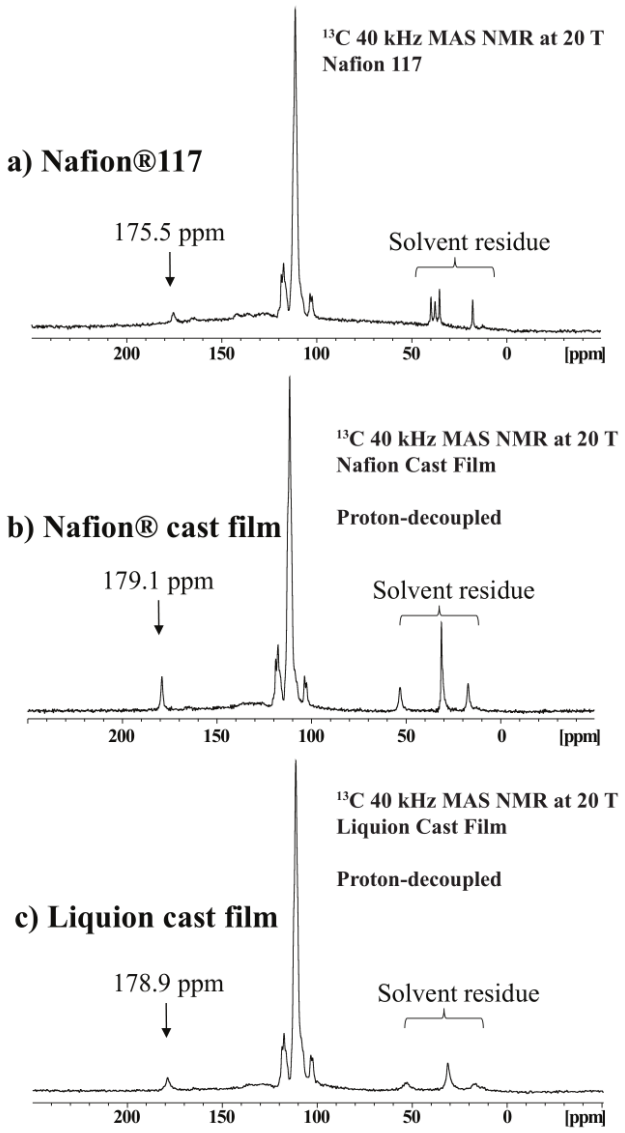

Figure 3. 12 ^{13}C ssNMR of (a) Nafion 117, (b) Nafion (EW1100) spun cast film, (c) Liquion (EW1100) spun cast film.

3.3.2.3 Diffusion Profile Analysis

The STXM and ssNMR analyses of the ionomer dispersion in cast film form demonstrate the chemical sensitivity of these spectroscopies for identification of different thin films. To further extend this investigation of PFSA cast films starting from different dispersions, the macroscopic diffusion profiles of those dispersions were

investigated *via* NMR spectroscopy. By doing so, the solvated molecular motion can be monitored, which provides insight into ionomer film formation in the catalyst layer (CL) and MEA in terms of ionomer-catalyst interfacial interaction.

Diffusion arises from Brownian motion, where the molecules move randomly in a fluid. It is often characterized by a diffusion coefficient, which is described according to the Stokes-Einstein equation as:

$$D = \frac{kT}{6\pi\eta r_s} \quad \textbf{(Equation 3.1)}$$

where k is Boltzmann constant, T is temperature, η is the viscosity of the liquid, r_s is the radius of the molecule. ^{19}F diffusion ordered NMR spectroscopy (DOSY) experiments for the PFSA dispersions were performed. The pulse sequence used in the current diffusion study can be found in the **Appendix 4.** The dispersions were obtained from Ion Power Inc. and diluted with NPA aqueous solution with volume ratio NPA: H_2O=3:1 to form 1 wt% concentrated solutions. By doing so, the difference in viscosity in the stock dispersion solutions can be neglected. By monitoring the attenuation of signal intensity, the diffusion coefficient can be extracted by plotting the signal intensity against gradient, according to

$$I = I_0 e^{-D\gamma^2 g^2 \delta^2 (\Delta - \delta/3)} \quad \textbf{(Equation 3.2)}$$

where D is diffusion coefficient, γ is the gyromagnetic ratio of the observing nucleus, g is the gradient strength, Δ is the diffusion time, and δ is the length of the gradient pulse.

In the current study, the molecular diffusion coefficients were extracted by ^{19}F DOSY experiments at different temperatures, by fitting

the signal attenuation trend to the experimental parameters used in the gradient pulse sequence based on the Stejskal and Tanner equation[55] using Bruker Dynamics Center software(v.2.2.1). The results are plotted in **Figure 3.13.**

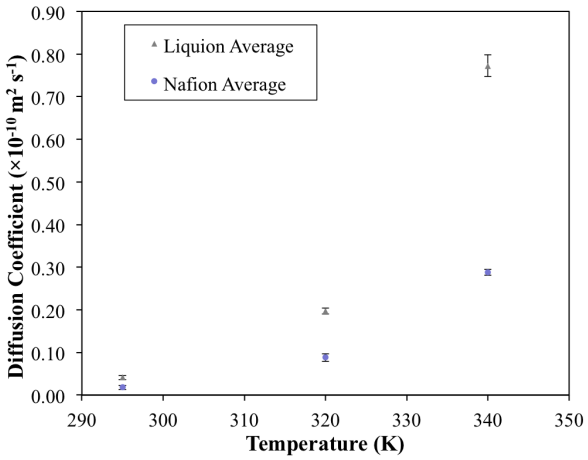

Figure 3. 13 Plot of temperature dependent proton diffusion coefficients in Nafion and Liquion liquid dispersions.

The profile diffusion coefficients for different PFSA dispersions were reported by averaging the values for all fluorine sites with 10% difference. The two PFSA dispersions were considered to have the same solution viscosity due to use of the same solvent system, as mentioned previously. In general, the Liquion dispersion has much higher diffusion coefficients at all temperatures, compared to the Nafion dispersion. Taking into account that the two PFSA dispersions were considered to have the same solution viscosity, and the inverse proportionality between the diffusion coefficient and the solvated radius (**Equation 3.1**), one can conclude that the molecular hydrodynamic radius of Liquion dispersion with 1 wt% concentration is smaller than that in a 1 wt% Nafion dispersion. Yet, despite the fact that the chemical compositions of these two dispersions are indistinguishable;

the macroscopic diffusion profiles effectively differentiate the two dispersions in terms of solvated molecular radius.

3.3.2.4 Concentration Dependent Diffusion Profile Analysis (Collaboration with AFCC)

In contrast to the previous diffusion comparison between two ionomer dispersion solutions with the same concentration, a series of ionomer dispersions with different concentrations were analyzed to extract ionomer diffusion profiles as a function of concentration. The goal is to understand the diffusive behavior of ionomers in different solvent systems under the influence of concentration. Additionally, the ionomer diffusion under the influence of solvent systems is also explored. As this work was under a non-disclosure agreement with AFCC, the specific details of the ionomers are not released here (general information of the solutions summarized in **Table 3.6)** and the discussion regarding the results remains generalized in this thesis.

Table 3. 6 Information of ionomer dispersion solutions obtained from AFCC.

Sample #	Ionomer type	Ionomer Concentration in the Sample, wt%	Concentration Info	Solvent Blend	
				NPA (n-PrOH)	H_2O
1a	A 720EW	3%	overlap (C*)	-	100%
1b	A 720EW	5%	ink	-	100%
2a	A 720EW	0.02%	overlap (C*)	25%	75%
2b	A 720EW	5%	ink	25%	75%
3a	Nafion 850EW	1%	overlap (C*)	75%	25%
3b	Nafion 850EW	5%	ink	75%	25%

In general, the diffusion depends on the viscosity of the solution and the radius of the solvated molecules as per **Equation 3.1.** It is therefore important to understand the concentration dependence of dynamic properties of ionomer in dispersion form. For comparison, two concentration classes are introduced: the ionomer overlap concentration

and the ink concentration.[56] The overlap concentration, labeled C*, defines the concentration at which the ionomer chains are not likely to interact with each other, which allows the polymer chains to have a relaxed morphology in the solvent. Conversely, the ink concentration refers to the ionomer dispersion concentration typically used during catalyst ink preparation, where the ionomers are expected to have a more densely packed arrangement in solution.

In an effort to extract the diffusion coefficients in different solvent systems, ^{1}H DOSY NMR measurements of water molecules present in the solvent systems were performed. The diffusion coefficients resulting from the analysis of the data are summarized in **Table 3.7.**

Table 3. 7 Summary of diffusion coefficients for water molecules in different solvent systems.

Sample #	H_2O in NPA	D (m^2/s)(E-9)	Error (E-9)
1a	100% H_2O	2.5	0.1
1b	100% H_2O	2.5	0.1
2a	75% H_2O	1.20	0.02
2b	75% H_2O	1.20	0.02
3a	25% H_2O	0.648	0.004
3b	25% H_2O	0.624	0.007

Between each pair of ionomer solutions (same solvent system but different ionomer concentrations), the diffusion coefficient of the water molecules remains constant within error. This suggests that the ionomer concentration difference (within the concentration range provided) does not influence the water diffusion behavior in the solvent system. Hence, according to **Equation 3.1** for water molecules in each solution pair, the parameters that affect the diffusion coefficient, such as solution viscosity, temperature and the molecular radius, are all equal. This implies that the ionomer concentration variation in the given case does not significantly affect the viscosity of the overall solution. Additionally, it is observed that in the presence of NPA the

water diffusion coefficient decreases, suggesting that the addition of NPA in the solvent system overall increases the viscosity of the solution.

From the ^{19}F NMR spectral comparison shown in **Figure 3.14**, samples 1a,b and 2a,b have equivalent ionomer content as demonstrated by the same relative intensity ratio between all observed fluorine sites (in **Figure 3.14a**).

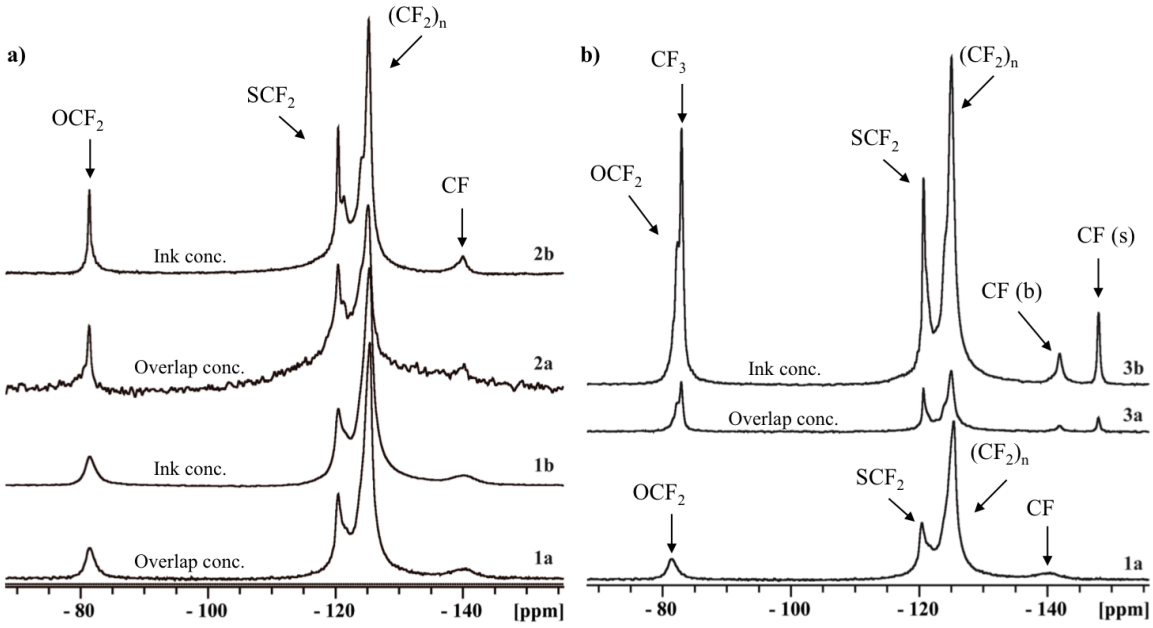

Figure 3. 14 Solution state ^{19}F NMR spectra for all the ionomer solutions. Solution concentrations are labeled as 'Ink conc.' and 'Overlap conc.' to help to distinguish a and b solutions in each pair. 1a,b and 2a,b share spectral similarity, which reflects the same ionomer in both pairs. 3a,b is Nafion-like long-side-chain (LSC) PFSA, therefore both spectra have different spectral features: two distinguishable CF signals.

Furthermore, from the observed chemical shift range, the ionomer in the solutions is likely to be a non-LSC PFSA. The more pronounced spectral features between -120 and -125 ppm in 2a,b are due to higher NPA content in the system (25% vs. 0%) as the added alcohol content makes the ionomer molecules more relaxed since the solvent system with NPA becomes less polar. The CF_2 groups at different locations along the

backbone with respect to the branch point –CF– are more exposed to the solvent system, therefore they tend to be more responsive to the applied magnetic field. In Figure **3.14b**, the 3a,b samples clearly contain a different type of ionomer in the solutions compared to the other two pairs. Based on the spectral analysis, there are two –CF– signals observed from the backbone and side chain. Therefore, the ionomer is a Nafion-like LSC-PFSA and the spectra are comparably similar to Nafion 117 shown in **Figure 3.11**, which agrees with the ionomer information provided by AFCC.

The diffusion coefficient analysis was performed using the Dynamic Center software developed by Bruker. The diffusion profile comparison between 1a,b is illustrated in **Figure 3.15.** Here we can use the generic Aquivion structure to represent the non-LSC PFSA to simplify the comparison. The two-dimensional (2D) plot maps out the diffusion coefficient as a function of chemical shift, with the contours showing the intensity of that specific site, providing a visual site-specific distribution of the diffusion coefficient. The backbone –CF– has the lowest D value compared to the other fluorine sites, with the rest of the sites exhibiting similar D values. The values for all three sample pairs are extracted and tabulated in **Table 3.8.** The difference between 1a and 1b is due to the concentration variation between the two samples. With higher concentration, the diffusion coefficient is lower, indicating that the hydrodynamic radius (r_s) is larger than that in the less concentrated solution, $r_{s,1b} > r_{s,1a}$. This is plausibly due to the lack of solvent molecules to solvate the ionomer molecule in the more highly concentrated solution.

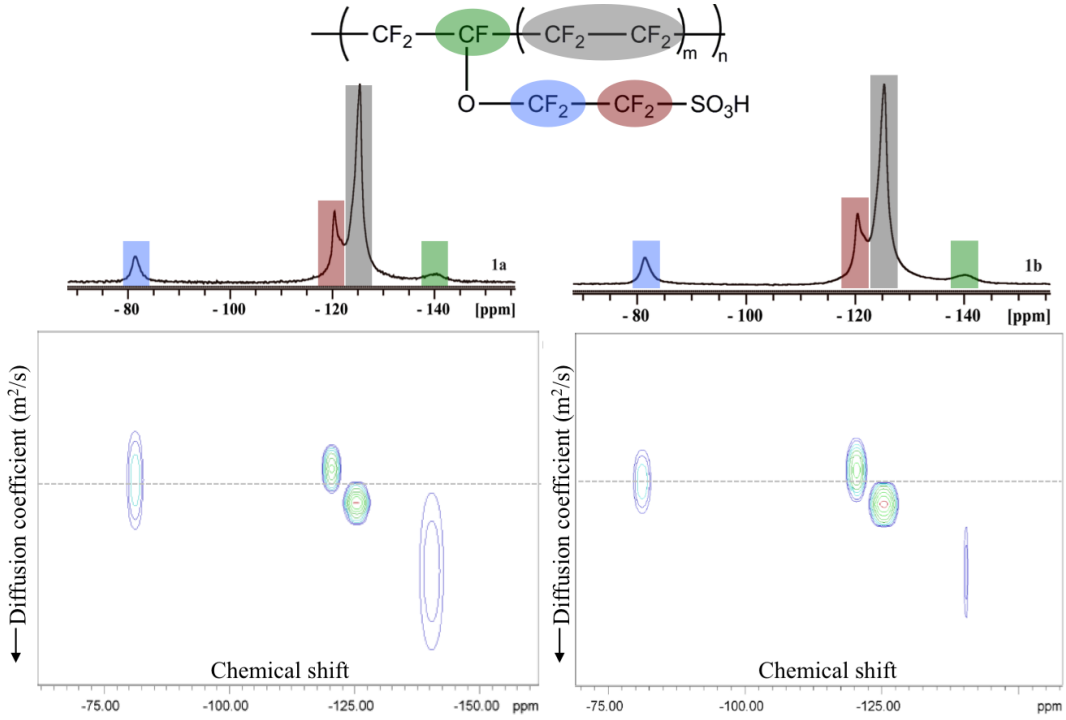

Figure 3. 15 The diffusion profile comparison of sample 1a and 1b, using Dynamic Center software. Aquivion structure is used here to demonstrate results from a non-LSC PFSA material. The dashed lines serve as a guide for diffusion coefficient comparison. The 2D plot illustrates the diffusion coefficient as a function of chemical shift, and the contour indicates the signal intensities.

Table 3. 8 Summary of diffusion coefficients of 1a,b. Each resolved fluorine signal was analyzed and the overall average of all the sites representing the entire molecule is also stated here.

Chemical Shift (ppm)	1a		1b	
	D (m^2/s) (E-11)	Error (E-11)	*D* (m^2/s) (E-11)	Error (E-11)
-81	3.30	0.20	3.00	0.10
-120	3.25	0.07	2.94	0.07
-125	3.41	0.05	3.08	0.05
-140	3.80	0.50	3.40	0.30
Overall Average	3.4	0.2	3.1	0.1

The same diffusion analysis was carried out on the second pair of solutions, however useful information from the 2a sample was not extractable. This was attributed to the low ionomer concentration in 2a. In order to have the signal-to-noise ratio required to extract

diffusion information, long experiment times and high applied gradients are typically necessary. Due to time constraints and instrumental limitations, the preliminary analysis of 2a was not possible. Nevertheless, the diffusion profile of 2b is illustrated in **Figure 3.16**, with the associated *D* values summarized in **Table 3.9.**

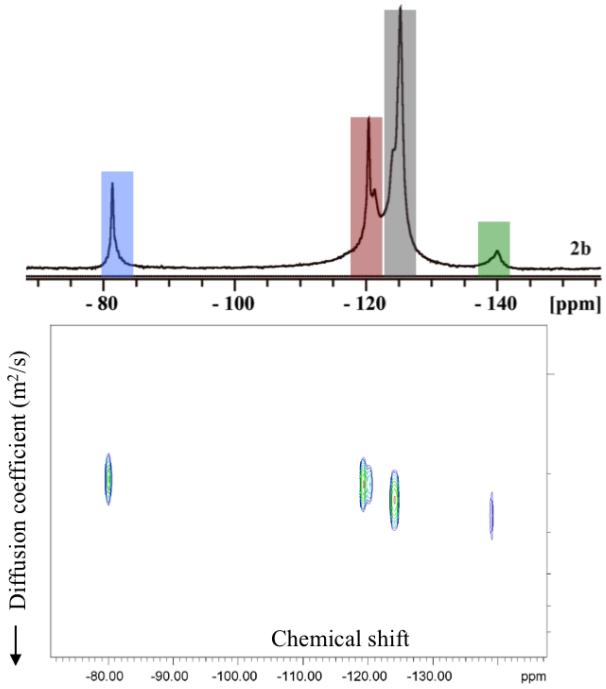

Figure 3. 16 The diffusion profile for sample 2b, analyzed using Bruker's Dynamic Center software.

Table 3. 9 Summary of diffusion coefficients of 2b. 2a has such low ionomer concentration, thus more experiments are needed to extract diffusion information. Each resolved fluorine signal was analyzed and the overall average of all the sites representing the entire molecule was also stated here.

Chemical Shift (ppm)	2b D (m^2/s) (E-12)	Error (E-12)
-81	2.9	0.4
-120	3.0	0.3
	3.0	0.3
-125	3.4	0.4
	3.2	0.4
-140	3.6	0.8
Overall Average	3.2	0.4

The shoulder peaks were analyzed and considered as part of the main peaks in both cases of the signals at -120 and -125 ppm. Since 1b and 2b have the same ionomer concentration, but in different solvent systems, the diffusive behaviors can be compared. As shown in **Table 3.7** where the solvent diffusion coefficients are summarized, the ratio of viscosities of sample 1b to 2b is $\eta_{1b} : \eta_{2b} = 0.48 : 1 \approx 1 : 2$ and the diffusion coefficients of the ionomer in 1b and 2b has a 10:1 ratio. The relationship between the hydrodynamic radii of ionomers in 1b and 2b can then be derived as follows:

$$\frac{D_{1b}}{D_{2b}} = \frac{\eta_{2b}}{\eta_{1b}} \cdot \frac{r_{s,2b}}{r_{s,1b}}$$

$$\Rightarrow \frac{10}{1} \approx \frac{2}{1} \cdot \frac{r_{s,2b}}{r_{s,1b}}$$

$$\Rightarrow \frac{r_{s,2b}}{r_{s,1b}} \approx \frac{5}{1}$$

From this derivation, it is clear that $r_{s,2b}$ is roughly 5 times greater than $r_{s,1b}$, suggesting that the difference in diffusion is introduced by the solvent system (NPA content 0% in 1b and 25% in 2b), where in 2b the molecules are more relaxed.

More interestingly, the comparison of 3a to 3b demonstrates the effects of the polymer backbone and side chain in terms of diffusion profiles, as shown in **Figure 3.17.** Two sets of dashed lines are drawn for clarity, the first one representing the fluorine signals from the backbone, while the other represents the fluorine signals from the side chain.

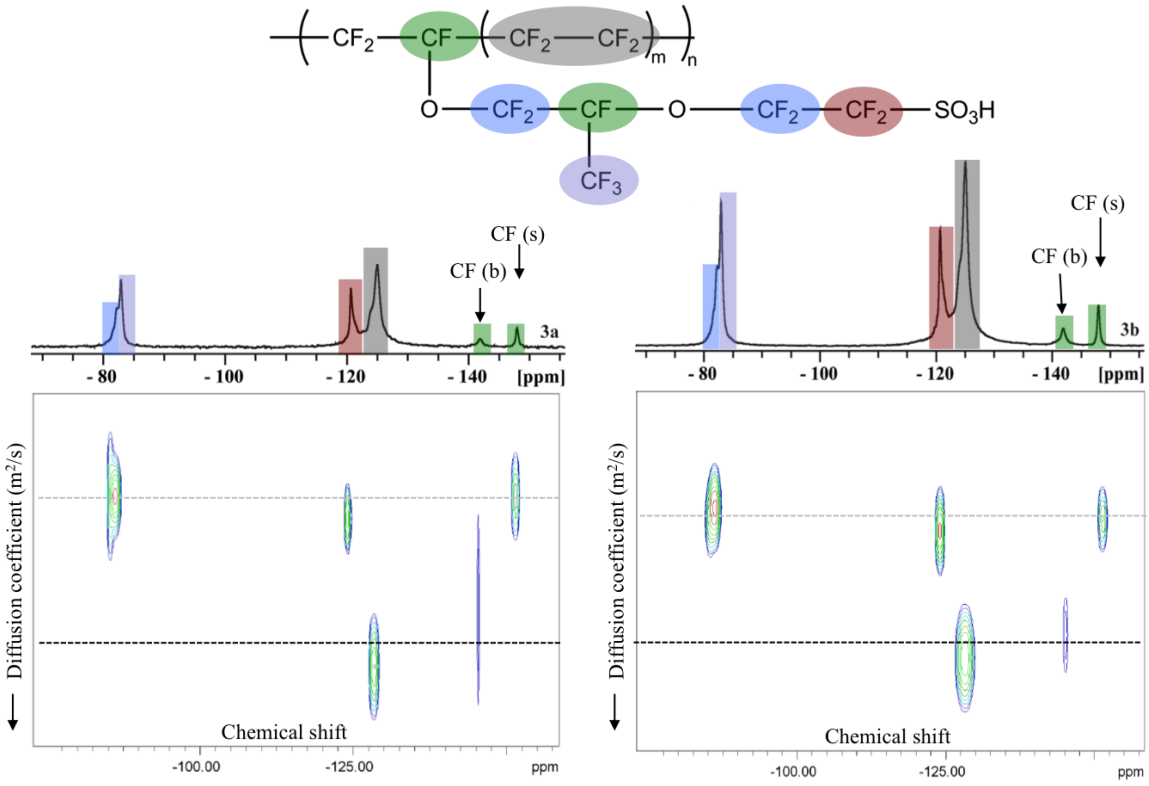

Figure 3. 17 The diffusion profile comparison of sample 3a and 3b, using Dynamic Center software. Two sets of dashed lines are drawn here to demonstrate the difference in diffusion coefficients of polymer backbone and side chain signals.

The diffusion coefficients from ^{19}F NMR measurements are summarized in **Table 3.10.** Note that the shoulder peaks were analyzed and considered as part of the main peaks. A similar comparison of 1a and 1b was made where it was observed that with the same solution viscosity, the difference in diffusion is attributable to concentration differences as the hydrodynamic radius is larger in less concentrated solutions. In general, the results of these comparisons suggest that the ionomer molecules in solutions with overlap concentration travel faster than those in the solutions with ink concentration, an effect that is introduced by a difference in the hydrodynamic radii.

Table 3. 10 Summary of diffusion coefficients of 3a,b. Each resolved fluorine signal was analyzed and the overall average of all the sites representing the entire molecule was also stated here.

Chemical Shift (ppm)	3a		3b	
	D (m^2/s) (E-12)	Error (E-12)	D (m^2/s)) (E-12)	Error (E-12)
-81	8.2	0.7	5.1	0.3
	8.1	0.5	4.9	0.3
	8.0	0.3	4.8	0.2
-120	8.4	0.4	5.0	0.2
	11	1.0	5.8	0.4
	11.5	0.8	7.0	0.3
-140	12	4.0	5.8	0.9
-147	8.3	0.6	4.9	0.2
Overall Average	9.4	1.0	5.4	0.3

By additionally comparing 1a,b and 3a,b, it is observed that the backbone and side chain signals seem to have different diffusion profiles, in which the difference is within error. As the molecule diffuses macroscopically, the difference between moieties within the molecule from diffusion profiles is unlikely to be seen. Nevertheless, more information is required in order to achieve the initial goal of describing the diffusive behavior of ionomers in different solvent environments and to provide insight into the ionomer arrangement in solution.

Overall, the additional diffusion study demonstrates the potential of ^{19}F diffusion NMR studies as an efficient approach to assist in the differentiation of different PFSA ionomer dispersions and provide self-diffusion profiles of the PFSA molecules. The role of overlap concentration and molecule morphology in solution is an interesting topic that is potentially better understood by this method, although technical difficulties still need to be overcome before accomplishing this goal.

3.4 Discussion

This study has explored the strengths and weaknesses of NEXAFS and ssNMR spectroscopies with respect to differentiating PFSA materials in different forms. Together they complement each other from several different perspectives. The STXM technique provides chemical analyses at the C 1s, F 1s, O 1s and S 2p edges for both membrane and electrode ionomer analysis. From the C 1s and F 1s NEXAFS investigation, the chemical differentiation was not as clear as we had hoped. Even with detailed transition assignments, the C 1s and F 1s NEXAFS spectra were not able to distinguish PFSA membranes with similar, but differing chemical structures. However, the O 1s NEXAFS was able to differentiate the three PFSA species studied, and thus potentially could be used to identify different PFSA membrane materials. From the O 1s NEXAFS spectral comparison, LSC-PFSA with two ether bonds, like Nafion, can be recognized and separated from the others. In contrast to NEXAFS, ^{19}F NMR analysis provides a powerful way to reveal the complete molecular structures at the fluorine atoms in bulk membrane samples, as demonstrated in **Figure 3.11.**

Another form of PFSA, ionomer dispersions, was also explored. The dispersion form is preferred in MEA manufacturing and CL casting in the industrial setting due to its tunability, which allows catalyst inks to reach desirable viscosity based on different formulations. When the material form switches from the bulk membrane to the cast thin film made from the ionomer dispersion, such thin films replicate the properties of PFSA materials in fuel cells without the complexity contributed from other MEA or CL components.

The O 1s NEXAFS spectra are sensitive to the chemical bonding between C and O. Spectroscopically the pre-peak at 532 eV is consistent with the presence of terminal carboxylic acid groups[43-44] an attribution which is supported by the ^{13}C NMR. From the NMR perspective, ^{19}F NMR is consistently able to reveal polymeric molecular structure of single-component materials. ^{13}C NMR study at high magnetic field positively identifies the terminal end groups on polymers and speciates residual solvent molecules. The ^{13}C NMR result supports the STXM finding, in that solvent residue signal appears at the lower chemical shift range (10 — 60 ppm) and carbonyl signal appears at the higher chemical shift range (175 — 180 ppm). The assignments of the 289 eV C 1s and the 532 eV O 1s signals are still debatable, since these transitions could arise from several possible sources. However the STXM and NMR results are consistent with each other regarding the existence of carbonyl group. To further support the NEXAFS peak assignments, additional small molecule investigations could be performed. For example studies of pentafluoropropionic acid (CF_3CF_2COOH) and its derivatives could help to define the spectra expected for carbonyl groups in a highly fluorinated environment.

By using solution-state NMR with an advanced gradient pulse sequence, the diffusion profiles of the ionomer dispersion were extracted and compared. This demonstrates the power of NMR for combined solid and liquid state studies of PFSA. However the diffusion experiment performs much more reliably if there are no additional components in the sample system. NMR can easily pick up interfering carbon signals in CL samples, but the existence of paramagnetic catalyst particles causes NMR signal line broadening. Additionally, the concentration and solvent dependence of the ionomer diffusion behavior

is also explored in collaboration with AFCC. The alcoholic component in the solvent demonstrates its ability to keep the ionomer in a more relaxed morphology.

The goal of this research was to explore the relative merits of NMR and NEXAFS spectroscopy for characterization of PFSA materials. While ssNMR is clearly more chemically sensitive than NEXAFS, it is not able to investigate the S or O environment directly. NEXAFS requires a synchrotron facility, which is less widely available than lab based ssNMR. However, if NEXAFS is measured with STXM, spatially resolved chemical mapping can be achieved which benefits investigations of systems with multiple components, such as CL and MEA samples.[5-9, 11-13] Together, this combination of techniques is able to probe subtle aspects of PFSA materials particularly for studies of degradation as a function of ionomer and membrane composition, following FC operation.[8]

3.5 Summary

This chapter reported an investigation of several different PFSA materials using two spectroscopic techniques, XAS and NMR, which provide different molecular perspectives. NEXAFS spectroscopy *via* STXM provides chemical sensitivity and spatially resolved (~30 nm) chemical mapping. Together, the C 1s, F 1s, O 1s and S 2p NEXAFS provide insights into the chemical bonding environment of these elements in PFSAs. S 2p edge studies have great potential to provide insight into selective chemical and electrochemical degradation study of PFSA materials in PEMFC.[8] ssNMR is much more sensitive than NEXAFS in material structure elucidation with qualitative identification and quantitation of different spin environments, since it can detect signals specific to

each distinct fluorine site in the repeat unit. However, the natural abundance ^{13}C ssNMR is a 'heroic' experiment (~64 h/sample) and ^{33}S ssNMR seems beyond reach of current instrumentation. Within their sensitivity limits, ^{19}F and ^{13}C ssNMR studies can greatly extend STXM analyses of PFSA. Both techniques detected signal from carboxyl groups, which unveils the possible termination of the polymer chain. The existence of carboxyl groups potentially reduces the acidity of the PFSA; however, it may be useful as a chemical stabilizer[43-44] to help ionomer solutions stay dispersed.

STXM analyses of CLs or MEAs can be complemented by reliable NMR reference data of PFSAs measured without any interference from C support or Pt catalysts, which are essential components in industrial fuel cell devices. At the same time, the S 2p and possibly O 1s NEXAFS can provide localized information on the proton conducting site, the sulfonic acid group, providing another tool to study ionomer materials, even in the presence of other fuel cell CL components. For example, the combination of S 2p NEXAFS and ^{19}F ssNMR would be a powerful approach to study membrane or catalyst layer degradation, or to analyze MEA activation or aging. A comprehensive STXM-ssNMR combination would have the potential to characterize both the spatial and chemical nature of operationally induced degradation. In particular, attack on PFSA side chains by electrochemically generated free radicals is implicated as a primary damage mechanism during PEMFC operation.[57] The ability to quantify side-chain loss by high-resolution ^{19}F ssNMR and sulfonic group loss by S 2p XAS would provide a unique vantage point on the degradation process. Furthermore, this approach could be used to evaluate the role of carboxylic acid groups in CL/membranes. Our proclivity is to further utilize STXM to evaluate full CL/MEA components, such that the

importance of polymer stability can be probed with spatial resolution. The collaborated work done on different ionomer solutions with AFCC has demonstrated the advantages of solution-state NMR diffusion method, where the concentration and solvent dependence of the ionomer diffusion behavior is explored. This technique is suggested to be an efficient approach in the differentiation of different ionomer dispersions and provide self-diffusion profiles of the PFSA molecules.

3.6 References

1. Gebel, G.; Diat, O., Neutron and X-ray Scattering: Suitable Tools for Studying Ionomer Membranes. *Fuel Cells* **2005**, *5* (2), 261-276.

2. Holdcroft, S., Fuel cell catalyst layers: a polymer science perspective. *Chem. Mater.* **2013**, *26* (1), 381-393.

3. Kreuer, K.-D.; Paddison, S. J.; Spohr, E.; Schuster, M., Transport in proton conductors for fuel-cell applications: simulations, elementary reactions, and phenomenology. *Chem. Rev.* **2004**, *104* (10), 4637-4678.

4. Mauritz, K. A.; Moore, R. B., State of understanding of Nafion. *Chem. Rev.* **2004**, *104* (10), 4535-4586.

5. Berejnov, V.; Saha, M.; Susac, D.; Stumper, J.; West, M.; Hitchcock, A. P., Advances in Structural Characterization Using Soft X-ray Scanning Transmission Microscopy (STXM): Mapping and Measuring Porosity in PEM-FC Catalyst Layers. *ECS Transactions* **2017**, *80* (8), 241-252.

6. Berejnov, V.; Susac, D.; Stumper, J.; Hitchcock, A. P., 3D chemical mapping of PEM fuel cell cathodes by scanning transmission soft X-ray spectrotomography. *ECS Transactions* **2013**, *50* (2), 361-368.

7. Hitchcock, A.; Wu, J.; Lee, V.; Appathurai, N.; Tyliszczak, T.; Shiu, H.-W.; Shapiro, D.; Berejnov, V.; Susac, D.; Stumper, J., Progress in Soft X-ray Microscopy Characterization of PEM Fuel Cell Catalyst Layers. *Microsc. Microanal.* **2016**, *22* (S3), 1290-1291.

8. Hitchcock, A. P.; Berejnov, V.; Lee, V.; West, M.; Colbow, V.; Dutta, M.; Wessel, S., Carbon corrosion of proton exchange membrane fuel cell catalyst layers studied by scanning transmission X-ray microscopy. *J. Power Sources* **2014**, *266*, 66-78.

9. Lee, V.; Berejnov, V.; West, M.; Kundu, S.; Susac, D.; Stumper, J.; Atanasoski, R. T.; Debe, M.; Hitchcock, A. P., Scanning transmission X-ray microscopy of nano structured thin film catalysts for proton-exchange-membrane fuel cells. *J. Power Sources* **2014**, *263*, 163-174.

10. Lepiller, C.; Gauthier, V.; Gaudet, J.; Pereira, A.; Lefevre, M.; Guay, D.; Hitchcock, A., Studies of Nafion—RuO2· xH2O Composite Membranes. *J. Electrochem. Soc.* **2008**, *155* (1), B70-B78.

11. Melo, L. G.; Hitchcock, A. P.; Jankovic, J.; Stumper, J.; Susac, D.; Berejnov, V., Quantitative Mapping of Ionomer in Catalyst Layers by Electron and X-ray Spectromicroscopy. *ECS Transactions* **2017**, *80* (8), 275-282.

12. Susac, D.; Berejnov, V.; Hitchcock, A. P.; Stumper, J., STXM study of the ionomer distribution in the PEM fuel cell catalyst layers. *ECS Transactions* **2011**, *41* (1), 629-635.

13. Susac, D.; Berejnov, V.; Hitchcock, A. P.; Stumper, J., STXM characterization of PEM fuel cell catalyst layers. *ECS Transactions* **2013**, *50* (2), 405-413.

14. Wang, C.; Duscher, G.; Paddison, S. J., Characterization of chain conformations in perfluorosulfonic acid membranes using electron energy loss spectroscopy. *RSC Advances* **2015**, *5* (3), 2368-2373.

15. Yakovlev, S.; Balsara, N. P.; Downing, K. H., Insights on the study of nafion nanoscale morphology by transmission electron microscopy. *Membranes* **2013**, *3* (4), 424-439.

16. Lis, G.; Botton, G.; Hitchcock, A. P., Quantification of the critical dose for radiation damage to perfluorosulfonic acid membranes using soft X-ray microscopy. *Microsc. Microanal.* **2015**, *21*, 2443.

17. Rightor, E.; Hitchcock, A.; Ade, H.; Leapman, R.; Urquhart, S.; Smith, A.; Mitchell, G.; Fischer, D.; Shin, H.; Warwick, T.,

Spectromicroscopy of poly (ethylene terephthalate): comparison of spectra and radiation damage rates in X-ray absorption and electron energy loss. *The Journal of Physical Chemistry B* **1997,** *101* (11), 1950-1960.

18. Wang, J.; Botton, G. A.; West, M. M.; Hitchcock, A. P., Quantitative evaluation of radiation damage to polyethylene terephthalate by soft X-rays and high-energy electrons. *The Journal of Physical Chemistry B* **2009,** *113* (7), 1869-1876.

19. Cody, G. D.; Heying, E.; Alexander, C. M.; Nittler, L. R.; Kilcoyne, A. D.; Sandford, S. A.; Stroud, R. M., Establishing a molecular relationship between chondritic and cometary organic solids. *Proceedings of the National Academy of Sciences* **2011,** *108* (48), 19171-19176.

20. Maia, L.; Mastelaro, V.; Schneider, J.; Parent, P.; Laffon, C., Structural studies in the BaO–B2O3–TiO2 system by XAS and 11B-NMR. *J. Solid State Chem.* **2005,** *178* (5), 1452-1463.

21. Vigolo, M.; Borsacchi, S.; Sorarù, A.; Geppi, M.; Smarsly, B. M.; Dolcet, P.; Rizzato, S.; Carraro, M.; Gross, S., Engineering of oxoclusters-reinforced polymeric materials with application as heterogeneous oxydesulfurization catalysts. *Applied Catalysis B: Environmental* **2016,** *182*, 636-644.

22. Hamrock, S. J.; Yandrasits, M. A., Proton exchange membranes for fuel cell applications. *Journal of Macromolecular Science, Part C: Polymer Reviews* **2006,** *46* (3), 219-244.

23. Kilcoyne, A.; Tyliszczak, T.; Steele, W.; Fakra, S.; Hitchcock, P.; Franck, K.; Anderson, E.; Harteneck, B.; Rightor, E.; Mitchell, G., Interferometer-controlled scanning transmission X-ray microscopes at the

Advanced Light Source. *Journal of synchrotron radiation* **2003,** *10* (2), 125-136.

24. Warwick, T.; Ade, H.; Kilcoyne, D.; Kritscher, M.; Tylisczcak, T.; Fakra, S.; Hitchcock, A.; Hitchcock, P.; Padmore, H., A new bend-magnet beamline for scanning transmission X-ray microscopy at the Advanced Light Source. *Journal of synchrotron radiation* **2002,** *9* (4), 254-257.

25. Kaznatcheev, K.; Karunakaran, C.; Lanke, U.; Urquhart, S.; Obst, M.; Hitchcock, A., Soft X-ray spectromicroscopy beamline at the CLS: commissioning results. *Nuclear Instruments and Methods in Physics Research Section A: Accelerators, Spectrometers, Detectors and Associated Equipment* **2007,** *582* (1), 96-99.

26. Ade, H.; Hitchcock, A. P., NEXAFS microscopy and resonant scattering: Composition and orientation probed in real and reciprocal space. *Polymer* **2008,** *49* (3), 643-675.

27. Hitchcock, A., Soft X-ray Imaging and Spectromicroscopy in Handbook on Nanoscopy, eds. G. Van Tendeloo, D. Van Dyck and SJ Pennycook. Wiley: 2012.

28. Hitchcock, A. P., Soft X-ray spectromicroscopy and ptychography. *J. Electron. Spectrosc. Relat. Phenom.* **2015,** *200*, 49-63.

29. Jacobsen, C.; Wirick, S.; Flynn, G.; Zimba, C., Soft X-ray spectroscopy from image sequences with sub-100 nm spatial resolution. *Journal of Microscopy* **2000,** *197* (2), 173-184.

30. Henke, B. L.; Gullikson, E. M.; Davis, J. C., X-ray interactions: photoabsorption, scattering, transmission, and reflection at E= 50-30,000 eV, Z= 1-92. *At. Data Nucl. Data Tables* **1993,** *54* (2), 181-342.

31. Hitchcock, A., aXis2000 is written in Interactive Data Language (IDL). *It is available free for noncommercial use from* http://unicorn.mcmaster.ca/aXis2000.html **2008.**

32. Stohr, J., NEXAFS Spectroscopy. Vol. 25. Springer-Verlag, NY: 1992.

33. Ma, Y.; Chen, C.; Meigs, G.; Randall, K.; Sette, F., High-resolution K-shell photoabsorption measurements of simple molecules. *Physical Review A* **1991**, *44* (3), 1848.

34. Ishii, I.; McLaren, R.; Hitchcock, A.; Jordan, K.; Choi, Y.; Robin, M., The σ* molecular orbitals of perfluoroalkanes as studied by inner-shell electron energy loss and electron transmission spectroscopies. *Can. J. Chem.* **1988**, *66* (8), 2104-2121.

35. Robin, M.; Ishii, I.; McLaren, R.; Hitchcock, A., Fluorination effects on the inner-shell spectra of unsaturated molecules. *J. Electron. Spectrosc. Relat. Phenom.* **1988**, *47*, 53-92.

36. Castner, D. G.; Lewis Jr, K. B.; Fischer, D. A.; Ratner, B. D.; Gland, J. L., Determination of surface structure and orientation of polymerized tetrafluoroethylene films by near-edge x-ray absorption fine structure, x-ray photoelectron spectroscopy, and static secondary ion mass spectrometry. *Langmuir* **1993**, *9* (2), 537-542.

37. Ohta, T.; Seki, K.; Yokoyama, T.; Morisada, I.; Edamatsu, K., Polarized XANES studies of oriented polyethylene and fluorinated polyethylenes. *Phys. Scr.* **1990**, *41* (1), 150.

38. Ziegler, C.; Schedel-Niedrig, T.; Beamson, G.; Clark, D.; Salaneck, W.; Sotobayashi, H.; Bradshaw, A., X-ray absorption study of highly oriented poly (tetrafluoroethylene) thin films. *Langmuir* **1994**, *10* (12), 4399-4402.

39. Sette, F.; Stöhr, J.; Hitchcock, A., Determination of intramolecular bond lengths in gas phase molecules from K shell shape resonances. *The Journal of chemical physics* **1984**, *81* (11), 4906-4914.

40. Sodhi, R. N.; Brion, C., Reference energies for inner shell electron energy-loss spectroscopy. *J. Electron. Spectrosc. Relat. Phenom.* **1984,** *34* (4), 363-372.

41. Hitchcock, A.; Ishii, I., Carbon K-shell excitation spectra of linear and branched alkanes. *J. Electron. Spectrosc. Relat. Phenom.* **1987,** *42* (1), 11-26.

42. Urquhart, S.; Hitchcock, A. P.; Priester, R.; Rightor, E., Analysis of polyurethanes using core excitation spectroscopy. Part II: Inner shell spectra of ether, urea and carbamate model compounds. *J. Polym. Sci., Part B: Polym. Phys.* **1995,** *33* (11), 1603-1620.

43. Curtin, D. E.; Lousenberg, R. D.; Henry, T. J.; Tangeman, P. C.; Tisack, M. E., Advanced materials for improved PEMFC performance and life. *J. Power Sources* **2004,** *131* (1-2), 41-48.

44. Ted, H. Y.; Liu, W.-G.; Sha, Y.; Merinov, B. V.; Shirvanian, P.; Goddard III, W. A., The effect of different environments on Nafion degradation: Quantum mechanics study. *Journal of membrane science* **2013,** *437*, 276-285.

45. Kosugi, N.; Kuroda, H., Efficient methods for solving the open-shell scf problem and for obtaining an initial guess. The "one-hamiltonian" and the "partial scf" methods. *Chem. Phys. Lett.* **1980,** *74* (3), 490-493.

46. Sharma, V.; Gabler, C.; Doerr, N.; Aswath, P. B., Mechanism of tribofilm formation with P and S containing ionic liquids. *Tribology International* **2015,** *92*, 353-364.

47. Hay, S. J.; Metson, J. B.; Hyland, M. M., Sulfur speciation in aluminum smelting anodes. *Industrial & engineering chemistry research* **2004,** *43* (7), 1690-1700.

48. Hudson, E.; Shirley, D.; Domke, M.; Remmers, G.; Puschmann, A.; Mandel, T.; Xue, C.; Kaindl, G., High-resolution measurements of near-edge resonances in the core-level photoionization spectra of SF 6. *Physical Review A* **1993,** *47* (1), 361.

49. Bernini, R.; Da Silva, L.; Rodrigues, F.; Coutinho, L.; Rocha, A.; de Souza, G., Core level (S 2p) excitation and fragmentation of the dimethyl sulfide and dimethyldisulfide molecules. *The Journal of Chemical Physics* **2012,** *136* (14), 144307.

50. Chen, Q.; Schmidt-Rohr, K., 19F and 13C NMR signal assignment and analysis in a perfluorinated ionomer (Nafion) by two-dimensional solid-state NMR. *Macromolecules* **2004,** *37* (16), 5995-6003.

51. Ghassemzadeh, L.; Kreuer, K.; Maier, J.; Müller, K., Evaluating chemical degradation of proton conducting perfluorosulfonic acid ionomers in a Fenton test by solid-state 19F NMR spectroscopy. *J. Power Sources* **2011,** *196* (5), 2490-2497.

52. Yan, Z. B.; Brouwer, D. H.; Goward, G. R., 19F Double Quantum NMR Spectroscopy: A Tool for Probing Dynamics in Proton-Conducting Fluorinated Polymer Materials. *Macromolecules* **2016,** *49* (19), 7331-7339.

53. Spera, S.; Bax, A., Empirical correlation between protein backbone conformation and C. alpha. and C. beta. 13C nuclear magnetic resonance chemical shifts. *J. Am. Chem. Soc.* **1991,** *113* (14), 5490-5492.

54. Wishart, D. S.; Bigam, C. G.; Holm, A.; Hodges, R. S.; Sykes, B. D., 1 H, 13 C and 15 N random coil NMR chemical shifts of the common amino acids. I. Investigations of nearest-neighbor effects. *J. Biomol. NMR* **1995,** *5* (1), 67-81.

55. Stejskal, E. O.; Tanner, J. E., Spin diffusion measurements: spin echoes in the presence of a time-dependent field gradient. *The journal of chemical physics* **1965,** *42* (1), 288-292.

56. Ying, Q.; Chu, B., Overlap concentration of macromolecules in solution. *Macromolecules* **1987,** *20* (2), 362-366.

57. Coms, F. D., The chemistry of fuel cell membrane chemical degradation. *Ecs Transactions* **2008,** *16* (2), 235-255.

4.

^{19}F DQ NMR – A New Tool for Probing Dynamics in Nafion

4.1 Introduction

This chapter focuses on the development of a ^{19}F double-quantum (DQ) NMR method specifically to characterize PFSA backbone and side chain dynamics. A standardization of the measurements is also discussed as a way to quantitatively compare PFSA materials in the same class. In this study, the commercial polymer electrolyte material, Nafion, was used in the demonstration and validation of the proposed NMR method. The main motivation for this study is that the role of side-chain dynamics in morphology development is not well-understood. Knowledge of the local dynamics within the various domains of PFSAs is valuable for gaining an understanding of ionomer performance within fuel cells, especially in catalyst ink formulations where the interactions between domains of PFSA and other ink components, i.e. conductive carbon, Pt catalyst and solvent blend, are poorly comprehended.

This chapter was adapted with permission from, *Macromolecules*. Copyright 2016 American Chemical Society (Z. B. Yan, D. H. Brouwer, G. R. Goward. **2016**, *49*, 7331-7339). All the materials preparation and treatment were done at McMaster University. The NMR pulse sequence was modified and optimized with help from Prof. Darren Brouwer. All ssNMR

experiments were performed at the NMR facility at McMaster University, and analyzed under the supervision of Prof. Gillian Goward. The initial drafts of the manuscript were written by the current author, Z. B. Yan.

In the case of PFSA, many NMR studies have been conducted based on different aspects such as structure and dynamics,[1-4] as well as morphology.[5-7] Magic-angle-spinning (MAS) ssNMR, coupled with two-dimensional (2D) ^{13}C—^{19}F heteronuclear correlation experiments have been applied to the structural analysis of PFSA materials.[1] This has provided a clear and unique assignment of the ^{13}C and ^{19}F chemical shifts to the backbone and side-chain carbon and fluorine atoms. In the investigation of PFSA degradation upon hydroxyl radical attack, ^{19}F ssNMR has been performed before and after the exposure to the hydroxyl radicals, followed by quantitative spectral analysis including spectral deconvolution.[8-9] From the individual segment analysis of the ionomer Nafion 211, the fluorine concentration associated with each fluorine site was studied as a function of exposure time to Fenton's reagent (which contains free radicals, as a strong oxidant).[8-9] The changes in concentration of the backbone and side-chain fluorine sites revealed that the backbone is resistant to radical attack. The vulnerability along the side chain was explicitly identified, as the free-radical attack was shown to cleave at a specific location.[8] This conclusion is consistent with the morphology of PFSA;[10] the free-radicals are formed and react within the hydrophilic domains, formed by the side chain-aqueous phase interaction. In contrast, the backbone regime is chemically more stable, as well as being hydrophobic, and thus inherently removed from the aqueous region where the hydroxyl radicals appear.

It is well-known that dynamics can be analyzed via NMR relaxation studies.[11-13] Both spin-lattice and spin-spin relaxation measurements, T_1 and T_2 respectively, as well as signal linewidth are often used to evaluate dynamics of molecules in solution as well as in solids.[1-2, 11-13] In solids, the second moment of the line shape can also be used to monitor dynamics, particularly when evaluating static spectra as a function of temperature.[14-16] For example, polytetrafluoroethylene (PTFE) fiber has been studied in this manner over a wide temperature range;[15, 17] however, such an approach without MAS lacks spectral resolution and cannot differentiate the dynamics occurring at different sites in the material. More recently, the $^{19}F/^{13}C$ NMR linewidth analysis of Nafion under MAS and $^{19}F-^{13}C$ chemical shift correlation indicates a dynamics gradient with respect to the backbone branch point, meaning that the dynamics increase along the side chain structure and are greatest at the terminal sulfonic acid group.[1-2] In these studies, the motion measured for the Nafion backbone agrees with the uniaxial rotation of PTFE,[17] while the side-chain motion is associated with sub-segmental motion, known as β-relaxation. This investigation focused on the use of chemical shielding anisotropy (CSA) changes as a function of hydration to evaluate the geometry of the side chain and backbone reorientations for Nafion.[1-2] Hence the dipolar recoupling NMR technique as an alternative approach for dynamics study is developed and implemented.

4.2 Experimental

4.2.1 Preparation of Fluorinated Polymer Materials

Pristine Nafion 117 was purchased from Sigma-Aldrich. Nafion was first washed in 3 wt% H_2O_2 for 1 hour at 90 °C and then washed with deionized water for another hour, changing the water four times. Subsequently, it was washed in 0.5 M H_2SO_4 solution for 1 hour. It was then washed in deionized water until a constant pH was obtained, again changing the water multiple times.[18] Finally, the materials were dried in vacuum oven at 80 °C for 24 hours.

4.2.2 Relative Humidity Control for NMR Samples

The relative humidity (%RH) condition was controlled by using ESPEC® Platinous series model ESL-2CA humidity chamber. The humidity range used in the study was 50% - 100%. Each condition was set up with constant mode at a 25 °C to reach the desired humidity condition. Nafion membrane material was packed into the working zirconia rotor uncapped. The packed rotor and Vespel™ cap were then placed into the chamber to equilibrate for 24 hours. The rotor was then capped before being taken out of the chamber for NMR analysis. The membrane sample was considered sealed at constant hydration level (λ) after the rotor was equilibrated for 24 hours at a given relative humidity. The associated λ value can be estimated based on the previous work done by Zawodzinski et al.[19] The λ value for sample that was treated under 50 %RH condition is ≈ 4; $\lambda \approx 14$ when the sample was under 100 %RH.

4.2.3 ^{19}F NMR

Solid-state NMR experiments were carried at on a Bruker Widebore-300 MHz Avance III system using a 4 mm double resonance probe. The MAS frequency in all experiments was 15 kHz. All ^{19}F MAS NMR

experiments were performed using a 97.5 kHz radiofrequency field after DQ efficiency optimization. The ^{19}F chemical shifts were relative to $CFCl_3$.

To accurately probe the dipolar interaction, reference NMR spectra were collected along with the DQ spectra and used in a normalization procedure. The reference spectra were obtained by modifying the receiver phase cycle,[20] compared to the DQ experiments where the phase cycle selectively allows the DQ coherence (DQC) to pass. The receiver phase of the reference experiment is designed to collect the coherences that are eliminated by the DQ experiment. In the current version of the pulse sequence (please refer to **Appendix 3**), the even steps of the receiver phase cycles between these two experiments have a 180° phase difference. The experiments were carried out based on the construction of the reference experiment, in accordance with Ref. 20. The interleaved 2D ^{19}F DQ recoupling experiments were carried out with 16 scans and 32 slices in the indirect dimension. The temperatures used in the variable-temperature measurements were calibrated using samarium stannate.[21-22]

4.3 Results and Discussion

4.3.1 Spectral Resolution of Nafion

The structure of Nafion is illustrated in **Figure 4.1**, together with the ^{19}F NMR spectrum collected using a single pulse experiment under MAS. Nafion (the most common PFSA) consists of a PTFE backbone and polyvinyl ether side chain terminated with a proton-conducting sulfonic acid group. The peak assignments of the ^{19}F MAS NMR spectrum are highlighted within **Figure 4.1.** The backbone CF_2 signal is the strongest

signal, at -122 ppm, and the backbone branching point CF(b) is observed at -138 ppm. The weaker side-chain fluorine signals are assigned as SCF_2 at -117 ppm, CF_3 and OCF_2 groups together at -80 ppm, and the CF(s) at -144 ppm. Designations of (b) and (s) refer to the backbone and side chain respectively.

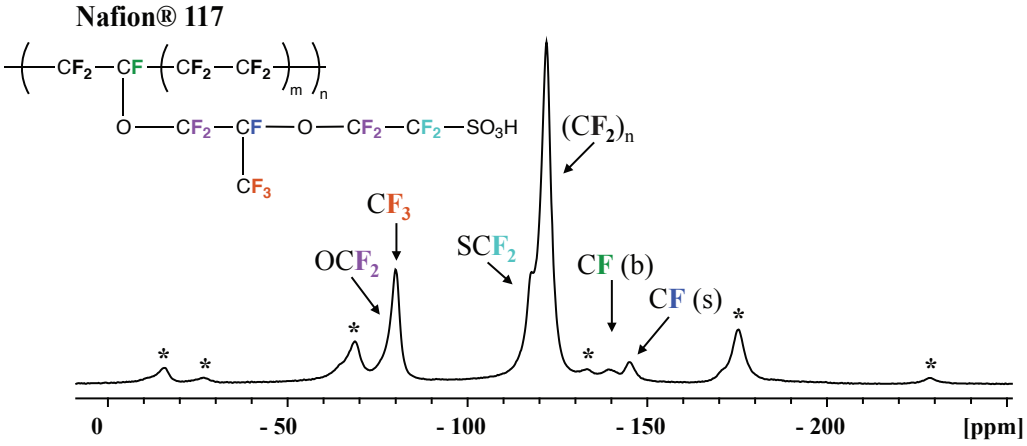

Figure 4. 1 The chemical structure of polymer material, long-side-chain PFSA (Nafion), and corresponding ^{19}F 15 kHz MAS NMR spectrum. Asterisks represent the spinning side bands.

4.3.2 Dynamics Analysis: Nafion

Here we demonstrate that ^{19}F DQ NMR experiments can be applied to probe the dynamics of PFSA ionomer materials, specifically protonated pristine Nafion 117. The conventional ^{19}F NMR provides confirmation of the PFSA structure, and the complete detailed assignment forms the basis of our site-specific dynamics investigation. The local dynamics analysis through ^{19}F DQ recoupling NMR is applied to the pristine Nafion material at different levels of hydration at various temperatures. The temperature range applied was below the glass transition of activated Nafion, and only the β-relaxation which corresponds to sub-segmental relaxation[23] was involved in this temperature range.[2, 24-26] According to

the analysis described in detail in **Chapter 2**, a typical set of normalized DQ (*nDQ*) build-up curves at the experimental temperature range is shown in **Figure 4.2.** As the temperature increases the build-up curve becomes shallower, consistent with the motional averaging of the ^{19}F–^{19}F dipolar coupling as polymer mobility increases, which results in proportionally weaker DQCs, and less signal intensity detected at the same recoupling times.

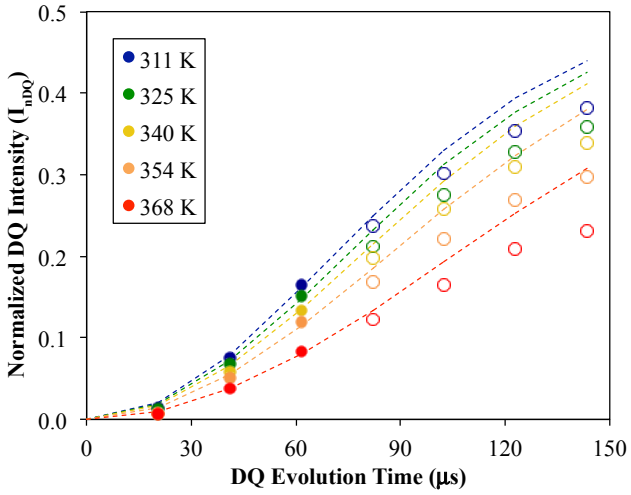

Figure 4. 2 A typical set of experimental *nDQ* curves of OCF_2/CF_3 (at -80 ppm) over a temperature range, which is used to extract dynamics information in the current study. Solid data points are used in the curve fitting to extract the apparent dipolar coupling constant D_{app}^{T} values from each data set.

Qualitatively, the observed decrease in the initial rise of the *nDQ* curves is indicative of an increase in relative dynamics, including some combination of the rate and amplitude of local motion as noted above, which contribute to an attenuation of the measured dipolar coupling constant. For a more quantitative analysis, the apparent dipolar coupling constant, D_{app}^{T}, is extracted based on **Equation 2.34** from curves that are similar to **Figure 4.2.** To investigate the

influence of temperature and relative humidity, the D_{app}^{T} values at four distinct chemical shift regions at the experimental temperature range under two hydration conditions are plotted in **Figure 4.3:** the branching point CF located on the backbone at -138 ppm, CF(b), the backbone CF_2 at -122 ppm, the side-chain signal that is the combination of OCF_2 and CF_3 at -80 ppm, and the side-chain terminal SCF_2 signal at -117 ppm. The SCF_2 is the closest fluorine site to the sulfonic acid group and the hydrophilic domain in PFSA; therefore it is expected to provide the strongest contrast in behavior relative to the backbone. With careful quantitative deconvolution of the one-dimensional ^{19}F NMR spectra, the SCF_2 signal is well separated from the main-chain signal $(CF_2)_n$. The detailed D_{app}^{T} values are summarized in **Table 4.1.**

Table 4. 1 D_{app} values extracted from the nDQ build-up curves in different %RH conditions at various temperatures.

	50 %RH λ ≈ 4				100 %RH λ ≈ 14			
Temperature (K)	**OCF_2/ CF_3**	**SCF_2**	**$(CF_2)_n$**	**CF(b)**	**OCF_2/ CF_3**	**SCF_2**	**$(CF_2)_n$**	**CF(b)**
311	7.4	6.7	8.3	10	6.1	4.8	7.2	8.5
325	6.7	5.3	7.8	9.4	5.8	4.0	6.7	7.6
340	6.1	4.2	7.3	8.4	5.5	3.1	6.6	7.3
354	5.4	3.6	6.8	7.3	5.0	3.6	6.3	7.1
368	4.3	1.9	6.1	6.1	4.1	1.7	5.7	6.1

Figure 4.3a represents experimental data obtained for treatment at λ ≈ 4, while **4.3b** are for treatment at λ ≈ 14. Under both hydration conditions, the side-chain signals have lower D_{app}^{T} values than the backbone, which indicates that the side chain is less constrained and has higher local dynamics than the backbone. The PFSA molecule experiences segmental motions associated with β-relaxation. More interestingly, SCF_2 in particular has the lowest D_{app}^{T} values of the four

chemical shift regions studied here. Thus, the terminal SCF_2 gives the highest local dynamics profile in the Nafion system, which is favourable for and consistent with its location adjacent to the proton-conducting site.

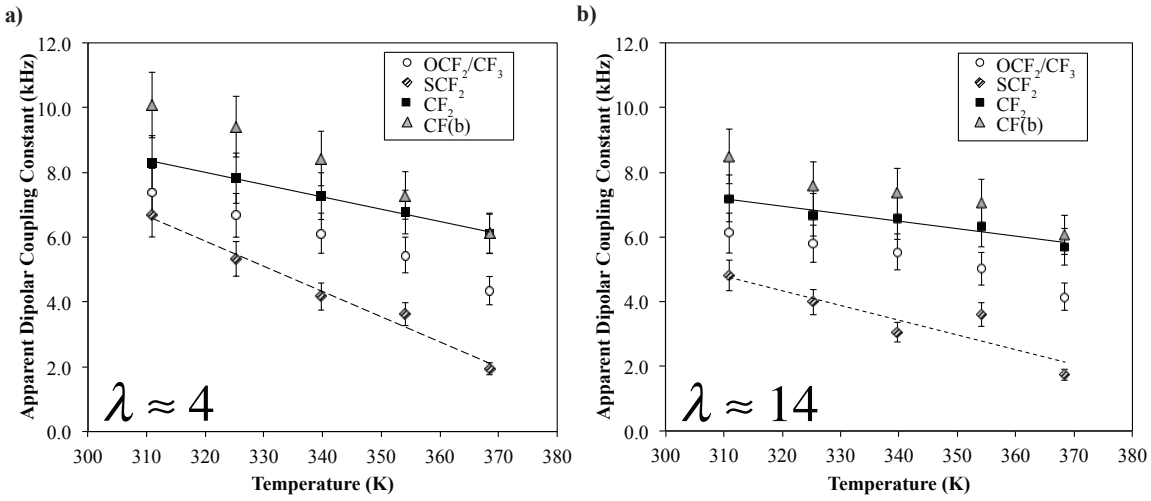

Figure 4. 3 The D_{app}^{T} value comparison of backbone branching point and side-chain terminal fluorines of Nafion 117 treated at 50 %RH (hydration level parameter, λ≈4) at 310 K – 370 K (a). The parallel analyses of backbone and side-chain fluorines of Nafion 117 treated at 100 %RH (hydration level parameter, λ≈14) are demonstated as (b). The solid line represents the trend line for the backbone signal while the dashed line highlights the behavior of the side-chain terminal SCF_2 signal.

Secondly, comparison between the local dynamics at different degrees of hydration can be clearly drawn. Similar temperature-dependent behavior is observed in the D_{app}^{T} for both hydration conditions within each set. At higher temperatures, lower values are observed in both side chain and backbone, which indicates that the available thermal energy induces molecular motion. Moreover, the D_{app}^{T} change in the backbone is less pronounced than that in the side chain over the same temperature range, indicating preferential increasing mobility in the side chain and associated hydrophilic domains. This is also

demonstrated in **Figure 4.3**, where the solid line represents the trend line for the backbone signal while the dashed line highlights the behavior of the side-chain terminal SCF_2 signal. The side chains are observed to have higher sensitivity towards temperature than the backbone as revealed by the distinct temperature dependence of the two spectrally resolved regions within the polymer. Through parallel comparison between the data sets at two degrees of hydration, overall the D_{app}^{T} values from both backbone and side-chain fluorines at $\lambda \approx 14$ are smaller than the values at $\lambda \approx 4$ (based on **4.3b**). As mentioned previously, the side chain has higher local dynamics as reflected by the comparatively lower D_{app}^{T} values. This observation can be explained by a model in which the side chains are clustered forming the hydrophilic domains in this micro-phase segregated ionomer, where the local motion is promoted by hydration. This is consistent with the finding that the side-chain regions are clustered and forming ionic/hydrophilic domains from previous studies[24-27], and the cluster domain size increases as hydration level is elevated.[28]

Moreover, comparing the side-chain trends, we note that the local dynamics of the fully hydrated membrane exceed those of the membrane with lower hydration level, and that the membrane with $\lambda \approx 4$ is more responsive to increasing temperature, consistent with lower hydration conditions requiring higher temperature to achieve favourable conductivity.[29-31]

Looking more carefully at the trends in the data sets, a range of dynamics can be seen from the side-chain fluorine behaviors. The D_{app}^{T} values of the terminal side chain fluorine (SCF_2) site has the lowest

value (indicative of comparatively high local dynamics) and the branching point (CF) on the backbone has the highest value overall. The values of OCF_2/CF_3 (along the side chain) fall in between the two extremes. As demonstrated above, the side-chain sites have higher local dynamics compared to the rigid backbone chain. The terminal SCF_2 is observed to be the most responsive towards both temperature and humidity elevations, while the side-chain signal at -80 ppm is less mobile compared to the terminal site. This is consistent with the expectation that the side chain with the sulfonic acid group is very sensitive towards the changes in humidification. The comparison between two hydration conditions demonstrates that at low levels of hydration, high temperature is more critical to enable local motion of the side chain, which enhances the formation of the ionic domains. This explains the finding that the proton conductivity is more temperature dependent at much dryer condition.[31] This local dynamics difference agrees with previous conductivity studies of Nafion 117 at various hydration conditions, where the bulk material has three times the conductivity at $\lambda \approx 14$ compared to $\lambda \approx 4$.[19, 31-32]

4.3.3 Dynamic Order Parameter for Comparison of Perfluorinated Ionomers

Proton conducting performance is often evaluated through macroscopic impedance spectroscopy to investigate the overall membrane conductivity performance. The micro-phase separation of hydrophobic and hydrophilic domains of proton-conducting polymeric materials is often used in explaining the differences in electrochemical performance, however there is not yet a standard evaluation of the material property from the fundamental chemistry point of view at a molecular level. The

dynamic order parameter, S^T, referenced here has been used in understanding the mechanical properties and local dynamics of synthetic polymers, and supramolecular systems, including poly(ethylene), polypeptides and dendritic-functionalized polymers.[33-35] This application of dynamic order parameter here is used to bring a standard metric in local dynamics studies for these PFSA ionomers that share similar chemical composition and structures. In the current analysis, the observed experimental apparent dipolar coupling constant (D_{app}^T) is scaled to the value that is calculated based on the theoretical model of a rigid Nafion-like structure. This provides a comparative dynamics profile of the material, and can be extended to other PFSA systems. More importantly, this is the first time that this dynamics analysis is applied to fluorine systems, which brings a new method to evaluate local motion among different samples that is independent to the absolute values of D_{app}^0 for specific conditions.

In order to establish the value of D_{app}^0, a reference state for the static case is required. Since there is not a known crystal structure of Nafion itself, the geometry-optimized molecular structure of perfluorohexane (C_6F_{14}, liquid state at room temperature) as the model of Nafion backbone[36]; and as well the geometry-optimized molecular structure of Nafion precursor[37], perfluoro-3,6-dioxa-4-methyl-7-octene-1-sulfonal fluoride ($C_7F_{14}O_4S$, liquid state at room temperature) have been chosen to represent the static structure of the side chain (**Figure 4.4**). The ^{19}F-^{19}F interactions considered in the calculation with **Equation 2.34** for D_{app}^T include all intramolecular distances within 5 Å.

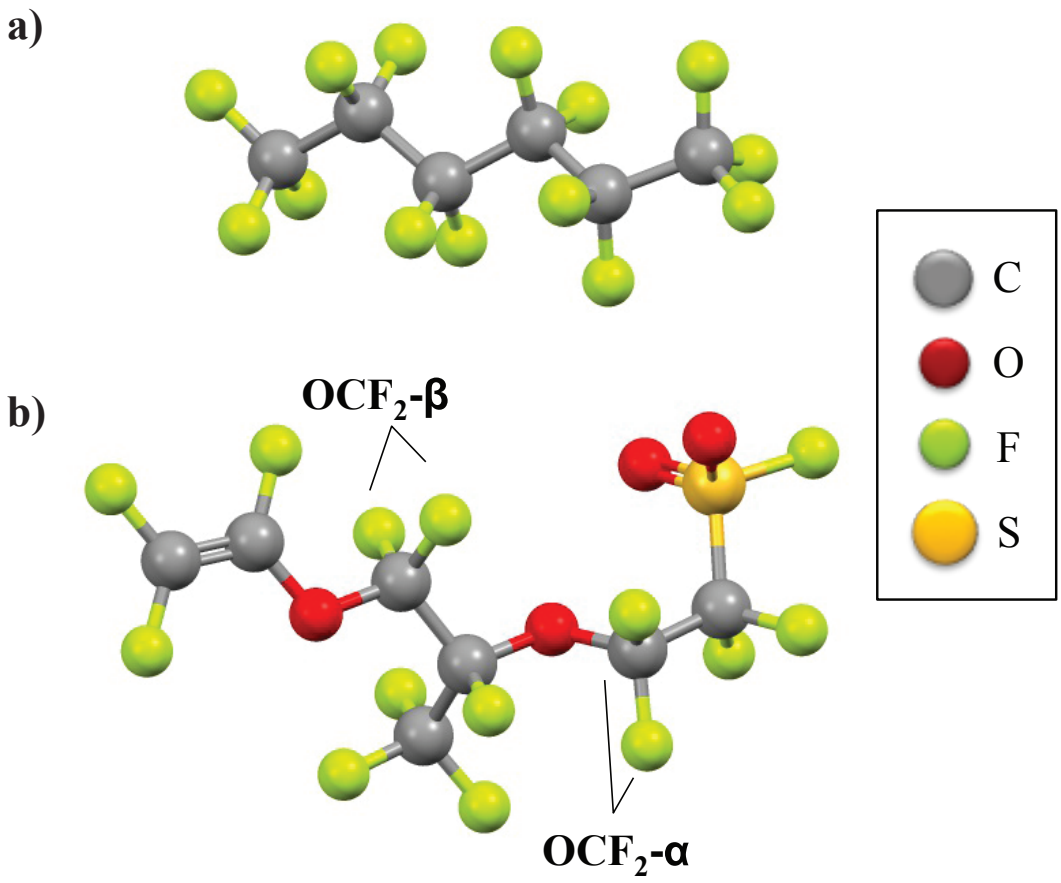

Figure 4. 4 The structures of C_6F_{14} (a) and $C_7F_{14}O_4S$ (b) are used in the D^0_{app} calculations.

The average D^0_{app} for geminal fluorines on the backbone is 16.06 kHz ($-CF_2-$). Without the geminal interaction, the D^0_{app} is calculated as 12.37 kHz to mimic the backbone branching point, CF(b). The example of a list of calculated dipolar coupling constants of C_6F_{14} was summarized in **Table 4.2**, where the fluorine was numbered in the insert of the table.

Table 4. 2 Summary of calculated dipolar coupling constants (between two fluorine nuclei) in model compound C_6F_{14}. Only interactions with internuclear distance within 5 Å were considered in the current study.

F11	Distance (Å)	D (kHz)	F10	Distance (Å)	D (kHz)
10	2.182	10.245	9	3.482	2.521
9	2.614	5.959	8	2.857	4.564
8	3.483	2.519	7	2.887	4.423
7	2.661	5.649	6	2.779	4.959
6	3.854	1.859	5	4.834	0.942
5	4.932	0.887	4	4.935	0.886
4	4.222	1.414	9'	3.482	2.521
9'	2.614	5.959	8'	2.857	4.564
8'	3.483	2.519	7'	2.887	4.423
7'	2.661	5.649	6'	2.779	4.959
6'	3.854	1.859	5'	4.834	0.942
5'	4.932	0.887	4'	4.935	0.886
4'	4.222	1.414			

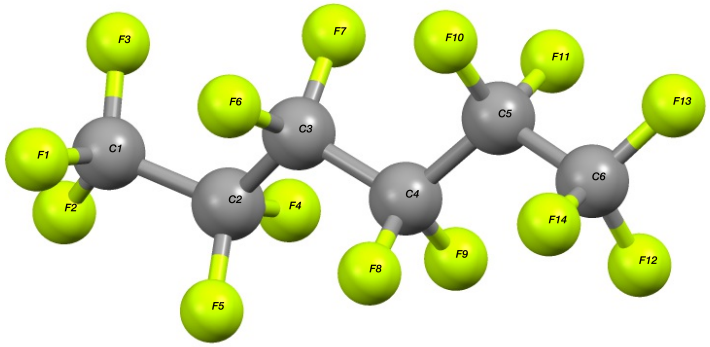

Similar calculations have been done for $C_7F_{14}O_4S$. Since there is no crystalline structure for $C_7F_{14}O_4S$, the geometry-optimized structure has been used for distance measurements between spins. The D_{app}^0 values are summarized in **Table 4.3** below based on the simplified model.

Table 4. 3 D_{app}^0 values for different fluorine sites in Nafion calculated based on the simplified model shown in **Figure 4.4** using **Equation 2.32.**

Theoretical	**OCF_2-β**	**OCF_2-α**	**CF_3**	**SCF_2**
D_{app}^0 (kHz)	12.40	14.95	16.04	12.49
Theoretical	**CF_2**	**CF (b)**	**CF (s)**	**OCF_2/CF_3**
D_{app}^0 (kHz)	16.06	12.37	13.79	14.46

The dynamic order parameters of the four chemical shift environments of interest are summarized in **Figure 4.5**, where the open circles represent data obtained at high hydration and solid grey squares represent dryer conditions. High hydration gives rise to lower order parameter values for all of the fluorine signals. This is due to the fact that higher humidity introduces more degrees of freedom of local motion throughout the entire molecule. Based on the calculation, the dynamic order parameters of SCF_2 range from 0.15–0.40, while for CF(b) S^T value ranges from 0.30–0.50. This drastic difference in dynamic order parameter can be explained by the differences in rate and amplitude of local fluctuations of the polymer structure, as discussed above.[33] This difference between the S^T values for SCF_2 and CF(b) confirms that the side chain has higher local mobility than the backbone, which agrees with the D_{app}^T value evaluation in **Figure 4.3.** Intriguingly, for all four fluorine sites, as temperature increases the S^T values converge, with each functional group reaching an equal value of S^T at the highest measured temperature under the two different degrees of hydration. This may indicate that temperature ultimately governs the local mobility, independent of the degree of hydration, which has implications for the functioning of the MEA at hotter, dryer conditions.

As shown in **Figure 4.5**, the four fluorine sites with different chemical shift regions are readily analyzed and distinguished. By doing so, the local dynamics for distinct but related materials can be simply compared.

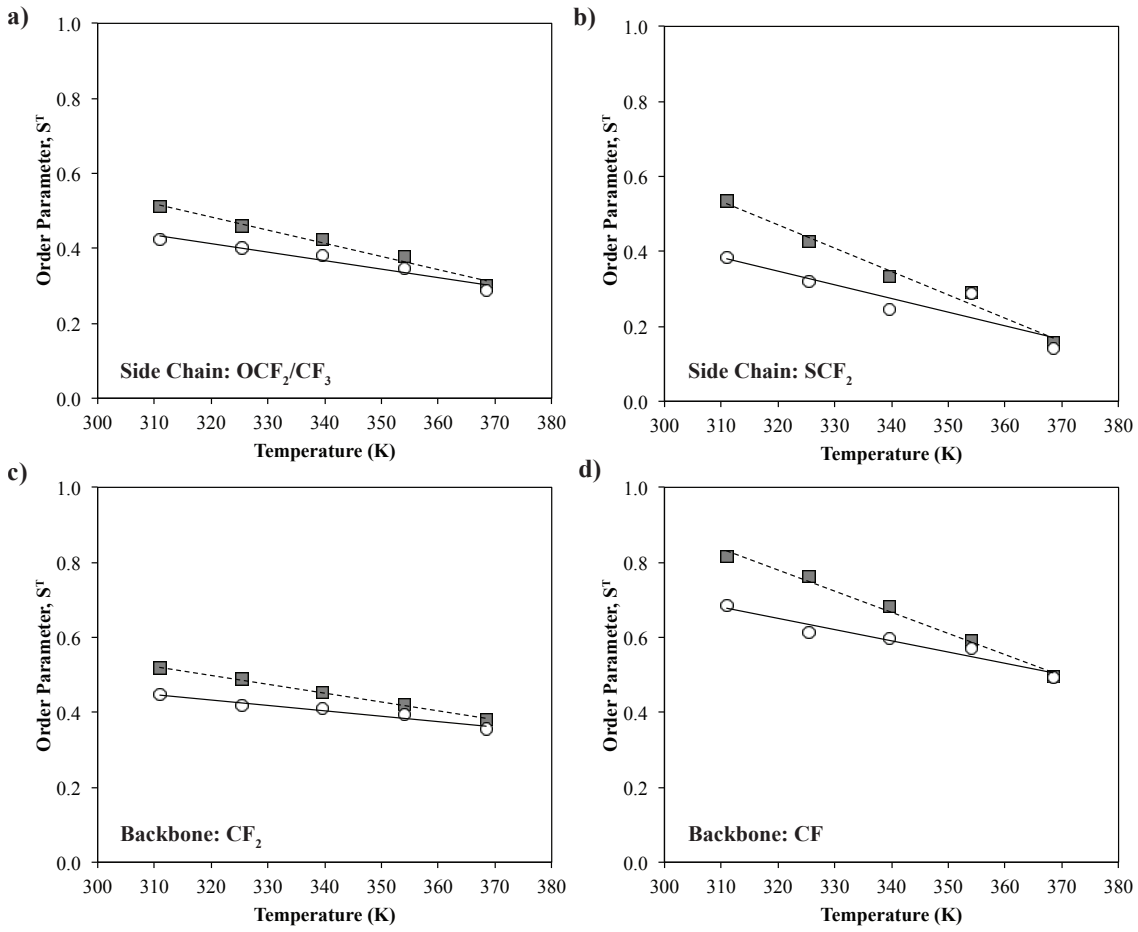

Figure 4. 5 Dynamic order parameter analyses for four fluorine sites: a) side-chain peak that corresponds to OCF_2 and CF_3 at -80 ppm; b) terminal side-chain SCF_2 signal at -117 ppm; c) backbone CF_2 at -122 ppm; d) branching point CF located on backbone at -138 ppm. The grey squares represent the values extracted for $\lambda \approx 4$ condition, while the clear dots demonstrate the values at $\lambda \approx 14$.

Furthermore, a pseudo-Arrhenius analysis is demonstrated in **Figure 4.6**, where the order parameter variation as a function of temperature has been explored. The backbone CF and side chain SCF_2 are chosen as representative for different parts of PFSA polymer chain. The linear regression demonstrates the thermodynamically-driven behaviour, which relates to the activation energy of local motion. The slopes of the pseudo-Arrhenius analysis are summarized in **Table 4.4.**

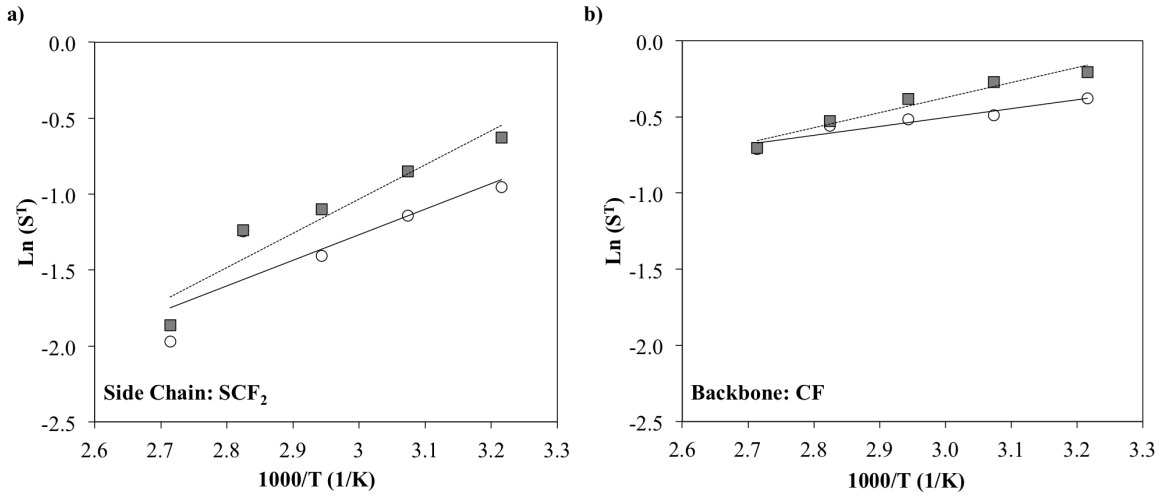

Figure 4. 6 Pseudo-Arrhenius analysis of dynamic order parameters. a) side-chain terminal side-chain SCF_2 signal at -117 ppm; b) backbone branching point CF located on backbone at -138 ppm. The grey squares represent the $\lambda \approx 4$ condition, while the clear dots represent $\lambda \approx 14$.

Table 4. 4 Summary of slope values for the pseudo-Arrhenius analysis, for side chain SCF_2 and backbone CF.

	SCF_2	CF
50% $\lambda \approx 4$	2.3 (1)	1.0 (1)
100% $\lambda \approx 14$	1.7 (2)	0.6 (1)

The slope values for SCF_2 are higher than the ones for CF, which indicates that there is probably a difference in the activation energy of polymer chain motions in these materials within the temperature range tested. Due to the more significant temperature dependence of SCF_2, it is likely that the side chain requires higher activation energy to promote local motion compared to the backbone. The side chain SCF_2 that 'carries' the proton conductive SO_3H group needs to overcome a certain energy barrier to pass on the protons. This explains the higher proton conductivity of Nafion at high temperature. On the other hand, the backbone (represented by CF) has a low activation energy requirement for local motion, yet it does not critically contribute to proton transport.

Interestingly, the slope values at higher hydration level are noticeably lower, which is indicative of hydration dependence of local motion. The hydration reduces the activation energy in both cases, SCF_2 and CF, yet the change in slope values is more significantly observed for SCF_2. This analysis demonstrates the thermodynamics behind the polymer chain local motion, as well as the temperature and hydration dependence within the test range. It is safe to say that the side chain local motion has greater effect on proton transport.

4.4 Summary

Local dynamics investigations of Nafion under different degrees of humidification were performed using a ^{19}F DQ recoupling NMR. The analysis of the initial *nDQ* build-up curves was shown to be an effective strategy for differentiating local dynamic behavior in perfluorinated ionomers. Through the analysis of the ^{19}F–^{19}F dipole-dipole interaction at elevated temperatures, local dynamics of different fluorine environments were investigated. This study focused on Nafion 117 as a bench mark experiment, in which the backbone was shown to have low local dynamics whereas the side chain had higher local dynamics, as determined by apparent dipolar coupling constant measurements. With different degrees of hydration, the side chain responded more sensitively towards the humidity change compared to the backbone. The ^{19}F DQ recoupling NMR technique including full D_{app}^{T} analysis is thus demonstrated as a qualitative and quantitative analysis method. The use of a dynamic order parameter, S^{T}, in the study of local dynamics in PFSA materials provides a valuable comparative measure which will allow this characterization strategy to be extended to related perfluoro ionomers.

This study has provided local dynamics difference between the hydrophobic and the ionic domains under macromolecular β-relaxation below the glass transition temperature. This helps us understand the link between the properties at the molecular level and bulk proton conductivity performance in ionomer materials. Our method can be potentially used in alternative materials, such as short-side-chain PFSA ionomers.

4.5 References

1. Chen, Q.; Schmidt-Rohr, K., 19F and 13C NMR signal assignment and analysis in a perfluorinated ionomer (Nafion) by two-dimensional solid-state NMR. *Macromolecules* **2004,** *37* (16), 5995-6003.

2. Chen, Q.; Schmidt-Rohr, K., Backbone Dynamics of the Nafion Ionomer Studied by 19F-13C Solid-State NMR. *Macromol. Chem. Phys.* **2007,** *208* (19-20), 2189-2203.

3. Boyle, N.; McBrierty, V. J.; Eisenberg, A., NMR investigation of molecular motion in Nafion membranes. *Macromolecules* **1983,** *16* (1), 80-84.

4. Schlick, S.; Gebel, G.; Pineri, M.; Volino, F., Fluorine-19 NMR spectroscopy of acid Nafion membranes and solutions. *Macromolecules* **1991,** *24* (12), 3517-3521.

5. Meresi, G.; Wang, Y.; Bandis, A.; Inglefield, P.; Jones, A.; Wen, W.-Y., Morphology of dry and swollen perfluorosulfonate ionomer by fluorine-19 MAS, NMR and xenon-129 NMR. *Polymer* **2001,** *42* (14), 6153-6160.

6. Giotto, M. V.; Zhang, J.; Inglefield, P. T.; Wen, W.-Y.; Jones, A. A., Nanophase structure and diffusion in swollen perfluorosulfonate ionomer: An NMR approach. *Macromolecules* **2003,** *36* (12), 4397-4403.

7. Slade, R. C.; Barker, J.; Strange, J. H., Protonic conduction and 1H self-diffusion in nafion film studied by ac conductivity and pulsed field gradient NMR techniques. *Solid State Ionics* **1989,** *35* (1-2), 11-15.

8. Ghassemzadeh, L.; Holdcroft, S., Quantifying the Structural Changes of Perfluorosulfonated Acid Ionomer upon Reaction with Hydroxyl Radicals. *J. Am. Chem. Soc.* **2013,** *135* (22), 8181-8184.

9. Ghassemzadeh, L.; Kreuer, K. D.; Maier, J.; Müller, K., Evaluating chemical degradation of proton conducting perfluorosulfonic acid ionomers in a Fenton test by solid-state< sup> 19</sup> F NMR spectroscopy. *J. Power Sources* **2011,** *196* (5), 2490-2497.

10. Kreuer, K.-D.; Paddison, S. J.; Spohr, E.; Schuster, M., Transport in proton conductors for fuel-cell applications: simulations, elementary reactions, and phenomenology. *Chem. Rev.* **2004,** *104* (10), 4637-4678.

11. Dong, R. Y., *Encyclopedia of Spectroscopy and Spectrometry: I-N*. Academic Press: 2000; Vol. 2.

12. Duer, M. J., *Introduction to Solid-state NMR Spectroscopy*. Blackwell Science: Oxford, UK, 2004.

13. Levitt, M. H., *Spin dynamics: basics of nuclear magnetic resonance*. John Wiley & Sons: Chichester, 2001.

14. Goc, R., Calculation of the NMR second moment for materials with different types of internal rotation. *Solid State Nucl. Magn. Reson.* **1998,** *13* (1), 55-61.

15. Hyndman, D.; Origlio, G. F., NMR absorption in Teflon fibers. *J. Appl. Phys.* **1960,** *31* (11), 1849-1852.

16. Tritt-Goc, J.; Piślewski, N.; Szczepańska, L.; Goc, R., Dynamics of a glycine molecule in a new ferroelectric glycine phosphite studied by proton NMR. *Solid State Commun.* **1998,** *108* (3), 189-192.

17. Vega, A.; English, A., Multiple-pulse Nuclear Magnetic Resonance of Solid Polymers. Polymer Motions in Crystalline and Amorphous Poly (tetrafluoroethylene). *Macromolecules* **1980,** *13* (6), 1635-1647.

18. Ye, G.; Janzen, N.; Goward, G. R., Solid-state NMR study of two classic proton conducting polymers: Nafion and sulfonated poly (ether ether ketone) s. *Macromolecules* **2006,** *39* (9), 3283-3290.

19. Zawodzinski, T. A.; Derouin, C.; Radzinski, S.; Sherman, R. J.; Smith, V. T.; Springer, T. E.; Gottesfeld, S., Water uptake by and transport through Nafion® 117 membranes. *J. Electrochem. Soc.* **1993,** *140* (4), 1041-1047.

20. Saalwächter, K.; Lange, F.; Matyjaszewski, K.; Huang, C.-F.; Graf, R., BaBa-xy16: Robust and broadband homonuclear DQ recoupling for applications in rigid and soft solids up to the highest MAS frequencies. *J. Magn. Reson.* **2011,** *212* (1), 204-215.

21. Grimmer, A. R.; Kretschmer, A.; Cajipe, V. B., Influence of magic angle spinning on sample temperature. *Magn. Reson. Chem.* **1997,** *35* (2), 86-90.

22. van Moorsel, G. J. M. P.; van Eck, E. R. H.; Grey, C. P., Pr2Sn2O7 and Sm2Sn2O7 as high-temperature shift thermometers in variable-temperature 119Sn MAS NMR. *J. Magn. Reson. A* **1995,** *113* (2), 159-163.

23. Priestley, R. D.; Ellison, C. J.; Broadbelt, L. J.; Torkelson, J. M., Structural relaxation of polymer glasses at surfaces, interfaces, and in between. *Science* **2005,** *309* (5733), 456-459.

24. Osborn, S. J.; Hassan, M. K.; Divoux, G. M.; Rhoades, D. W.; Mauritz, K. A.; Moore, R. B., Glass transition temperature of perfluorosulfonic acid ionomers. *Macromolecules* **2007,** *40* (10), 3886-3890.

25. Page, K. A.; Cable, K. M.; Moore, R. B., Molecular origins of the thermal transitions and dynamic mechanical relaxations in perfluorosulfonate ionomers. *Macromolecules* **2005,** *38* (15), 6472-6484.

26. Yeo, S. C.; Eisenberg, A., Physical properties and supermolecular structure of perfluorinated ion-containing (Nafion) polymers. *J. Appl. Polym. Sci.* **1977,** *21* (4), 875-898.

27. Kreuer, K., On the development of proton conducting polymer membranes for hydrogen and methanol fuel cells. *Journal of membrane science* **2001,** *185* (1), 29-39.

28. Gierke, T.; Munn, G.; Wilson, F., The morphology in nafion perfluorinated membrane products, as determined by wide-and small-angle x-ray studies. *Journal of Polymer Science: Polymer Physics Edition* **1981,** *19* (11), 1687-1704.

29. Anantaraman, A. V.; Gardner, C. L., Studies on ion-exchange membranes. Part 1. Effect of humidity on the conductivity of Nafion®. *J. Electroanal. Chem.* **1996,** *414* (2), 115-120.

30. Paul, D. K.; Fraser, A.; Karan, K., Towards the understanding of proton conduction mechanism in PEMFC catalyst layer: Conductivity of adsorbed Nafion films. *Electrochem. Commun.* **2011,** *13* (8), 774-777.

31. Sone, Y.; Ekdunge, P.; Simonsson, D., Proton Conductivity of Nafion 117 as Measured by a Four-Electrode AC Impedance Method. *J. Electrochem. Soc.* **1996,** *143* (4), 1254-1259.

32. Rieke, P. C.; Vanderborgh, N. E., Temperature dependence of water content and proton conductivity in polyperfluorosulfonic acid membranes. *Journal of membrane science* **1987,** *32* (2-3), 313-328.

33. Hansen, M. R.; Graf, R.; Spiess, H. W., Solid-State NMR in Macromolecular Systems:
Insights on How Molecular Entities Move. *Acc. Chem. Res.* **2013,** *46* (9), 1996-2007.

34. Hansen, M. R.; Graf, R.; Spiess, H. W., Interplay of Structure and Dynamics in Functional Macromolecular and Supramolecular Systems As Revealed by Magnetic Resonance Spectroscopy. *Chem. Rev.* **2016,** *116* (3), 1272-308.

35. Rapp, A.; Schnell, I.; Sebastiani, D.; Brown, S. P.; Percec, V.; Spiess, H. W., Supramolecular assembly of dendritic polymers elucidated by 1H and 13C solid-state MAS NMR spectroscopy. *J. Am. Chem. Soc.* **2003,** *125* (43), 13284-13297.

36. National Center for Biotechnology Information. PubChem Compound Database;CID=9639,https://pubchem.ncbi.nlm.nih.gov/compound/Perfluorohexane#section=Top. (accessed Novermber 27, 2015).

37. National Center for Biotechnology Information. PubChem Compound Database;CID=85958,https://pubchem.ncbi.nlm.nih.gov/compound/85958#section=Top. (accessed Novermber 27, 2015).

5.

Local Dynamics of PFSA Materials: A ^{19}F Solid-State NMR Method

Part 1

5.1 Introduction

This chapter focuses on the extensive application of the double quantum (DQ) NMR technique in an investigation of the local dynamics in a number of PFSA materials. As introduced previously in **Chapters 1** and **3**, PFSA materials are considered among the most promising ion conductors for proton exchange membrane fuel cell (PEMFC) systems. Three types of PFSA materials with various equivalent weights (EWs) were studied here using the advanced DQ NMR technique, with emphasis on the alternative PFSA materials, Aquivion and 3M PFSAs. Nafion is briefly mentioned at the beginning of this chapter as a reference point. The dynamic order parameter applied to the Nafion system introduced in the previous chapter has been applied to the study presented in the first part of this chapter. To comprehend the differences in performance, an

understanding of the morphology development at a molecular level is essential for improving electrolyte materials and hydrogen fuel cell designs.

This work was written as preparation for a future manuscript submission. This manuscript is planned to be submitted to *Canadian Journal of Chemistry* by the end of 2018. All the materials preparation and treatment were done at McMaster University. PFSA membrane samples were obtained from our industrial collaborators, the Solvey and 3M companies. The NMR pulse sequence used throughout this chapter was modified and optimized with the help from Prof. Darren Brouwer (co-author). All ssNMR experiments were performed at the NMR facility at McMaster University and analyzed under the supervision of Prof. Gillian Goward. The current author, Z. B. Yan, wrote the initial drafts of the manuscript.

PFSA material is the preferred proton conducting membrane material in current PEMFCs. PFSA consists of a polytetrafluoroethylene (PTFE) backbone and perfluorinated vinyl ether side chains terminated with sulfonic acid groups. Morphology evolution, which involves the micro-phase separation between hydrophobic and hydrophilic domains introduced by the side chains and backbones upon hydration, facilitates proton transport during fuel cell operation.[1-3] Nafion is commercialized as a benchmark PFSA membrane in PEMFCs, which is a long-side-chain (LSC) PFSA material that has two ether groups. Short-side-chain (SSC) analogues with only one ether group, such as Aquivion, are considered to be promising alternatives to Nafion, and have been heavily investigated due to their relatively low cost (due to a simpler fluorine chemistry) and high ion exchange capacity, etc.[2] Another modification to the PFSA side chain is the new design introduced by 3M which is similar to the typical

SSC-PFSA.[4] These three different categories of PFSA materials shown in **Chapter 1** are used in the current study.

The reason behind the alteration in the side chain of PFSA is that the hydroxyl radicals generated from fuel cell operation mainly attack the ether bond(s) due to its relatively high electrophilicity[5]. The resulting breakdown of the PFSA side chain reduces the amount of hydrophilic domains, which leads to a reduction of fuel cell efficiency. The two alternative materials, Aquivion and 3M PFSAs, have been investigated due to their lower cost and high ion exchange capacity. The role of local dynamics of polymer chains in material morphology development still remains not well understood. Probing the local dynamics of the domains of the PFSAs becomes valuable in interpreting ionomer performance within fuel cells.

With the advantageous ^{19}F spectral resolution and detailed assignment, an advanced ^{19}F dipolar recoupling NMR technique has been developed and demonstrated on Nafion itself, by utilizing the site-specific homonuclear dipolar interaction to probe local dynamics.[6] For a fully fluorinated system like PFSA, probing ^{19}F-^{19}F dipolar interaction allows us to understand the physicochemical properties from the polymer aspect. The recent development of a ^{19}F double-quantum filter (DQF) NMR method provides an efficient alternative approach to probe the polymer dynamics for materials that require site resolution from magic angle spinning (MAS).[6] A standardized measurement was introduced and demonstrated to quantitatively compare PFSA materials with similar structures. We have illustrated the different local dynamics profiles of Nafion side chain and backbone using the ^{19}F DQ NMR method and the application of a dynamic order parameter.

The current study is an expansion of our previous work. Here we apply the local dynamics approach *via* ^{19}F DQ NMR technique to different types of PFSA membranes. All of the materials have the same base structure including the hydrophobic PTFE backbone and hydrophilic sulfonic acid side chain. The standardized measurements are used here to compare this class of materials.

5.2 Experimental

5.2.1 Activation of PFSA Membranes

Pristine Nafion 117 was purchased from MilliporeSigma. Aquivion PFSA membranes were obtained from Solvay, Italy. 3M PFSA membranes were obtained from 3M, St. Paul, MN. All the PFSA membranes were washed in 3 wt% H_2O_2 for 1h at 90 °C and then rinsed with deionized water for another hour, while refreshing the water every 15 min. They were washed with 0.5 M H_2SO_4 solution for 1 h at 90 °C subsequently, following by a deionized water wash until a constant pH of the solution was reached. Finally, the materials were dried in a vacuum oven at 80 °C for 24 h. The membrane samples with their corresponding chemical compositions are summarized in **Table 5.1.**

Table 5. 1 Summary of PFSA membranes materials used in this study, including their chemical compositions, and EWs. EW = 100× mass of PFSA per side chain. It is the unit molecular weight per sulfonic acid group.

Membrane	EW[a] (g/mol/acid)	m	Formula
Nafion 117	1100	6.5	$C_{20}F_{39}SO_5H$
Aquivion 98	980	7	$C_{18}F_{35}SO_4H$
Aquivion 87	870	6	$C_{16}F_{31}SO_4H$
3M 825	825	4.5	$C_{13}F_{25}SO_4H$
3M 725	725	3.5	$C_{15}F_{29}SO_4H$

5.2.2 Relative Humidity Regulation for Membranes

The relative humidity (%RH) conditions of the samples were controlled by using a Dongguan Lixian Scientific HZ2006 environmental test chamber. The humidity range used in the study was 50%-100%. Each condition was set up with constant mode at 25 °C to reach the desired humidity condition. The PFSA membranes were pre-cut into small pieces and packed into the working zirconia rotor uncapped. The packed rotor and Vespel cap were then placed into the test chamber to let it equilibrate for 2 hours. The rotor was then sealed with the cap before being taken out of the chamber for NMR analysis. The membrane samples were considered sealed at constant hydration level after the equilibration at set humidity.

5.2.3 ^{19}F NMR Spectroscopy

ssNMR experiments were conducted on a Bruker Widebore 300 MHz Avance III system using a 4 mm double resonance probe. All ^{19}F MAS NMR experiments with 15 kHz rotor spinning speed were performed using a 97.5 kHz radiofrequency field after DQ efficiency optimization. The ^{19}F chemical shift was referenced to $CFCl_3$ at 0 ppm. The NMR experimental temperatures have been calibrated using samarium stannate.[7-8] The interleaved two-dimensional (2D) ^{19}F DQ recoupling experiments were carried out with 16 scans and 12 slices in the indirect dimension. The pulse sequence was explained in **Chapter 2** and the full version of the sequence is stated in **Appendix 3.**

5.3 Results and Discussion

5.3.1 NMR Spectral Resolution

The structure and ^{19}F NMR spectrum of Nafion has been extensively reported in previous studies.[5-6, 9] It consists of a PTFE backbone, which is represented by the strongest signal at -122 ppm in the ^{19}F NMR spectrum. The signal at -138 ppm corresponds to the backbone CF(b) group. The side chain CF(s) group is shown at -144 ppm. The other side chain fluorine atoms are assigned as SCF_2 at -117 ppm, and CF_3 and OCF_2 overlapped at -80 ppm. The spectral deconvolution of Nafion was based on the linewidth analysis and chemical shift assignment published by Chen et al.[11], and the detailed assignments are illustrated in **Figure 5.1.** The ^{19}F spectrum was collected at 368 K and 100 %RH, so that the SCF_2 signal is well resolved from the backbone signals at -122 ppm, which provides reliable site-specific analysis.

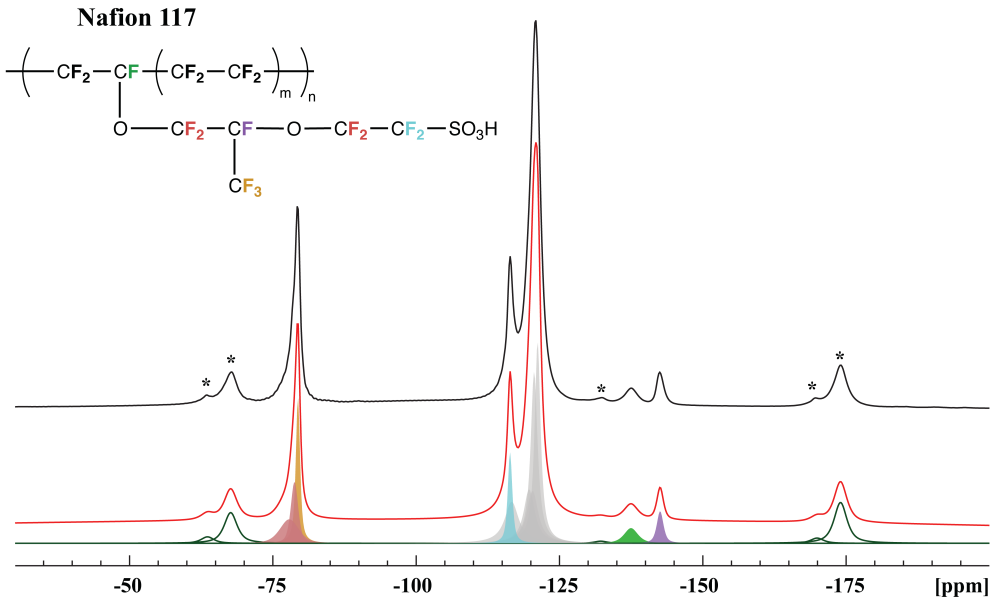

Figure 5. 1 ^{19}F MAS ssNMR spectrum of Nafion with deconvolution. Different fluorine sites are resolved and colour-coded based on the chemical structure. Asterisks represent the spinning side bands.

Similar to our previous Nafion study, ^{19}F MAS spectra for Aquivion and 3M PFSAs have undergone spectral deconvolution. The detailed chemical shift assignments of Aquivion PFSA (Aquivion 98 as an example) are demonstrated in **Figure 5.2a.** Fortunately, the side chain signals are well separated from the backbone signals. The CF_2 backbone is represented at -122 ppm, the CF branching point located on the backbone is at -138 ppm. The OCF_2 is at -78 ppm, while the SCF_2 is next to the backbone CF_2 at -117 ppm.

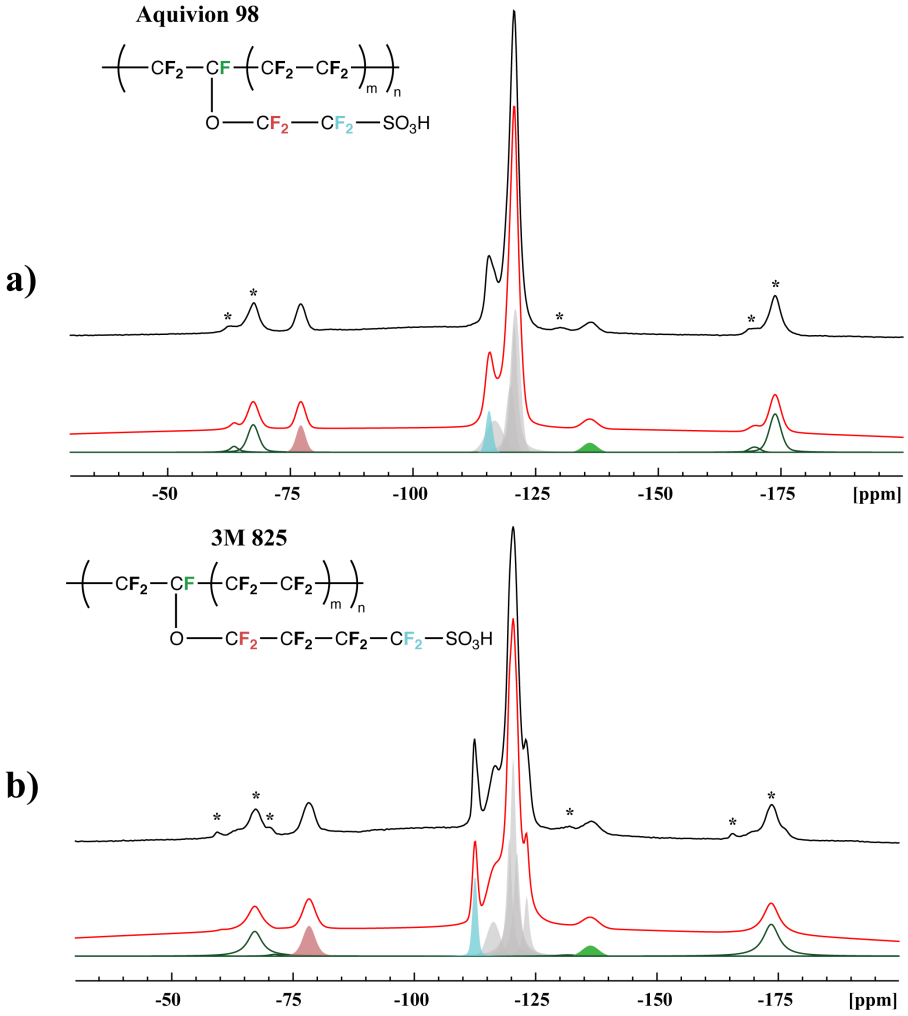

Figure 5. 2 ^{19}F MAS ssNMR spectra with deconvolution: a) Aquivion (Aquivion 98 as an example); b) 3M (3M 825 as an example). Different fluorine sites are resolved and colour-coded based on the chemical structure. Asterisks represent the spinning side bands.

The same chemical shift assignments were made for the 3M PFSA materials (3M 825 as an example) shown in **Figure 5.2b.** Similar to **Figure 5.1**, the backbone CF_2 is at -122 ppm and CF branching point is at -139 ppm; interestingly, the SCF_2 at -114 ppm is much further away from the backbone CF_2 signal. This is possibly caused by the difference in magnetic field that the fluorine nuclei experience, which is referred as chemical shielding and is explained in **Chapter 2.** Similar to the chemical shielding effect observed in solution systems[10], the SCF_2 in the 3M PFSA is a couple of C-C bonds away from the backbone structure, where the heavily fluorinated system (electronegative) does not affect the fluorine nuclei of the SCF_2 in 3M PFSA as much as the effect on SCF_2 in Aquivion PFSA. The two shoulder peaks in **Figure 5.2b** are persistent in variable temperature (VT) experiments with observable line narrowing but no coalescence (see **Figure 5.3a**). From the previous ^{19}F MAS NMR linewidth analysis of Nafion, the line broadening of the fluorine sites close to the branching point is observed and attributed to 'sequence effects'.[9] Chen et al. discussed this phenomenon as the observed spectral features like the line broadening near the branching point were attributed to the proximity of another branch point to the one observed[11], i.e. how far away the observed site was from the branch points. The fluorine sites that are near the branching point have increased linewidth. Based on the more detailed chemical structure of 3M 825 PFSA in **Figure 5.3b**, the shoulder peak at -116 ppm is assigned as the side chain CF_2 groups (shaded in blue), while the other peak that is much narrower at -123 ppm is attributed to the CF_2 group that is furthest from the branching point (shaded in green). The SCF_2 is well separated from the forest of backbone fluorine signals. Therefore, the analysis in side chain local mobility will not be affected. A correct

fluorine signal assignment is important for the backbone local dynamics analysis, yet future carbon-fluorine correlation studies are necessary to confirm the proposed fluorine signal assignments.

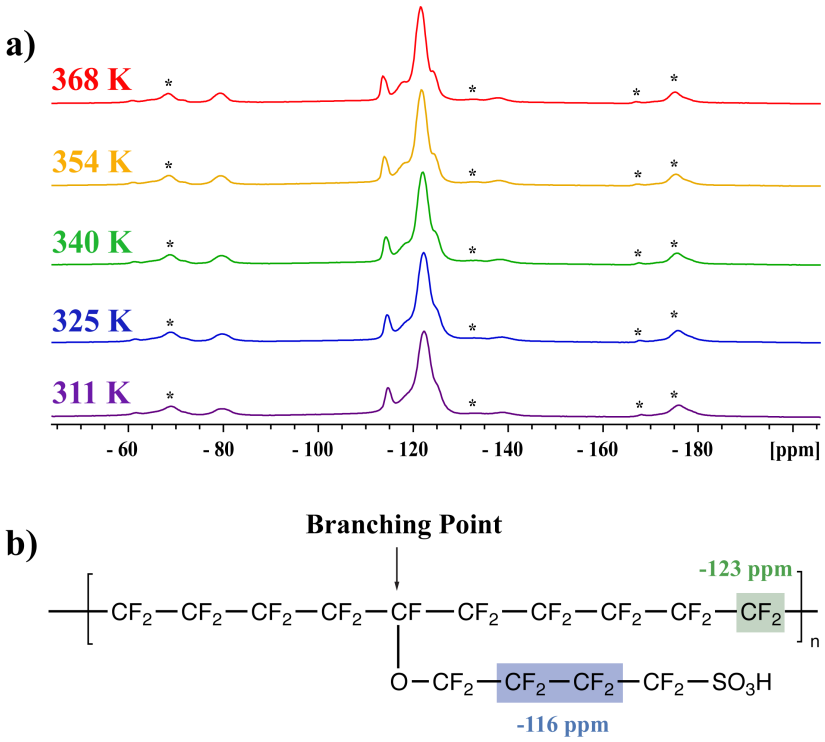

Figure 5. 3 a) Stack plot of ^{19}F VT NMR spectra of 3M 825 PFSA. b) Detailed chemical structure of 3M 825 PFSA, with more specific fluorine site assignments: peak at -116 ppm is the side chain CF_2 in blue, while the one at -123 ppm is the backbone CF_2 group located the furthest from the branching point in green.

5.3.2 Local Dynamics Analysis

As demonstrated in our previous study, the interleaved 2D NMR experiment collects a 'reference' spectrum (*REF*) and a 'double quantum' spectrum (*DQ*) at the same dipolar recoupling time τ_{DQ}.[6] With this setup, the normalization of DQ build-up curves can be accomplished, which is essential since it compensates for relaxation effects and imperfect pulses during NMR experiments. This concept was introduced and developed for ^{1}H DQ approaches for hydrocarbon polymers.[12-14] The

normalized double quantum (*nDQ*) build-up curve was simply calculated from $nDQ=DQ/\Sigma MQ$, and $\Sigma MQ=DQ+REF$.[6, 12-14] For example, the *nDQ*, build-up curves of Nafion 117 are extrapolated as a function of τ_{DQ} shown in **Figure 5.4**, where the backbone peak at -122 ppm and side chain signal at -80 ppm are indicated and compared.

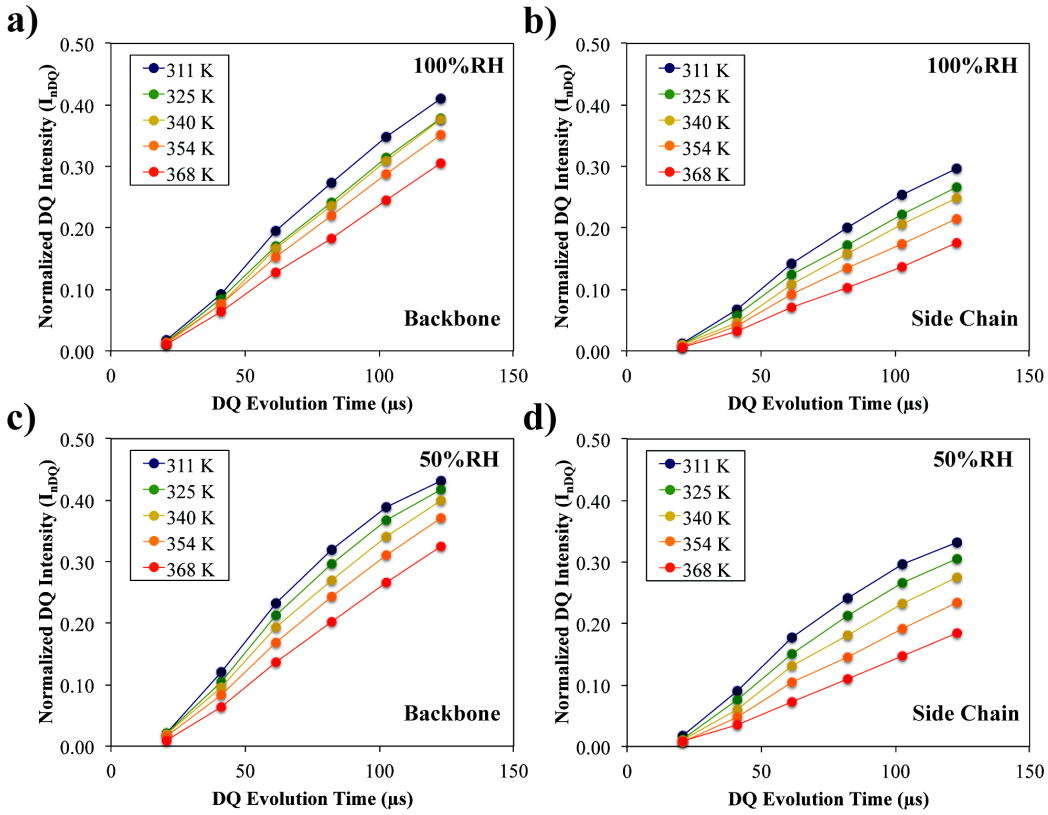

Figure 5. 4 The *nDQ* build-up curves of Nafion (normalized DQ intensities against dipolar coupling time): a) backbone and b) side chain fluorines treated at 100 %RH at the temperature range 310 – 370 K. The parallel analyses of backbone and side chain fluorines of Nafion 117 treated at 50 %RH are demonstrated in c) and d). The data sets were coloured with corresponding temperatures.

The initial rise of the *nDQ* curve is indicative of the effective dipolar interaction, which is shown to be sensitive towards temperature elevation, especially in the case of the side chain profiles. The apparent dipolar coupling constant, D^{T}_{app}, can be extracted from a Gaussian-type of approximation that was proposed by Saalwächter et al.[14],

and this approach was applied to our previous study on Nafion 117.[6] Furthermore, the application of a dynamic order parameter was used for PFSA materials for the first time, where the experimental D^{T}_{app} was compared to a theoretical value D^{0}_{app} calculated from a rigid model. The differences in local dynamics between the Nafion side chain and backbone under the influences of temperature and humidity were successfully established. This implementation provides a metric for local dynamics study to compare different types of PFSAs.[6]

Similar plots of *nDQ* curves of other PFSA samples were obtained for the current analysis, and the D^{T}_{app} values were determined from fitting the initial rise of the *nDQ* build-up curves using the Gaussian-type approximation. The D^{T}_{app} values of spectroscopically resolved fluorine sites for the PFSA samples tested are summarized in the **Table 5.2.** They are illustrated in **Figure 5.5,** where the D^{T}_{app} values are plotted against the experimental temperature under two hydration conditions: 50 %RH and 100 %RH. All the fluorine sites show different degrees of temperature dependence, which is thought to be caused by the segmental motions associated with β-relaxation of the polymer chains. Most importantly, the side chain SCF_2 (the blue diamond data points) in all PFSA cases has the lowest D^{T}_{app} value compared to the backbone signals, which is indicative of higher local motion as we have observed in Nafion 117.[6] The backbone is more constrained with regards to local motion, whereas the side chain possesses higher local dynamics. Because of the similarity in chemical structure and predicted morphology evolution, the SCF_2 is demonstrated to be more responsive towards the hydration compared to the PFSA backbone in all of the PFSA materials, as expected.

Table 5. 2 The summary of D^{T}_{app} values of spectroscopically resolved fluorine sites for the Aquivion and 3M PFSA samples.

Aquivion 98	50 %RH				100 %RH			
	D^{T}_{app} (kHz)				D^{T}_{app} (kHz)			
T (K)	OCF_2	SCF_2	CF_2	CF	OCF_2	SCF_2	CF_2	CF
311	8.55	6.77	7.27	17.89	7.65	5.05	6.62	10.57
325	8.40	6.97	7.15	18.99	7.42	5.38	6.44	8.85
340	8.70	6.66	7.08	15.23	7.31	4.99	6.32	9.56
354	8.23	6.48	6.67	13.87	7.17	4.36	6.24	9.65
368	7.74	6.37	6.20	8.88	6.94	4.48	6.16	8.88
Aquivion 87	**50 %RH**				**100 %RH**			
	D^{T}_{app} (kHz)				D^{T}_{app} (kHz)			
T (K)	OCF_2	SCF_2	CF_2	CF	OCF_2	SCF_2	CF_2	CF
311	7.81	3.27	7.15	9.15	7.19	3.44	6.16	8.80
325	7.56	4.13	6.77	8.81	6.92	3.91	6.05	7.70
340	7.26	3.67	6.55	8.01	6.60	3.14	5.89	7.57
354	7.18	3.56	6.49	8.79	6.73	3.79	5.76	7.04
368	6.99	3.95	6.36	8.16	6.55	3.06	5.81	7.47
3M 825	**50 %RH**				**100 %RH**			
	D^{T}_{app} (kHz)				D^{T}_{app} (kHz)			
T (K)	OCF_2	SCF_2	CF_2	CF	OCF_2	SCF_2	CF_2	CF
311	9.18	4.29	7.85	10.62	10.76	5.26	8.57	12.86
325	8.77	4.28	7.62	10.73	9.62	5.37	7.36	11.39
340	8.29	3.88	7.24	9.55	9.27	4.13	7.59	9.90
354	7.74	3.21	6.78	8.73	8.36	3.75	6.85	9.59
368	6.77	2.93	6.04	7.18	7.53	3.57	6.40	7.98
3M 725	**50 %RH**				**100 %RH**			
	D^{T}_{app} (kHz)				D^{T}_{app} (kHz)			
T (K)	OCF_2	SCF_2	CF_2	CF	OCF_2	SCF_2	CF_2	CF
311	7.43	4.24	6.89	11.32	7.04	3.61	6.11	9.65
325	7.17	4.21	6.56	10.07	6.78	3.47	5.91	8.30
340	7.05	3.90	6.43	9.10	6.49	3.37	5.60	8.41
354	7.04	3.76	6.25	8.15	6.40	3.30	5.64	8.50
368	6.49	3.92	5.90	9.82	6.21	3.47	5.48	8.43

This difference in response between backbone and side chain is shown in **5.5b, d, f,** and **h,** where the D^{T}_{app} (SCF_2) are reduced compared to the parallel analysis under 50 %RH in **5.5a, d, e,** and **g.** This observation agrees with what was seen in Nafion which is the benchmark

material in our previous study.[6] The polymer undergoes phase-separation where the hydrophilic side chains form ionic domains when hydration is introduced, thus indicating that the local motion is promoted by hydration, which is similar to Nafion in previous studies.[15-19] A gradient of local dynamics along the polymer chain is also illustrated in **Figure 5.5.** The OCF_2 has lower D^T_{app} value compared to CF_2, which shows higher local mobility. The local dynamic parameters, D^T_{app}, of these two fluorine sites in both Aquivion and 3M PFSAs are valued between the backbone branching point CF and the side chain SCF_2 that is adjacent to the terminal SO_3H. This further confirms that the PFSA polymer molecule undergoes morphology development due to a difference in hydrophilicity. The comparison of two hydration levels of 3M 825 is noticeably different compared to the other PFSA samples, where the 50 %RH has slightly lower D^T_{app} values compared to 100 %RH, and the difference in values is not significantly large; thus it is possible that the conditions investigated here are not distinct enough for this PFSA to have notable local dynamics difference.

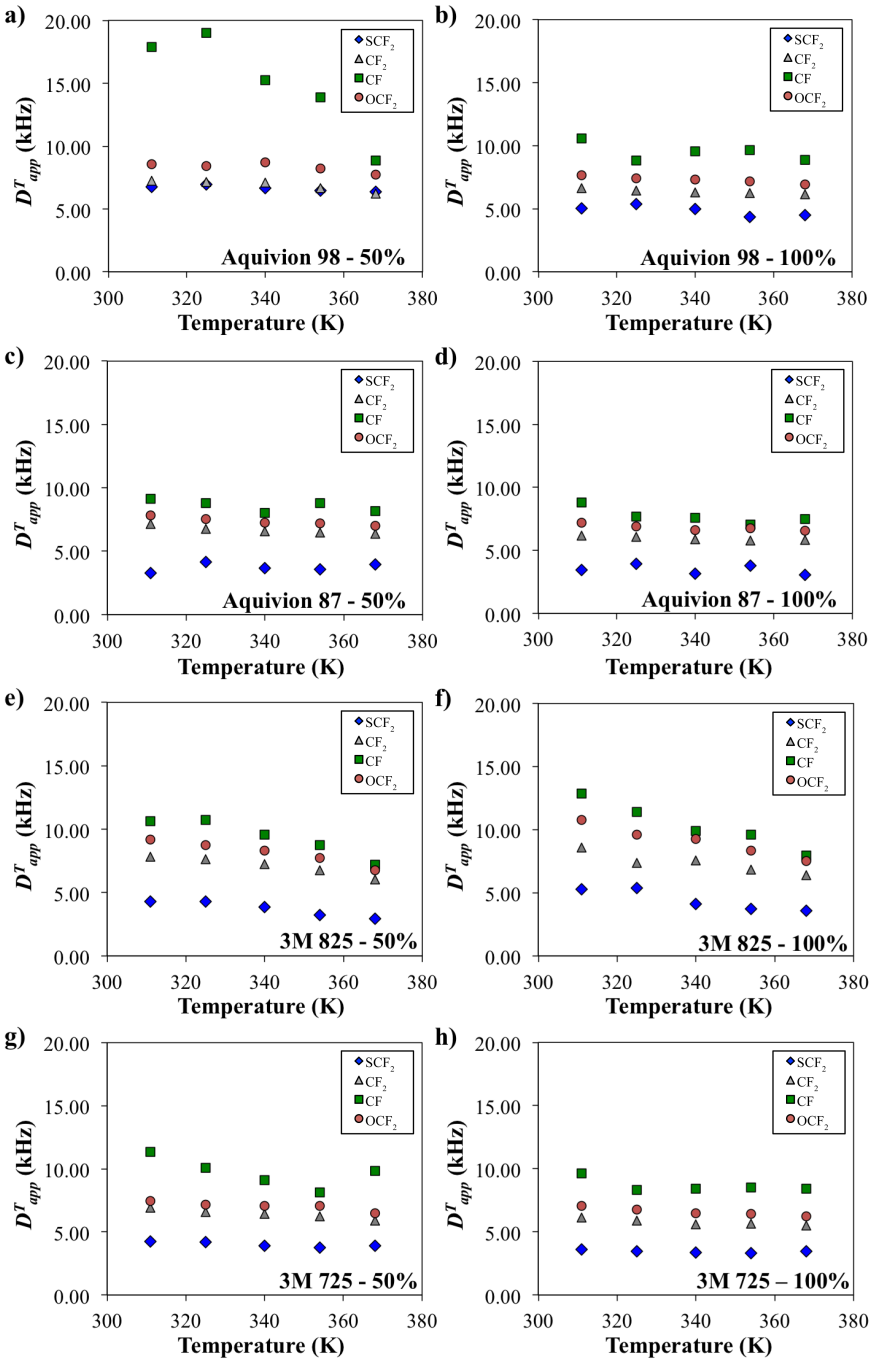

Figure 5. 5 D^T_{app} value comparisons of different fluorine sites of Aquivion and 3M PFSAs treated at 50 %RH (a, c, e, g) and 100 %RH (b, d, f, h). SCF_2- blue diamond points; CF_2- grey triangle points; CF- green square points; OCF_2- coral round points. Each pair of graphs represent one PFSA: Aquivion 98: a, b; Aquivion 87: c, d; 3M 825: e, f; 3M 725: g, h.

Among the four PFSA comparisons, the last three pairs show only a marginal difference in local motion, while the first pair shows a much more significant difference in D^{T}_{app}. The later three PFSAs do all have much lower EW (<900) compared to Aquivion 98 (close to 1000 EW). The difference in local dynamics responses towards hydration could be related to the morphology development in the polymer matrix. The low EW could correlate to the insignificant dynamics evolution observed in Aquivion 87 and the 3M PFSAs. At low EW, the hydrophilic side chains are highly concentrated per polymer chain, which can form ionic domains more recurrently. As a result, the local dynamics have already become greater compared to PFSA with high EW at the same condition (for example 50 %RH here). At the treatment condition in this study, changing 50 %RH to 100 %RH at 25 °C does not bring a dynamics difference large enough to become distinguishable, which is suggested by the three comparisons of Aquivion 87, 3M 725 and 825 in **Figure 5.5.** Nevertheless, further investigation of PFSAs with a large range of EWs will be helpful to validate this explanation.

The introduction of a dynamic order parameter potentially provides a standardized metric to compare PFSAs. In order to apply this comparative measure, structures without molecular motion are necessary for the calculations. To obtain the reference state for the rigid model of different PFSAs, the geometry-optimized molecular structure of perfluorohexane C_6F_{14} was used as the model of PSFA backbones, as performed previously for Nafion.[6] The side chains are modeled based on the geometry-optimized structures of perfluoro-3-oxa-4-pentene-1-sulfonal fluoride ($C_4F_8O_3S$, liquid at room temperature) for Aquivion PFSA and perfluoro-3-oxa-4-heptene-1-sulfonal fluoride ($C_6F_{12}O_3S$, liquid at room temperature) for 3M PFSA. The two side chain structural models are

shown in **Figure 5.6.** The ^{19}F-^{19}F interactions considered in the calculation of D^0_{app} include all the intramolecular distances within 5 Å, which is done by taking the root-sum-square of the dipolar coupling constants to each of its nearby proximity.[6, 13, 20] The calculated D^0_{app} values are tabulated in **Table 5.3** based on the simplified models shown in **Figure 5.6.**

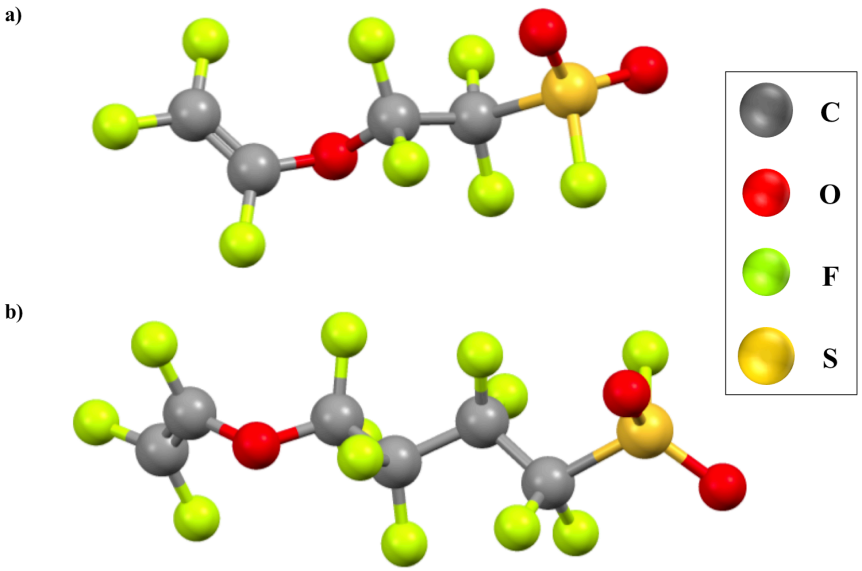

Figure 5. 6 Structures of $C_4F_8O_3S$ (a) and $C_6F_{12}O_3S$ (b) are used in the D^0_{app} calculations for Aquivion and 3M PFSAs.

Table 5. 3 D^0_{app} values for all the fluorine sites in Aquivion and 3M PFSAs calculated based on the simplified models shown in **Figure 5.6.**

D^0_{app} (kHz)	OCF_2	SCF_2	CF_2	CF
Aquivion 980/870	11.86	11.51	16.06	12.37
3M 725/825	13.68	13.36	16.06	12.37

The dynamic order parameters S^T are calculated and compared for all PFSAs; however, here we demonstrate only the comparison between backbone CF and side chain SCF_2, i.e. the extreme cases of local dynamics, for simplification purposes. In **Figure 5.7**, the open circles

represent values at high hydration and solid grey triangles represent values at low hydration. Generally, the order parameter values are lower at higher hydration levels, which is attributed to the higher local motion induced by higher humidity. The S^T values are greater than 1 in some cases shown in **Figure 5.7**, which is caused by the fact that the theoretical values for D^0_{app} used here based on the simplified rigid models are underestimated due to the lack of the consideration of intermolecular interactions of the polymer stacking.

One interesting observation is that among the PFSAs there is a notable difference in response to temperature elevation; for Aquivion 98 the data points for two hydration conditions are more distinguishable (**5.7a, b**) compared to the other PFSAs. The separation between the two hydration levels is similar to what was observed in Nafion 117 under the same conditions. Aquivion 98 is the closest to Nafion 117 in terms of EW, 980 vs. 1100; therefore, the hydrophobic segmentations (backbone chain repeating unit) per sulfonic acid group are very similar. On the other hand, the other PFSAs have much lower EWs, which results in more frequent appearance of the hydrophilic side chain with sulfonic acid groups along the polymer structure. The ionic cluster formation could occur more randomly in PFSAs with a low EW, which is reflected by indistinguishable side chain local motions at elevated hydration levels in **Figure 5.7.** The analysis of local dynamics in the form of an order parameter provides a standardized metric to compare different PFSAs.

Future systematic studies of PFSA ionomers with one type of side chain structure and different EWs will reveal the role of EW plays in PFSA morphology development. By doing so, the factor of side chain type can be eliminated.

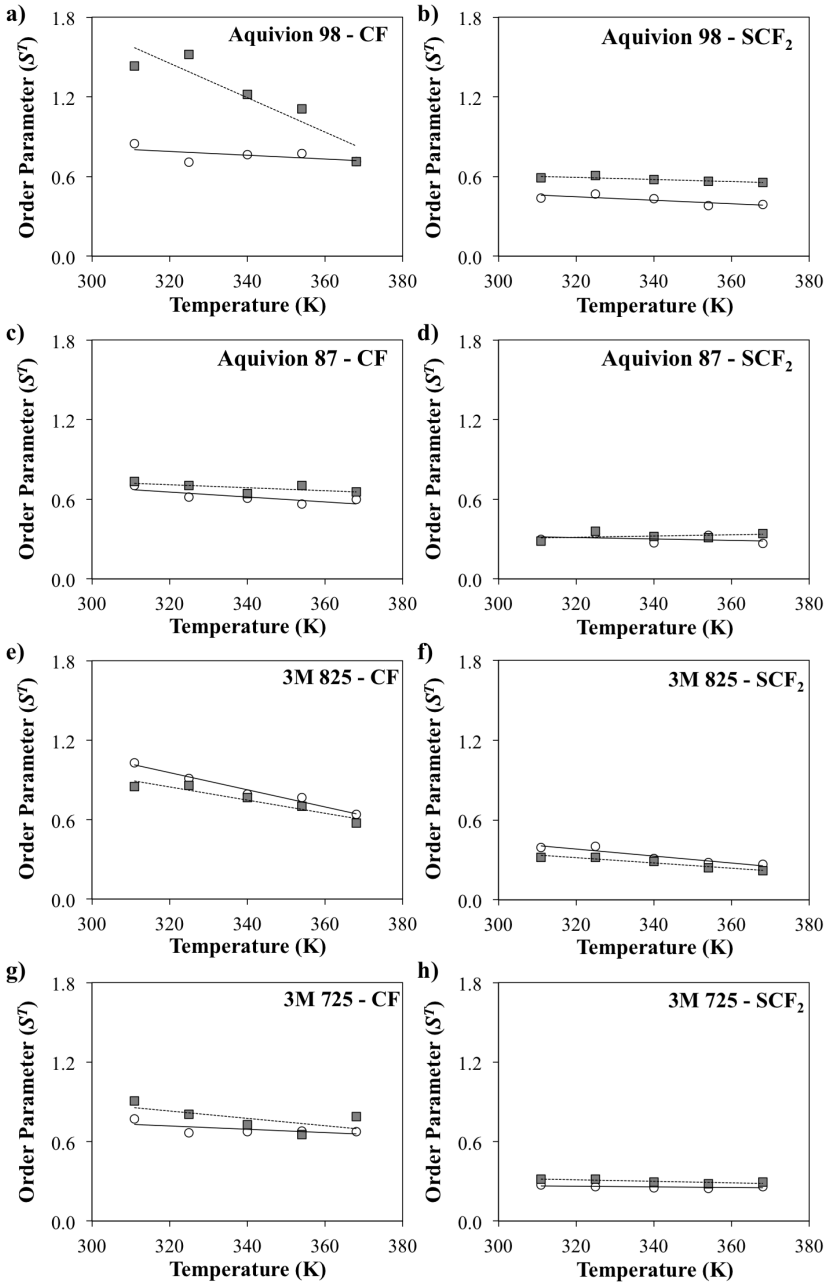

Figure 5. 7 Dynamic order parameter analyses for CF and SCF_2 for Aquivion and 3M PFSAs. Each pair of graphs represent one PFSA: Aquivion 98: a, b; Aquivion 87: c, d; 3M 825: e, f; 3M 725: g, h. The grey squares represent the values extracted for 50 %RH, while the white circles demonstrate the values at 100 %RH.

5.4 Summary

In this study, we demonstrate the application of the ^{19}F-^{19}F DQ ssNMR method to probe the local dynamics of PFSA materials under different degrees of humidification. A meticulous spectral deconvolution for different types of PFSAs provides a great handle for site-specific analysis. The local dynamics parameter, D^T_{app}, was extracted from fitting the initial rise of the *nDQ* build-up curve. Distinct fluorine sites from Aquivion and 3M PFSAs were examined and analyzed, which was then compared to the benchmark Nafion local dynamics profiles. With different degrees of hydration, the polymer side chain has increased local dynamics upon hydration, which is reflected in the much weaker effective dipolar interaction. Additionally, the side chain of PFSA with low EW is shown to be less responsive towards hydration changes compared to PFSA with high EW (Aquivion 98 and Nafion 117). The application of the dynamic order parameter, S^T, is displayed in PFSA comparisons. Due to the lack of a crystal structure for PFSAs, the rigid models used in this study have been shown to underestimate the strength of dipolar interaction; therefore, the usage of S^T seems undervalued. Nevertheless, S^T analysis provides a normalized approach to investigate the local dynamics difference between the hydrophobic and hydrophilic domains for related perfluoro polymers below the glass transition temperature. Our method demonstrates a quantitative and qualitative method to understand the morphology development in ionomer materials.

Part 2

5.5 Introduction

The second part of this chapter has extensive attention on the temperature and relative humidity conditions for all the PFSA materials. In this work, all three types of PFSA materials including Nafion, Aquivion and 3M PFSAs were evaluated using the aforementioned ssNMR method to probe the local dynamics. More importantly, the samples were also evaluated as electrolytes by electrochemical performance analyses. The current study has the purpose of linking the material performance to the fundamental material chemistry.

This work was adapted from the work that has been published by *Physical Chemistry Chemical Physics*, in June 2018 (Z. B. Yan, A. P. Young, G. R. Goward. **2018**, *20*, 19098-19109). All the material preparation and treatment work for the NMR studies were done at McMaster University. The ssNMR experiments were performed at the NMR facility at McMaster University, and analyzed under the supervision of Prof. Gillian Goward. The electrochemical performance analyses were done at Ballard Power Systems (BPS) in Burnaby, BC through two separate industrial internships. The test results were evaluated and reviewed under the supervision of Alan P. Young (co-author). The initial drafts of the manuscript were written by the current author Z. B. Yan.

Understanding the structure-property-performance relationship is essential to the development and improvement of fuel cell devices. The combination of *in situ* fuel cell performance diagnosis and *ex situ* single-component characterization is used here to bridge the fundamental

chemistry aspect with the bulk material properties. Among many operating issues, polymer electrolyte degradation and fuel loss that occurs during operation are challenges for fuel cell (FC) commercialization in automotive applications.[5, 21-24] Understanding the impact of the electrolyte materials on proton transport properties will help overcome the current design challenges, such as excessive Ohmic losses that arise at high current density due to resistive proton transport. Additionally, reducing the gas permeability of hydrogen through the membrane will improve fuel efficiency.

PFSA polymers have been intensively employed as electrolyte membranes because of their high stability and high proton conductivity. Minimizing the membrane thickness has become common practice to steer away from the performance loss caused by membrane resistance. However, one main drawback of this approach of thinning the PFSA membrane is the resulting poor mechanical durability,[25-26] which can be often solved by reinforcement during manufacturing.[26-32] Another major drawback is the increased fuel crossover caused by use of the thin membranes. Fuel crossover describes the hydrogen gas passing through the polymer membrane electrolyte from the anode to the cathode, during fuel cell operation. This phenomenon induces the reduction of the open circuit potential, and wastes fuel. The crossed-over H_2 will react with the O_2 directly on the cathode side without capture of the electrochemical energy thus 'de-polarizing' the cathode resulting in low cell efficiency. Moreover, the undesired redox reaction causes localized heating of the membrane, which leads to induced thermal degradation.[24] An increased possibility of peroxide radical formation due to fuel crossover has also been observed.[22, 32] As a result of the presence of the peroxide radical, the polymer chains, mainly the side chain, are

attacked and degraded by cleaving. This induced membrane degradation will eventually evolve pinholes in PFSA, which directly results in cell failure. This process has been investigated experimentally from many perspectives.[5, 22-23, 32]

Many methods have been developed to probe the gas permeability, especially focusing on H_2, of PFSA membranes, to tackle the fuel loss issue. The time-lag technique has been used by monitoring the pressure change as a function of time based on the establishment of the steady-state condition.[33-35] Analytical techniques, such as gas chromatography, have been applied in the permeability studies of PFSA membranes.[33] Furthermore, mass spectrometry has also been applied in the analysis of gas species.[36-37] More commonly, electrochemical analysis including linear sweep voltammetry and cyclic voltammetry (CV) has been widely used in *in situ* fuel cell performance investigation.[38] This method is intuitive and straightforward, as it deciphers the fuel crossover/H_2 permeability from the electrochemical measurements. Gas permeability is typically correlated with humidity and temperature, and many gas transport mechanisms have been proposed.[39-40] Permeability has been proven to correlate to the micro-phase separation and water channel formation within the polymer.[24, 26, 33, 39-41] To link the bulk material performance with the microscopic physicochemical properties, advanced NMR spectroscopy is applied here in the analysis of PFSA dynamics. Recent work done on Nafion 117 using ^{19}F ssNMR has demonstrated a unique and efficient approach in differentiating local dynamics of the polymer by targeting the polymer directly. The side chain has been illustrated to have higher local motion compared to the backbone (main chain), which is demonstrated by a low apparent dipolar coupling constant value.

The current study has the purpose of linking the bulk H_2 permeability and proton conductivity to the fundamental material chemistry. Three different types of PFSA materials with different EWs have been carefully investigated, through *in situ* electrochemical analyses and *ex situ* ssNMR measurements. The H_2 permeability and the side chain local dynamics in PFSA membranes have been coupled. This is the first time that PFSA polymer local dynamics probed directly *via* ^{19}F ssNMR are associated to the conductivity performance and H_2 permeability of the membrane electrode assemblies (MEAs) under the same conditions. Thereby, the correlations are established at the molecular level, with the goal of understanding the proton transport and gas permeation mechanisms.

5.6 Methods

5.6.1 Electrochemical Analysis

5.6.1.1 Membrane Electrode Assembly (MEA) Preparation: A Single Cell Assembly

The catalyst ink (provided by BPS) was coated onto a transfer film and hot pressed onto both sides of the PFSA membranes (listed in **Table 5.1** except replacing Nafion 117 with NR211) through a bonding process at 150 °C at 3 atm for 3 minutes. The fully catalyst-coated membrane was then assembled with gas diffusion layers into a single MEA with active area of 45 cm^2. The cathode and anode catalyst loadings (Pt/C) were both 0.1 mg Pt cm^{-2}. In order to extract the electrochemical properties of the PFSA membranes, a double-layered membrane design was applied. By doing so, the electrical resistance component of the high-frequency resistance (HFR) is eliminated and the membrane

resistance can be then isolated. Two sheets of membrane materials were both coated with the catalyst layer on one side, then the two sheets of membranes were bonded together with the non-coated sides facing each other. Prior to the performance analysis at the BPS fuel cell research test station, the MEA was conditioned at 80 °C with 100 %RH under 58.5 A powered for 16 hours with working gases, H_2 and air at 5 psig.

5.6.1.2 Electrochemical Characterizations

CV is commonly used in diagnostics of fuel cell catalyst activity. This *in situ* technique provides a measure of the effective catalyst surface area of the gas diffusion electrodes, as well as H_2 crossover capacity.[26, 38, 42-44] As the potential of the system is linearly cycled between two voltage limits, the current is measured. A plot of the cell current against the potential is called a cyclic voltammogram.[21, 38, 45-46] The driving force for current flow is described by Nernst's equation for half-cell potentials as defined in **Equation 5.1** for the hydrogen oxidation reaction[21, 46]:

$$E = E_0 + \frac{RT}{nF} ln\left(\frac{C_{H_2}^{0.5}}{C_{H^+}}\right) \quad \textbf{(Equation 5.1)}$$

where E_0 is the standard cell potential for this half-cell reaction, R is the gas constant, T is cell temperature, n is the number of electrons transferred in the hydrogen oxidation reaction, F is the Faraday constant. $C_{H_2}^{0.5}$ is the concentration of H_2 gas on the active electrode, and the value of the exponent is determined by the coefficient of the

reaction, C_{H^+} is the concentration of proton produced. The overall $\left(\frac{C_{H_2}^{0.5}}{C_{H^+}}\right)$ is in the form of reaction quotient of the cell reaction.

Hydrogen oxidation from gas permeating through the membrane quickly becomes mass transport limited, as the hydrogen flux through the membrane is slower than the reaction rate. At this point the current plateaus and reaches its limiting current. The gas crossover probed here is not related to the cathode reaction, but simply to the membrane's susceptibility to gas permeation as a function of humidity and temperature.

The flux of reactant is extracted from the limiting current, I [$C\ s^{-1}$] using Faraday's Law (**Equation 5.2**):

$$I = nFJA \quad \textbf{(Equation 5.2)}$$

where n is the number of electrons transferred in the hydrogen oxidation reaction, F [$C\ mol^{-1}$] is the Faraday constant, J [$mol\ s^{-1}m^{-2}$] is the flux of reactant and A [m^2] is the active area. The crossover capacity can be calculated from the H_2 flux, which is described as follows:

$$J = \frac{I}{nFA} \qquad \left(\text{unit calculation: } \frac{[C/s]}{[C/mol][m^2]} = \frac{mol}{s \cdot m^2}\right)$$

$$\Rightarrow P_{H_2} = \frac{J \cdot d_{PFSA}}{p_{H_2}} \qquad \left(\text{unit calculation: } \frac{\left[\frac{mol}{s \cdot m^2}\right][m]}{[Pa]} = \frac{mol}{s \cdot m \cdot Pa}\right)$$

where P_{H_2} is H_2 permeability, p_{H_2} is the H_2 pressure at the preset conditions, d_{PFSA} is the thickness of the PFSA membrane.

The electrochemical impedance spectroscopy (EIS) is a standard diagnostic tool to evaluate material resistance in fuel cell study. EIS employs an AC voltage to the cell with a broad range of frequencies, and

the magnitude and phase of the resulting signals are monitored as a function of frequency. The complex impedance of the electrochemical system can be determined. The transmission line circuit model was used to extract the MEA resistances in the current study, since the Warburg impedance is considered in the fuel cell.[21, 47]

The CV and EIS measurements were performed *in situ*, using Metrohm AutoLab potentiostat (PGSTAT302N) and booster (BOOSTER20A). The CV measurements were collected at 40 °C and 80 °C with a range of %RH from 20% to 100%. The cathode was fed with N_2 at 9 lpm and served as the working electrode. The anode was fed with H_2 at 4.45 lpm, which serves as reference and counter electrode functioning as a dynamic hydrogen electrode (DHE). The CV measurements were conducted with a 10 mV/s scan rate from 0.05 V to 1.00 V. The impedance experiments were collected under 0.45 V with a 0.2 Hz to 80 kHz frequency range.

All the conditions for the measurements were obtained at the test station with gases treated using an in-house vaporizer and heater.

5.6.2 NMR Analysis

5.6.2.1 PFSA Materials and Preparation

Pristine Nafion membrane was purchased from Sigma-Aldrich. The Aquivion and 3M membranes were obtained from the Solvay and 3M companies separately. All of the PFSA materials were washed with 5 wt% H_2O_2 solution at 90 °C for 1 hour and then washed with deionized water for another hour. Membranes were then washed in 0.5 M H_2SO_4 solution for 1 hour, and finally washed with deionized water until a constant pH was obtained, changing the fresh water multiple times. The materials were then dried in a vacuum oven at 80 °C for 24 hours.

The membrane samples were cut into small pieces in order to pack inside a zirconia NMR rotor with 4 mm outer diameter.

5.6.2.2 Relative Humidity and Thermal Control

The %RH conditions were controlled by using Dongguan Lixian Scientific HZ2006 environmental test chamber. The PFSA membrane pieces were packed into the NMR rotor uncapped. The rotor and Vespel cap were then stored inside the desktop humidity chamber to equilibrate for 2 hours. The rotor was then capped before being taken out of the chamber for NMR measurements. The conditions were kept within the same range as the test station conditions for easy comparison.

5.6.2.3 ^{19}F NMR Spectroscopy Dynamics Study

Local dynamics investigation *via* ^{19}F dipolar coupling recoupling NMR has demonstrated a sufficient sensitivity to distinguish different dynamic domains within the fluorinated polymer material.[6] The side chain and backbone signals were carefully deconvoluted and analyzed.[5-6, 9, 11] Local motion of PFSA side chains has been shown by us to be more mobile than the backbone upon elevated temperature and hydration level by comparing the apparent dipolar coupling constant, D_{app}.[6] This dipolar coupling interaction is built on the interactions between two ^{19}F nuclei within proximity, and it is essentially the square root of the sum of all the interactions (**Equation 5.3a, 5.3b**).[13-14, 48] These two equations are restated based on **Equation 2.28, 2.29.**

$$D_{app} = \left(\sum_{k} D_{jk}^{2} \right)^{1/2} \qquad \textbf{(Equation 5.3a)}$$

$$D_{jk} = \frac{\mu_0}{4\pi} \frac{\gamma_j \gamma_k h}{r_{jk}^{3}} \qquad \textbf{(Equation 5.3b)}$$

where μ_0 is the vacuum permeability, γ_j and γ_k are the gyromagnetic ratios of nuclei j and k, r_{jk} is the internuclear distance, and θ the angle between the internuclear vector and the external magnetic field. This D_{app} value can be experimentally extracted based on the Gaussian-type of approximation from fitting the initial rise of the normalized dipolar coupling build-up curve.[6] A dynamics order parameter was introduced to standardize the comparison, from which the difference in local motion between side chain and backbone has been confirmed.[6, 49] The same NMR analytical method has been employed in the current study.

SsNMR experiments were conducted on a Bruker Widebore 300 MHz Avance III system using a 4 mm double resonance probe. All ^{19}F MAS NMR experiments were performed using a 97.5 kHz radio-frequency field with 15 kHz MAS speed. $CFCl_3$ was used to reference the ^{19}F chemical shifts.

Following the normalization procedure described in our previous study, the interleaved 2D ^{19}F DQ recoupling experiments were performed with 16 scans and 16 slices in the indirect dimension. The detailed pulse sequence and normalization process can be referred to **Appendix 3.**

The temperatures used in the variable-temperature measurements, 300 K – 380 K, were calibrated using samarium stannate.[7-8]

This study is a collaboration of the advanced NMR method and fundamental electrochemical analysis, thus the sample conditions for both methods are required to be the same. 40 and 80 °C at 50 %RH and 100 %RH for the main correlation investigation have been chosen since these are the bounds of PEMFC operation. In addition, the lifetime of the MEA samples and the access to the ssNMR instrument have put constraint on the experimental time. However, in the correlation studies presented later, it is sufficient to use the ten data points

resulting from two temperatures with two hydration levels for the five PFSA materials.

5.7 Results and Discussion

Many amphiphilic polymer materials are known to have significant water uptake ability. The water uptake of PFSA membrane has been extensively studied in order to develop a morphological picture of its phase separation under the influence of hydration and temperature.[26, 41, 50] At low hydration levels, the membrane is favored to stay 'dry'; while at high hydration levels, the hydrophilic domains are well connected, which makes the water uptake facile.[26] As the hydrophilic sulfonic acid side chain component facilitates the water uptake, PFSA are well known to have dimensional instability upon hydration. The dimensional stability strongly correlates to the membrane resistance due to the thickness change. The thickness is required to take into account the determination of the gas permeability and ionic conductivity. Here, liquid water swelling tests for all of the PFSA materials used in the MEA production was performed after the acid activation. Thicknesses were measured and tabulated in **Table 5.4.** It is worth mentioning that Nafion NR211 was used in the MEA testing instead of Nafion 117 which was used in NMR study, since the reduced thickness of NR211 was much preferred in MEA preparation. The conductivity and gas permeability measurements of the membranes were normalized by the thickness. The actual membrane thickness during the operation was unknown due to the constraints placed on the MEA by the flow field plate. Using dynamic vapour sorption the water uptake curves can be determined as a function of RH. The inflection at approximately 80%RH signifies the start of

dimensional swelling; therefore, the assumption was made that at and below 80 %RH the membranes retained their dry thicknesses. For 100 %RH, the wet thickness value was used in the calculation.[51]

Table 5. 4 Swelling test: PFSA thickness measurements before and after 80 °C water bath.

Membrane*	EW (g/mol/acid)	Dry Thickness (μm)	Wet Thickness (μm)	% Increase
Nafion (*NR211*)	1100	23 ± 0.1	30 ± 0.7	29
Aquivion 98 (*AQ980*)	980	50 ± 2.0	57 ± 1.0	15
Aquivion 87 (*AQ870*)	870	55 ± 2.4	68 ± 2.7	22
3M 825 (*3M825*)	825	51 ± 1.4	63 ± 0.4	23
3M 725 (*3M725*)	725	55 ± 1.8	70 ± 0.1	28

*The two-letter initial for PFSA type and the 3-digit number for PFSA EW are used for labeling in the figures (**5.8** and **5.10**).

5.7.1 Conductivity

Ionic conductivity at working conditions is critical to the function of the polymer electrolyte materials in the PEMFC. EIS was used to measure the HFR of the MEA, which consists of the membrane and total cell electrical resistance.

The EIS tests were performed for the single-membrane and double-membrane MEAs. The HFR was extracted from an EIS measurement for both the single and double membrane MEAs, labelled R_{single} and R_{double} respectively. During the MEA preparation, the stack of MEA components underwent a bonding press with high pressure and high temperature (beyond the glass transition temperature of the PFSA). In theory, the pristine membrane resistance can be then calculated by simple subtraction of the HFR R_{single} from R_{double}, under the assumption that the interfacial interaction between the two membrane sheets in the

double-layered MEA is negligible. This subtraction eliminates the catalyst-membrane contact resistances, leaving the membrane resistance as a function of operating conditions. The EIS measurements were performed at 40 °C and 80 °C across 20 to 100 %RH.

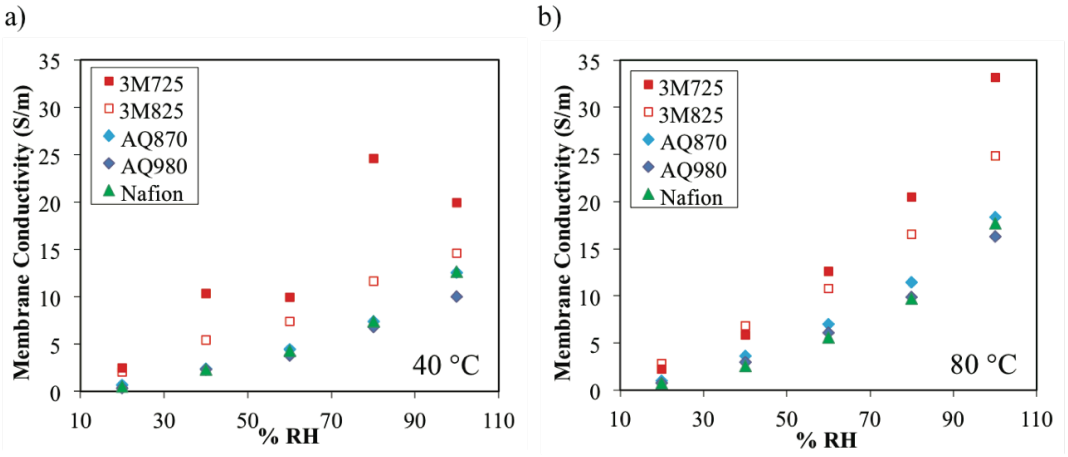

Figure 5. 8 Polymer conductivities at various %RH measured using EIS at Ballard research test station of different PFSA membranes: a) at 40 °C; b) at 80 °C. (Solid red square-3M725; Hollow red square-3M825; Light blue diamond-AQ870; Blue diamond-AQ980; Green triangle-NR211)

Figure 5.8 illustrates the conductivity values for different PFSA at different %RH at two different temperatures. The thickness and EW information is summarized in **Table 5.4.** As the EW of the PFSA decreases, its conductivity increases. EW is the inverse of material's ion exchange capacity (IEC). Therefore, lower EW indicates higher IEC, which is positively correlated to ionic conductivity. At both testing temperatures, PFSA that has lower EW has higher conductivity during the measurements throughout the entire %RH range. As %RH increases, the conductivity increases exponentially in all PFSAs. This observation about the %RH factor agrees with many previous studies regarding the relationship between PFSA bulk conductivity and material hydration level.[41, 51] Greater ionomer hydration creates connected water channels that facilitate solvated proton transport in the system. The

temperature dependence was also pronounced comparing **Figure 5.8b** to **5.8a.**[52-54] The materials' performances at 40 °C (**Figure 5.8a**) demonstrate more scattering of the data points, which could be caused by low conductivity of some of the membranes at this relatively low temperature, which is difficult to measure reliably. Nonetheless, the overall trend with respect to the EW is still valid at such temperature (40 °C).

5.7.2 Gas Permeability: H_2 Crossover

As described previously, hydrogen oxidation reaches its limiting current, and the current is measured from the offset of the cyclic voltammogram from the zero axis – DHE. This offset current is denoted as the H_2 crossover current. The H_2 crossover capacity values were calculated by converting the offset current into hydrogen flux after thickness normalization for various PFSA membranes. Both anode and cathode gases were humidified at varying levels before feeding into the fuel cell stack. During the CV analysis, the current density going through the MEA was monitored as the applied potential ramped linearly between the set potentials. The concept involving the interaction between the gas molecules and the catalyst surface is often referred as the 'pseudocapacitance', which contributes to the oxygen evolution reaction[55]; yet, the interactions are outside the region where the crossover currents are measured.

An example of a typical CV voltammogram collected in this study is shown in **Figure 5.9**, in which the hydrogen adsorption and desorption onto the Pt catalyst surface are labeled.[21, 38] The interactions between gas molecules and Pt surface, where the pseudocapacitance can take place, are at <0.4 V in **Figure 5.9**, which is outside the region of interest. The center region of the voltammogram, where the currents

from the forward and reverse processes are almost parallel to each other, is referred as the non-Faradaic region or the double-layer region. The H_2 crossover current/offset current is indicated as well.

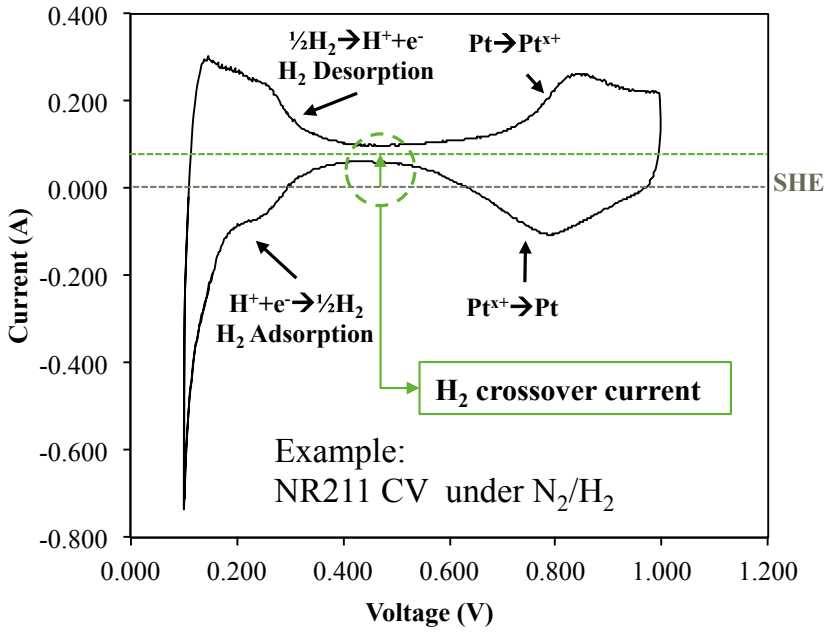

Figure 5. 9 Example of CV curve (voltammogram) of NR211 MEA stack, where the crossover current density (arrow between the two dash lines) is identified as the offset from the mid-point of the double-layer current density (green dash line) to the zero value (grey dashed line).

The H_2 crossover current and permeability (P_{H_2}) values of all the PFSA materials are summarized in **Figure 5.10.** In the top two figures **5.10a** and **5.10b,** the crossover currents were reported and plotted against %RH change at two temperature conditions. In general, it is shown that the elevated %RH causes the H_2 crossover current to increase. The currents at 80 °C are greater than the values at 40 °C in all membrane cases. The difference between the data set of Nafion and the other ionomers is caused by the difference in membrane thickness. Based on **Table 5.4,** the Nafion membrane which was tested has 1/2 – 1/3 of the thickness as the other PFSA membranes. The two general trends observed

here with respect to the increase in %RH and temperature are consistent with previous H_2 crossover studies for PFSAs.[33]

To eliminate the gas permeation path length factor (membrane thickness), the crossover current was converted into H_2 flux based on **Equation 5.2.** The H_2 crossover capacity, i.e. permeability, was then calculated and normalized to H_2 flux in each condition with various %RH and temperature. Similarly, the H_2 permeability information was plotted against %RH for two different thermal conditions, shown in **5.10c** and **5.10d.** Elevated H_2 permeability is observed at increased %RH at both temperatures, and the expected trend that high temperature promotes gas permeation is confirmed with higher permeability summarized in **5.10d.** The correlation with %RH for P_{H_2} is much more pronounced and exponential after the thickness and area normalization. The %RH dependence in all PFSA samples is consistent with previous studies on Nafion.[26, 33, 39-40]

A recent study of gas permeability with electrochemical methods and modeling has demonstrated the mixed pathway of H_2 movement through the aqueous and solid phases of hydrated membrane.[39-40] The formation of water channels creates the aqueous phase in the membrane which provides an alternative route for the gas molecules to travel through the membrane. The increase in water content is likely to fill in the gaps between PFSA molecules. As a result, the %RH eases the H_2 permeation by creating a connected water channel network. Nevertheless, the H_2 permeability values at 80 °C are higher than those at 40 °C, and this temperature dependence is explained by thermally promoted Brownian motion.[39-40, 52-53]

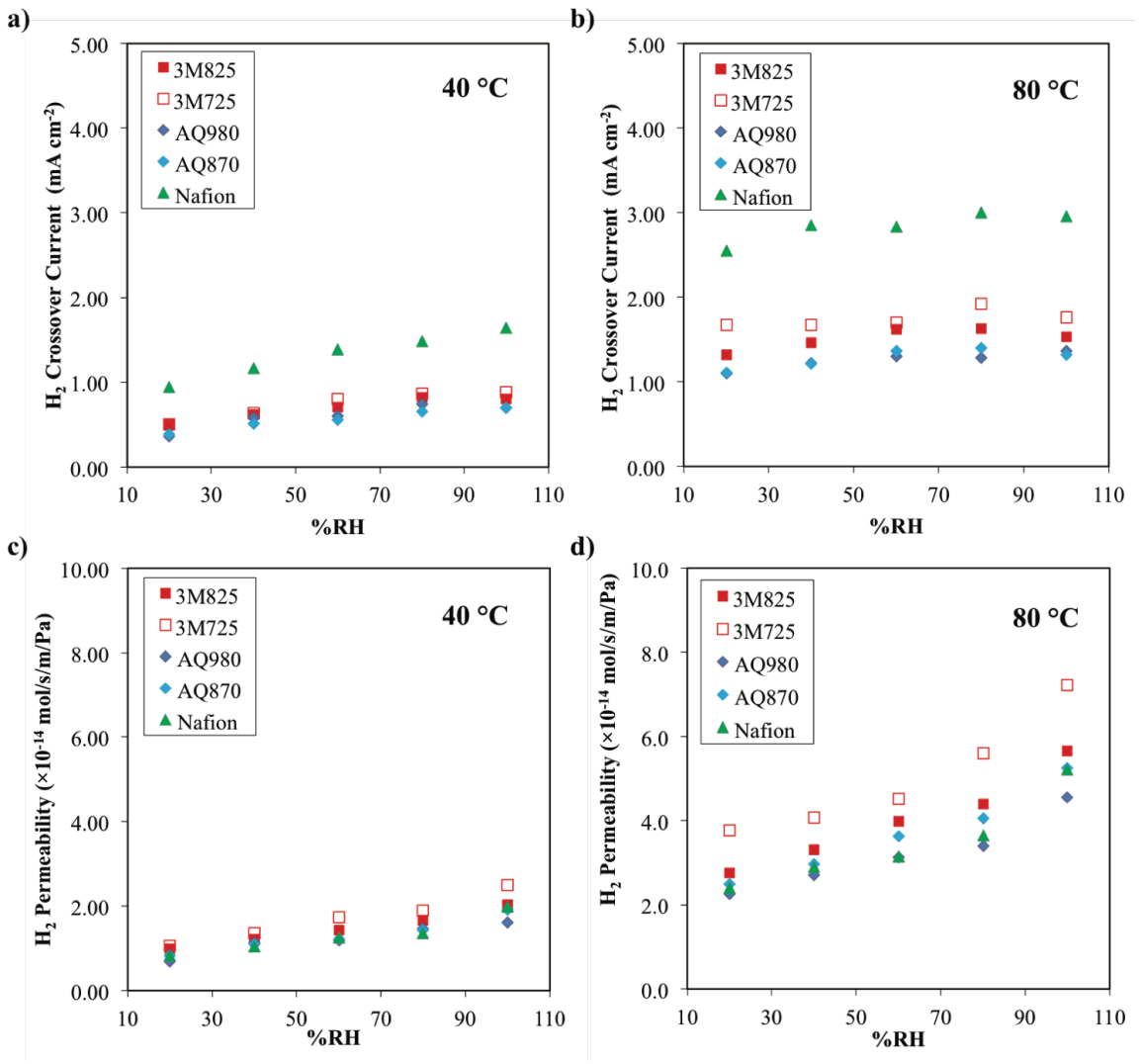

Figure 5. 10 H_2 crossover current measurements of PFSA at various %RH at a) 40 °C and b) 80 °C, the value variation among PFSAs was as a function of material thickness. H_2 permeability of PFSAs was calculated by normalizing the thickness of the materials, and then compared with respect to different temperature and %RH conditions in c) for 40 °C and d) for 80 °C. As the %RH increases, the permeability of H_2 increases. High temperature gives higher permeability as well when comparing d) to c).

Moreover, by simply looking at **Figure 5.10**, the two 3M PFSAs would seem to allow more gas to move across, while the Aquivion and Nafion PFSAs have relatively similar performance. The 3M PFSAs have relatively low EW, which means under the same conditions the PFSA with low EW will

have a better water channel network due to the presence of more ionic side chains. This conceivably leads to the higher gas permeability in those cases. Further investigation is required to fully uncover whether the side chain length and type play a role during the gas permeation process.

5.7.3 Local Dynamics Profile Parameter

NMR has been applied to study dynamics in the polymeric systems in various research fields. Some typical examples include electrolyte materials and bio macromolecule. Proton nuclear spin relaxation time studies have been used in proton conductive materials, including poly-ionic salt, hydrocarbon polymeric electrolyte and PFSAs.[56-60] The spin-lattice relaxation study in imidazolium ionic liquid with respect to the temperature change along with the diffusion analysis provides a thermodynamic picture of the ionic liquids.[59] Proton spin-spin relaxation analyses for polymeric materials through water dynamics provide insight into the proton conductivity of these types of materials. Dipolar coupling interaction oriented NMR techniques have been used in many aspects, especially for macromolecules.[12, 49, 61-64] Rotational-echo double-resonance (REDOR) NMR has been used in unveiling the structure and internuclear distance of influenza M2 proton channels. By carefully monitoring the strength of the dipolar coupling interaction, the proton conduction mechanisms in M2 proton channels are proposed.[61-62] Dipolar coupling driven DQF spectroscopy has been developed and widely applied in hydrocarbon polymeric systems, targeting both homonuclear and heteronuclear interactions.[12-14, 49] In the current study, for fully fluorinated materials, focusing on the ^{19}F aspect is beneficial to understand the fundamental chemistry of the polymer and to

reveal the relationship between material properties and structure. Monitoring the ^{19}F spin relaxation time is not reliable due to resonance overlapping and the existence of chemical shift anisotropic (CSA) relaxation mechanisms. ^{19}F and ^{13}C CSA strategies using NMR have been developed, yet both require long experimental time, especially with the low natural abundance ^{13}C.[9, 11] An efficient ^{19}F DQF method will address the dynamics analysis for different fluorine sites in the polymer structure.

A new ^{19}F NMR method and analysis has been developed to probe the local dynamics of PFSA ionomers as described earlier in this document.[6] Method development of this ^{19}F DQF tool was previously performed using Nafion 117 itself; the gold standard of the PFSA membrane materials.[6] In this study, the side chain and backbone local dynamics profiles were well separated and analyzed.[6] The quantitative measure of apparent dipolar coupling constant (D_{app}) was carefully and sensibly extracted to compare at different hydration levels and temperatures. The side chain fluorine signals have lower D_{app} values than the backbone, which suggests the side chain has more dimensional freedom than the backbone. From **Equation 5.3a** and previous study[6], it is easy to addressed that the static D_{app} is dominated by the strength of ^{19}F-^{19}F dipolar coupling in the CF_2. Other contributions are summed and contributed as a function of $1/r^3$ (in **Equation 5.3b**). This suggests that the static D_{app} is a local measure, and it is unlikely that any possible structural disorder would attribute to any substantial changes. Recent proton network study[63] has demonstrated that the static values in solid acid systems reaches a plateau (>15 Å) as the range of consideration for the proton-proton interactions increase. Similarly, in the fluorine system the theoretical values of D_{app} should reach a plateau as well. Although

the attenuation in the D_{app} may be caused by both structural disorder and dynamics, the experimental attenuation determined has suggested that the structural disorder alone does not contribute to the substantial reduction in D_{app}. The CF_2 will remain within van der Waals distances of each other, (within ~3 Å at the closest) with or without structural disorder; on the other hand, the dynamics would become the main reason to the attenuation. In many morphology studies, the heterogenous phase development or cluster formation is usually at a nanometer length-scale[65-67], which is beyond that which would impact the D_{app} values. Therefore, the D_{app} becomes the local dynamics indicator.

Most importantly, SCF_2 has the highest local dynamics profile in the Nafion system, which is represented by the lowest D_{app} values for all the conditions studied. This is consistent with its proximity to the terminal proton-conducting site. Therefore, it is very appropriate to use the D_{app} value for the SCF_2 site as an indicator of the local dynamics parameter of the PFSA side chains. Here we show for the first time that this tool is able to differentiate behavior as a function of membrane composition, and those trends are correlated with gas permeability and conductivity, key performance parameters for fuel cells. As shown in **Figure 5.11**, three types of PFSA have been used in the current study, Nafion, Aquivion and 3M. The spectra were previously reported in our spectroscopic analysis.[68] With an appropriate spinning rate, the ^{19}F MAS NMR spectra of the PFSAs were well resolved. With deconvolution, different fluorine sites are easily distinguished as seen in various Nafion studies.[5-6, 9, 11] All of the side chain resonances are deconvoluted and separated from the backbone signals. The SCF_2 sites for different PFSAs are shaded in purple in **Figure 5.11.**

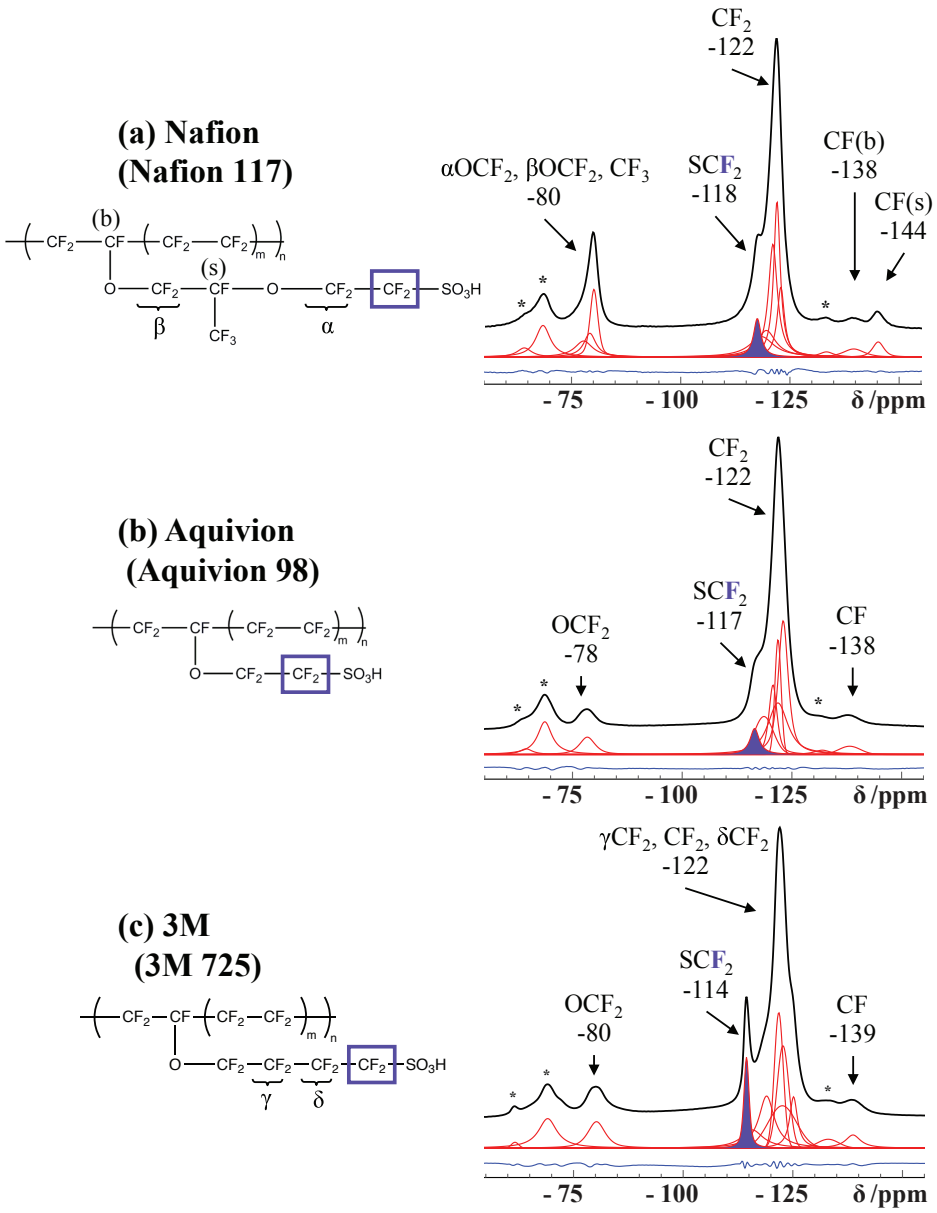

Figure 5. 11 ^{19}F MAS NMR spectra for three types of PFSAs with deconvolutions: a) Nafion (Nafion 117); b) Aquivion (Aquivion 98) c) 3M (3M 725). The experimental spectra are black, the deconvoluted resonances are red, and the spectral residue is navy located at the bottom of each set. Different fluorine sites are well labeled, and the purple shades indicate the side chain SCF_2 fluorine is the focus to reveal the local dynamics. Asterisks represent NMR spinning side bands.

5.7.4 Correlation between Local Motion and Performance

In the current study, the relationship between bulk proton conductivity and molecular local dynamics was investigated. As previously suggested through morphology evolution by PFSA backbone and side chain, the formation of water channels promotes proton conductivity.[17, 41, 51, 67] Similar to the benchmark DQ experiment of Nafion done previously, five different PFSA membranes were studied in the same fashion.[6] The PFSA membranes were conditioned in the environmental chamber with targeted %RH and temperature, in order to match the *in situ* MEA experimental conditions at the test station. The local dynamics profile parameter D_{app} was extracted based on normalized DQ build-up curves for the SCF_2 site for the five PFSA samples.

The membrane conductivity is extrapolated against D_{app} (SCF_2) for experiments done at 40 °C and 80 °C at two different hydration levels, 50 %RH and 100 %RH, as shown in **Figure 5.12.** The overall correlation is shown in the center, and the four corners are occupied by the four different conditions. All five PFSA membranes were examined under these conditions. A strong correlation is observed between these two sets of values, whereas D_{app} increases, the conductivity exponentially decays accordingly. The exponential trend with $y = ae^{-bx}$ function serves as the guide to the eye. As previously mentioned, the lower the D_{app} value is, the higher the local dynamics it represents. The attenuation observed in the D_{app} value is predominantly attributed to the local dynamics rather than changes in the nano-scale structural disorder. Thus, high local dynamics profile corresponds to high membrane ionic conductivity. Although the datasets with two temperatures did not show significant separation, the modest shift towards the lower D_{app} values of the 80 °C set is observed. In **Figure 5.12**, the data points from different

conditions were colour-mapped accordingly, and the mapping follows the exponential trend line as the condition goes from 'hot, wet' to 'cold, dry'. It is clear that the 'hot, wet' condition promotes local motion, i.e. low D_{app} value, which facilitates proton conductivity, and the 'cold, dry' shows the opposite along the trend line. Despite the scattering in the data points, the trend between the conductivity and D_{app} is clear.

The local dynamics parameter allows one to investigate the chemical environment on the side chain at the terminal conducting acid group. Upon hydration-driven phase separation, SCF_2 is considered to be located close to the interface or the phase boundary. The local motion of SCF_2 is promoted by the hydration of the hydrophilic SO_3H group. The more local motion the side chain retains which is reflected by the lower D_{app} values at SCF_2, the higher conductivity is observed. This correlation is not the first time that studies attempt to link the dynamics to material conductivity. As mentioned in the previous section, other techniques including some pioneering ssNMR studies that were interested in dynamics analyses to understand the membrane morphology and performance correlations, focusing on investigating the proton-conducting site.[56-57] The behavior of the proton-conducting site is very important but does not directly indicate side chain motion. In a recent proton dynamics study using a quasi-elastic neutron scattering technique, proton transport at low %RH was attributed to mostly hydronium hopping within the interface, and diffusive fast proton transport in water channels were both observed and analyzed.[69] With a ^{19}F NMR dynamics study, the polymer chain behaviours become easily accessible. From the observation from **Figure 5.12**, it is clear that the side chain local dynamics promotes the proton conductivity and is

favoured at high temperature and %RH. The difference in SCF_2 local dynamics represents the difference in interfacial conditions. At high %RH (100 %RH case) the membrane takes up water molecules and the disorder of interface enlarges ranging from 4.5 to 2.8 kHz, the proton conductivity increases much faster. This is caused by diffusive proton motion in the connected water channel network dominating the conductive performance, which is a well-established theory.[17-18, 41, 69] At low %RH (50 %RH case), the water network that could easily form at high %RH is not sufficient for proton transport. The interface gets more disordered (reflected by lower D_{app} values, ranging from 7.0 to 4.0 kHz), and the proton conductivity rises slowly due to mostly hydronium hopping within the interface. Thus, a low degree of interface disorder limits the proton conductivity at low %RH condition. Additionally, the different distribution of the four groups of data points in **Figure 5.12** shows that at 50 %RH the difference between the data groups at 40 °C and 80 °C is marginal compared to that at 100 %RH. This suggests that the sensitivity of conductivity towards temperature is relatively small compared to the sensitivity towards hydration level. The proton conductivity trend correlates to the microphase separation in the polymer material, where the ionic domains form effectively by the induced hydration. The difference between the dependence on temperature and hydration level seen in **Figure 5.12** is consistent with the previous elastic modulus and stress relaxation studies.[66-67]

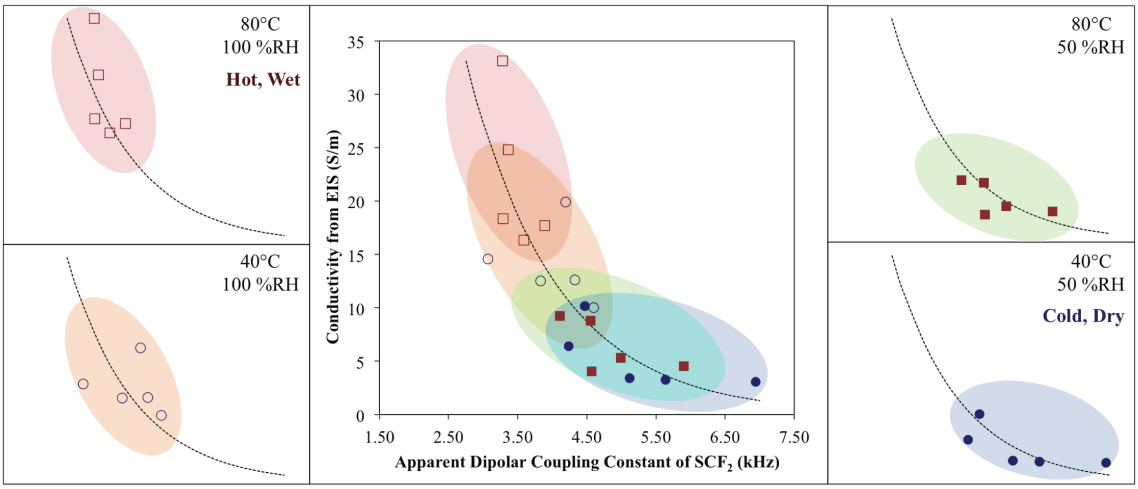

Figure 5. 12 Correlation between bulk membrane conductivity *via* EIS and local dynamics parameter, D_{app}, of the polymer side chain, SCF_2. Top left: at 80 °C, 100 %RH (red hollow squares). Bottom left: at 40 °C, 100 %RH (blue hollow circles). Top right: at 80 °C, 50 %RH (red solid squares). Bottom left: at 40 °C, 50 %RH (blue solid circles). Center plot: The overall correlation is summarized with color-coded regions indicating different conditions. The dashed curve is the exponential fitting of the overall correlation, which is illustrated in all parts.

The electrochemical performance of PFSA materials has been under intensive investigation for several decades. Proton conductivity has proven to be dependent on PFSA nanostructure and water content.[33, 50, 70] Two main proton motion mechanisms have been proposed: the surface diffusion mechanism, where the proton moves between sulfonate anions through water diffusion, 'surface proton hopping'; and the Grotthuss mechanism where proton is passed on between hydronium ions; the bulk diffusion of hydronium ion.[67] The surface proton diffusion and the hydronium diffusion mechanisms can be referred as the 'vehicular mechanism'. Schematic pictures are shown in **Figure 5.13.** Proton conductivity solely depends on the proton transport speed, thus the distribution of ionic domains and water channels within the membrane significantly affect this process.

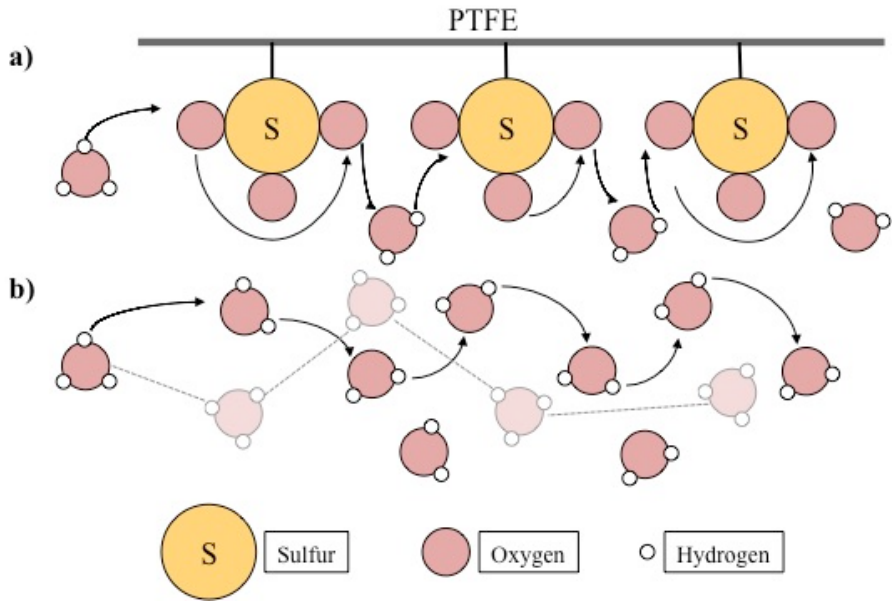

Figure 5. 13 A schematic demonstration of proton transport mechanisms.[67] a) Surface proton hopping between sulfonic acid groups and water molecules; b) Grotthuss mechanism between water molecules, and hydronium bulk diffusion (dashed line).

The exponential behavior in **Figure 5.12** suggests that for PFSA membranes the higher side chain local dynamics represents a less-organized interfacial environment. The proton conductivity at high %RH (in the 100 %RH condition, ~D_{app}<4.50 kHz) increases as D_{app} decreases as a result of the increased connections and amount of water channels from high hydration level. On the other hand, at 50 %RH when ~D_{app}>4.00 kHz in the figure, as the D_{app} value decreases the conductivity measurement increases much slower compared to the high hydration level case. This suggests that the at low hydration level, the side chain local dynamics predominately influence conductive performance due to the insufficiency of connection between ionic domains – i.e. water channels. Based on the correlation observed among all the PFSA tested, the surface proton hopping mechanism in **5.13a** is favoured at low

hydration promoted by side chain local dynamics; while the other mechanisms in **5.13b** are more preferred at a more hydrated condition.

Similarly, the H_2 permeability of PFSA has also been probed and compared. As another key performance evaluation of PFSA in the PEMFC membrane, it is prominently influenced by the microphase separation of the polymer, which is controlled by the temperature and hydration level factors.

The H_2 permeability measurements suggest that it is dependent on the distribution and the size/proportion of the hydrophilic ionic domain. In many polymeric materials, studies have been done using neutron scattering techniques, where the scattering intensity was analyzed as a function of temperature and scattering vector.[71-72] In the substituent study of polyacetylenes, the size of the side chain influences the local dynamics of the polymer, which leads to different motional regimes. A polymer with fast side chain motion provides high gas permeability, and *vice versa*.[71] Modeling work of gas permeability of Nafion using a resistor network model has illustrated the significance of the aqueous and hydrophilic phases formation and the microscopic phase distribution.[40] This is strongly influenced by the hydrophilicity of the polymer backbone and side chain.

The correlation between the H_2 permeability and D_{app} has been illustrated in **Figure 5.14.** The data points at the two temperatures are well separated, as at the lower temperature the gas permeability is much smaller compared to the higher temperature case. Gas permeation is solely a diffusive motion through mediums, the temperature dependence observed in both **Figure 5.10** and **5.14**, is attributed to the temperature parameter in the exponential Boltzmann distribution, which describes the thermally driven process. More interestingly, the two sets share a

similar trend with respect to the D_{app} values. As the local motion indicator decreases in value, the permeability demonstrates elevation exponentially, where the fitted curves (with exponential function $y = ae^{-bx}$) as the guide to the eye. The correlations in both temperature conditions are strong, moreover at the 80 °C the permeability does show a much faster response as D_{app} drops, where the exponential decay constant b is 1.3 times bigger and the pre-exponential factor a is 3.4 times bigger than those at 40 °C where b = 0.22 and a = 4.33.

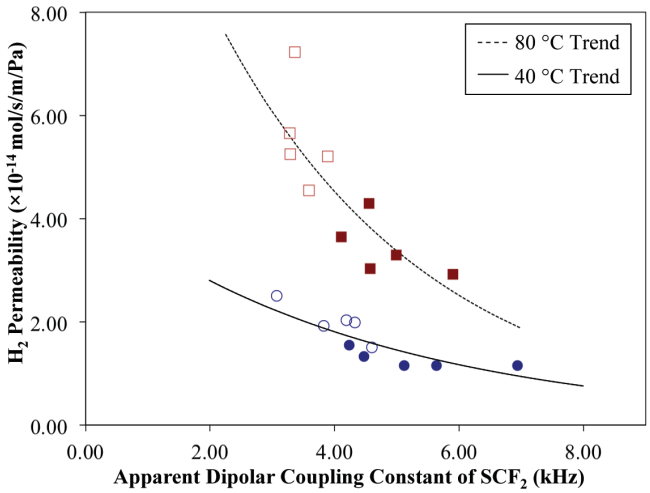

Figure 5. 14 Correlation between H_2 permeability and local dynamics parameter, D_{app}, of the polymer side chain, SCF_2. Similar data point labeling scheme is applied here, as seen in Figure 5: 80 °C, 100 %RH - red hollow squares; 80 °C, 50 %RH - red solid squares; 40 °C, 100 %RH - blue hollow circles; 40 °C, 50 %RH - blue solid circles. The dashed exponential fitting is illustrated to represent the correlation for 80 °C data set, while the solid exponential fitting is for that at 40 °C.

From **Figure 5.14**, the 50 %RH data sets are located at low local motion of the side chain (high D_{app} values) with low P_{H_2}, while the 100 %RH data sets favour the higher P_{H_2}. As the local dynamics of the side chain increase, the H_2 permeability increases exponentially at both temperature conditions. The response towards %RH increase is caused by

the gradual formation of water channels, i.e. the aqueous phase in the polymer matrix, which provides alternative gas permeation paths through the PFSA.[39-40] Thus, the total gas permeation is attributed to a mix of pathways involving different phases. The resistor network modeling work suggests the significance of permeation occurs in the intermediate phase which is essentially the phase boundary, and in the softened/swollen polymer solid phase.[18] There are many parameters/factors involved in understanding the impact of hydration level on gas permeability, but the general trend of reducing water content resulting in a decrease in gas permeability is expected; and that is observed here in **Figure 5.14.**

In the modeling work, Schalenbach et al. suggest that the relationship between permeability and water content could only be fitted by a model where a softened solid phase has occurred, and the permeation through the intermediate and solid phases affect the total permeation much more at lower hydration condition.[39-40] The local dynamics parameter of the side chain SCF_2, established by our ^{19}F NMR studies, represents the local environment of the phase boundary or intermediate phase. The correlation shows that the more local mobility the intermediate phase has the higher gas permeation observed. In all PFSA cases, hydration brings more disorder or local dynamics, which weakens the intramolecular and intermolecular van der Waals forces, easing the permeation through this interfacial boundary. This conclusion supports the modeling study on the impact of permeation through the intermediate phase. To further demonstrate the difference in permeation within solid phase, the H_2 permeability data was plotted against the backbone local dynamics parameter, D_{app}, of CF_2. A similar correlation analysis was attempted and demonstrated in **Figure 5.15.**

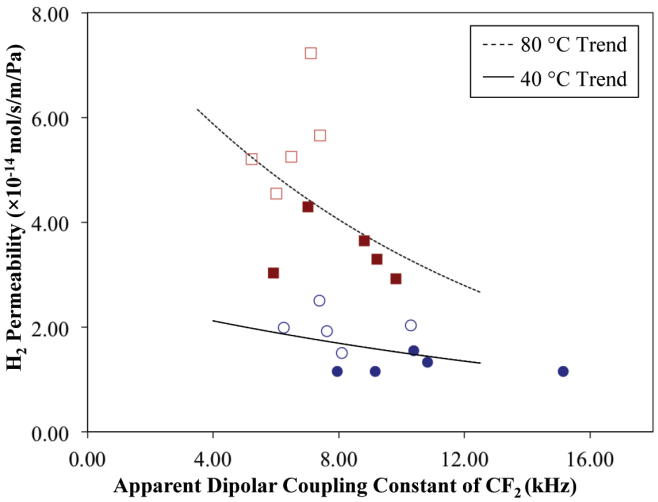

Figure 5. 15 Correlation between H_2 permeability and local dynamics parameter, D_{app}, of the polymer backbone, CF_2. Similar data point labeling scheme is applied here, as seen in Figure 5 and 6: 80 °C, 100 %RH – red hollow squares; 80 °C, 50 %RH – red solid squares; 40 °C, 100 %RH – blue hollow circles; 40 °C, 50 %RH – blue solid circles. The dashed exponential fitting is illustrated to represent the correlation for 80 °C data set, while the solid exponential fitting is for that at 40 °C.

Compared to **Figure 5.14**, the data points are more scattered, and the correlations observed have much smaller exponential decay constants, b = 0.09 and 0.06, a = 8.52 and 2.65 at 80 °C and 40 °C respectively. Equivalently, the CF_2 local dynamics parameter describes the polymer backbone, which can be considered as the solid phase in the polymer matrix. The data points at both temperatures are nearly distributed vertically, especially at 80 °C. At 40 °C, the diffusive permeation process is not effectively activated, which leads to marginal differentiation between data points. Despite the different data distributions between these two temperature conditions, the lack of exponential features in **Figure 5.15** (compared to **Figure 5.14**) suggests that the gas permeability is less related to the local dynamics of the solid phase. Therefore, the intermediate phase plays a more crucial role in gas permeation compared to the solid phase. To improve the

polymer electrolyte membrane material, the side chain local dynamics representing an intermediate phase environment is the limiting factor to the gas permeation process. Nonetheless, temperature dependence is a much stronger factor, which is unavoidable due to the thermodynamic nature of the permeation process.

As described above, the hydrophilic side chain evidently promotes proton transport, especially at low %RH; yet at high %RH, a populated water channel network allowing the hydronium diffusion favors the proton transport in aqueous phase in the polymer matrix. The correlation between D_{app} (SCF_2) and proton conductivity supports this. A local dynamics parameter evaluation can also be performed representing the intermediate phase to understand its impact towards gas permeation. As a result of comparing polymer side chain and backbone, it is concluded that the intermediate phase exhibited by the side chain behavior has a more limiting effect on the permeation process than that of the polymer backbone. The correlations (**Figure 5.12** and **5.14**) are both clearly established. This is the first study that aims to connect the material physicochemical properties using *ex situ* ^{19}F NMR technique to the operando electrochemical performance measurements, to parameterize the impact and to provide insight into the improvement of polymer electrolyte materials.

5.8 Summary

MEAs made with different types of PFSAs were assembled into fuel cell stacks and tested for electrochemical performance under a range of %RH at 40 °C and 80 °C. Through EIS and CV analyses, proton conductivity and H_2 permeability information were obtained and

normalized with respect to membrane thickness and test area. As temperature and %RH increase, the conductivity and H_2 permeability increase in all the PFSAs. In parallel, ^{19}F ssNMR dynamics studies have been performed on identical PFSAs after matching the conditioning using an environmental chamber. D_{app} of SCF_2 is reintroduced in this study to use as an indicator of the side chain local motion at a molecular level. A strong correlation between the proton conductivity and D_{app}, as well as that between the H_2 permeability and D_{app} are observed. As local dynamics increase with elevated hydration and temperature, both the conductivity and the gas permeability concurrently increase. The formation of the hydrophilic domains during hydration leads to improvement of proton conductivity, and also inevitably promotes H_2 permeation, which is critical to conductive performance with decreasing %RH. Additionally the H_2 permeation behavior is expected to extend to other gases, especially diatomic gases such as O_2. High O_2 transport through the ionomer in the catalyst layer will help to facilitate proton consumption on the electrode to minimize the mass transport limitations of the MEAs. Understanding how H_2 and O_2 permeate in the membrane and ionomer in the catalyst layer will help in the larger scale design of the fuel cell to mitigate H_2 fuel loss and facilitate O_2 transport. Finding optimal membrane materials with high proton conductivity and advantageous gas permeability is one of the key improvements required to commercialize PEMFCs in automotive applications.

5.9 References

1. Berejnov, V.; Martin, Z.; West, M.; Kundu, S.; Bessarabov, D.; Stumper, J.; Susac, D.; Hitchcock, A. P., Probing platinum degradation in polymer electrolyte membrane fuel cells by synchrotron X-ray microscopy. *Phys. Chem. Chem. Phys.* **2012,** *14* (14), 4835-4843.

2. Holdcroft, S., Fuel cell catalyst layers: a polymer science perspective. *Chem. Mater.* **2013,** *26* (1), 381-393.

3. Kreuer, K.-D.; Paddison, S. J.; Spohr, E.; Schuster, M., Transport in proton conductors for fuel-cell applications: simulations, elementary reactions, and phenomenology. *Chem. Rev.* **2004,** *104* (10), 4637-4678.

4. Hamrock, S. J.; Yandrasits, M. A., Proton exchange membranes for fuel cell applications. *Journal of Macromolecular Science, Part C: Polymer Reviews* **2006,** *46* (3), 219-244.

5. Ghassemzadeh, L.; Holdcroft, S., Quantifying the Structural Changes of Perfluorosulfonated Acid Ionomer upon Reaction with Hydroxyl Radicals. *J. Am. Chem. Soc.* **2013,** *135* (22), 8181-8184.

6. Yan, Z. B.; Brouwer, D. H.; Goward, G. R., 19F Double Quantum NMR Spectroscopy: A Tool for Probing Dynamics in Proton-Conducting Fluorinated Polymer Materials. *Macromolecules* **2016,** *49* (19), 7331-7339.

7. Grimmer, A. R.; Kretschmer, A.; Cajipe, V. B., Influence of magic angle spinning on sample temperature. *Magn. Reson. Chem.* **1997,** *35* (2), 86-90.

8. van Moorsel, G. J. M. P.; van Eck, E. R. H.; Grey, C. P., Pr2Sn2O7 and Sm2Sn2O7 as high-temperature shift thermometers in variable-temperature 119Sn MAS NMR. *J. Magn. Reson. A* **1995,** *113* (2), 159-163.

9. Chen, Q.; Schmidt-Rohr, K., Backbone Dynamics of the Nafion Ionomer Studied by 19F-13C Solid-State NMR. *Macromol. Chem. Phys.* **2007,** *208* (19-20), 2189-2203.

10. Emsley, J.; Phillips, L., Fluorine chemical shifts. *Prog. Nucl. Magn. Reson. Spectrosc.* **1971,** *7*, 1-520.

11. Chen, Q.; Schmidt-Rohr, K., 19F and 13C NMR signal assignment and analysis in a perfluorinated ionomer (Nafion) by two-dimensional solid-state NMR. *Macromolecules* **2004,** *37* (16), 5995-6003.

12. Graf, R.; Heuer, A.; Spiess, H. W., Chain-Order Effects in Polymer Melts Probed by H 1 Double-Quantum NMR Spectroscopy. *Phys. Rev. Lett.* **1998,** *80* (26), 5738.

13. Saalwächter, K., Robust NMR Approaches for the Determination of Homonuclear Dipole—Dipole Coupling Constants in Studies of Solid Materials and Biomolecules. *ChemPhysChem* **2013,** *14* (13), 3000-3014.

14. Saalwächter, K.; Lange, F.; Matyjaszewski, K.; Huang, C.-F.; Graf, R., BaBa-xy16: Robust and broadband homonuclear DQ recoupling for applications in rigid and soft solids up to the highest MAS frequencies. *J. Magn. Reson.* **2011,** *212* (1), 204-215.

15. Yeo, S. C.; Eisenberg, A., Physical properties and supermolecular structure of perfluorinated ion-containing (Nafion) polymers. *J. Appl. Polym. Sci.* **1977,** *21* (4), 875-898.

16. Page, K. A.; Cable, K. M.; Moore, R. B., Molecular origins of the thermal transitions and dynamic mechanical relaxations in perfluorosulfonate ionomers. *Macromolecules* **2005,** *38* (15), 6472-6484.

17. Kreuer, K., On the development of proton conducting polymer membranes for hydrogen and methanol fuel cells. *Journal of membrane science* **2001,** *185* (1), 29-39.

18. Kreuer, K.-D., The role of internal pressure for the hydration and transport properties of ionomers and polyelectrolytes. *Solid State Ionics* **2013**, *252*, 93-101.

19. Osborn, S. J.; Hassan, M. K.; Divoux, G. M.; Rhoades, D. W.; Mauritz, K. A.; Moore, R. B., Glass transition temperature of perfluorosulfonic acid ionomers. *Macromolecules* **2007**, *40* (10), 3886-3890.

20. Zorin, V. E.; Brown, S. P.; Hodgkinson, P., Quantification of homonuclear dipolar coupling networks from magic-angle spinning1H NMR. *Mol. Phys.* **2006**, *104* (2), 293-304.

21. Barbir, F., *PEM fuel cells: theory and practice*. Academic Press: New York, 2012.

22. Collier, A.; Wang, H.; Yuan, X. Z.; Zhang, J.; Wilkinson, D. P., Degradation of polymer electrolyte membranes. *Int. J. Hydrogen Energy* **2006**, *31* (13), 1838-1854.

23. Ghassemzadeh, L.; Kreuer, K. D.; Maier, J.; Müller, K., Evaluating chemical degradation of proton conducting perfluorosulfonic acid ionomers in a Fenton test by solid-state< sup> 19</sup> F NMR spectroscopy. *J. Power Sources* **2011**, *196* (5), 2490-2497.

24. Weber, A. Z., Gas-crossover and membrane-pinhole effects in polymer-electrolyte fuel cells. *J. Electrochem. Soc.* **2008**, *155* (6), B521-B531.

25. Tang, H.; Peikang, S.; Jiang, S. P.; Wang, F.; Pan, M., A degradation study of Nafion proton exchange membrane of PEM fuel cells. *J. Power Sources* **2007**, *170* (1), 85-92.

26. Zhang, H.; Li, J.; Tang, H.; Lin, Y.; Pan, M., Hydrogen crossover through perfluorosulfonic acid membranes with variable side chains and

its influence in fuel cell lifetime. *Int. J. Hydrogen Energy* **2014,** *39* (28), 15989-15995.

27. Banerjee, S. Fuel cell incorporating a reinforced membrane. 5795668, 1998.

28. Grot, W. G. Process for making articles coated with a liquid composition of perfluorinated ion exchange resin. 4453991, 1984.

29. Spethmann, J. E.; Keating, J. T. Composite membrane with highly crystalline porous support. 6110333, 2000.

30. Tang, H.; Wang, X.; Pan, M.; Wang, F., Fabrication and characterization of improved PFSA/ePTFE composite polymer electrolyte membranes. *Journal of Membrane Science* **2007,** *306* (1), 298-306.

31. Xiao, P.; Li, J.; Tang, H.; Wang, Z.; Pan, M., Physically stable and high performance Aquivion/ePTFE composite membrane for high temperature fuel cell application. *Journal of membrane science* **2013,** *442*, 65-71.

32. Curtin, D. E.; Lousenberg, R. D.; Henry, T. J.; Tangeman, P. C.; Tisack, M. E., Advanced materials for improved PEMFC performance and life. *J. Power Sources* **2004,** *131* (1), 41-48.

33. Broka, K.; Ekdunge, P., Oxygen and hydrogen permeation properties and water uptake of Nafion® 117 membrane and recast film for PEM fuel cell. *J. Appl. Electrochem.* **1997,** *27* (2), 117-123.

34. Sakai, T.; Takenaka, H.; Torikai, E., Gas diffusion in the dried and hydrated Nafions. *J. Electrochem. Soc.* **1986,** *133* (1), 88-92.

35. Chen, J.; Loo, L. S.; Wang, K., A novel time lag method to measure the permeation of vapor-gas mixtures. *Journal of Membrane and Separation Technology* **2012,** *1* (2), 94-99.

36. Baik, K. D.; Hong, B. K.; Kim, M. S., Effects of operating parameters on hydrogen crossover rate through Nafion® membranes in

polymer electrolyte membrane fuel cells. *Renewable energy* **2013,** *57*, 234-239.

37. Baik, K. D.; Hong, B. K.; Kim, M. S., Novel technique for measuring oxygen crossover through the membrane in polymer electrolyte membrane fuel cells. *Int. J. Hydrogen Energy* **2013,** *38* (21), 8927-8933.

38. Wu, J.; Yuan, X. Z.; Wang, H.; Blanco, M.; Martin, J. J.; Zhang, J., Diagnostic tools in PEM fuel cell research: Part I Electrochemical techniques. *Int. J. Hydrogen Energy* **2008,** *33* (6), 1735-1746.

39. Schalenbach, M.; Hoefner, T.; Paciok, P.; Carmo, M.; Lueke, W.; Stolten, D., Gas permeation through nafion. Part 1: measurements. *The Journal of Physical Chemistry C* **2015,** *119* (45), 25145-25155.

40. Schalenbach, M.; Hoeh, M. A.; Gostick, J. T.; Lueke, W.; Stolten, D., Gas Permeation through Nafion. Part 2: Resistor Network Model. *The Journal of Physical Chemistry C* **2015,** *119* (45), 25156-25169.

41. Schalenbach, M.; Lueke, W.; Lehnert, W.; Stolten, D., The influence of water channel geometry and proton mobility on the conductivity of Nafion®. *Electrochim. Acta* **2016,** *214*, 362-369.

42. Koponen, U.; Kumpulainen, H.; Bergelin, M.; Keskinen, J.; Peltonen, T.; Valkiainen, M.; Wasberg, M., Characterization of Pt-based catalyst materials by voltammetric techniques. *J. Power Sources* **2003,** *118* (1), 325-333.

43. Srinivasan, S.; Ticianelli, E.; Derouin, C.; Redondo, A., Advances in solid polymer electrolyte fuel cell technology with low platinum loading electrodes. *J. Power Sources* **1988,** *22* (3-4), 359-375.

44. Wang, M.; Lou, T.; Zhai, Y.; Kim, D.-k., Defining catalyst layer ingredients in PEMFC by orthogonal test and C–V method. *Int. J. Hydrogen Energy* **2005,** *30* (4), 381-384.

45. Oldham, K.; Myland, J., *Fundamentals of electrochemical science*. Academic Press: San Diego, 2012.

46. Kissinger, P. T.; Heineman, W. R., Cyclic voltammetry. *J. Chem. Educ* **1983,** *60* (9), 702.

47. Young, A.; Stumper, J.; Gyenge, E., Characterizing the structural degradation in a PEMFC cathode catalyst layer: carbon corrosion. *J. Electrochem. Soc.* **2009,** *156* (8), B913-B922.

48. Levitt, M. H., *Spin dynamics: basics of nuclear magnetic resonance*. John Wiley & Sons: Chichester, 2001.

49. Hansen, M. R.; Graf, R.; Spiess, H. W., Interplay of Structure and Dynamics in Functional Macromolecular and Supramolecular Systems As Revealed by Magnetic Resonance Spectroscopy. *Chem. Rev.* **2016,** *116* (3), 1272-308.

50. Li, Y.; Zhao, T.; Yang, W., Measurements of water uptake and transport properties in anion-exchange membranes. *Int. J. Hydrogen Energy* **2010,** *35* (11), 5656-5665.

51. Zawodzinski, T. A.; Derouin, C.; Radzinski, S.; Sherman, R. J.; Smith, V. T.; Springer, T. E.; Gottesfeld, S., Water uptake by and transport through Nafion® 117 membranes. *J. Electrochem. Soc.* **1993,** *140* (4), 1041-1047.

52. Boltzmann, L., *Lectures on gas theory*. Courier Corporation: 2012.

53. Rogers, C., *Permeation of gases and vapours in polymers*. 1985; Vol. 2, p 11-73.

54. Springer, T. E.; Zawodzinski, T.; Gottesfeld, S., Polymer electrolyte fuel cell model. *J. Electrochem. Soc.* **1991,** *138* (8), 2334-2342.

55. Eftekhari, A., From pseudocapacitive redox to intermediary adsorption in oxygen evolution reaction. *Materials Today Chemistry* **2017,** *4*, 117-132.

56. Ye, G.; Janzen, N.; Goward, G. R., Solid-state NMR study of two classic proton conducting polymers: Nafion and sulfonated poly (ether ether ketone) s. *Macromolecules* **2006,** *39* (9), 3283-3290.

57. Ye, G.; Hayden, C.; Goward, G., Proton dynamics of Nafion and Nafion/SiO2 composites by solid state NMR and pulse field gradient NMR. *Macromolecules* **2007,** *40* (5), 1529-1537.

58. Lee, Y. J.; Bingöl, B.; Murakhtina, T.; Sebastiani, D.; Meyer, W. H.; Wegner, G.; Spiess, H. W., High-resolution solid-state NMR studies of poly (vinyl phosphonic acid) proton-conducting polymer: Molecular structure and proton dynamics. *The Journal of Physical Chemistry B* **2007,** *111* (33), 9711-9721.

59. Chung, S. H.; Lopato, R.; Greenbaum, S. G.; Shirota, H.; Castner, E. W.; Wishart, J. F., Nuclear Magnetic Resonance Study of the Dynamics of Imidazolium Ionic Liquids with– CH2Si (CH3) 3 vs– CH2C (CH3) 3 Substituents. *The Journal of Physical Chemistry B* **2007,** *111* (18), 4885-4893.

60. Lee, D. K.; Saito, T.; Benesi, A. J.; Hickner, M. A.; Allcock, H. R., Characterization of water in proton-conducting membranes by deuterium NMR T 1 relaxation. *The Journal of Physical Chemistry B* **2011,** *115* (5), 776-783.

61. Cady, S. D.; Schmidt-Rohr, K.; Wang, J.; Soto, C. S.; DeGrado, W. F.; Hong, M., Structure of the amantadine binding site of influenza M2 proton channels in lipid bilayers. *Nature* **2010,** *463* (7281), 689-692.

62. Hu, F.; Luo, W.; Hong, M., Mechanisms of proton conduction and gating in influenza M2 proton channels from solid-state NMR. *Science* **2010**, *330* (6003), 505-508.

63. Foran, G. Y.; Brouwer, D. H.; Goward, G. R., Quantifying Site-Specific Proton Dynamics in Phosphate Solid Acids by 1H Double Quantum NMR Spectroscopy. *The Journal of Physical Chemistry C* **2017**, *121* (46), 25641-25650.

64. De Almeida, N. E.; Harris, K. J.; Samoson, A.; Goward, G. R., 1H–1H Double Quantum NMR Investigation of Proton Dynamics in Solid Acids. *The Journal of Physical Chemistry C* **2016**, *120* (36), 19961-19969.

65. Lehmani, A.; Durand-Vidal, S.; Turq, P., Surface morphology of Nafion 117 membrane by tapping mode atomic force microscope. *J. Appl. Polym. Sci.* **1998**, *68* (3), 503-508.

66. Satterfield, M. B.; Benziger, J. B., Viscoelastic properties of Nafion at elevated temperature and humidity. *J. Polym. Sci., Part B: Polym. Phys.* **2009**, *47* (1), 11-24.

67. Choi, P.; Jalani, N. H.; Datta, R., Thermodynamics and proton transport in Nafion II. Proton diffusion mechanisms and conductivity. *J. Electrochem. Soc.* **2005**, *152* (3), E123-E130.

68. Yan, Z. B.; Hayes, R.; Melo, L. G.; Goward, G. R.; Hitchcock, A. P., X-ray Absorption and Solid-State NMR Spectroscopy of Fluorinated Proton Conducting Polymers. *The Journal of Physical Chemistry C* **2018**, *122* (6), 3233-3244.

69. Martinez, N.; Morin, A.; Berrod, Q.; Frick, B.; Ollivier, J.; Porcar, L.; Gebel, G.; Lyonnard, S., Multi-Scale Water Dynamics in a Fuel Cell by Operando Quasi Elastic Neutron Scattering. *The Journal of Physical Chemistry C* **2017**, *122*, 1103-1108.

70. Anantaraman, A.; Gardner, C., Studies on ion-exchange membranes. Part 1. Effect of humidity on the conductivity of Nafion®. *J. Electroanal. Chem.* **1996,** *414* (2), 115-120.

71. Inoue, R.; Kanaya, T.; Masuda, T.; Nishida, K.; Yamamuro, O., Relationship between the Local Dynamics and Gas Permeability of Para-Substituted Poly (1-chloro-2-phenylacetylenes). *Macromolecules* **2012,** *45* (15), 6008-6014.

72. Kanaya, T.; Tsukushi, I.; Kaji, K.; Sakaguchi, T.; Kwak, G.; Masuda, T., Role of local dynamics in the gas permeability of glassy substituted polyacetylenes. A quasielastic neutron scattering study. *Macromolecules* **2002,** *35* (14), 5559-5564.

6.

Summary and Outlook

6.1 Summary

This thesis has described the use of state-of-the-art analytical spectroscopy techniques to study structures, chemical compositions and local environments of polymer electrolyte materials used in hydrogen fuel cell (FC) devices. The results of the detailed spectroscopic analyses target the structure-performance relationship. A novel ssNMR method has been developed with the purpose of probing local dynamics in the polymers. The ^{19}F dipolar recoupling NMR approach has been validated and applied to PFSA membranes at different temperature and hydration conditions. STXM coupled with X-ray absorption spectroscopy (XAS) has supplied complementary chemical structural information for a number of PFSA materials. The electrochemical evaluation of electrolyte membranes in the membrane electrode assembly (MEA) has provided bulk performance details, which helps to establish the relationship between molecular physicochemical properties and the macroscopic *in situ/operando* performance. The main focus of this thesis is to demonstrate the applicability of the ssNMR approach to investigate local dynamics and the associated findings. A summary of the overall impact of this thesis and future directions is offered below.

6.1.1 Spectroscopic Analysis of PFSA

Chapter 3 summarizes a structural investigation of three PFSA materials (Nafion, Aquivion, and 3M PFSAs) using XAS analysis via STXM combined with ^{19}F and ^{13}C ssNMR spectroscopy, providing complementary structural information about the polymers of interest. A collaborative study using two modern analytical spectroscopies for the PFSA systems was reported for the first time. Additionally, a fluorine diffusion study by solution-state NMR is discussed in detail here to further distinguish the differences in ionomer dispersions.

The ssNMR spectral analyses have been done for Nafion with 1100EW (EW = equivalent weight), through correlation between the ^{13}C and ^{19}F signals.[1-2] However, the possible signals (carbon species) outside the main spectral span have never been reported for PFSA systems. In the initial XAS-based structural study, the F 1s near edge X-ray absorption fine structure (NEXAFS) is incapable of separating different PFSA species. Fortunately, the chemical sensitivity of ^{19}F NMR significantly aids in the differentiation of various types of PFSA materials. Conventional ^{19}F ssNMR with detailed spectral deconvolution resolves the polymer side chain and backbone signals effectively.

In a parallel XAS analysis of PFSA membranes and cast films from ionomer dispersion solutions at the C 1s and O 1s edges, the possibility of residual solvent (likely alcoholic species) from the manufacturing process, and the existence of a carboxyl group at the terminal end of the polymer chain have been proposed. The heroic natural abundant ^{13}C ssNMR results collected at a high magnetic field (~64 h/sample) support this hypothesis. With the low elemental content of O and S in the polymer system, ^{17}O and ^{33}S NMR measurement without any enrichment is

nearly impossible. Synchrotron-based STXM that takes advantage of soft X-rays is able to study the material at the O 1s and S 2p edges, such that the full chemical speciation of the side chain is revealed. The two spectroscopies provide a detailed interpretation of all spectral features, such that complementary information can be gained in the analysis of PFSA materials.

The molecular diffusion study of the ionomer dispersions with the same ionomer EW, Nafion and Liquion, is additionally reported towards the end of **Chapter 3.** The difference in diffusion profiles of the PFSA solutions as a function of temperature is illustrated. This result indicates that the molecular radius in the Liquion dispersion is smaller than that in Nafion with 1 wt% ionomer concentration. The different macroscopic diffusion profiles effectively differentiate the two solutions despite the fact that they have the same chemical composition with the same EW.

The exploration of the relative assets of STXM and ssNMR in characterizing PFSA materials has been successful. NMR is more chemically sensitive, but it does not provide easy access to the S or O environment directly. XAS analysis using STXM requires a synchrotron facility, which is less readily available than institute-based ssNMR; however, it provides a direct way to probe S and O elements and it is capable of spatially resolved chemical mapping for systems with multiple components, such as the catalyst layer (CL) and MEAs. The combination of the two techniques has great potential to provide detailed information on the subtle alterations in PFSA materials.

6.1.2 Dynamics Analysis Using ^{19}F Homonuclear Dipolar Recoupling Sequence

The importance of the dipolar interaction was thoroughly described in **Chapter 2.** A dipolar recoupling ssNMR approach has been developed for probing the local dynamics of the PFSA systems, which is explained after the introduction of the homonuclear dipolar interaction. This alternative method is very essential for materials that have multiple sites and require magic angle spinning (MAS) to achieve spectral resolution. The typical benchmark material, Nafion, was initially studied, and a scheme for comparing the motion for different regimes as a function of relative humidity (%RH) and temperature was developed and described in **Chapter 4.** A standardized metric is also introduced and applied to Nafion in order to quantitatively compare different PFSA materials in the same class.

Dynamics in a variety of materials can be analyzed via NMR relaxation studies using both spin-lattice and spin-spin relaxation measurements.[3-5] In solids, the second moment of the line shape can also be used to monitor dynamics.[6-8] Unfortunately, such an approach without MAS lacks spectral resolution and cannot differentiate the dynamics occurring at different sites in the material. Recent $^{19}F/^{13}C$ NMR linewidth analysis of Nafion under MAS and ^{19}F–^{13}C chemical shift correlation investigations indicate a dynamics gradient with respect to the backbone branch point.[1-2] This investigation focused on the use of CSA changes to evaluate the geometry of the side chain and backbone reorientations for Nafion;[1-2] however, it is not efficient with respect to the required experimental time. Therefore, a dipolar recoupling NMR technique as an effective alternative approach for dynamics studies of the polymer chain was developed and implemented.

The R-symmetry based dipolar recoupling ^{19}F NMR method combined with a second-moment approximation presents a quantitative and qualitative way to extract the effective/apparent ^{19}F-^{19}F homonuclear dipolar coupling constant from the initial normalized double quantum build-up curve. The analysis of the dipolar interaction at various hydration levels and temperatures and the difference in local dynamics at distinct fluorine sites has been monitored. In the investigation of Nafion 117, the backbone is shown to have low local dynamics whereas the side chain has higher dynamics, a result that is determined by the measurement of apparent dipolar coupling constants, D_{app}. The side chain shows increased sensitivity towards the humidity change relative to the backbone. The finding is correlated to the previous proton conductivity measurements, and the correlation is supported by the morphology development hypothesis.[9-10] The application of the dynamic order parameter, S^T, provides a comparative measure that allows the analysis to be extended to a wider range of related ionomer materials.

In **Chapter 4**, the development of the dipolar recoupling NMR method does not only present an efficient way to measure the local dynamics of the perfluorinated polymer quantitatively and qualitatively compared to the previous NMR methods, but also demonstrates the potential to be used in screening ionomer materials to understand the link between the molecular properties and bulk material performance.

6.1.3 Linking the Material Performance to the Molecular Physicochemical Properties

Local dynamics investigations using ssNMR have been applied to different types of PFSA materials, including Nafion, Aquivion and 3M PFSAs, with differences in side chain structures and EWs. The extended

study is reported in **Chapter 5.** In the first half, the NMR dynamics method was applied to PFSAs that are treated with the same experimental conditions as the Nafion material in **Chapter 4.** By doing so, parallel comparison amongst the PFSAs was made. The difference in side chain and backbone local dynamics in the Aquivion and 3M PFSA materials is temperature and hydration dependent, which agrees with the general trend observed in the Nafion system. Similar to the Nafion study, due to the lack of crystalline structure of the PFSA molecules, the geometry optimized small molecule structures that can represent the side chain and backbone are applied in the theoretical dipolar interaction calculations. S^T at different conditions can be extracted and compared. This local dynamics analysis of different PFSA materials (used throughout this thesis), which is reflected in the comparison of D_{app} values and S^T, is reported here for the first time.

Interestingly the difference in the side chain and backbone local dynamics in the PFSA systems at 25 °C with 50 %RH and 100 %RH suggests that PFSAs with higher EWs (~1000) show more sensitivity towards humidity changes, such as in the cases of Nafion with 1100EW and Aquivion with 980EW. On the other hand, the PFSA with low EW is shown to be less responsive towards condition changes in terms of the side chain local dynamics. This preliminary analysis presents a normalized approach to investigate the local dynamics difference between the hydrophobic and hydrophilic regimes for perfluorinated polymers below their glass transition temperature. This method further demonstrates the potential for these methods in unveiling the morphology development in ionomer materials.

In the second part of **Chapter 5**, the goal of the study was to understand the structure-property-performance relationship in PFSA

polymer electrolyte materials. The combination of *in situ* fuel cell performance evaluation and *ex situ* single-component NMR characterization has created a connection between the fundamental chemistry and the properties of the bulk material. The current FC operating challenge, fuel loss, was addressed here, along with analysis of proton conductivity properties. The benefit of this study is to mitigate the current FC design challenges, such as Ohmic losses caused by resistive proton transport that occurs at high current density.

The PFSA materials with different side chain types and EWs for the *ex situ* NMR study are conditioned parallel to the MEA operating condition at 40 °C and 80 °C with 50 %RH and 100 %RH. The EIS and CV analyses are performed on those materials simultaneously in the MEA form under operating conditions at the fuel cell test station. Both proton conductivity and H_2 permeability were found to increase as temperature and %RH increase. A ^{19}F ssNMR local dynamics study is reintroduced to study the side chain local motion at the molecular level. The strong correlation between proton conductivity and the D_{app} values of the SCF_2 site, as well as that correlation between the H_2 permeability and D_{app} were observed and investigated. The results suggested that the formation of the hydrophilic domains during hydration leads to an improvement in proton conductivity, while unfortunately promoting gas permeability.

Based on the proposed proton transport mechanism, the local dynamics of the side chain in PFSA plays a significant role in transporting protons while the hydration is insufficient due to the lack of a water network when the Grotthus mechanism dominates. Conversely, with sufficient water content the formation of water networks promotes the vehicular mechanism, in which the side chain local dynamics do not

contribute as significantly as they did at dryer conditions. Another exciting finding is that when the correlations between gas permeability and polymer chain local dynamics are compared, the correlation of the side chain local motion is more pronounced compared to that of the backbone. This suggests that the intermediate phase, which is reflected and represented by the D_{app} values of SCF_2, between the aqueous phase (water network) and solid phase (polymer hydrophobic backbone) has a much more limited impact on gas permeation.

This is the first study with the goal of connecting the material physicochemical properties determined by *ex situ* ^{19}F NMR techniques to *in operando* electrochemical performance measurements. This work aims to parameterize the structural impact at a molecular level and to provide insight into methods for improving polymer electrolyte materials.

6.2 Future Work and Outlook

This thesis outlines the combination of modern spectroscopic techniques that can be used to probe structure-performance relationship of proton exchange membranes, specifically PFSA materials. The novel results from the current work produce a better understanding of PFSA structure related morphology development and provide important insight for future membrane and hydrogen fuel cell development.

The analysis of PFSA materials in this thesis demonstrates the importance of a combined spectroscopic approach through the acquisition of complementary NMR and NEXAFS spectra. Nevertheless, there are still uncertainties regarding the NEXAFS transition assignments mentioned in **Chapter 3.** Additional small molecule investigations could potentially provide evidence to support the existence of the carbonyl group in the

PFSA materials. For instance, measurements of fluorinated carboxylic acids such as pentafluoropropionic acid (CF_3CF_2COOH) and its derivatives could assist in the identification of the carbonyl groups within a highly fluorinated environment.

As ssNMR is very sensitive towards fluorine environments, it is a great tool for both quantitative and qualitative structure elucidation of PFSA species. The conventional ^{19}F NMR analysis of single-component PFSA can provide reference data without additional interference from the carbon support or Pt catalysts. Meanwhile, the S 2p and O 1s NEXAFS are informative regarding local environment on the proton-conducting site, i.e. the sulfonic acid group. This serves as another tool to study ionomer materials, even in the presence of other fuel cell components. The application of S 2p NEXAFS *via* STXM coupled with ^{19}F ssNMR will be an appropriate and powerful approach to investigate membrane or ionomer degradation in the CL, or to study the MEA aging processes. Ultimately, the STXM-ssNMR combination would offer characterization of both the spatial and chemical nature of operationally induced degradation. The ability to quantify side-chain loss by highly resolved ^{19}F ssNMR and sulfonic group loss by S 2p XAS will provide remarkable information in MEA degradation studies. At the same time, the combined spectroscopic approach can be used to study the role of chemical stabilizers that help ionomer solutions stay dispersed such as carboxylic acid groups in PFSA materials.

In the local dynamics study for different PFSAs, an advanced ssNMR method has been developed and validated. The dynamics difference between the polymer side chain and backbone has been observed and well characterized by comparing the D_{app} and the S^T values at different experimental conditions. Unfortunately, each class of PFSA only has one

or two examples to investigate, and thus the specific roles of EW and the nature of the side chain in polymer local dynamics are unable to be generalized here. Studying PFSAs with the same side chain structure but varying EWs using the NMR dynamics method at different temperature and hydration conditions will specifically probe only the effect of the EW. The side chain behavior will be explored as the EW changes in the PFSA system. As one promising alternative PFSA to replace Nafion, a series of 3M PFSA materials with EWs ranging from 580 to 1100 can additionally be explored. The 3M PFSAs have similar side chain lengths at the atomic level and only one vulnerable ether bond, in comparison to the gold standard, Nafion, which has two. Nevertheless, *in situ* electrochemical performance analysis for this class of PFSA will also be an excellent way of achieving an in depth understanding of how the structure influences the performance. Furthermore, investigating PFSAs with the same EW but different side chain types will reveal the impact of the PFSA side chain type especially since the side chain structure heavily affects the morphology development in PFSA systems.

Monitoring the apparent homonuclear dipolar interactions in the fluorine systems creates a unique and effective handle to probe the local dynamics in polymeric systems. This technique can also be applied to hydrocarbon-based proton conducting materials to yield similar dynamics insight. Many examples have demonstrated the successful use of ^{1}H-^{1}H homonuclear dipolar interaction measurements in macromolecular or supramolecular systems using the dipolar recoupling NMR technique for structure elucidation.[11-16] The application to hydrocarbon polymers will assist with the identification of proton transport mechanisms from the perspective of both the polymeric backbone and the conducting proton species simultaneously.

Discovering the structure-performance relationship of electrolyte materials is important for hydrogen fuel cell development. Studying PFSAs in membrane form provides the ability to evaluate the electrolyte component in the device. The ionomer component in the CL, with the same chemical structure as PFSA membranes, plays a crucial role in FC operation as well. The CL requires high O_2 transport ability to facilitate proton consumption on the electrode, thus minimizing the mass transport limitations in the MEA. O_2 permeability in the ionomer and how the polymer structural properties influence the permeation process has become a riveting topic in the fuel cell community. To correlate the O_2 gas permeability and the PFSA polymer local dynamics profiles and to understand how the gas molecules permeate in the ionomer within the CL will help to mitigate H_2 fuel loss and facilitate O_2 transport. The exploration and discovery of optimal membrane/ionomer materials with high proton conductivity and advantageous gas permeability is required for the commercialization of PEMFCs in automotive applications.

Ultimately, with the fast development of specialized spectroscopy instrumentations, which will promote the use of *in situ/in operando* experiments, studying the MEA component under operational conditions will become possible. Many outstanding *in situ* studies using NMR and STXM involving electrochemical reactions have demonstrated the advantages of monitoring the chemical process during operation.[17–20] Although purging H_2 and O_2 into an analytical instrument is potentially risky and challenging, doing so could provide critical information to aid in the development of future PEMFCs. The developments presented in this thesis illustrate a much clearer picture of PFSA chemical compositions and how the molecular dynamics profile within the polymer chain correlates to the material's electrochemical performance using

advanced NMR techniques. The key findings from the current study demonstrate the importance of the intermediate phase of the polymer (between the solid phase and aqueous phase) in the gas permeation process and the significance of side chain local motion in proton transport. Materials with small intermediate phase domains that have good local mobility in the side chain are therefore optimal targets for future PEMFC electrolyte materials.

6.3 References

1. Chen, Q.; Schmidt-Rohr, K., 19F and 13C NMR signal assignment and analysis in a perfluorinated ionomer (Nafion) by two-dimensional solid-state NMR. *Macromolecules* **2004,** *37* (16), 5995-6003.

2. Chen, Q.; Schmidt-Rohr, K., Backbone Dynamics of the Nafion Ionomer Studied by 19F-13C Solid-State NMR. *Macromol. Chem. Phys.* **2007,** *208* (19-20), 2189-2203.

3. Dong, R. Y., *Encyclopedia of Spectroscopy and Spectrometry: I-N*. Academic Press: 2000; Vol. 2.

4. Duer, M. J., *Introduction to Solid-state NMR Spectroscopy*. Blackwell Science: Oxford, UK, 2004.

5. Levitt, M. H., *Spin dynamics: basics of nuclear magnetic resonance*. John Wiley & Sons: Chichester, 2001.

6. Goc, R., Calculation of the NMR second moment for materials with different types of internal rotation. *Solid State Nucl. Magn. Reson.* **1998,** *13* (1), 55-61.

7. Hyndman, D.; Origlio, G. F., NMR absorption in Teflon fibers. *J. Appl. Phys.* **1960,** *31* (11), 1849-1852.

8. Tritt-Goc, J.; Piślewski, N.; Szczepańska, L.; Goc, R., Dynamics of a glycine molecule in a new ferroelectric glycine phosphite studied by proton NMR. *Solid State Commun.* **1998,** *108* (3), 189-192.

9. Kreuer, K.-D.; Paddison, S. J.; Spohr, E.; Schuster, M., Transport in proton conductors for fuel-cell applications: simulations, elementary reactions, and phenomenology. *Chem. Rev.* **2004,** *104* (10), 4637-4678.

10. Zawodzinski, T. A.; Derouin, C.; Radzinski, S.; Sherman, R. J.; Smith, V. T.; Springer, T. E.; Gottesfeld, S., Water uptake by and

transport through Nafion® 117 membranes. *J. Electrochem. Soc.* **1993,** *140* (4), 1041-1047.

11. Baek, S. B.; Moon, D.; Graf, R.; Cho, W. J.; Park, S. W.; Yoon, T. U.; Cho, S. J.; Hwang, I. C.; Bae, Y. S.; Spiess, H. W.; Lee, H. C.; Kim, K. S., High-temperature in situ crystallographic observation of reversible gas sorption in impermeable organic cages. *Proc. Natl. Acad. Sci. U. S. A.* **2015,** *112* (46), 14156-61.

12. Graf, R.; Heuer, A.; Spiess, H. W., Chain-Order Effects in Polymer Melts Probed by H 1 Double-Quantum NMR Spectroscopy. *Phys. Rev. Lett.* **1998,** *80* (26), 5738.

13. Hansen, M. R.; Graf, R.; Spiess, H. W., Solid-State NMR in Macromolecular Systems:
Insights on How Molecular Entities Move. *Acc. Chem. Res.* **2013,** *46* (9), 1996-2007.

14. Hansen, M. R.; Graf, R.; Spiess, H. W., Interplay of Structure and Dynamics in Functional Macromolecular and Supramolecular Systems As Revealed by Magnetic Resonance Spectroscopy. *Chem. Rev.* **2016,** *116* (3), 1272-308.

15. Pfeffermann, M.; Dong, R.; Graf, R.; Zajaczkowski, W.; Gorelik, T.; Pisula, W.; Narita, A.; Mullen, K.; Feng, X., Free-Standing Monolayer Two-Dimensional Supramolecular Organic Framework with Good Internal Order. *J. Am. Chem. Soc.* **2015,** *137* (45), 14525-32.

16. Saalwächter, K.; Lange, F.; Matyjaszewski, K.; Huang, C.-F.; Graf, R., BaBa-xy16: Robust and broadband homonuclear DQ recoupling for applications in rigid and soft solids up to the highest MAS frequencies. *J. Magn. Reson.* **2011,** *212* (1), 204-215.

17. de Groot, F. M.; de Smit, E.; van Schooneveld, M. M.; Aramburo, L. R.; Weckhuysen, B. M., In-situ scanning transmission X-ray microscopy of

catalytic solids and related nanomaterials. *Chemphyschem* **2010,** *11* (5), 951-62.

18. Tzvetkov, G.; Graf, B.; Fernandes, P.; Fery, A.; Cavalieri, F.; Paradossi, G.; Fink, R. H., In situ characterization of gas-filled microballoons using soft X-ray microspectroscopy. *Soft Matter* **2008,** *4* (3), 510-514.

19. Krachkovskiy, S. A.; Bazak, J. D.; Werhun, P.; Balcom, B. J.; Halalay, I. C.; Goward, G. R., Visualization of steady-state ionic concentration profiles formed in electrolytes during Li-ion battery operation and determination of mass-transport properties by in situ magnetic resonance imaging. *J. Am. Chem. Soc.* **2016,** *138* (25), 7992-7999.

20. Ogawa, K.; Haishi, T.; Aoki, M.; Hasegawa, H.; Morisaka, S.; Hashimoto, S., NMR measurement system including two synchronized ring buffers, with 128 rf coils for in situ water monitoring in a polymer electrolyte fuel cell. *Rev. Sci. Instrum.* **2017,** *88* (1), 014701.

Appendix 1.

Material Performance Study

This work is under the non-disclosure agreement between the Goward research group at McMaster University and Ballard Power Systems (BPS). Experimental details cannot be released. This work was completed during an internship at BPS, fully funded by a CaRPE-FC grant. The publication of this section has been allowed with permission from BPS.

A.1.1 Introduction

Besides the cyclic voltammetry (CV) analysis mentioned in **Chapter 5**, another in situ performance evaluation method of PFSA is the polarization curve. As one of the standard fuel cell (FC) diagnostic tools, it is essentially a plot of cell potential against current density under operational conditions. It aims to provide information regarding the performance losses. A steady-state polarization curve is often plotted by recording cell potential as cell current changes. This was the method applied during the membrane electrode assembly (MEA) evaluation study at BPS.

Governed by the Butler-Volmer Equation[1, 2], the cell potential undergoes activation loss/polarization when the current densities are low. This loss is solely due to the slow kinetics of the oxygen

reduction reaction (ORR) on the cathode. Once the activation overpotential becomes relatively stable, Ohmic loss becomes important for intermediate current densities. The resistance that proton flow experiences between electrodes causes a drop in cell potential. In this region, the cell potential decreases linearly with the current density. At higher current densities, reactant is consumed rapidly, especially at the electrode, during operation; therefore, concentration gradients are created. Based on the Nernst Equation (see **Equation 5.1** in **Chapter 5**), the gradient created at the interface between the electrode and electrolyte, the reaction quotient increases, and therefore the cell potential decreases. This is defined as the concentration loss. This phenomenon is also referred as the mass transport effect. An ideal polarization curve is demonstrated in **Figure A1.1**, in which the three main losses are labeled accordingly.

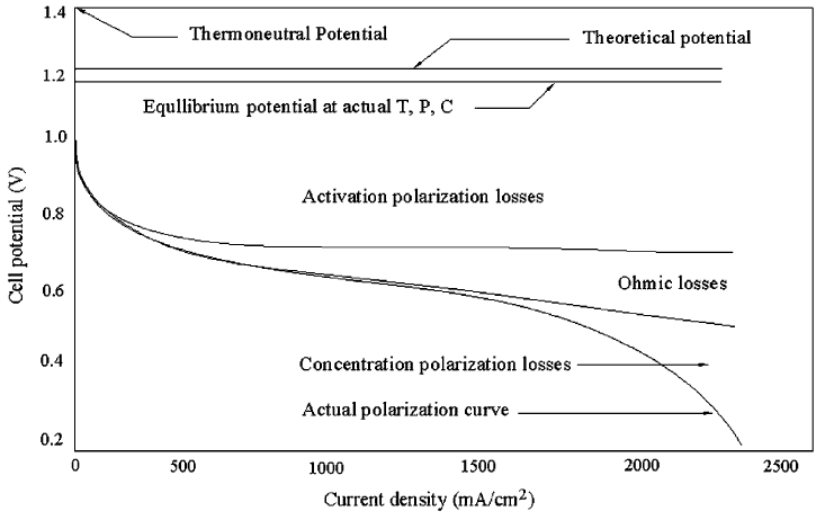

Figure A1. 1 Ideal polarization curve for an operating polymer electrolyte membrane fuel cell (PEMFC), with corresponding labels for different losses.[1, 2] [Reprinted with permission from Ref.2]

Many model schemes are proposed to elucidate the electrochemical behavior of PEMFC based on polarization curves. Many empirical

equations are introduced, including the Tafel equation to understand activation losses. However, for the purpose of extracting PFSA membrane resistance information, only the Ohmic region is considered in this study. From the linearity, the resistance experienced by the ion flow can be extrapolated and calculated. With the MEA designs of single-layered (SL) and double-layered (DL) membrane, the through-plane membrane resistance was extracted and compared to an EIS study mentioned previously in **Chapter 5.**

A.1.2 Experimental

All polarization curves were collected at the MEA test station located at BPS, Burnaby, BC, Canada. MEAs used for testing in this section were the same as the MEAs that were prepared for the CV analysis.

The current used in the polarization curve analysis ranged from 0 A to 99 A under operating conditions, which was supplied by a load bank. The gases used were supplied through customized vapour conditioners with thermal and humidity control, at 80 °C with 100 %RH. H_2 gas was fed into the anode, while the O_2 or 21% O_2 in N_2 was fed into the cathode, with the inlet pressure at 5 psig for both gas supplies. The cell potential was collected with different current inputs. The detailed current input program is not provided here.

The curve was analyzed using the Excel Macro program written in visual basic for applications (VBA) developed by the research department at BPS. Using input parameters describing the catalyst loading, active MEA area, gas flow rate, temperature and RH, the resistance at the Ohmic region was calculated.

A.1.3 Results and Discussion

A.1.3.1 Polarization Curves of MEAs

As discussed earlier in **Chapter 5**, the purpose of designing MEAs with SL and DL membrane(s) is to extract the membrane properties without the influence of other MEA components. An example set of polarization curves at FC operating condition is shown in **Figure A1.2.** NR211 was used as a standard PFSA membrane, and its MEA polarization curve analysis is presented. In **Figure A1.2**, the blue data set represents the MEA with SL NR211, while the green dataset is for the MEA with DL NR211. All of the polarization curves were collected with the same operating parameters, except for the O_2 concentration on the cathode. The hollow data points were collected under H_2/O_2(21%), while the solid points were under H_2/O_2(100%). The fitted curves for SL NR211 MEA generated using the program developed by BPS show agreement between the model and the experimental measurements. The DL MEA shows worse performance than the SL. This is the result of doubling the ion transport path length, i.e. the distance between electrodes. From the fitted curves, the cell resistance can be extrapolated from the Ohmic region, which is the slope of the linear region. Assuming the interface has a minimal contribution to cell resistance, the membrane resistance can be calculated by subtracting R_{Single} from R_{Double}, where the resistance contribution from other MEA components can be simply ignored.

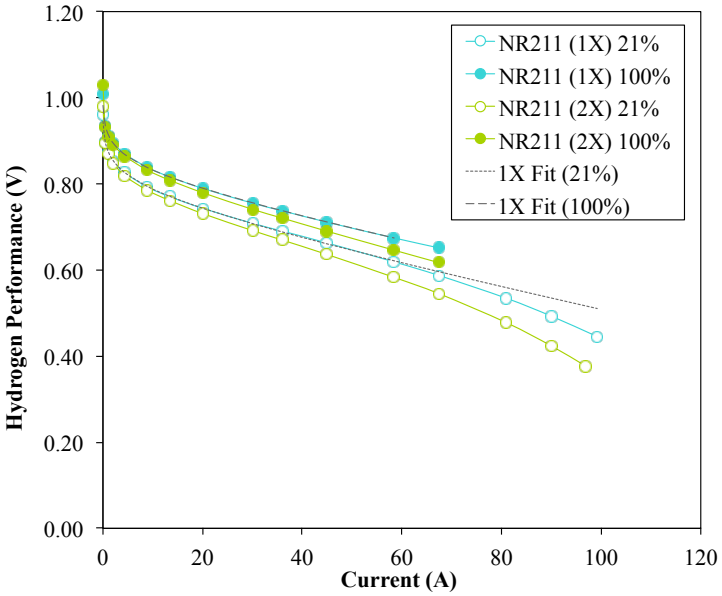

Figure A1. 2 An example set of polarization curves with SL and DL MEA designs using NR211 membrane. The experiments were performed with 100% O_2 or 21% O_2 at 100 %RH 80 °C.

When comparing cell performance under different O_2 concentrations, the cell at 100% O_2 performed better than at 21% O_2, which is shown by a lower voltage loss and no significant mass transport loss. It is caused by a more efficient ORR on cathode from the high concentration of O_2. Hence, the membrane resistance values were analyzed using the cells operated using 100% O_2.

A.1.3.2 PFSA Membrane Resistance

Resistance and conductivity values for PFSA membranes are summarized in **Table A1.1.** The detailed description and the labeling system have been introduced in **Chapters 1** and **5.** All the resistance values were converted into conductivities normalized for membrane thickness, based on the following equations:

$$\sigma = \frac{1}{\rho}$$

$$\rho = R\frac{A}{l}$$

$$\therefore \sigma = \frac{l}{R \cdot A}$$

where σ is the ionic conductivity, ρ is the resistivity, A is the active cross-sectional area, l is the ion conductive path length, and R is the resistance.

Table A1. 1 Summary of PFSA resistance and conductivity in this study.

PFSA	Resistance ($\times 10^3$ Ω/cm^2)	Conductivity (S/cm)
3M725	1.0	17.8
3M825	0.8	22.2
AQ870	1.3	13.7
AQ980	1.2	14.8
NR211	0.5	13.8

The PFSA membrane conductivity values from electrochemical impedance spectroscopy (EIS) measurements introduced in **Chapter 5** are compared with the conductivity data extracted from the polarization performance analysis here. The comparison of conductivity from these two electrochemical methods is shown in **Figure A1.3.** Theoretically, the conductivity values from different methods should be equal (grey dashed line), however there is a systematic inconsistency in the experimental data. The conductivity data collected from the EIS method were greater than the ones calculated from the polarization curves. In the polarization performance analysis, there are more FC components involved in the process, compared to the EIS measurements collected under N_2/H_2 environment. The increase in complexity possibly attributes to the lower conductivity results.

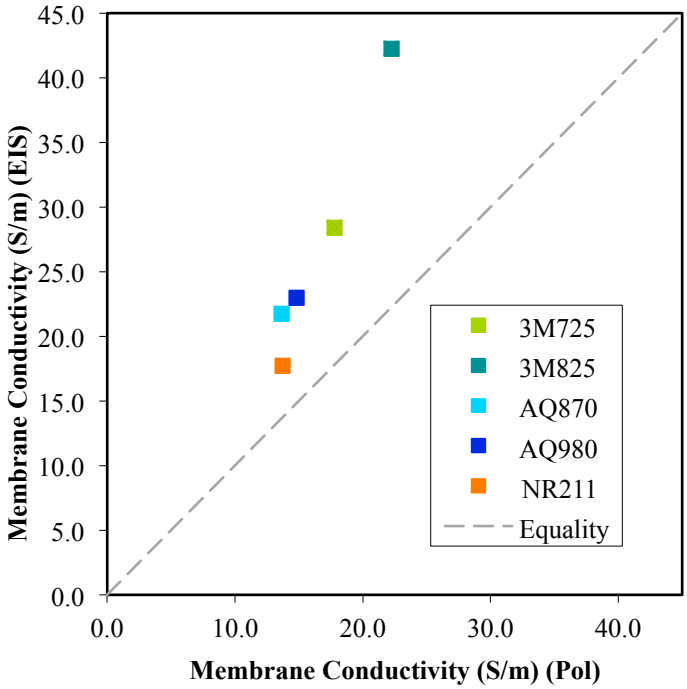

Figure A1. 3 PFSA conductivity comparison between two different electrochemical methods: EIS and polarization performance analysis.

A.1.4 Summary and Remark

The purpose of the internship was to explore and to familiarize the electrochemical evaluation methods in an industrial setting, including preparing MEA test cell, setting up the test station, collecting and analyzing raw data. Understanding the chemistry behind the polarization curve and extracting conductivity information from it provides an access to the conductive properties of the PFSA materials.

This study aims to evaluate the PFSA membranes under operational conditions in MEA form along with other FC components. The polarization curves were successfully collected and analyzed. The PFSA conductivity values were reported and compared with EIS data (shown in **Figure A1.3**). A systematic inconsistency between these two methods was observed, which is attributed to a different sample matrix. The polarization curve can

capture every single step in a fuel cell operation. The analysis of polarization curve can unveil many other useful information of a cell function. On the other hand, for the purpose of investigating the membrane properties, the EIS method is more beneficial compared to the polarization study since it eliminates additional influences such as the catalysis efficiency.

A.1.5 References

1. F. Barbir, *PEM fuel cells: theory and practice*, Academic Press, New York, 2012.
2. J. Wu, X. Z. Yuan, H. Wang, M. Blanco, J. J. Martin and J. Zhang, *Int. J. Hydrogen Energy*, 2008, **33**, 1735-1746.

Appendix 2.

Gas Permeability Study

This work is under the non-disclosure agreement between the Goward research group at McMaster University with BPS. Experimental details cannot be released. The work from this section was completed during an internship at Ballard Power Systems (BPS) (mainly in 2017), fully funded by a CaRPE-FC grant. The publication of this section has been allowed with permission from BPS.

A.2.1 Introduction

Gas permeation is a major concern in PEM development. As described in **Chapter 5**, H_2 permeation causes cell deficiency due to fuel loss.[1-6] Similarly, O_2 can pass through the membrane causing reduction of FC performance, especially because the oxygen reduction reaction (ORR) is the rate-limiting step for the operating process. Many studies have addressed this issue and reported the permeability of various PEM materials.[1, 2, 7, 8] The O_2 permeability (P_{O_2}) is reported to be much smaller than the H_2 permeability (P_{H_2}), thus its significance is often de-emphasized. The exploration of P_{O_2} measurements will be addressed in this section.

Similar to the P_{H_2} study described in **Chapter 5**, the P_{O_2} of different PFSA materials has been measured via two different electrochemical techniques: ORR limiting current studies and the time-lag method. The overall effectiveness of different methods is addressed in this section.

Both methods are well established in theory. The time-lag method setup was recently developed by BPS, for single cell and stack evaluation. Therefore, prepared MEAs were required, and the health and seal of a MEA is critical to the success of this method. On the other hand, the P_{O_2} from the ORR limiting current study focuses on the PFSA material itself. The experimental setup was essentially a solution-based three-electrode cell with a rotating disk electrode (RDE) as the working electrode. Thus, the stability of the PFSA in the cell becomes a major challenge.

A.2.2 Methodology

A.2.2.1 Time-Lag Method

The time-lag method is also known as the transient pressure change method.[9] A known quantity of gas is introduced to the system, and the pressure change as a function of time is monitored. The steady state permeability condition is established once the supply gas pressure has built up and remains constant. This method will detect a linear change in pressure with time change. The cathode outlet pressure was monitored using a digital barometer in this study. Different gas pairs purged independently onto the cathode and anode at the same time. In order to create a baseline for the measurement, N_2/N_2 pair was used to determine

the systematic gas loss in the cell, if any. N_2/H_2, O_2/N_2 and O_2/H_2 gas pairs were used sequentially under this method to extract H_2 and O_2 permeability. Each gas pair was denoted as the cathodic gas supply versus the anodic gas supply. H_2 permeates through the MEA from anode to cathode, while the O_2 permeation is from cathode to anode. The investigation under O_2/H_2 pair is to analyze any additional influence when the cathode and anode gases are reactive towards each other.

A.2.2.2 ORR Limiting Current Analysis using RDE

The limiting current analysis for the ORR using RDE has been mainly applied in catalysis efficiency studies, and it is a method that is often used in the laboratory.[7, 8, 10] The 3-electrode cell is in the electrolyte solution, and connected to a potentiostat. A CV curve is collected as described in **Chapter 5**; however with different potential limits since only the cathode reaction is involved. The benefits of this method include: it separates the cathodic and anodic reactions, such that unnecessary factors can be minimized or eliminated; it is a much faster process and requires much less material compared to preparing a MEA, therefore it is efficient as a preliminary method. Theoretically, it is a straightforward method in this case for the measurements of O_2 permeation in PFSA.

The working electrode (RDE) used was a pure Pt electrode supported with stable polymer materials (e.g. polytetrafluoroethylene, poly (ether ether ketone). The electrolyte solution used was freshly prepared 0.1 M $HClO_4$ (with 18 MΩ water).

Additionally the CV curve analysis on the Pt electrode along with the PFSA can also provide information regarding anion adsorption on the

surface.[8, 10] This was the secondary goal for this study, however the system used was far from ideal and this part of the study has been discontinued. The explanation is delivered below.

A.2.3 Results and Discussion

A.2.3.1 Gas Permeability Using Time-Lag Method

The time-lag method requires minimal gas leakage of the cell (stack), to achieve optimal accuracy and to minimize possible O_2 release for safety concerns. All MEAs prepared were imaged using an infrared camera to detect pinholes or leakages prior to this study. Unfortunately, due to the shortage of PFSA materials, a limited number of MEAs with different PFSAs were prepared and used for performance analysis (in **Appendix 1**) a few months prior to the gas permeation project. Several of them were damaged, showing pinhole formations and non-ideal seals, therefore they were not used in the current study. There were three MEAs investigated using the time-lag method, and each MEA was monitored at 80 °C and 50% or 100% RH, resulting in six data points.

With this in mind, the objective of measuring P_{O_2} for different PFSA materials switched to exploring the method and establishing an understanding of the measurements and analysis. Furthermore, results from the time-lag method have been compared to the information collected using CV analysis.

A typical set of permeability curves is demonstrated in **Figure A2.1.** As mentioned earlier, the gas pairs N_2/H_2, O_2/N_2 and O_2/H_2

were used sequentially after the N_2/N_2 baseline was obtained. Another N_2/N_2 baseline was collected and compared at the end of each set, and the average of the two baselines was used for calculations (not shown in **A2.1**). The pressure change under N_2/H_2 was positive because the H_2 is likely to pass through the membrane to the cathode side (see **A2.1b**). Thus, the pressure monitored on cathode increases as the H_2 gas is supplied. The cathodic pressure drops when N_2 or O_2 is supplied, resulting in negative lines of best fit (see **A2.1a, A2.1c** and **A2.1d**).

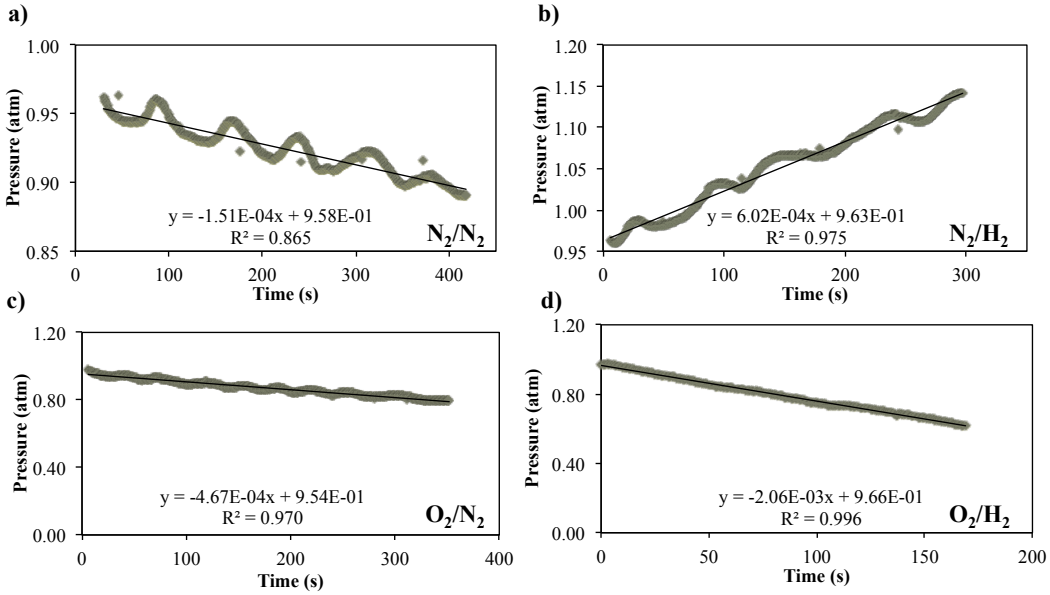

Figure A2. 1 A set of permeability curves of NR211 MEA (SL PFSA) using time-lag method under four different gas conditions. a) N_2/N_2. b) $N_2/H2$. c) O_2/N_2. d) O_2/H_2. The line of best fit was resulted from linear regression analysis.

From the change in pressure as a function of time, the permeability can be converted from the flux, where flux was computed based on the pressure change. Under N_2/H_2 conditions, the CV curves were also collected simultaneously to further calculate P_{H_2}. By doing so, it provided two methods to monitor the H_2 permeation behaviour in parallel. The resulting comparison is shown in **Figure A2.2.**

The time-lag method shows higher results compared to the CV analysis in **A2.2.** The difference between the two methods lies between 4-33%. This is possibly due to the absence of calibration in the CV analysis. The baseline calibration may have over-corrected the systematic gas loss.

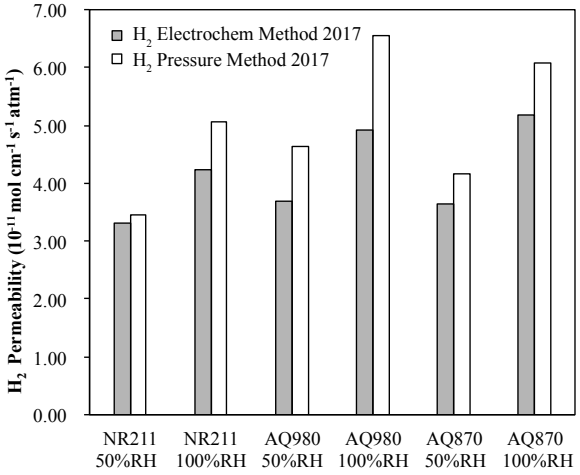

Figure A2. 2 P_{H_2} comparison between the CV method and the time-lag method. Only three MEAs passed the leakage-imaging test (infrared camera), which were reported here.

To validate the time-lag method, the permeability of H_2 and O_2 were compared, since the P_{H_2} is expected to be roughly 1.5 times higher than the P_{O_2} .[1] The correlation is shown in **Figure A2.3.** The linearity indicates the 1.5 times correlation between P_{O_2} and P_{H_2} , and the experimental data points using the time-lag method generally follow this correlation, as observed in the literature with minor deviations.[1] From the six data points obtained, the agreement between the experimental results and the literature correlation is observed. Furthermore, from the comparison in **A2.2**, the time-lag method is likely to overestimate the permeability, however it provides an effective method to measure the

bulk P_{O_2} directly, which is usually difficult to obtain with the MEA setup. With the knowledge of the overestimation, the actual P_{O_2} can be predicted.

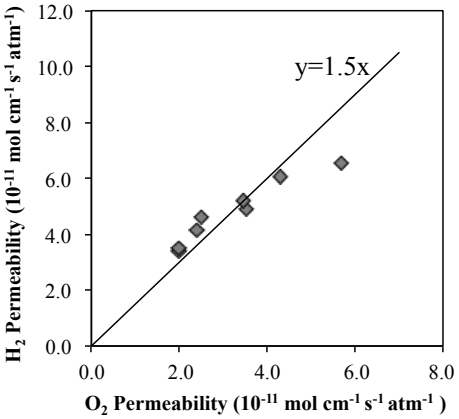

Figure A2. 3 Correlation between H_2 and O_2 permeability of the three MEAs tested using the time-lag method. The linear correlation is function: y=1.5x.

Damage was observed in the infrared imaging of the MEAs. There were only 3/10 MEAs that were testable, despite the fact that they were all stored in deionized water (DIW) at room temperature. A different degree of damage in prepared MEAs is expected. To confirm this, P_{H_2} values as reported in **Chapter 5** (collected in 2016) were compared to the new set of data. The bar-diagram comparison (similar to **A2.2**) is demonstrated below in **Figure A2.4.** The H_2 permeability values from CV analyses in 2016 and 2017 are compared, along with the values calculated from the time-lag method.

Disregarding the overestimation of the time-lag method, the data collected in 2017 show higher values compared to 2016. The aged MEAs become more permeable as a result of routine MEA testing and improper storage. It is possible that there are small pinholes formed following

MEA testing without being detected under infrared. Increases in permeability have been observed in MEA lifetime studies under 50 hrs.[4] The time between the two current CV analyses was 8 months, so it is unsurprising that the MEAs have been damaged.

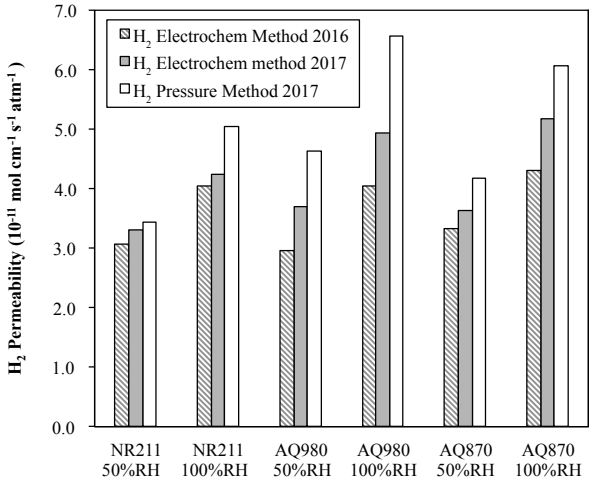

Figure A2. 4 H_2 permeability comparison from CV analyses conducted in 2016 and 2017, along with information calculated from the time-lag method obtained in 2017.

The permeability values of the PFSA collected at different time under different methods generally follow the same trend: higher %RH promotes the gas permeation, and the PFSA with lower equivalent weight (EW) has slightly higher gas permeability. This observation can be explained by higher proportion of the hydrophilic ionic domain. This increase in hydrophilic domain occurs when the hydration level is high, and especially for PFSA with low EW it has more hydrophilic side chains per unit weight. The detail discussion can be found in **Chapter 5.**

The time-lag method will overestimate the permeability compared to the electrochemical method (CV analysis) by over-correcting the systematic gas leakage. Yet, it is the most effective way to probe bulk O_2 permeation in MEA form. With proper adjustment, the gas permeability can be reliably estimated. Additionally, aging effects and storage

conditions are influential to MEA damage, which leads to increased gas permeability. Therefore, to have more accurate results for the current research purposes, freshly prepared MEAs are necessary.

A.2.3.2 Limiting Current Analysis of the ORR using RDE

The CV curve analysis for the ORR is useful for providing information regarding anion adsorption of the electrode and gas permeability of the attached film. To investigate gas permeation through the PFSA material, PFSA thin films were deposited onto the working electrode (RDE) from ionomer dispersion solutions with various concentrations ranging from 0.125 wt% to 5 wt%.

As described in section A.2.2.2, the system is very sensitive towards the cell environment. With limited control of the cell setup and experimental time constraints, setting up an experiment with reliable results becomes challenging. The general objective/work flow chart is illustrated in **Figure A2.5.**

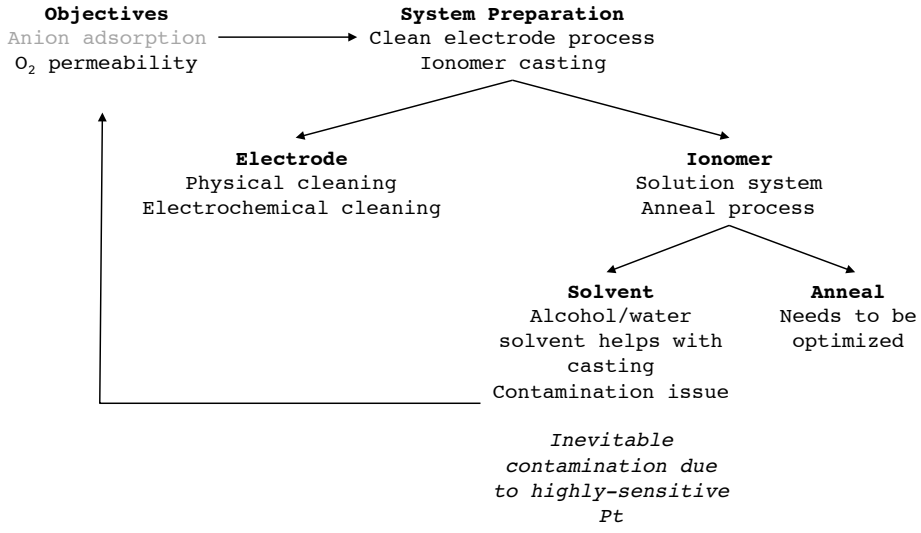

Figure A2. 5 Work flow chart of ORR study using RDE. Objective – anion adsorption has been greyed out. The explanation is stated below.

Throughout the working process, there are two key factors to the success of the study: uniform stable ionomer thin films and a clean cell environment. The physical and electrochemical cleaning of the Pt electrode was tested and proved to be effective when compared to literature, by comparing the limiting current of the bare electrode at different rotation speeds.[8] In order to obtain a uniformly cast thin film, spin coating with different rotation speeds and dispersion solutions with different solvent systems (with various alcoholic contents) were both examined. The alcoholic solvent system helps to reduce the surface tension of the dispersion droplet interacting onto the smooth Pt electrode surface. With proper rotation speed, a uniformly coated thin film can be formed; however, the alcohol species introduces contamination into the cell, especially in the case where pure Pt is used as an electrode, which is extremely sensitive towards contamination. To test the cleanness of the cell, a cell with a clean Pt RDE was soaked into freshly prepared electrolyte solution. A non-ideal CV performance was observed in a closed environment after an hour without any addition of foreign chemicals as shown in **Figure A2.6**, and this unanticipated non–ideal CV performance is due to the contamination on Pt surface. The contaminants are likely from the non-ideal closed cell and glassware. Therefore, the contamination of the Pt electrode is inevitable. The initial objective to probe anion adsorption has been abandoned (it has been greyed out in **A2.5**, since it requires an extremely clean cell environment to achieve.

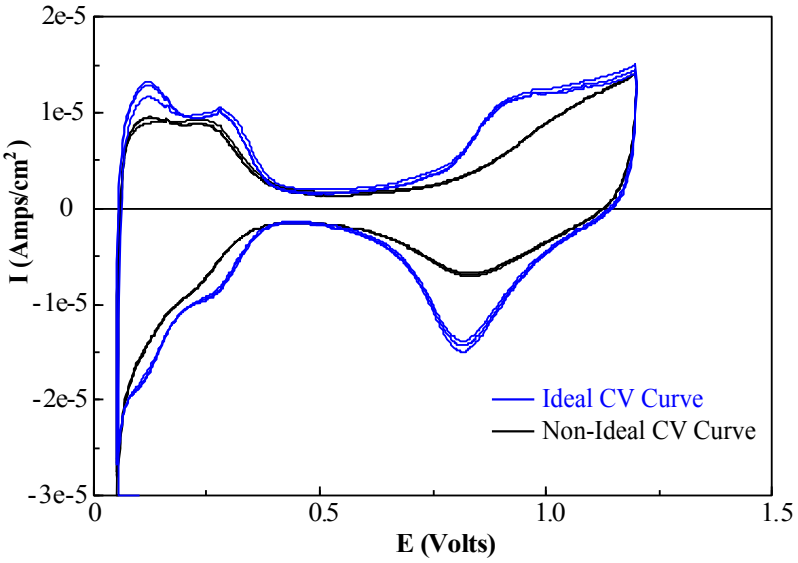

Figure A2. 6 The CV performance of bare Pt electrode comparison, and each analysis was done in three cycles: blue – ideal CV curves; black – non-ideal CV curves.

Another objective of this study is to investigate O_2 permeation. The measurement through the limiting current analysis of ORR in $HClO_4$ electrolyte solution has been conducted. The limiting current of ORR is governed the Levich equation, which models the diffusion and kinetic flow conditions at the interface around the RDE, expressed below.[8, 11]

$$I_L = (0.620)\, nFAD^{\frac{2}{3}}\omega^{\frac{1}{2}}\upsilon^{\frac{-1}{6}}C$$

where I_L is the Levich current or limiting current, n is the number of moles of electrons transferred in the half reaction (n equals 4 in this case), F is the Faraday constant, A is the electrode area (it is 0.196 cm^2 for a standard Pt RDE), D is the diffusion coefficient, ω is the angular rotation rate of the electrode, υ is the solution viscosity, and C is the analyte concentration (O_2 in this case). The solution viscosity and O_2 concentration in the electrolyte solution have been determined previously in the literature.[12] For O_2 in a solution system, the product of the concentration of the gas and the diffusion

coefficient is indicative of the permeability of O_2 through the cast thin film.

From the Levich equation, the limiting current is linearly dependent on the square root of the rotation speed, because the permeability of O_2 in all cases should be a constant value. The experiments were simply conducted in electrolyte solution with saturated O_2, and the limiting current values were measured by reading out the current at the plateaus. By comparing the limiting current resulting from RDE with PFSA coating to that of the pure Pt electrode at different rotation speeds, the permeability of O_2 through that specific coating can be calculated.[8] Example curve sets of the limiting current study are shown in **Figure A2.7.**

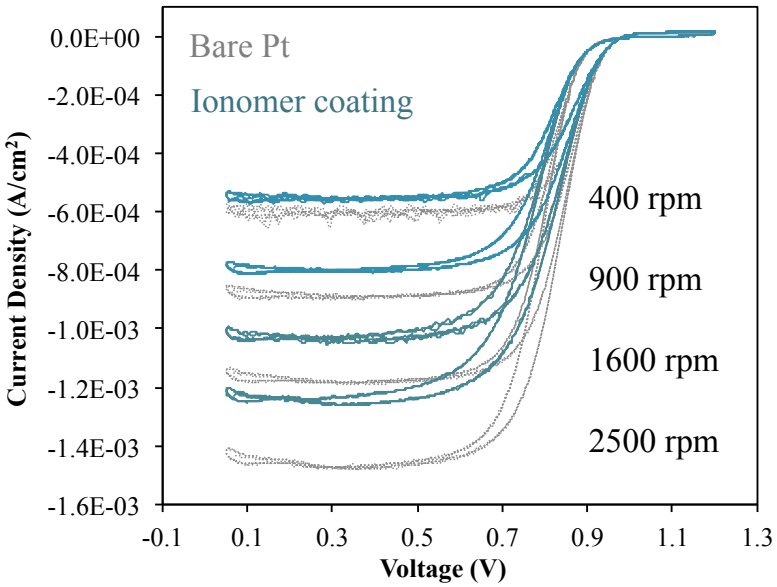

Figure A2. 7 Limiting current comparison between bare Pt electrode and electrode coated with thin PFSA layer, at different rotating speeds.

It is clear that the electrode with PFSA coating has lower current density compared to the bare electrode. This is caused by the PFSA coating, which blocks the access of O_2 to the Pt. This blockage results

in a reduced limiting current. O_2 permeability can be extracted from the ratio between limiting currents with and without PFSA coating, and normalized based on the thickness of the film.[8] During normalization, the assumption made was that the imperfection of the film coating can be neglected, including full coverage of the electrode surface and uniform thickness.

The ORR study has proven to be reliable and effective to evaluate different ionomers, and more importantly to probe catalytic activities.[7, 8, 10, 12] Unfortunately, some of the PFSA thin films ended up dissolving into the electrolyte solution during the electrochemical cleaning and ORR analysis. To overcome this issue, an annealing procedure has been investigated. The results are inconclusive; therefore, future experiments are required to produce a stable PFSA coating in the electrolyte solution. It is difficult to determine when the film starts to dissolve, since film thinning only causes minor current drift, often within detection error.

In summary, a system for ORR study requires extreme cleanness, which is difficult to achieve and maintain. Therefore, anion adsorption measurements are not under consideration with the current experimental setup. The O_2 permeation in the solution state, i.e. the product of diffusivity and concentration in the film, can be probed using the limiting current analysis of ORR using RDE. However, it is quite different compared to the non-solution environment experienced by a real cell in MEA form. This method will definitely provide useful information regarding O_2 permeation of the PFSA alone, since it can separate PFSA from other components in the MEA. For the current project, many challenges including dissolved PFSA cast film and non-clean cell environments have been encountered. The oxygen permeability

measurement from ORR study was not fully successful; however another useful electrochemical method that is often used in FC research has been explored.

A.2.4 Summary and Remark

This work serves the purpose of exploring the alternative methods to measure gas permeability. The time-lag method is an effective way to evaluate bulk gas permeation especially for O_2, and it has been commonly used in FC manufacturing for quality control purpose. The limiting current analysis of ORR using the RDE method allows one to separate the cathodic reaction from the complex FC operation. Nevertheless, there are several challenges to overcome in the future. The time-lag method is likely to overestimate the overall permeability and is sensitive to the preparation of the MEA. The limiting current study is extremely sensitive towards contamination in the cell setup due to Pt's activity, and it can only provide permeation information in the solution state. Furthermore, the PFSA thin film in the solution cell for the ORR study needs to be stable, thus the annealing procedure needs to be optimized.

The time-lag method is an efficient method towards measuring bulk gas permeability of a MEA or a stack of fuel cells. The limiting current analysis is ideal for focusing on half-cell reactions without any interference. For the purpose of evaluating the O_2 permeability of PFSA in membrane form, time-lag method is preferred.

A.2.5 References

1. K. Broka and P. Ekdunge, *J. Appl. Electrochem.*, 1997, **27**, 117-123.
2. A. Z. Weber, *J. Electrochem. Soc.*, 2008, **155**, B521-B531.
3. J. Wu, X. Z. Yuan, H. Wang, M. Blanco, J. J. Martin and J. Zhang, *Int. J. Hydrogen Energy*, 2008, **33**, 1735-1746.
4. H. Zhang, J. Li, H. Tang, Y. Lin and M. Pan, *Int. J. Hydrogen Energy*, 2014, **39**, 15989-15995.
5. M. Schalenbach, T. Hoefner, P. Paciok, M. Carmo, W. Lueke and D. Stolten, *The Journal of Physical Chemistry C*, 2015, **119**, 25145-25155.
6. M. Schalenbach, M. A. Hoeh, J. T. Gostick, W. Lueke and D. Stolten, *The Journal of Physical Chemistry C*, 2015, **119**, 25156-25169.
7. D. Banham, S. Ye, K. Pei, J.-i. Ozaki, T. Kishimoto and Y. Imashiro, *J. Power Sources*, 2015, **285**, 334-348.
8. S. Gottesfeld, I. Raistrick and S. Srinivasan, *J. Electrochem. Soc.*, 1987, **134**, 1455-1462.
9. J. Chen, L. S. Loo and K. Wang, *Journal of Membrane and Separation Technology*, 2012, **1**, 94-99.
10. S. J. Lee, S. I. Pyun, S. K. Lee and S. J. L. Kang, *Isr. J. Chem.*, 2008, **48**, 215-228.
11. B. Levich, *Discussions of the Faraday Society*, 1947, **1**, 37-49.
12. C. Song and J. Zhang, *Electrocatalytic oxygen reduction reaction*, 2008.

Appendix 3.

Pulse Sequence for ^{19}F Dipolar Recoupling NMR

The fluorine double quantum (DQ) NMR pulse sequence using $R26_4^{11}$ composite pulse. This is an interleaved pseudo 2D experiment. A detailed explanation is stated in **Chapter 2**, along with the process of normalizing the DQ intensity.

```
; PARAMETERS
;-------------------------------------------------
;d1  : recycle delay
;d20 : delay b/w presaturation pulses
;l20 : number of presaturation pulses

;p1  : 90 deg pulse (F1)
;pl1  : 90 deg pulse power (F1)

;cnst31 : spinning frequency (in Hz)
;l1 : N symmetry number
;l2 : n symmetry number
;l3 : nu symmetry number
;p11 : length of R element 90 pulse
;p12 : length of R element 270 pulse
;pl11 : R sequence power level (F1)
;l11 : no. pairs of R elements in excitation and reconversion for first
slice
```

```
;l10 : increment step size for l11 in next slices
;d11 : length of excitation and reconversion periods
;d10 : Z-filter delay
;d31 : rotor period


; CALCULATIONS
;-------------------------------------------------
;calculate length of one rotor period
"d31 = 1.0s/cnst31"

;calculate length of excitation and reconversion periods
"d11 = 2*l11*d31*l2/l1"

;calculate the 90 and 270 pulse lengths for R element
"p11 = 0.25*d31*l2/l1"
"p12 = 0.75*d31*l2/l1"

;calculate the R element phases (phi=nu/N*pi)
"cnst1=(180.0*l3)/l1"               ; phi
"cnst2=cnst1+180"             ; phi+180
"cnst3=-1*cnst1"              ;-phi
"cnst4=-1*cnst1+180"                ;-phi+180

"acqt0=-p1/2"

define loopcounter nfid
"nfid=td1/2"


; PULSE SEQUENCE
;-------------------------------------------------

; DQ spectrum (uses ph31 phase list for receiver)
;-------------------------------------------------
1 ze
  d11
```

```
  d31

;PRESATURATION (on F1)
2 d20
  (p1 ph20 pl1):f1
  lo to 2 times l20

;RECYCLE DELAY
  d1 pl11:f1

;DQ EXCITATION (on F1)
3 p11 ph11+cnst1
  p12 ph11+cnst2
  p11 ph11+cnst3
  p12 ph11+cnst4
 lo to 3 times l11

;DQ RECONVERSION (on F1)
4 p11 ph12+cnst1
  p12 ph12+cnst2
  p11 ph12+cnst3
  p12 ph12+cnst4
 lo to 4 times l11

;Z-FILTER
  d10

;OBSERVE PULSE (on F1)
  (p1 pl1 ph13):f1

;ACQUISITION
  go=2 ph31
  30m wr #0 if #0 zd    ;save data to disk and reset phase lists


; REFERENCE spectrum (uses ph30 phase list for receiver)
;-----------------------------------------------
```

```
;PRESATURATION (on F1)
12 d20
  (p1 ph20 pl1):f1
  lo to 12 times l20

;RECYCLE DELAY
  d1 pl11:f1

;DQ EXCITATION (on F1)
13 p11 ph11+cnst1
  p12 ph11+cnst2
  p11 ph11+cnst3
  p12 ph11+cnst4
 lo to 13 times l11

;DQ RECONVERSION (on F1)
14 p11 ph12+cnst1
  p12 ph12+cnst2
  p11 ph12+cnst3
  p12 ph12+cnst4
 lo to 14 times l11

;Z-FILTER
  d10

;OBSERVE PULSE (on F1)
  (p1 pl1 ph13):f1

;ACQUISITION
  go=12 ph30
  30m wr #0 if #0 zd    ;save data to disk and reset phase lists

;INCREMENT LOOP COUNTER
15 1m iu11
  lo to 15 times l10
```

```
;LOOP BACK TO BEGINNING
  lo to 2 times nfid

exit

;PHASE LISTS
ph20 =  0
ph11 =  0
ph12 =  1 2 3 0
ph13 =  0 0 0 0  1 1 1 1  2 2 2 2  3 3 3 3
ph31 =  0 2 0 2  1 3 1 3  2 0 2 0  3 1 3 1
ph30 =  0 0 0 0  1 1 1 1  2 2 2 2  3 3 3 3
```

Appendix 4.

Pulse Sequence for Diffusion NMR

The pulse field gradient stimulated echo (diffSte) sequence used in the diffusion profile study. NMR experiments were carried out with a Bruker Avance III NMR spectrometer equipped with a Diff50 probehead.

The diffusion measurements were performed with a range of maximum gradient value, 960 G/cm – 440 G/cm, at temperature range 295 K – 340 K. The gradient strength was set to increase linearly in 8 steps depending on expected diffusion coefficient, up to the maximum strength mentioned earlier. Diffusion time (Δ) was set to 20 ms at 295 K and 10 ms at 320 and 340 K. Effective gradient pulse duration time (δ) was set to 1 ms at 295 K and 0.5 ms at 320 and 340 K.

```
;diffSte
;new version using built in gradient functions as shapes 13.12.2007 KLZ
;pl2 --> pl12, lock during DELTA removed, comments improved 29.05.2008
KLZ
;1D mode included 22.08.08 KLZ
;variable gradient amplitude ramp included 30.09.09 KLZ
;LED included 22.12.2009 KLZ
;new mc syntax and use of ZGOPTNS rather than loop counters 16.06.11 KLZ
;ZGOPTNS corrected 22.12.2011 KLZ
;spoilRec included 28.01.2013 KLZ
;
;$CLASS=diff
;$DIM=2D
;$TYPE=exp


#include <Grad.incl>
```

```
#include <Avance.incl>
#include <Grad_Pulse.incl>

define list<gradient> diff_ramp=<$GPNAM31>

"acqt0=0"
;-------------------------------------------------------------------------
------

ze
10u
5m pl1:f1                                   ;set rf power level

start,      100u
#ifdef DEC
                  1u pl12:f2                    ; decoupler use pl12
            1u do:f2                      ; decoupler off during d1
#endif
#ifdef LOCK
            d1 LOCKH_OFF                  ; lock on during d1
                  d11 UNBLKGRAD                 ; unblank gradient
amplifier, lock hold during experiment
#endif
#ifndef LOCK
                  d1  H2_PULSE
                  d11 UNBLKGRAMP                ; unblank gradient
amplifier
#endif
;------------------------- Spoiler recovery sequence -------------------
-----------
#ifdef SpoilRec
                  p1:f1 ph11
                  p23:gp23                  ;(10m:1=18 G/cm)
                  d2
                  p1:f1 ph12
                  p24:gp24                  ;(1m:-5=-90 G/cm)
                  d2
                  d23   BLKGRAMP
                  d11 UNBLKGRAMP                  ; unblank gradient
amplifier
#endif
;-------------------------- Start of dummy gradient loop ---------------
------------
#ifdef dummyGrad
                  dummy, 1u
                        gradPulse( cnst1, cnst2, cnst3, d17, d18, d16,
l8, l9, diff_ramp)
                        d2                                ; gradient
stabilisation time
                        d9 BLKGRAMP                 ; tau
#ifdef spoil
                  d11 UNBLKGRAMP                ; unblank gradient
amplifier
                              p19:gp5                             ;
spoiler gradient, sine shape
```

```
                              d2                        ; gradient
stabilisation time
#endif
                        d5 BLKGRAMP                   ; long tau
                        d11 UNBLKGRAMP                  ; unblank gradient
amplifier
                  lo to dummy times l13       ; l13 number of dummy
gradient pulses
#endif
;-------------------------- Start of experiment ------------------------
-----------
                  p1:f1 ph1                         ; 90 degree pulse
            gradPulse( cnst1, cnst2, cnst3, d17, d18, d16, l8, l9,
diff_ramp)
                  d2                                ; gradient
stabilisation time
                  d9 BLKGRAMP                     ; tau
                  p1:f1 ph2                       ; 90 degree pulse
#ifdef spoil
                d11 UNBLKGRAMP                  ; unblank gradient
amplifier
                        p19:gp5                           ; spoiler
gradient, sine shape
                        d2                        ; gradient stabilisation
time
#endif
                  d5 BLKGRAMP                     ; long tau
                  d11 UNBLKGRAMP                    ; unblank gradient
amplifier
                  p1:f1 ph3                       ; 90 degree pulse
            gradPulse( cnst1, cnst2, cnst3, d17, d18, d16, l8, l9,
diff_ramp)
                  d2                                ; gradient
stabilisation time
                  d10 BLKGRAMP                ; tau
;-------------------------- Start of LED module  ------------------------
------------
#ifdef LED
            p1:f1 ph4
#ifdef spoil
            d11 UNBLKGRAMP                    ; unblank gradient
amplifier
                  p19:gp5*-1                        ; spoiler
gradient, sine shape
#endif
                  d2                                ; gradient
stabilisation time
            d19 BLKGRAMP
            p1:f1 ph5
#endif
;-------------------------- End of LED module  -------------------------
----------
#ifdef DEC
            go=start ph31 cpd2:f2           ; start acquisition with
decoupling
```

```
#endif
#ifndef DEC
            go=start ph31                    ; start acquisition
#endif
            100u mc #0 to start F1QF(calgrad(diff_ramp))
#ifdef DEC
        100m do:f2                           ; wait for data storage,
decoupler off
#endif
#ifndef DEC
        100m                                 ; wait for data storage
#endif
#ifdef LOCK
      100m rf #0 LOCKH_OFF                   ; reset file pointer, lock on
#endif
#ifndef LOCK
      100m rf #0                                ; reset file pointer
#endif
      lo to start times l1                      ; l1 = Number of
repetitions
exit

ph11= 0
ph12= 1
#ifndef LED
ph1= 0 0 0 0 2 2 2 2  1 1 1 1 3 3 3 3
ph2= 1 3 0 2
ph3= 1 3 0 2
ph31=0 0 2 2 2 2 0 0  3 3 1 1 1 1 3 3
#endif
#ifdef LED
ph1= 0 0 0 0 0 0 0 0  2 2 2 2 2 2 2 2 1 1 1 1 1 1 1 1  3 3 3 3 3 3 3 3
ph2= 0 0 0 0 0 0 0 0  2 2 2 2 2 2 2 2 1 1 1 1 1 1 1 1  3 3 3 3 3 3 3 3
ph3= 0 0 0 0 0 0 0 0  2 2 2 2 2 2 2 2 1 1 1 1 1 1 1 1  3 3 3 3 3 3 3 3
ph4= 0 0 0 0 2 2 2 2  2 2 2 2 0 0 0 0 1 1 1 1 3 3 3 3  3 3 3 3 1 1 1 1
ph5= 0 1 2 3 2 3 0 1  2 3 0 1 0 1 2 3 1 2 3 0 3 0 1 2  3 0 1 2 1 2 3 0
ph31=0 1 2 3 0 1 2 3  2 3 0 1 2 3 0 1 1 2 3 0 1 2 3 0  3 0 1 2 3 0 1 2
#endif

;pl1: f1 channel - power level for pulse (default)
;pl2: f2 channel - default not used
;pl12: f2 channel - decoupling power
;p1: f1 channel -  90 degree pulse
;d17: gradient ramp up time
;d16: gradient ramp down time
;d18: gradient duration
;p19: spoil gradient duration
;d1: relaxation delay; 1-5 * T1
;d2: gradient stabilisation time
;d5: DELTA remainder
;d9: tau remainder
;d10: tau remainder, used to shift trigger position
;d11: gradient amplifier unblank delay 200 us
;d23: spoiler recovery delay
```

```
;ns: 16 * n
;l1: Number of repetitions
;td1: number of experiments
;l13: number of dummy gradient pulses


;$Id: diffSte,v 1.10 2013/02/11 15:37:34 ber Exp $
```

Appendix 5.

Calcium L-Edge XAS Analysis

The Ca 2p spectra of PFSA 770 and PFSA 825 membranes were collected to determine the possible cation contamination, which suggests the high Ca content in PFSA 825. The green spectrum belongs to PFSA 770, and the blue spectrum belongs to PFSA 825.